

DISSERTATION

THE MICROTUBULE-ASSOCIATED PROTEIN SHE1 REGULATES DYNEIN-MEDIATED  
SPINDLE POSITIONING IN BUDDING YEAST

Submitted by

Kari Ecklund

Department of Biochemistry and Molecular Biology

In partial fulfillment of the requirements

For the Degree of Doctor of Philosophy

Colorado State University

Fort Collins, Colorado

Fall 2020

Doctoral Committee:

Advisor: Steven Markus

Jennifer DeLuca

Olve Peersen

Diego Krapf

Copyright Kari Hope Ecklund 2020

All Rights Reserved

## ABSTRACT

### THE MICROTUBULE-ASSOCIATED PROTEIN SHE1 REGULATES DYNEIN-MEDIATED SPINDLE POSITIONING IN BUDDING YEAST

Microtubules are polar filamentous proteins part of a complex cytoskeletal network within cells that provides an organized interface with which motors use to transport vesicular cargoes and organelles, and mediate positioning of the mitotic spindle during cell division. There are two groups of molecular motor proteins that use microtubules as a track: (1) kinesins, the predominant anterograde motors and which are represented by six distinct different motors in budding yeast and (2) dynein, the predominant retrograde motor to which there is only one, cytoplasmic dynein, in budding yeast. Regulation of motor proteins is paramount to ensure that these various functions are achieved efficiently in a time and space-sensitive manner. There are many ways microtubules regulate their track, including through a class of highly diverse proteins called microtubule-associated proteins (MAPs), one of which in budding yeast is She1. In budding yeast, the only currently known role of cytoplasmic dynein is positioning the mitotic spindle during cell division. To direct the polarized movement of the spindle towards the daughter-cell, dynein relies on the MAP She1. To understand the mechanism by which She1 may regulate dynein-mediated spindle positioning, we first characterized the effects of She1 on dynein motility using recombinant protein. Our results demonstrated that She1 affects dynein motility by enhancing dynein-microtubule binding through simultaneous interactions with the dynein microtubule binding domain (MTBD) and the microtubule. From our *in vitro* data, we suggested a model where She1 assists dynein force generation to pull the large nucleus into the narrower bud neck connecting mother and daughter cells. However, we tested this model *in vivo* and found no such effects on nuclear translocation success, leaving us to investigate an

alternative model where She1 polarizes spindle movements towards the daughter cell through inhibiting dynein activity in the mother cell. We explored this model *in vivo* using a comprehensive analysis of dynein-mediated spindle movements which revealed She1 ensures dynein in the daughter cell maintains bud neck proximity by inhibiting dynein activity and the initiation of dynein-mediated spindle movements in the mother cell. Moreover, we find that this process depends on She1 binding to aMTs in the mother cell and not spindle microtubules where She1 also localizes. Finally, we provide evidence that She1 requires the MTBD of dynein for some aspects of this inhibition, reconciling, in part, our *in vitro* and *in vivo* data. Our data provides a fascinating new mechanism of regulation by a MAP and suggests a new angle to approach future exploration of MAP-mediated regulation in higher eukaryotes.

## ACKNOWLEDGEMENTS

The work presented in this dissertation is the product of a long, and at times difficult journey which would not have been possible without the mentorship of my advisor Steven Markus and my committee, and the friendships with those that lived it with me. Thus, it is my pleasure to acknowledge those individuals specifically, for their impacts on myself and my career as a research scientist.

Firstly, I would like to thank my advisor Steven Markus, for taking a chance and accepting me into your lab. You have a contagious drive for scientific research that knows no bounds and your mentorship and patience has both helped and allowed me to develop my skills and confidence as a scientific researcher.

Thank you to my committee, Jake DeLuca, Olve Peersen, and Diego Krapf, who always offered insightful discussion to help me think critically about my project.

There are many individuals who contributed to this work that I would also like to acknowledge. Thank you Megan Bailey and Chip Asbury for performing the optical trapping experiments, and Carsten Dietvorst for writing the cortical proximity and bud neck distance code. I would also like to thank Jeff Moore for kindly providing  $\Delta$ CAP-Gly yeast strains and Cécile Boscheron for providing the TUB1-G437R integration plasmid. Finally, I would like to thank Luke Rice and Elizabeth Geyer for their guidance while I was establishing the yeast tubulin protein purification in our lab.

I would like to thank my lab family Lindsay Lammers, Matt Marzo, Tyler Biebighauser, Matt Dilsaver, and Jackie Griswold, for making this chapter in my life an epic one that I will never forget. Lindsay and Matt, you are the most supportive and empowering individuals I have had the pleasure of calling friends, which has made a permanent, positive impact in my life.

I would like to thank my family, who, without your influence, I would not be the same person that I am. Thank you mom, for instilling in me an iron, and almost stubborn will, that has

helped me succeed in the most difficult of times. And thank you dad, for nurturing my curiosity in the workings of the world at a young age. And my sister Meghan, who reminds me that a creative and imaginative approach can lead to new discoveries. Finally, Nihad, your belief and encouragement in my abilities was instrumental in realizing my goals. Thank you for your unwavering support day after day.

## DEDICATION

To Nihad Ziga and Meghan Ecklund. I love you so much!

## TABLE OF CONTENTS

ABSTRACT.....	ii
ACKNOWLEDGEMENTS.....	iv
DEDICATION.....	vi
LIST OF FIGURES.....	ix
CHAPTER 1 – Introduction.....	1
1.1 Literature review & thesis rationale.....	1
1.2 Overview of findings.....	10
1.2 Figures.....	12
CHAPTER 2 – She1 affects dynein through direct interaction with the microtubule and the dynein microtubule-binding domain.....	14
2.1 Introduction.....	14
2.2 Results.....	17
2.3 Discussion.....	27
2.4 Methods.....	31
2.5 Figures.....	42
CHAPTER 3 – The MAP She1 coordinates dynein-mediated spindle positioning by spatially restricting dynein activity in yeast.....	57
3.1 Introduction.....	57
3.2 Results.....	59
3.3 Discussion & future directions.....	72
3.4 Methods.....	88
3.5 Figures.....	90
REFERENCES.....	110
APPENDIX 1 – Supplementary figures for Chapter 2.....	130
APPENDIX 2 – A glycine to arginine mutation in Tub1 position 437 compromises She1 binding and reveals new insight into $\alpha$ -tubulin isoforms.....	144
A2.1 Introduction.....	144
A2.2 Results.....	146
A2.3 Discussion & future directions.....	149

A2.4 Methods.....	151
A2.5 Figures.....	154
APPENDIX 3 – Systematic investigation into She1 binding domains.....	158
A3.1 Introduction.....	158
A3.2 Results.....	158
A3.3 Discussion & future directions.....	160
A3.4 Methods.....	161
A3.5 Figures.....	164
APPENDIX 4 – She1 mass-spectrometry reveals phosphorylation sites & protein interactions .....	167
A4.1 Introduction.....	167
A4.2 Results & discussion.....	167
A4.3 Methods.....	169
APPENDIX 5 – Purification of yeast tubulin and assessment of She1 binding and dynein motility .....	172
A5.1 Introduction.....	172
A5.2 Results & discussion.....	173
A5.3 Methods.....	174
A5.4 Figures.....	184

## LIST OF FIGURES

Figure 1.1.....	13
Figure 2.1.....	43
Figure 2.2.....	45
Figure 2.3.....	47
Figure 2.4.....	49
Figure 2.5.....	51
Figure 2.6.....	53
Figure 2.7.....	55
Figure 3.1.....	91
Figure 3.2.....	93
Figure 3.3.....	95
Figure 3.4.....	97
Figure 3.5.....	99
Figure 3.6.....	101
Figure 3.7.....	103
Figure 3.8.....	105
Figure 3.9.....	107
Figure 3.10.....	109
Figure A1.1.....	131
Figure A1.2.....	133
Figure A1.3.....	134
Figure A1.4.....	136
Figure A1.5.....	138
Figure A1.6.....	140
Figure A1.7.....	142
Figure A2.1.....	155
Figure A2.2.....	156
Figure A3.1.....	165

Figure A3.2.....	166
Figure A5.1.....	185
Figure A5.2.....	186

## CHAPTER 1

### INTRODUCTION

#### 1.1 LITERATURE REVIEW & THESIS RATIONALE

Motion is an integral part of what we all might include in our definition of life. The flagellum of an *E. Coli* beats like a rigid propeller guiding the bacterium to its next meal, and within eukaryotic cells, complex cytoskeletal networks comprised of protein polymers actin, microtubules, and intermediate filaments span the length of the cell, providing a molecular “highway” with which to direct the movement of molecular motors to transport vesicular cargoes and organelles. This motion, which specifically implies purpose rather than the consequences of random diffusion, are some of the most fascinating concepts in biology. Biologists did not widely accept the concept of a cellular cytoskeleton in all eukaryotes until the 1960’s with the improvement of electron microscope technology, believing previously that many molecules simply floated freely within the cytoplasm of cells (reviewed in Frixione et al., 2000). Today, we understand the importance of cytoskeletal structures in their ability to provide a polarized, directional track with which to direct the movement of molecules to all parts of the cell and to provide the organized backbone for a multitude of processes (reviewed in van Beuningen et al., 2016; Guedes-Dias et al., 2019; reviewed in Robison et al., 2017).

Microtubules are one such component of the cytoskeleton. Microtubules are essential polymers formed from the polymerization of conserved  $\alpha$ - and  $\beta$ -tubulin heterodimers. These large proteinaceous ensembles are highly dynamic, switching stochastically between polymerization and depolymerization, an essential behavior called dynamic instability, in order to achieve the diverse roles they play within cells (Mitchison et al., 1984; Manka et al., 2018). Tubulin heterodimers typically assemble head-to-tail, with  $\beta$ -tubulin on the leading edge of microtubule growth to make hollow, cylindrical rods of varying flexibility and shape depending on

$\beta$ -tubulin GTP or GDP containing status and other regulatory factors (Igaev et al., 2018; Mitchison et al., 1984; Voter et al., 1984). Additionally, the shape and flexibility of the microtubule is different at the so called GTP-cap, a GTP rich region at the plus end, which can define the localization of various microtubule-associated factors and regulate the dynamics of a growing and shrinking microtubule (Zhang et al., 2015; Alushin et al., 2014). In most organisms, the circumference of the hollow cylinder typically contains ~13-14 protofilaments, which can be affected by tubulin isoforms and microtubules associated proteins (MAPs), like doublecortin (DCX) (Fourniol et al., 2010; Howes et al., 2017). A nucleation event typically occurs at centrosomes composed of another tubulin type,  $\gamma$ -tubulin, which can act as a conformationally favorable base with which to help drive nucleation (Sulimenk et al., 2006). One heterodimer has two GTP-binding sites, one in  $\alpha$ -tubulin that exists within the dimer, near the binding contact with  $\beta$ -tubulin, and cannot be hydrolyzed, and one in  $\beta$ -tubulin that can be hydrolyzed to harness the chemical energy of GTP. Fascinatingly, this GTP is hydrolyzed after contact from a tubulin dimer of the growing end, in which case the  $\alpha$ -tubulin contact completes the binding pocket like a puzzle piece to allow cleavage of GTP to GDP+Pi (Alushin et al., 2014). It is critical that this hydrolysis occur after the right contacts with the  $\alpha$ -tubulin on the new heterodimer are made, otherwise this will lead to a catastrophe event and subsequent depolymerization (Mitchison et al., 1984; Dimitrov et al., 2008; Gardner et al., 2011). Upon ATP hydrolysis, conformational changes in  $\alpha$ -tubulin has been shown to lead to global rearrangements which induce strain upon the lattice and also adjust contacts between protofilaments (Yajima et al., 2012; Alushin et al., 2014). However, in the context of a cell, such regulation is critical to maintain highly dynamic structures the reorganize and reshape the cytoskeletal matrix, and to regulate the specific factors associated with microtubules.

Regulation of microtubule processes is achieved intrinsically through post-translational modifications on the heterodimer C-terminal tails, and through expression of various isoforms of both  $\alpha$  and  $\beta$ -tubulins that exhibit different properties for microtubule polymers (Lacroix et al.,

2010; Sirajuddin et al., 2014; Parker et al., 2018; Bode et al., 2003; Saillour et al., 2014; reviewed in Yu et al., 2015). However, there are many other modes through which microtubules and microtubule-based processes are regulated. Microtubules are a platform bound by many different proteins that are critical for the regulation of microtubule-based processes. Microtubule-associated proteins, or MAPs, are strewn about the microtubule lattice to regulate binding of other proteins, motility of motors, and alter the properties and structure of microtubules themselves. Many microtubule-associated proteins (MAPs) have specialized roles in regulating both microtubules and the binding of other MAPs. Some MAPs behave as enzymes that can break or depolymerize microtubules. The first report of a microtubule severing enzyme was in *X. laevis* egg extracts, which was named katanin, after the Japanese samurai sword (Vale et al., 1991; McNally et al., 1993). The microtubule severing enzymes spastin and katanin are a family of ATPase enzymes found throughout higher eukaryotes that catalytically remove tubulin dimers from the microtubule lattice (reviewed in Roll-Mecak et al., 2010; Diaz-Valencia et al., 2011; McNally et al., 1993). Katanin exhumes tubulin heterodimers from the GDP rich region of microtubules, resulting in nanoscale damage, observed *in vivo* and *in vitro* (Srayko et al., 2006; Zhang et al., 2011; Vemu et al., 2019; Roll-Mecak et al., 2006). Fascinatingly, this microtubule-damaging function, like spastin, has been shown to maintain microtubule density *in vivo*, serving as a critical factor in maintenance of microtubule arrays in neurons (Sherwood et al., 2004; Ahmad et al., 1999; Trotta et al., 2004; Lombino et al., 2019) and regulating the architecture and length of the mitotic spindle (reviewed in McNally et al., 2018; McNally et al., 2006; Loughlin et al., 2011; Zhang et al., 2007).

There are also many classes of MAPs that bind along the length of microtubules to perform many important functions in cells including maintenance of the cytoskeleton (e.g. katanin and spastin, mentioned before) and crosslinking antiparallel microtubules (e.g. PRC1). PRC1 localizes specifically to antiparallel microtubules that overlap in the midzone of the mitotic spindle, maintaining stability there (Bieling et al., 2010; Subramanian et al., 2010). MAPs also

perform “traffic control” of transport along microtubules driven by motor proteins in many cell types. Many of these MAPs that have been identified exhibit “roadblock” like properties, meaning they inhibit transport of more than one category of motor protein (reviewed in Bodakuntla et al., 2019). Such lack of specificity implies these MAPs act a physical barrier against the movement of motors on microtubules, rather than directly binding them. For example, tau, which has been implicated in intracellular transport of synaptic vesicles and organelles *in vivo*, inhibits both kinesin-1 and kinesin-3 motors. It does not have a dramatic effect on dynein motility, but does cause the motor to pause and take side steps or backwards steps (Ebner et al., 1998; Mandelkow et al., 2003; Monroy et al., 2020). The same can be said of MAP2, also a neuronal MAP that inhibits kinesin-1 and kinesin-3 families, and incidentally, shares similar microtubule binding repeats putting it in the same family of MAPs (Dehmelt et al., 2005; Monroy et al., 2020). The tau family also includes a non-neuronally expressed MAP4 that contains the same microtubule binding repeats, and which is interesting in its own right (Chapin et al., 1991). MAP4 is expressed in mammalian neurons like its tau and MAP2 counterparts, and also in nearly all other tissue types and has been linked to cardiovascular disease. MAP4 functions both at the mitotic spindle and astral microtubules of mammalian cells to assist in dynein-mediated spindle positioning along with a microtubule-cortex anchoring MAP CLASP1 (Tokuraku et al., 2010; Parysek et al., 1985; Kotani et al., 1988; Samora et al., 2011; Lansbergen et al., 2006; Li et al., 2020). MAP4 regulates the large dynein cofactor dynactin likely through obscuring the microtubule from dynactin binding (Samora et al., 2011). A novel MAP, TPX2, found in *X. laevis* egg extracts, is involved in both dynein and kinesin transport during mitosis. Specifically, it is required for the transport of kinesin-like motor XKlp2 to minus ends by hitchhiking on the minus-end directed motor dynein, for pole focusing during mitosis (Boleti et al., 1996; Wittmann et al., 2000).

Other groups of MAPs specialize in associating with the microtubule plus ends (+TIPs; reviewed in Akhmanova et al., 2015). These include the XMAP215 family, which promote

microtubule polymerization through enhancing the recruitment of tubulin dimers at the farthest distal end the growing microtubule tip (Brouhard et al., 2008; Zanic et al., 2013; Maurer et al., 2014). This family of MAPs are characterized by the presence of variable copies of tubulin binding TOG domains which recognize the curved (distal plus end) conformation of unbound tubulin dimers and, perhaps, the microtubule sheets at plus ends. They track the microtubule ends through a diffusional process controlled by weakly binding, disordered regions (Widlund et al., 2011; Brouhard et al., 2008; Ayaz et al., 2014). Another +TIP, EB1, is suspected to promote the lateral attachments of protofilament interactions by putting GTP hydrolysis into overdrive and therefore accelerating maturation of microtubules (Maurer et al., 2014). The structural domains that confer binding recognition of EB1 to the GTP-cap of microtubules is well understood to be through calponin homology domains (CH domains; highly positively charged) flanked by negatively charged, disordered linkers that tune their interactions with microtubules (Hayashi et al., 2003; Xia et al., 2014; Slep et al., 2007; Buey et al., 2011). Interestingly, it is suspected that the binding position of the EB1 protein, which spans two tubulin heterodimers, may recognize the protofilament strain induced by GTP hydrolysis, mentioned previously, to preferentially associate with the GTP-cap (Vitre et al., 2008; Maurer et al., 2012; Alushin et al., 2014). This kind of structural preference for GTP containing protofilaments has been demonstrated with other MAPs, including DCX (Francis et al., 1999; Bechstedt et al 2014; Ettinger et al., 2016).

Some +TIP factors, like CLIP-170, are suspected to require the bonafide +TIP trackers (like EB1) in order to concentrate at the plus ends of microtubules. For instance, Bik1/CLIP-170, contains a CAP-Gly domain that recognizes EEY/F motifs, specifically, it recognizes the aromatic tyrosine (mammals) or phenylalanine (yeast) on microtubule C-terminal tails and the c-terminus of Bim1/EB1, which can be highly sensitive to post-translational modifications as a means to regulate binding (Peris et al., 2006). A small nonpolar motif, SxIP (where x is any amino acid), has also been linked among EB-binding proteins (Badin-Larçon et al., 2004;

Stangier et al., 2018; reviewed in Kumar et al., 2012), a process which is seen in yeast and mammalian cells (Bieling et al., 2008; Honnappa et al., 2009; Honnappa et al., 2006; Mishima et al., 2007). Fascinatingly, in several examples, regulation of plus end localization is achieved through direct competitive binding of EB1/Bim1 binding proteins that contain SxIP motifs and those containing CAP-Gly domains, suggesting a novel mode of regulating +TIPs and complexes that localize there, such as assemblies of EB1, CLIP-170, and the p150Glued (CAP-Gly domain) which can serve as platforms for mammalian dynein motor targeting *in vitro* and in budding yeast mitosis (Duellberg et al., 2014; Roberts et al., 2014; Lammers et al., 2015).

Additionally, microtubules serve as molecular highway for motile MAPs, or motor proteins, which drive transport and movement of vesicles and organelles during intracellular transport and cell division. There are two groups of motor proteins that use microtubules as their molecular tracks: (1) kinesins are a large superfamily of motor proteins defined by 14 families and is the predominant anterograde (plus-end directed) motor, though with exceptions to this rule. The kinesin-14 family of motors are evolutionarily conserved retrograde kinesin motors in eukaryotes. There are over 45 different kinesins specialized for various roles in mitosis and cell transport. Several kinesin families, specifically kinesin-8 have been shown to track the plus ends through interaction with EB1 through MCAK (SxIP motif containing protein) to promote microtubule depolymerization (Tanenbaum et al., 2011). (2) Dynein is part of smaller family of motors, unlike kinesin, there are only two families which are axonemal and cytoplasmic dynein. Most retrograde (minus-end directed) transport is achieved by this motor, a fascinating conundrum when it comes to the overwhelming number of functions dynein is involved in (Moore et al., 2009; Egan et al., 2012; Koonce et al., 2000; Driskell et al., 2007; Presley et al., 1997; Gross et al., 2002; Tsai et al., 2007; Collins et al., 2012). This suggests that dynein must require a plethora of regulatory factors to tune its localization and motility within a cell, to succeed at its broad range of functions. As previously mentioned, dynein is targeted to microtubule plus ends, where it is activated to perform many roles in transport in cells and

spindle positioning during cell division. In budding yeast, cytoplasmic dynein performs only one function (that we know of so far) which is positioning the mitotic spindle during cell division (Moore et al., 2009). Cytoplasmic dynein is suspected to interact with Pac1 in the cytoplasm where it is stabilized by Pac1 from an autoinhibited, to an uninhibited, conformation (Marzo et al., 2020). Then, dynein is targeted to plus ends of astral microtubules through Pac1 interaction with the +TIP Bik1 (CLIP-170), which fascinatingly, does not require Bim1 to tip-track like mammalian cells (but may play a role in its localization there) (Lee et al., 2003; Lee et al., 2005; Sheeman et al., 2003; Markus et al., 2009; Marzo et al., 2020).

As previously mentioned, microtubule organizing centers (MTOCs) which are centrosomes (or simply spindle pole bodies in *S. cerevisiae*) are the origin point of microtubule growth, and though they can vary greatly between organisms, this main purpose is resolute (Porter et al., 1966; Voter et al., 1984; reviewed in Sanchez et al., 2017). Centrosomes are the epicenter for building the mitotic and meiotic spindles from nucleation of microtubule protofilaments. In *S. cerevisiae*, or budding yeast, the functionally equivalent centrosome is the spindle pole body (SPB) – though it is structurally different from centrosome – and is the only MTOC unit in yeast. The SPBs are embedded within in the nuclear envelope with inner and outer plaques that face either the nucleoplasm or the cytoplasm. The inner plaque is associated with spindle and interpolar microtubules whereas the outer plaque nucleates astral microtubules (aMTs) (Byers et al., 1975; Moens et al., 1971). Throughout the cell cycle in budding yeast, the nucleus remains intact (and therefore the spindle pole bodies remain embedded in the nucleus as well), a unique feature of these organisms (Fig 1.1a). The nucleus houses the mitotic spindle and genetic material, which, given the asymmetric nature of budding yeast mitosis, must be positioned between mother and daughter cells for proper cell division. This region, called the bud neck, is the site of cytokinesis (Fig 1.1a). The astral microtubules that emanate from the spindle pole bodies are used to position the mitotic spindle through two compensatory, nearly redundant pathways: (1) Kar9 (karyogamy mutant 9) is localized to microtubule plus ends of the

bud-inherited spindle pole body through interaction with +TIP Bim1 (Liakopoulos et al 2003; Kusch et al., 2002). To align the spindle, Myo2 (Myosin V actin-based transport motor protein), is bound by the Bim1-Kar9 complex, linking the astral microtubule bound by Bim1 with the actin cytoskeletal network (Miller et al., 2000). Myo2 walks along actin cables emanating from the bud tip to tug the spindle and nucleus with it as it walks towards the bud tip (Yin et al., 2000; reviewed in Hwang et al., 2003; Maekawa et al., 2003). And (2) the pathway already alluded to, the dynein pathway. Dynein is targeted to the plus ends as previously noted, and through a currently unknown mechanism, dynein (in an active conformation, with a microtubule binding domain that is competent for microtubule binding) does not actively walk towards the minus end until it has been offloaded upon an astral microtubule encountering the cell cortex. Dynein, without Pac1 and along with the large dynein cofactor dynactin, is offloaded to the cortical receptor and adaptor protein Num1 (Lammers et al., 2015; Marzo et al., 2020). After offloading dynein engages in minus end directed motility (towards SPBs) on astral microtubules, leading to movement of the spindle and nucleus into the bud neck prior to cell division (Fig 1.1b).

In budding yeast, there are representatives from all categories of MAPs (including microtubule motors, to which there are 9 kinesins and one dynein). Of the plus-end localized MAPs, there are Bik1 and Bim1 (CLIP-170 and EB1 orthologues) as well as CLASP and XAMP215 orthologues Stu1 and Stu2, respectively (Berlin et al., 1990; Pasqualone et al., 1994; Schwartz et al., 1997; Wang et al., 1997). Two MAPs that localize to the spindle are IRC15 (unknown homolog) and Ase1 (PRC1 orthologue) which regulate microtubule dynamics and crosslink microtubules in fission yeast, respectively (Keyes et al., 2009; Lo'iodice et al., 2005). But additionally, there is the most fascinating of the yeast MAPs, She1, which also belongs to the category of indiscriminate microtubule lattice binders. She1 has been shown to localize to spindle microtubules and astral microtubules (Pigula et al., 2009; Woodruff et al., 2009; Markus et al., 2012) and is a potent binder of microtubules *in vitro*, suggesting She1 is a bonafide MAP *in vivo* (Markus et al., 2012). At the spindle midzone, it is suspected to regulate metaphase

spindle stability (Zhu et al., 2017) and kinetochore function through interaction with kinetochore component Mcm21 and Bim1 (Wong et al., 2007), and facilitate spindle disassembly prior to cytokinesis (Woodruff et al., 2010; Pigula et al., 2014). She1 functions at the kinetochore have also been implicated in regulating Ipl1 (Aurora B in mammalian cells) (Wong et al., 2007; Woodruff et al., 2010; Zhu et al., 2017). Additionally, She1 has been implicated in regulating dynein pathway function. Specifically, overexpression of She1 leads to a mispositioning defect as severe as *dyn1Δ*, moreover, this phenotype was exacerbated by *kar9Δ* and not *dyn1Δ* (Markus et al., 2012). Additionally, *she1Δ* cells exhibited dramatic spindle movements that were dynein-dependent, suggesting She1 suppresses dynein activity (Woodruff et al., 2009). Notably, this suppression appears to polarize spindle movement towards the bud neck, through an unknown mechanism (Markus et al., 2012). It was noted that She1 has an effect on dynein plus-end localization (it is reduced) and plus end localization of dynactin complexes (which is increased), suggesting She1 may be inhibiting dynein activity through restricting dynein-dynactin interaction at plus ends (Woodruff et al., 2009; Markus et al., 2011), yet She1 does not directly interact with any dynactin components nor prevent interactions between dynactin subunits, leaving the mechanism behind how She1 is indirectly preventing dynactin localization largely unknown (Bergman 2012; Markus et al., 2011). *In vitro* studies revealed that She1 is a potent inhibitor of dynein motility, even in the absence of dynactin, a behavior that is specific to dynein and not kinesin motors, suggesting, along with the *in vivo* data, that She1 may be directly inhibiting dynein motors in cells (Markus et al., 2012). Additionally, whether this regulation is achieved by spindle localized She1, or She1 on astral microtubules or the bud neck (where She1 also localizes), is unknown, as is the relevance of the *in vitro* data. The mechanism behind how She1 regulates dynein-mediated spindle positioning is unknown, as is the mechanism behind how She1 inhibits dynein motility *in vitro*, and hereby begins the focus of the findings in this dissertation.

## 1.2 OVERVIEW OF FINDINGS

In chapter 2, to determine the mechanism behind the potent effects of She1 on dynein motility *in vitro*, as described above, we enlisted basic biochemical techniques to systematically characterize the specifics of how dynein motility is affected by She1 using recombinant proteins. We found that She1 reduces the rate at which dynein consumes ATP by enhancing dynein-microtubule interaction and reducing the dissociation rate of dynein from microtubules, unsurprisingly leading to a reduced stepping frequency. Fascinatingly, we also found that She1 must simultaneously bind to the microtubule binding domain dynein and microtubule to exert these effects on dynein. No prior MAPs have been shown to exhibit this behavior which made it exciting to postulate how She1 could be contributing to the regulation of dynein-mediated spindle positioning in budding yeast. Given that She1 enhances dynein-microtubule interactions, we proposed a hypothesis where She1 assists dynein in moving the large nucleus into the narrow bud neck.

In chapter 3, we investigated our hypothesis that She1 assists dynein-mediated spindle positioning by assisting nuclear translocation into the bud neck. Importantly, we explored the relevance of our prior *in vitro* data to She1 function in cells. To begin, we characterized the consequences of *she1* $\Delta$  cells on spindle positioning and cell cycle progression and corroborated prior findings that She1 is important for spindle positioning. We next tested our hypothesis regarding nuclear translocation but determined this hypothesis was wrong. Revisiting our previous hypothesis, we carefully analyzed the effects of *she1* $\Delta$  on dynein-mediated spindle movement. We defined in moderate detail two parameters describing motor motility and three metrics describing general dynein activity in cells. We found that She1 inhibits dynein hyperactivity on astral microtubules, by localizing within the mother compartment and specifically inhibiting the initiation of dynein-mediated spindle pulling events. We also present evidence supporting that this inhibition is through She1 binding to both microtubules and the dynein microtubule binding domain. We were unable to determine the mechanism behind how

She1 regulates dynactin, but we concluded that She1 inhibition in the mother cell maintains the spindle within close proximity to the bud neck to ensure proper positioning (Fig 1.1b).

Appendix 2 includes valuable data that demonstrates the tubulin mutant used in chapter 3 has reduced She1 binding *in vivo*. This tubulin mutant was used to test She1-microtubule binding in the dynein spindle positioning phenotype. We determined that the tub-G437R mutation leads to reduced She1 binding to spindle, and presumably astral, microtubules. A fascinating, yet coincidental finding of this investigation was that the widely accepted representation of  $\alpha$ -tubulin isoforms in cells may be different than previously thought. We determined that spindle microtubules incorporate equal amounts of the two  $\alpha$ -tubulin isoforms, Tub1 and Tub3. Future studies are needed to test this hypothesis.

Our prior work demonstrated that She1 binds the microtubule binding domain, narrowing down the binding region on dynein from 500kD to 123 amino acids. We also corroborated that She1 binds the C-terminal tails of microtubules and that neighboring residues on the C-terminal  $\alpha$ -helix may also be critical for She1 binding. We wondered if we could similarly narrow down the regions on She1 that binds microtubules and dynein. We attempted to do this in appendix 3 by using yeast-2-hybrid and single molecule assays. We surmised that the microtubule binding region lies somewhere in C-terminal fragment 169-338 (corroborating results published by another lab during this time) and the dynein binding region is likely encompassed within regions on the N-terminus and C-terminus.

Previous studies have shown that a phosphomimic mutant of She1 inhibits dynein motility more potently than wildtype. We wondered if phosphorylation is a mechanism to temporally and spatially control She1 inhibition of dynein activity during mitosis. In appendix 4, we describe mass-spectrometry results that revealed novel phosphorylation sites on She1. Importantly, these sites are from cells where She1 is expressed at endogenous levels and arrested in metaphase, when we believe She1 actively inhibits dynein.

Finally, in appendix 5 we discuss the importance of using yeast microtubules for our future *in vitro* assays. For example, yeast Bim1 has been shown to tip track on yeast but not mammalian microtubules (Howes et al., 2018), indicating that subtle structural and sequence differences affect the behavior of MAPs. This appendix describes the purification steps and polymerization steps in detail to ensure this difficult protein purification can be done by others successfully in the future. Preliminarily, we also found differences in the inhibitory effects of She1 on dynein in single molecule assays using yeast microtubules.

### **1.3 FIGURES**

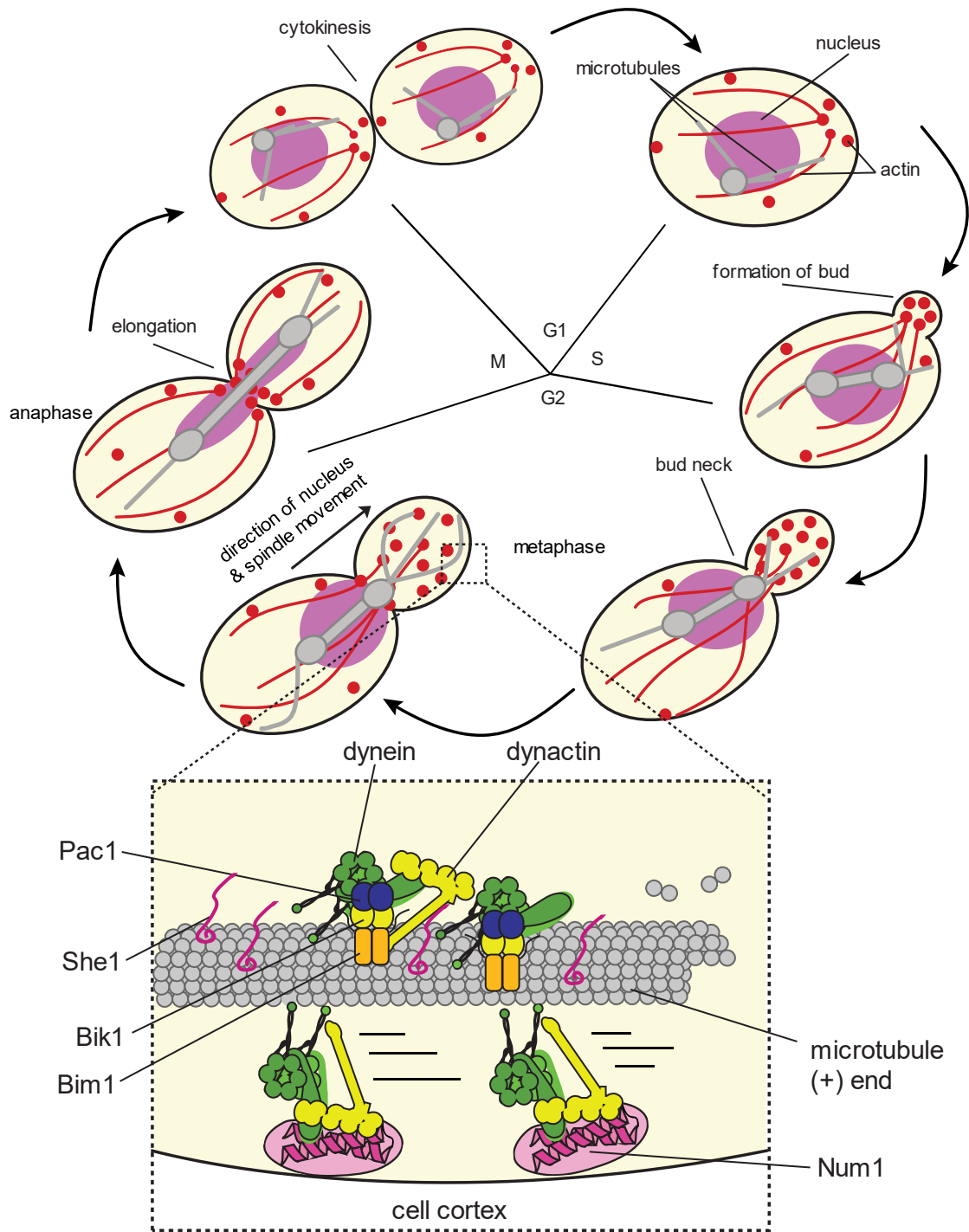


**Figure 1.1 Dynein-mediated spindle positioning during mitosis.** (a) Budding yeast cell cycle. (b) She1 inhibits dynein activity *in vivo* through binding the dynein MTBD and the microtubule. This inhibition is specific to the mother cell, where She1 is spatially restricted to mother-associated aMTs. How She1 regulates dynactin at plus ends is an outstanding question.

## CHAPTER 2

# SHE1 AFFECTS DYNEIN THROUGH DIRECT INTERACTION WITH THE MICROTUBULE AND THE DYNEIN MICROTUBULE-BINDING DOMAIN<sup>1</sup>

## 2.1 INTRODUCTION

The large size and crowded environment of a typical eukaryotic cell necessitates the tightly regulated active transport of myriad cargoes to various subcellular sites. In eukaryotic cells, this transport is mediated by a large family of molecular motors that walk along polarized actin and microtubule filaments (reviewed in Vale et al., 2003). The kinesin and dynein families of microtubule motors are responsible for cargo transport toward the plus and minus ends of microtubules (with few exceptions) that are generally situated at the cell periphery and cell center, respectively. Given the strict spatial and temporal requirements for motor-mediated cargo transport, precisely tuned motor activity is imperative for the development and maintenance of a healthy cell and tissue.

Rather than existing as bare tracks, microtubules are bound by various classes of microtubule-associated proteins (MAPs), including those that bind along the lattice (*e.g.*, MAP1A, tau, TPX2, PRC1) (Halpain et al., 2006; Dehmelt et al., 2005; Brunet et al., 2004; Mollinari et al., 2002), those that concentrate at the plus (*e.g.*, EB1, CLIP170, CLASP; Mimori-Kiyosue et al., 2000; Rickard et al., 1990; Akhmanova et al., 2001) or minus ends (*e.g.*, Patronin; Goodwin et al., 2010), and a large number of microtubule motors. Several studies

<sup>1</sup>This chapter was published in 2017 under the same name. S.M.M. designed the study. S.M.M. and K.H.E. generated the reagents, performed experiments, and analyzed the single molecule and binding data. L.G.L. performed the ATPase assays, and analyzed the data. T.M. and T.J.S. performed the high resolution stepping analysis. S.M.M., M.G.M. and K.H.E. acquired and analyzed the spindle oscillation and orientation data. S.M.M. performed the two-hybrid assay, and wrote the manuscript.

Reference:

Ecklund KH, Morisaki T, Lammers LG, Marzo MG, Stasevich TJ, and Markus SM. She1 affects dynein through direct interactions with the microtubule and the dynein microtubule-binding domain. *Nature Communications*. 2017;8:2151.

have revealed the response of some motors to such “roadblocks”. For instance, *in vitro* studies have revealed that single molecules of kinesin slow down and are more likely to dissociate when encountering either high concentrations of other kinesins (Conway et al., 2012; Telley et al., 2009) or tau (Dixit et al., 2008). Similar studies have revealed that upon encountering tau, dynein motors tend to reverse direction rather than detach (Dixit et al., 2008; Soundararajan et al., 2014), whereas MAP4 (a neuronal and non-neuronal tau family member) reduces the velocity of dynein motors *in vitro* (Samora et al., 2011) and their run length *in vivo* (Semenova et al., 2014).

In addition to exhibiting “roadblock” activity (*i.e.* inducing detachment or reducing velocity), several MAPs have been shown to recruit kinesins to various microtubule structures. For instance, studies in several model systems have shown that the microtubule cross-linking protein PRC1 (Ase1 in fission and budding yeasts) is important for the recruitment of the kinesins Xklp1 (*Xenopus laevis*), Cin8 (budding yeast), and Kpl9 (fission yeast), all of which affect spindle midzone functions (Bieling et al., 2010; Khmelinskii et al., 2009; Fu et al., 2009). Similarly, the MAP TPX2 has been shown to be important for recruitment of the kinesin-5, Eg5, to spindle microtubules where it functions in spindle assembly (Ma et al., 2011; Eckerdt et al., 2008). In addition to a recruitment role, Tpx2 has also been shown to reduce the velocity of Eg5 (Ma et al., 2011; Balchand et al., 2015). Thus, understanding how various motors navigate around or are affected by MAPs is critical to understanding the molecular regulation of cellular motor activity.

In contrast to the kinesin family of motors, which are represented by at least 45 proteins in human cells (Miki et al., 2001), only one variant of cytoplasmic dynein (dynein-1) is encoded by eukaryotic genomes and is responsible for nearly all minus end-directed microtubule transport. Given its varied cellular roles it’s unsurprising that numerous regulators contribute to *in vivo* dynein function. These include LIS1 (human homolog of yeast Pac1), the dynactin complex, and the growing family of adaptor proteins that link dynein to dynactin and various

cellular sites (*e.g.*, Bicaudal-D, Hook, Spindly). These effectors each exhibit unique activities and mechanisms of action. For instance, the LIS1 homolog Pac1 reduces dynein velocity through direct binding to the AAA (ATPase associated with various cellular activities) ring, which sterically blocks its mechanochemical cycle (Toropova et al., 2014). The dynactin complex, on the other hand, activates metazoan dynein motility (Schlager et al., 2014; McKenney et al., 2014) through a mechanism that likely involves promotion of microtubule binding (McKenney et al., 2016), and orienting the two motor domains appropriately for processive motility (Zhang et al., 2017; Urnavicius et al., 2015). These dynactin-mediated activities require adaptor proteins that promote binding between dynactin and the N-terminal tail domain of dynein (or tail-bound accessory chains; Schlager et al., 2014; McKenney et al., 2014; Urnavicius et al., 2015; Splinter et al., 2012). Although it is unclear if other regions of the dynein motor are targets for regulation, the size, architecture, and complex mechanochemical cycle of dynein suggest at least the potential for various sites of regulation. For instance, the crowded microenvironment of the microtubule lattice raises the possibility that MAPs may regulate dynein activity via direct interactions with regions of the motor that are in close proximity to the microtubule (*i.e.* the microtubule-binding domain, MTBD, or the coiled-coil that links the MTBD to the AAA ring). However, no such activity has yet been identified.

Here we focus on understanding the mechanism by which the MAP She1 affects dynein motility. The role for She1 in dynein function is currently unclear, although *in vivo* studies have shown that deletion of She1 leads to defects in daughter cell-directed spindle movements, while *in vitro* studies have shown that She1 is a potent effector of dynein motility (Markus et al., 2012). Specifically, She1 reduces dynein velocity and increases the duration of time dynein spends bound to microtubules. Interestingly, She1 exhibits high specificity for dynein and has no apparent effect on the motility of either human kinesin-1 or the yeast kinesin Kip2. Thus, in spite of them possessing distinct cellular roles, She1 and Pac1 (the latter of which is important for plus end-binding activity of dynein (Lee et al., 2003) affect dynein motility similarly (Markus et

al., 2011; Huang et al., 2012), raising the possibility that She1 affects dynein activity in a similar manner. Using recombinant proteins we show that She1 in fact affects dynein motility using a unique mechanism of action. Through direct binding between the microtubule and the dynein MTBD, She1 reduces dynein microtubule dissociation, which results in reduced ATPase activity, stepping frequency and velocity, and increased microtubule dwell times. We confirm the She1-MTBD interaction by generating a chimeric dynein mutant that exhibits a reduced binding affinity for She1 and is less sensitive to She1 effects *in vitro* and *in vivo*. Interestingly, we find that She1 recognizes a specific conformational state of the MTBD that is representative of the nucleotide-free, high microtubule binding-affinity state. Taken together, our findings reveal the first mechanism by which a MAP may affect dynein activity and also reveal the MTBD as a novel target for dynein regulation.

## **2.2 RESULTS**

### ***2.2.1 She1 reduces dynein ATPase activity***

To understand the molecular mechanism by which She1 affects dynein motility, we first asked whether She1 has any effect on dynein's mechanochemical cycle. It is fairly well established that for every step it takes, dynein binds and hydrolyzes at least one ATP at an active site within the first AAA module (AAA1; Kon et al., 2014). ATP binding and hydrolysis have been shown to trigger a cascade of conformational changes that ultimately lead to (1) movement of the mechanical linker element to its pre-powerstroke state (Burgess et al., 2003; Kon et al., 2004, Schmidt et al., 2015; Robert et al., 2012; Bhabha et al., 2014), and (2) reduced affinity of the dynein microtubule-binding domain (MTBD) for microtubules (Gibbons et al., 2005; Kon et al., 2009; Imamula et al., 2007). Phosphate release (ADP-P<sub>i</sub> to ADP) on the other hand is thought to be triggered upon microtubule rebinding (Uchimura et al., 2015), which consequently leads to (1) powerstroke of the linker (Kon et al., 2005; Kon et al., 2009; Kon et al., 2012), and (2) adoption of a high microtubule binding affinity conformation of the MTBD

(Kon et al., 2004; Gibbons et al., 2005; Imamula et al., 2007; Redwine et al., 2012). Thus, the ATPase cycle is tightly coordinated with the microtubule-bound state of the motor. One potential mechanism by which She1 may affect dynein motility is through direct modulation of dynein's ATPase activity.

To determine what effect, if any, She1 has on dynein's ATPase activity, we measured the rate of ATP hydrolysis of dynein in response to 0-2  $\mu\text{M}$  microtubules, and in the absence or presence of recombinant She1. For these studies we used a purified, artificially dimerized (via glutathione S-transferase, GST), motility-competent dynein motor domain fragment (Reck-Peterson et al., 2006) that is sensitive to She1-mediated inhibition (Markus et al., 2012; GST-dynein<sub>331</sub>; see Fig. 2.1a). We found that She1 indeed reduces dynein's maximal microtubule-stimulated ATPase activity ( $k_{\text{cat}}$ ) from  $17.7 \pm 1.1$  (SE of fit) to  $11.0 \pm 0.4$  motor domain<sup>-1</sup> sec<sup>-1</sup> (Fig. 2.1b and c). However, She1 had no significant effect on the basal ATPase rate (from 2.4  $\pm$  0.9 to  $3.1 \pm 0.5$  motor domain<sup>-1</sup> sec<sup>-1</sup>; Fig. 1c,  $k_{\text{basal}}$ ), suggesting that She1 does not directly affect ATP turnover in the absence of microtubule binding. Interestingly, we found that She1 increased the binding affinity of dynein for microtubules, as was apparent by the 2.3-fold reduction in  $K_{m(\text{MT})}$  (from  $0.10 \pm 0.03$  to  $0.04 \pm 0.01$   $\mu\text{M}$ ;  $\pm$  SE of fit; Fig. 2.1c,  $K_{m(\text{MT})}$ ). These data suggest that She1 may affect dynein motility by directly affecting ATP turnover at one of the AAA modules within the motor domain. Alternatively, given that She1 reduces dynein velocity, it's equally plausible that She1 reduces the rate at which dynein binds and hydrolyzes ATP as a consequence of a reduced stepping rate.

### **2.2.2 She1 reduces dynein stepping frequency**

The fact that She1 increases the binding affinity of dynein for microtubules (see Fig. 2.1c,  $K_{m(\text{MT})}$ ), likely as a consequence of reduced dissociation rates (Fig. 2.1d; as determined from single molecule experiments), suggests that She1 may slow down dynein motility by prolonging the periods of microtubule attachment between individual steps, thus reducing the overall stepping frequency of dynein. To determine how She1 affects the stepping behavior of

dynein, we used an established method (Reck-Peterson et al., 2006) to attach a bright photostable quantum dot (Qdot) to the C-terminus of one of the two dynein motor domains within a GST-dimerized complex (Fig 2.2a). We then imaged these molecules at high temporal resolution ( $\sim 10 \text{ sec}^{-1}$ ) in either the absence or presence of She1. Consistent with previous findings, in the absence of She1 and the presence of saturating ATP concentrations (1 mM), dynein motors moved at a rate that matched or exceeded the temporal resolution of our imaging conditions (Fig. 2.2b, green trace). This made it difficult to accurately track these motors and thus determine dynein's stepping behavior (*e.g.*, stepping frequency and step size). Thus, we reduced the velocity of dynein by using limiting concentrations of ATP (1  $\mu\text{M}$ ), which permitted accurate assessment of dynein stepping behavior due to the longer dwells between individual steps (Fig. 2.2b, blue traces).

In the absence of She1, the distribution of dynein step sizes revealed a major peak at approximately 16 nm (Fig. 2.2c) and a small fraction (10.9%) of backwards steps (Fig. 2.2g), both of which are consistent with previous findings (Reck-Peterson et al., 2006). In contrast to dynein motility in the absence of She1, the presence of She1 sufficiently reduced the stepping frequency of dynein in saturating ATP concentrations (1 mM) to permit the observation of discrete steps with pauses in between (Fig. 2.2b, red and brown traces). We observed a stepping rate of  $2.4 \text{ sec}^{-1}$  in the presence of 10 nM She1, which was reduced to  $1.2 \text{ sec}^{-1}$  by 25 nM She1, a value that closely matched that of dynein alone in 1  $\mu\text{M}$  ATP ( $1.0 \text{ sec}^{-1}$ ; Fig. 2.2f and Fig. A1.1c). Interestingly, we also observed an increased fraction of backwards (plus end-directed) and large steps in the presence of She1 (Fig. 2.2c-e, yellow boxes, and 2.2g and h). Taken together, our findings reveal that She1 indeed reduces dynein stepping frequency, likely as a consequence of the reduced microtubule dissociation rate (Fig. 2.1d).

### **2.2.3 She1 microtubule binding is required to affect dynein motility**

Given that She1 binds microtubules with nanomolar affinity (Markus et al., 2012), we next asked whether this activity of She1 is required for it to affect dynein motility. To this end, we

proteolytically removed the unstructured carboxy-terminal tails of  $\alpha$ - and  $\beta$ -tubulin (*i.e.*, E-hooks) from microtubules using the protease subtilisin (Fig. 2.3a and b). Although She1 was no longer able to bind to these microtubules (Fig. 2.3c), dynein was capable of binding and walking along them (Fig. 2.3d). Consistent with previous findings (Markus et al., 2012), addition of 10 nM She1 was sufficient to drastically alter dynein motility on undigested control microtubules (Fig. 2.3d-f, “+ E-hooks”, and Fig. A1.2). However, in stark contrast to control microtubules, dynein motility on subtilisin-treated microtubules was completely unaffected by the presence of She1 (Fig. 2.3d-f, “- E-hooks”, and Fig. A1.2). Thus, microtubule binding by She1 is indeed required for it to affect dynein motility.

#### **2.2.4 She1 binds directly to the dynein motor domain**

Although the mechanism by which She1 affects dynein motility is unknown, previous single molecule data suggested that She1 and dynein may interact along microtubules (Markus et al., 2012). However, direct evidence for an interaction between these two molecules is lacking. To test whether the two molecules interact directly, we took advantage of the fact that dynein, but not She1, is able to bind to subtilisin-treated microtubules (see Fig. 2.3). If the two molecules interact, then microtubule-bound dynein would recruit She1 to the microtubule, and this binding could be observed and quantitated by total internal reflection fluorescence (TIRF) microscopy (Fig. 2.4a). A fixed concentration of fluorescent She1-TMR (40 nM) was incubated with subtilisin-digested microtubules in the absence or presence of increasing concentrations of a monomeric, non-processive, GFP-tagged dynein motor domain fragment (GFP-dynein<sub>331</sub>; Fig. A1.3b). We observed robust recruitment of She1 to subtilisin-digested microtubules by increasing concentrations of the dynein motor domain, thus demonstrating a direct interaction between She1 and dynein (Fig. 2.4b and c).

The aforementioned binding experiment (Fig. 2.4c) was performed in the absence of nucleotide. In these conditions, dynein adopts a conformation in which the linker is in the post-powerstroke state and the MTBD is in a high microtubule binding affinity state (Kon et al., 2004;

Burgess et al., 2003; Kon et al., 2005; Bhabha et al., 2014; Imamula et al., 2007). To determine if She1 preferentially binds to a particular dynein conformational state, we repeated the binding experiment with either no nucleotide (as above) or with ATP and vanadate ( $V_i$ ). The latter traps dynein in an ADP- $V_i$  intermediate (ADP- $P_i$  mimic) in which the linker is in the pre-powerstroke state and the MTBD is in the low microtubule binding affinity state (Burgess et al., 2003; Schmidt et al., 2015; Bhabha et al., 2012; Fig. 2.4d). To correct for the differential microtubule binding affinity of dynein in the absence of nucleotide versus in the presence of ATP +  $V_i$  (Fig. A1.3a), we correlated the degree of microtubule binding by GFP-dynein<sub>331</sub> in each condition to the extent of She1 microtubule recruitment (*i.e.*, fluorescence intensity of GFP-dynein<sub>331</sub> versus She1-TMR). We found that for a given degree of GFP-dynein<sub>331</sub> microtubule binding, more She1 was recruited to microtubules in the absence of nucleotide than in the presence of ATP +  $V_i$  (Fig. 2.4e). These data suggest that She1 has a higher affinity for dynein in the apo state than in the ADP- $V_i$  state. Moreover, they indicate that She1 recognizes a structural feature of dynein that undergoes a nucleotide-induced conformational change.

Although our findings indicate that She1 binds preferentially to one conformation over another, She1 was indeed able to bind to dynein in both nucleotide states. If true we reasoned that She1 would stay bound to dynein as it walked along subtilisin-treated microtubules (*i.e.*, those to which She1 is unable to bind) and thus progressed through many iterations of its mechanochemical cycle. Consistent with this notion, we observed several examples of such events in which She1-TMR was observed colocalizing with moving single molecules of GST-dynein<sub>331</sub> (Fig. 2.4f; only 14 such events were observed out of several hundred moving dynein molecules). Thus, in spite of its preferred affinity for the apo state, She1 can indeed remain bound to dynein throughout its entire mechanochemical cycle.

### **2.2.5 She1 binds directly to the dynein microtubule-binding domain**

Since microtubule binding by She1 is required for it to affect dynein motility (Fig. 2.3), and She1 and dynein interact directly (Fig. 2.4), we reasoned that She1 might exert its effect on

dynein motility by binding to a surface of the motor domain that is in close proximity to the microtubule. To test this hypothesis, we generated recombinant protein fragments that encompass the dynein MTBD and the coiled coil (CC; which links the AAA ring to the MTBD) fused to seryl tRNA synthetase (SRS; Fig. 2.5a, left). It has been shown that a nearly identical fusion protein derived from mouse dynein adopts a native fold and retains microtubule-binding activity (Gibbons et al., 2005; Redwine et al., 2012; Carter et al., 2008). We expressed and purified this dynein fragment (dynein<sub>CC+MTBD</sub>) from bacteria (Fig. A1.3b) and performed the microtubule recruitment assay described above with subtilisin-treated microtubules. As a control we generated an SRS fusion that is linked to the microtubule-binding domain of human kinesin-1 via a flexible linker (kinesin<sub>MTBD</sub>; see Fig. 2.5b, left, and Fig. A1.3b). Consistent with the notion that She1 binds to a region of dynein that is in close proximity to the microtubule, we found that dynein<sub>CC+MTBD</sub>, but not kinesin<sub>MTBD</sub>, recruited She1 to microtubules in a concentration dependent manner, thus demonstrating a direct interaction between She1 and dynein<sub>CC+MTBD</sub> (Fig. 2.5c and d, green bars).

To further refine the She1 binding surface within dynein, we generated an SRS fusion construct that included only the 124 amino acid dynein MTBD. To best ensure the MTBD adopted a native fold and retained microtubule-binding activity, we replaced the native dynein CC with one from SRS (SRS<sub>CC</sub>-dynein<sub>MTBD</sub>; see Fig. 2.5a, middle, and Fig. A1.3b and c). To rule out the possibility that She1 microtubule recruitment was being mediated by the SRS coiled-coil, we generated a similar fusion protein that included the kinesin MTBD in place of the dynein MTBD (SRS<sub>CC</sub>-kinesin<sub>MTBD</sub>; see Fig. 2.5b, middle, and Fig. A1.3b). We found that SRS<sub>CC</sub>-dynein<sub>MTBD</sub>, but not SRS<sub>CC</sub>-kinesin<sub>MTBD</sub>, was sufficient to robustly recruit She1 to microtubules, indicating that She1 directly contacts the dynein MTBD (Fig. 2.5d, red bars, and e).

As above, we correlated the degree of microtubule binding by SRS<sub>CC</sub>-dynein<sub>MTBD</sub> and dynein<sub>CC+MTBD</sub> to the extent of She1 microtubule recruitment by each (*i.e.*, fluorescence intensity of GFP-SRS fusion versus She1-TMR). This revealed that for a given degree of microtubule

binding, more She1 was recruited to microtubules by SRS<sub>CC</sub>-dynein<sub>MTBD</sub> than by dynein<sub>CC+MTBD</sub>, thus indicating that She1 has a higher affinity for the former, in spite of the latter encompassing a larger region of dynein (Fig. 2.5f). Given the difference in apparent affinity of She1 for dynein in the apo versus ADP-V<sub>i</sub> state (Fig. 2.4e), we hypothesized that the difference in She1 binding affinity for the two different SRS fusion proteins was due to possible differences in the conformation of the MTBD. It is well established that the MTBD undergoes conformational changes in response to its nucleotide and microtubule-bound state (Schmidt et al., 2015; Imamula et al., 2007; Uchimura et al., 2015; Redwine et al., 2012; Carter et al., 2008). The structural plasticity of this domain allows the motor to cycle through periods of high (in its apo and ADP-bound state) and low (in its ATP and ADP-vanadate) microtubule binding affinity during processive runs. We found that SRS<sub>CC</sub>-dynein<sub>MTBD</sub> exhibited a ~9-fold higher microtubule-binding affinity than dynein<sub>CC+MTBD</sub> (Fig. A1.3d;  $0.9 \pm 0.1 \mu\text{M}$  versus  $7.8 \pm 3.0 \mu\text{M}$ ;  $\pm$  SE of fit) which indicates that the two MTBD fusions are indeed in distinct conformational states. These data also confirm that She1 exhibits higher affinity for the dynein MTBD in its high microtubule-binding affinity conformation (see Fig. A1.4a and Discussion).

To confirm the interaction between She1 and the dynein MTBD, we performed a yeast two-hybrid assay. We expressed various DNA-binding domain (GAL4-DBD) fusions (*i.e.*, GAL4-DBD-dynein<sub>CC+MTBD</sub>, GAL4-DBD-SRS<sub>CC</sub>-dynein<sub>MTBD</sub>, or GAL4-DBD-SRS<sub>CC</sub>-kinesin<sub>MTBD</sub>) along with either a transcriptional activation domain (GAL4-AD)-She1, or negative control (GAL4-AD-large T antigen) fusion in yeast cells harboring GAL4 responsive reporter genes. Positive interactions are detected by growth on histidine-deficient media. Consistent with our *in vitro* data, this analysis revealed an interaction between She1 and SRS<sub>CC</sub>-dynein<sub>MTBD</sub>; however, we observed no detectable two-hybrid interaction between She1 and either SRS<sub>CC</sub>-kinesin<sub>MTBD</sub> or dynein<sub>CC+MTBD</sub> (Fig. A1.3e), the latter of which is consistent with a significantly weaker interaction as determined by our *in vitro* assay (see Fig. 2.5f).

We next asked whether She1 exhibits any affinity for regions of dynein outside the MTBD. To this end, we performed a recruitment assay on undigested (“+ E-hook”) microtubules. Incubation of microtubules with high concentrations of She1 (40nM) and a dynein mutant (45 nM) lacking its MTBD (GFP-dynein<sub>331</sub><sup>ΔMTBD</sup>, Fig. A1.3b) resulted in no apparent microtubule recruitment of GFP-dynein<sub>331</sub><sup>ΔMTBD</sup> by She1 (Fig. A1.3f and g). Taken together our results indicate that She1 binds exclusively to the dynein MTBD.

### **2.2.6 Generation of a dynein motor with reduced sensitivity to She1**

If She1 indeed affects dynein motility through interactions with the dynein MTBD, then we reasoned that mutations within this region that reduce She1 binding would also disrupt any She1-mediated effects on dynein motility. Thus, we sought to introduce mutations within the MTBD that would disrupt She1 binding. Rather than generate a library of random mutants that would potentially disrupt MTBD structure or function (*e.g.*, microtubule-binding activity), we instead developed a strategy in which the dynein MTBD from an evolutionarily distant organism was used to replace that from yeast *DYN1* (dynein heavy chain), thus generating a chimeric dynein MTBD mutant. We hypothesized that She1 may exhibit binding specificity for yeast dynein and may therefore exhibit reduced binding to metazoan dynein. To test this possibility, we generated a chimeric GST-dynein<sub>331</sub> fragment in which only the globular MTBD was replaced by the corresponding MTBD from mouse dynein (GST-dynein<sub>331</sub><sup>mMTBD</sup>; Fig. 2.6a and b). Sequence analysis revealed 41% identity and 70% similarity between yeast and mouse dynein MTBDs, indicating significant divergence in primary sequence between the two motors (Fig. 2.6a, Fig. A1.4b). To our surprise, the GST-dynein<sub>331</sub><sup>mMTBD</sup> chimera was capable of walking along microtubules, albeit with slightly altered motility parameters with respect to wild-type GST-dynein<sub>331</sub> (Fig. 2.6c-e, and Fig. A1.5). Specifically, GST-dynein<sub>331</sub><sup>mMTBD</sup> walked at roughly half the velocity in single molecule assays (68.9 nm sec<sup>-1</sup> vs. 128 nm sec<sup>-1</sup>), but moved microtubules faster than wild-type dynein in an ensemble microtubule gliding assay (using equivalent concentrations of coverslip-immobilized motors; see Methods). Moreover, the chimeric mutant

walked longer distances and spent more time bound to microtubules than the wild-type motor in single molecule assays (Fig. A1.5).

Consistent with the notion that She1 makes contacts with the MTBD, GST-dynein<sub>331</sub><sup>mMTBD</sup> exhibited reduced sensitivity to She1 in terms of its effects on velocity (in single molecule and ensemble assays; Fig. 2.6f and h) and dwell time (Fig. 2.6g). We used our microtubule recruitment assay to compare the relative affinity of She1 for monomeric GFP-dynein<sub>331</sub> and GFP-dynein<sub>331</sub><sup>mMTBD</sup> (Fig. 2.7a; Fig. A1.3b), and found that the reduced effects of She1 on GST-dynein<sub>331</sub><sup>mMTBD</sup> motility were indeed due to compromised She1-dynein binding. Although GFP-dynein<sub>331</sub><sup>mMTBD</sup> was capable of recruiting She1 to subtilisin-treated microtubules, the relative degree of recruitment was lower than that of the wild-type motor domain (Fig. 2.7b), indicating a significantly lowered affinity of She1 for the chimeric motor. We confirmed the reduced affinity of She1 for the mouse dynein MTBD using the two-hybrid assay, which revealed no detectable two-hybrid interaction between She1 and a mouse dynein variant of the SRS<sub>CC</sub>-dynein<sub>MTBD</sub> fragment (Fig. 2.7c).

### **2.2.7 Dynein<sup>mMTBD</sup> mutant cells exhibit She1-insensitive phenotypes**

Overexpression of She1 in yeast leads to defects in dynein pathway function as is apparent by errors in spindle positioning (see Fig. A1.7a) and synthetic genetic interactions with *KAR9* (Markus et al., 2012), the latter of which functions in a parallel spindle orientation pathway (Markus et al., 2012). Although the precise cause for dynein dysfunction in these cells is unclear, She1 overexpression leads to a relocalization of dynein from microtubule plus ends (Fig. 2.7d, left, and e, blue arrow) – from where it is offloaded to Num1 cortical receptor sites (Fig. 2.7e, blue arrowhead) – to along the length of astral microtubules (Fig. 2.7d, right, and e, red arrows). We hypothesized that this relocalization may be a consequence of She1 enhancing dynein's microtubule binding affinity via direct interactions between astral microtubules (see Fig. 2.3) and the dynein MTBD (see Fig. 2.5). To distinguish between this possibility and one in which the relocalization is a consequence of a redistribution of the dynein plus end targeting

complex (which is comprised of Bik1, Pac1 and Bim1 in yeast (Lee et al., 2003; Sheeman et al., 2003; Blake-Hodek et al., 2010), we assessed: (1) whether the dynein MTBD, which is dispensible for plus end targeting (Lammers et al., 2015), is required for the relocalization phenotype, and (2) whether Pac1, which is necessary for plus end targeting (Lee et al., 2003), is required for this phenotype (see Fig. A1.6a). For these experiments, we assessed dynein localization (either wild-type Dyn1-3YFP, or Dyn1<sup>ΔMTBD</sup>-3YFP) in *GAL1p:SHE1* cells grown in either the absence or presence of galactose, a potent stimulant of the *GAL1* promoter (*GAL1p*). Consistent with the notion that the relocalization phenotype is a consequence of She1 enhancing dynein's microtubule-binding affinity, we found that deletion of the MTBD prevented dynein relocalization, whereas loss of Pac1 had no impact on the relocalization phenotype (Fig. A1.6b and c).

Next, we asked whether the mouse MTBD chimera exhibits reduced sensitivity to She1 in cells. In the absence of She1-overexpression, dynein<sup>mMTBD</sup> localizes to microtubule plus ends and the cell cortex in a manner similar to that of wild-type dynein (Fig. 2.7f, blue arrows and arrowheads). Consistent with the notion that dynein<sup>mMTBD</sup> is less sensitive to She1, it was not redistributed along astral microtubules upon She1 overexpression (Fig. 2.7f). In spite of this, we noted that its plus end and cortical localization were reduced with respect to cells not overexpressing She1, and there appeared to be cytoplasmic aggregates of dynein<sup>mMTBD</sup> (Fig. 2.7f, red arrowhead). Although the basis for this mislocalization is unclear, it is the likely basis for the prevalence of misoriented spindles in these cells (Fig. A1.7a).

Although loss of She1 does not lead to a significant spindle mispositioning defect (Fig. A1.7b), She1 has been implicated in polarizing dynein-mediated spindle movements toward the daughter cell. Specifically, cells deleted for She1 exhibit a reduced fraction of dynein-mediated spindle movements that result in the spindle traversing the mother-bud neck in a spindle oscillation assay (Markus et al., 2012). In this assay, the movements of pre-anaphase spindles are monitored in *kar9Δ* hydroxyurea (HU)-arrested cells, the latter of which eliminates spindle

movements due to spindle elongation during anaphase. Deletion of *KAR9* leads to an enhancement of dynein-mediated spindle movements (Yeh et al., 2000; Moore et al., 2009) and also eliminates any movements that might be mediated by the *KAR9* pathway for spindle orientation.

Although dynein<sup>mMTBD</sup> appeared to possess nearly wild-type activity as assessed by a single time point spindle positioning assay (Fig. A1.7b; see Methods), and was capable of mediating spindle movements in the spindle oscillation assay, the frequency of these movements was reduced to approximately 61% of wild-type (Fig. 2.7g). Moreover, we noted that the fraction of dynein-mediated spindle movements that resulted in neck crossing was greatly reduced in the *dyn1<sup>mMTBD</sup>* cells (Fig. 2.7h). Although deletion of She1 reduced neck crossing by 53% in *DYN1* (wild-type dynein) cells, deletion of She1 had no additional impact on the degree of neck crossing in *dyn1<sup>mMTBD</sup>* cells (Fig. 2.7h and Fig. A1.7c). Taken together, our data indicate that the mouse MTBD chimera indeed exhibits reduced sensitivity to She1, and further confirm that the MTBD is the main site of interaction for She1.

## 2.3 DISCUSSION

Our study provides the first detailed molecular dissection of the mechanism by which a MAP can affect the function of a microtubule motor. Specifically, we have found that She1 affects dynein motility by increasing its microtubule binding affinity (as a consequence of reducing its microtubule dissociation rate; Fig. 2.1d), which causes a reduction in stepping frequency (Fig. 2.2b and f) and consequent ATP turnover (Fig. 2.1b and c). These effects are due to the simultaneous and direct interactions between She1, the microtubule (via the C-terminal tails of tubulin), and the small (124 amino acids) globular dynein microtubule-binding domain (Fig. 2.5). In light of the fact that She1 and dynein directly interact, we can extract an approximate She1-dynein binding affinity from the She1 concentration value at which dynein velocity is half-maximally reduced: 0.17 nM (Markus et al., 2012). To our knowledge this is the

first time that any such regulatory molecule has been shown to contact the dynein MTBD.

Although She1 is a yeast-specific dynein regulatory factor, it may define a new class of motor regulatory MAP. Moreover, our work identifies the dynein MTBD as a target for MAP-mediated dynein regulation.

She1 is the first molecule identified to date that has the capacity to alter dynein stepping behavior (*i.e.*, increases the frequency of large and backward steps; Fig. 2.2g and h). Although the reasons for this are unclear, we hypothesize that these changes in stepping behavior are a consequence of one of the motor heads within a dimer becoming unbound from She1 for brief periods of time. In such a scenario, one motor head unbinds from microtubule-bound She1 and steps forward. Given the lower likelihood of the lagging She1-bound head unbinding from the microtubule (due to reduced dissociation rates; see Fig. 2.1d), the leading She1-unbound head in this scenario will unbind from the microtubule and consequently steps backward.

Alternatively, given that the leading head is generally less likely to detach from the microtubule at increased interhead separations (due to tension exerted on the linker; Cleary et al., 2014), the lagging She1-bound head may eventually detach at sufficiently large interhead separations, which may result in larger than normal step sizes. Simultaneous two-color imaging of both heads will be required to understand the basis for the altered stepping behavior.

We found that She1 exhibits an enhanced affinity for dynein in the apo (nucleotide-free) state, during which the MTBD is in a high microtubule binding affinity state (Imamula et al., 2007). We observed this preferential binding in the context of the full motor domain (apo vs. ADP-vanadate; Fig. 2.4e) and with an isolated dynein MTBD fragment (SRS<sub>CC</sub>-dynein<sub>MTBD</sub> vs. dynein<sub>CC+MTBD</sub>; Fig. 2.5f and Fig. A1.3d), the latter of which we confirmed using a yeast two-hybrid assay (Fig. A1.3e). A previous study demonstrated a similar nucleotide-specific interaction between metazoan LIS1 and dynein. In this example, LIS1 was only found to interact with dynein in its ADP-V<sub>i</sub> state (McKenney et al., 2010; the same is not true for yeast dynein and the LIS1 homolog, Pac1, which interact in a nucleotide-independent manner; Huang et al.,

2012). Given the fact that Pac1 interacts with the dynein AAA ring (between AAA3 and AAA4; Huang et al., 2012) the mechanism by which She1 recognizes the nucleotide state of dynein is therefore distinct. Structural studies have revealed the basis for differential microtubule-binding affinity of dynein in its various nucleotide-bound conditions. The largest conformational changes that take place in the MTBD when the motor undergoes changes in microtubule-binding affinity are the movement of helix 1 (H1, root mean square deviation of 10.1 Å; see Fig. 2.6a and Fig. A1.4a) and CC1 (RMSD = 8.1 Å; Redwine et al., 2012). Thus, it is reasonable to hypothesize that She1 makes contacts with a region of the MTBD that encompasses these elements.

It is currently unclear what the relevance of this conformational specificity of She1 for dynein is, especially in light of the fact that She1 can remain bound to a walking dynein motor (along subtilisin-treated microtubules; see Fig. 2,4f), which is undergoing many iterations of the mechanochemical cycle. One possibility may be that in the context of non-subtilisin-treated microtubules, She1 holds dynein to microtubules by locking the motor in its high microtubule binding affinity state. In this model, upon encountering each other along microtubules, She1 would bind dynein in its apo (or ADP-bound) state, which is the predominant microtubule-bound state of dynein (Uchimura et al., 2015). Given the high affinity interaction between dynein and She1 (< 0.2 nM; see above), it's possible that even upon ATP binding, the dynein MTBD would be prevented from switching to the low microtubule binding affinity state. Such a scenario would result in a reduced microtubule dissociation rate (see Fig. 2.1d), and, since microtubule rebinding has been shown to be critical for phosphate release, also a slowed rate of apparent ATP hydrolysis (see Fig. 2.1b and C). However, if this were true, then even in the absence of microtubule binding an MTBD-bound She1 would likely lock the MTBD in the high microtubule affinity state and consequently reduce the rate of ATP hydrolysis, microtubule dissociation rates, and thus velocity. Our findings show that none of these things are true (see Fig. 2.1c,  $k_{\text{basal}}$ , and Fig. 2.3e and f). Thus, understanding the relevance of this binding specificity will be the focus of future work.

We found that a chimeric yeast dynein mutant with an MTBD derived from mouse dynein exhibits reduced sensitivity (Fig. 2.6f-h) and affinity (Fig. 2.7b and c) for She1. Given that She1 preferentially binds to the MTBD when the latter is in its high microtubule binding affinity state (see above), one possible explanation for this reduced sensitivity to She1 is that the mouse MTBD – at least in the context of the chimeric motor mutant – is locked in a low (or lower) microtubule affinity state. Consistent with this notion, we found that the GFP-dynein<sub>331</sub><sup>mMTBD</sup> chimera exhibited a somewhat lower affinity for microtubules than wild-type GFP-dynein<sub>331</sub> (Fig. A1.4c). Alternatively, the reduced affinity of She1 for the chimera may simply be a consequence of amino acid substitutions within the MTBD. A comparison of primary sequences between yeast and mouse dynein MTBDs indicates a large number of differences in surface-exposed residues (*i.e.*, those likely contacted by She1; see Fig. A1.4b). Specifically, we found there to be 48 surface-exposed residues that are dissimilar, of which 22 are charge substitutions (*i.e.*, changes that either add, remove, or switch a charge), and 11 are non-polar/polar substitutions. Given the high prevalence of basic residues throughout She1 (isoelectric point of She1 = 10.4), it's possible that the charge substitutions are the basis for disrupted She1-dynein binding in the chimeric mMTBD mutant. As evidence for an electrostatic component to the interaction between She1 and dynein, we previously found that a phosphomimetic She1 mutant (She1<sub>5D</sub>) exhibited a greater effect on dynein motility than wild-type recombinant She1, in spite of the mutant exhibiting a lower microtubule binding affinity (Markus et al., 2012). The majority of residue differences between yeast and mouse MTBDs – including charge substitutions – appear to lie on the right face of the MTBD (Fig. A1.4b). In light of this fact, and that the bulk of the conformational changes induced by nucleotide binding and hydrolysis are clustered on the left face of the MTBD (see above, and Fig. A1.4a), we hypothesize that She1 recognizes a composite binding surface that encompasses both faces of the MTBD. Such a mechanism of binding could account for the apparent high affinity interaction between She1 and dynein ( $K_D < 0.2$  nM; see above), and the high degree of potency with which She1 affects dynein with respect

to the only other known molecule that effects dynein similarly: Pac1 (~350-fold difference in half-maximal inhibition (Huang et al., 2012). Further study will be required to understand the precise nature of the interaction between She1 and dynein.

The mechanism by which She1 affects dynein-mediated spindle movements is currently unclear. We previously proposed a model in which She1 specifically inhibits dynein activity in the mother cell, which would lead to a relative enhancement in daughter cell-based dynein activity, and consequent daughter cell-directed spindle movements (Markus et al., 2012). Although future studies will focus on testing this model, it was unclear from previous work whether the defective spindle neck-cross phenotype in *she1*Δ cells was due to other, non-dynein-related activities of She1. For instance, She1, which localizes prominently to the bud neck and the mitotic spindle (Wong et al., 2007; Woodruff et al., 2009), has been implicated in affecting spindle disassembly and kinetochore function, the latter of which may be mediated by Mcm21, a She1 interacting factor and kinetochore component (Woodruff et al., 2010) that affects localization of the kinetochore kinase, Ipl1 (homolog of human Aurora B kinase; Vizeacoumar et al., 2010). Thus, it's possible that the observed defect in spindle neck crossing is attributable to either the bud neck or spindle-localized She1 pools, which presumably do not affect dynein pathway function, as opposed to the astral microtubule-localized She1 (Woodruff et al., 2010), which is the pool of molecules that likely affects dynein function. Our finding that *dyn1<sup>mMTBD</sup>* cells are not further impacted by loss of She1 on spindle neck crossing indicates that it is She1's effect on dynein activity in particular that affects this process in wild-type cells, and that it is likely the astral microtubule-bound population of She1 molecules that are responsible.

## **2.4 METHODS**

### **2.4.1 Media and strain construction**

Strains are derived from W303, YEF473A (Bi et al., 1996), or Y2HGold/Y187 (Clontech, catalog number 630489), and are listed in Table A1.1. We transformed yeast strains using the

lithium acetate method (Knop et al., 1999). Strains carrying mutations or tagged components were constructed by PCR product-mediated transformation (Longtine et al., 1998) or by mating followed by tetrad dissection. Proper tagging and mutagenesis was confirmed by PCR, and in some cases sequencing. Fluorescent tubulin-expressing yeast strains were generated using plasmids and strategies described previously (Markus et al., 2015). Yeast synthetic defined (SD) media was obtained from Sunrise Science Products (San Diego, CA).

#### **2.4.2 Plasmid construction**

A region of dynein corresponding to the coiled-coil and microtubule-binding domains (CC+MTBD; amino acids 3015-3309; note this fragment is equivalent to the “85:82”, “ $\alpha$  registry” fragment generated previously) (Carter et al., 2008) was amplified using forward and reverse primers flanked with Sall and HindIII restriction sites. A bacterial expression vector with mouse dynein<sub>CC+MTBD</sub> fused to seryl tRNA synthetase (Gibbons et al., 2005) was obtained from Addgene (www.addgene.com; plasmid 22393), digested with Sall and HindIII, and then ligated with the digested yeast dynein<sub>CC+MTBD</sub> PCR product to generate pSRS:dynein<sub>CC+MTBD</sub>. To generate an N-terminally-tagged EGFP variant of this fragment (see Fig. 2.5ai), isothermal assembly was used (Gibson., 2009). PCR products corresponding to EGFP (from pFA6a-GFP(S65T)-TRP (Longtine et al., 1998) and a portion of the CC+MTBD (amino acids 1-164) were amplified. After amplification, the 5' end of the EGFP PCR contained 20 nucleotides of sequence identity with NdeI digested pSRS:dynein<sub>CC+MTBD</sub>, and the 5' and 3' ends of the CC+MTBD PCR product contained 20 nucleotides of sequence identity with the 3' end of EGFP, and NdeI digested pSRS:dynein<sub>CC+MTBD</sub>, respectively. After digesting pSRS:dynein<sub>CC+MTBD</sub> with NdeI (which excises sequence corresponding to amino acids 1-164 of CC+MTBD), the gel purified PCR products and digested vector were assembled *in vitro* as described (Gibson et al., 2009), yielding pEGFP-SRS:dynein<sub>CC+MTBD</sub>.

To generate pEGFP-SRS:SRS<sub>CC</sub>-dynein<sub>MTBD</sub> (*i.e.*, in which the native yeast dynein coiled-coil is replaced with one from SRS; see Fig. 2.5a and Fig. A1.3c), a region corresponding

to the dynein MTBD (amino acids 3097-3220) was amplified using a forward primer with sequence corresponding to SRS helix 1 (REVQELKKRLQEVQTERNQVAKR) preceded on the 5' end by a Sall restriction site, and a reverse primer with sequence corresponding to SRS helix 2 (EEKEALIARGKALGEEAKRLEEALREKEA) preceded on the 5' end by a HindIII restriction site. Subsequent to amplification, the PCR product was digested with Sall and HindIII, and ligated into pEGFP-SRS:dynein<sub>CC+MTBD</sub> digested similarly, yielding pEGFP-SRS:SRS<sub>CC</sub>-dynein<sub>MTBD</sub>. A similar construct with the mouse dynein MTBD (amino acids 3279-3401; pEGFP-SRS:SRS<sub>CC</sub>-dynein<sub>mMTBD</sub>) was generated as an intermediate step in constructing the corresponding two-hybrid plasmid (see below). pEGFP-SRS:SRS<sub>CC</sub>-kinesin<sub>MTBD</sub> (see Fig. 2.5b) was generated similarly, with the only exception being that the forward and reverse primers specifically amplified the kinesin MTBD (amino acids 1-337). Moreover, pEGFP-SRS:linker-kinesin<sub>MTBD</sub> (*i.e.*, in which the kinesin MTBD is fused to SRS by a flexible linker; see Fig. 2.5b) was also generated similarly, with the exception being that the forward and reverse primers included nucleotide sequence that encoded flexible linkers (EGKSSGSG on the N-terminus, and KEGGSSG on the C-terminus).

To generate GAL4-DNA binding domain (DBD) vectors for the two-hybrid assay, SRS-dynein<sub>CC+MTBD</sub>, SRS-SRS<sub>CC</sub>-dynein<sub>MTBD</sub>, SRS-SRS<sub>CC</sub>-dynein<sub>mMTBD</sub>, and SRS-SRS<sub>CC</sub>-kinesin<sub>MTBD</sub> were amplified from the respective pEGFP-SRS vectors (described above). After amplification, the 5' and 3' ends of each PCR product contained 20 nucleotides of sequence identity with EcoRI and BamHI-digested pGBKT7 (Clontech). After digesting pGBKT7 with EcoRI and BamHI, the gel purified PCR products and digested vector were assembled *in vitro* as described (Gibson et al., 2009), yielding pGBKT7:SRS-dynein<sub>CC+MTBD</sub> and pGBKT7:SRS-SRS<sub>CC</sub>-dynein<sub>MTBD</sub>. To construct the GAL4-activation domain (AD)-She1 fusion, a PCR product corresponding to the *SHE1* open reading frame was amplified. After amplification, the PCR product contained 20 nucleotides of sequence identity with EcoRI and BamHI-digested pGADT7 (Clontech). After digesting pGADT7 with EcoRI and BamHI, the gel purified PCR product and

digested vector were assembled *in vitro*, yielding pGADT7:*SHE1*. We found that the *ADH1* promoter upstream of *GAL4-AD-SHE1* in pGADT7 drove sufficiently high expression of She1 to result in growth arrest (not shown), as has been reported previously for She1-overexpressing cells (Markus et al., 2012; Espinet et al., 1995). Thus, we sought to generate a lower-expressing *GAL4-AD-She1* vector. To this end, we PCR amplified 352 nucleotides of genomic DNA sequence upstream of the native yeast *SHE1* locus (which presumably contains the native *SHE1* promoter, or *SHE1p*) along with the *GAL4-AD-SHE1* open reading frame from pGADT7:*SHE1*. After amplification, the 5' and 3' ends of the two PCR products (*SHE1p* and *GAL4-AD-SHE1*) contained 20 nucleotides of sequence identity with each other (*i.e.*, the 3' end of *SHE1p* matched the 5' end of *GAL4-AD-SHE1*) and with BamHI and NotI-digested pRS315<sup>66</sup> (*i.e.*, the 5' end of *SHE1p* matched the BamHI site, and the 3' end of *GAL4-AD-SHE1* matched the NotI site). After digesting pRS315 with BamHI and NotI, the gel purified PCR products and digested vector were assembled *in vitro*, yielding pRS315:*SHE1p:GAL4-AD-SHE1*. Yeast cells transformed with this vector did not exhibit any apparent growth defects (see Figure A1.3e, “+HIS” growth). The negative controls (*GAL4-DBD-p53* expression vector, pGBKT7-53; and, *GAL4-AD-large T* antigen-expression vector, pGADT7-T) were obtained from Clontech.

### **2.4.3 Protein purification**

We purified She1-HALO as previously described (Markus et al., 2012), but with minor modifications. Briefly, *E. coli* BL21 (Rosetta DE3 pLysS) cells transformed with pProEX-HTb-TEV:*SHE1-HALO* were grown at 37°C in LB supplemented with 1% glucose, 100 µg/ml carbenicillin and 34 µg/ml chloramphenicol to OD<sub>600</sub> 0.4-0.6, shifted to 16°C for 2 hours, then induced with 0.1 mM IPTG for 14-16 hours at 16°C. The cells were harvested, washed with cold water, resuspended in 0.5 volume of cold 2X lysis buffer [1X buffer: 30 mM HEPES pH 7.2, 50 mM potassium acetate, 2 mM magnesium acetate, 0.2 mM EGTA, 10% glycerol, 1 mM DTT, and protease inhibitor tablets (Pierce)] and then lysed by sonication (5 x 30 second pulses) with 1 minute on ice between each pulse. The lysate was clarified at 22,000 x g for 20 minutes,

adjusted to 0.01% triton X-100, then incubated with glutathione agarose for 1 hour at 4°C. The resin was then washed three times in wash buffer (30 mM HEPES pH 7.2, 50 mM potassium acetate, 2 mM magnesium acetate, 0.2 mM EGTA, 300 mM KCl, 0.01% Triton X-100, 10% glycerol, 1 mM DTT, protease inhibitor tablets) and twice in TEV digest buffer (10 mM Tris pH 8.0, 150 mM KCl, 0.01% Triton X-100, 10% glycerol, 1 mM DTT). To fluorescently label She1-HALO, the bead-bound protein was incubated with 6.7  $\mu$ M HaloTag-TMR ligand (Promega) for 15 minutes at room temperature. The resin was then washed three more times in TEV digest buffer, then incubated in TEV buffer supplemented with TEV protease for 1 hour at 16°C. The resulting eluate was collected using a centrifugal filter unit (0.1  $\mu$ m, Millipore), aliquoted, drop frozen in liquid nitrogen and stored at -80°C. For the ATPase assays, purified She1-HALO was dialyzed against dynein motility buffer (see below) lacking EGTA, but supplemented with 1 mM DTT.

Purification of ZZ-TEV-6His-GFP-3HA-GST-dynein<sub>331</sub>-HALO (under the control of the galactose-inducible promoter, *GAL1p*) was performed as previously described<sup>33</sup>, with minor modifications. Briefly, yeast cultures were grown in YPA supplemented with 2% galactose, harvested, washed with cold water, and then resuspended in a small volume of water. The resuspended cell pellet was drop frozen into liquid nitrogen and then lysed in a coffee grinder (Hamilton Beach). After lysis, 0.25 volume of 4X lysis buffer (1X buffer: 30 mM HEPES, pH 7.2, 50 mM potassium acetate, 2 mM magnesium acetate, 0.2 mM EGTA, 1 mM DTT, 0.1 mM Mg-ATP, 0.5 mM Pefabloc SC, 0.7  $\mu$ g/ml Pepstatin) was added, and the lysate was clarified at 22,000 x g for 20 min. The supernatant was then bound to IgG sepharose 6 fast flow resin (GE) for 1 hour at 4°C, which was subsequently washed three times in wash buffer (30 mM HEPES, pH 7.2, 50 mM potassium acetate, 2 mM magnesium acetate, 0.2 mM EGTA, 300 mM KCl, 0.005% Triton X-100, 10% glycerol, 1 mM DTT, 0.1 mM Mg-ATP, 0.5 mM Pefabloc SC, 0.7  $\mu$ g/ml Pepstatin), and twice in TEV buffer (50 mM Tris, pH 8.0, 150 mM potassium acetate, 2 mM magnesium acetate, 1 mM EGTA, 0.005% Triton X-100, 10% glycerol, 1 mM DTT, 0.1 mM

Mg-ATP, 0.5 mM Pefabloc SC). Note that for binding experiments involving vanadate (*e.g.*, Fig. 2.4e), EGTA was excluded from the TEV buffer. To fluorescently label 6His-GFP-GST-3HA-dynein<sub>331</sub>-HALO (for single molecule analyses), the bead-bound protein was incubated with either 6.7  $\mu$ M HaloTag-TMR or HaloTag-PEG-biotin ligand (Promega) for 15 minutes at room temperature. The resin was then washed four more times in TEV digest buffer, then incubated in TEV buffer supplemented with TEV protease for 1 hour. Following TEV digest, the bead solution was transferred to a spin column (Millipore) and centrifuged at 20,000 x g for 10 seconds. The resulting protein solution was aliquoted, flash frozen in liquid nitrogen, and then stored at -80°C. Protein concentrations were determined by running a dilution series of dynein along with a dilution series of tubulin on a 4-12% SDS-PAGE gel, and then staining the gel with Sypro Red gel stain (Thermo Fisher). Band intensities were quantitatively determined following imaging on a Typhoon gel imaging system (FLA 9500).

Purification of the SRS fusion proteins (dynein<sub>CC+MTBD</sub>, kinesin<sub>MTBD</sub>, SRS<sub>CC</sub>-dynein<sub>MTBD</sub>, and SRS<sub>CC</sub>-kinesin<sub>MTBD</sub>; see Fig. 2.5a and b) were performed essentially as described (Gibbons et al., 2014; Carter et al., 2008) with minor modifications. *E. coli* BL21 cells transformed with the appropriate vector (described above in *Plasmid construction*) were grown at 30-37°C in LB, 30  $\mu$ g/ml kanamycin and 34  $\mu$ g/ml chloramphenicol to OD<sub>600</sub> 0.4-0.6, shifted to 16°C for 2 hours, then induced with 0.1 mM IPTG for 14-16 hours at 16°C. The cells were harvested, washed with cold water, resuspended in cold lysis buffer (30 mM HEPES pH 8.0, 50 mM potassium acetate, 2 mM magnesium acetate, 10% glycerol, 10 mM imidazole, 5 mM  $\beta$ -mercaptoethanol, protease inhibitor tablets) and then lysed by sonication (5 x 30 second pulses) with 1 minute on ice between each pulse. The lysate was clarified at 22,000 x g for 20 minutes, then incubated with Ni-NTA agarose (Qiagen) for 1 hour at 4°C. The resin was then washed three times in lysis buffer, after which the resin was transferred to a disposable column, and the protein was eluted with elution buffer (30 mM HEPES pH 8.0, 50 mM potassium acetate, 2 mM magnesium acetate, 10% glycerol, 200 mM imidazole, 5 mM beta-mercaptoethanol). Peak fractions were

pooled and applied to a Superdex 200 (10/300) gel filtration column (using an AKTA fast protein liquid chromatography system) equilibrated in lysis buffer. Peak gel filtration fractions were pooled, concentrated (to between 47 and 89  $\mu\text{M}$ ) in a centrifugal filter device (Amicon Ultra-2ml, Millipore), aliquoted, and drop frozen in liquid nitrogen. We noted that we were able to obtain higher SRS-fusion protein concentrations in pH 8.0 than in pH 7.2 buffer. We ensured that these pH differences between protein purification buffers were carefully controlled for in the binding assays described below (see *Microtubule recruitment assays*, below).

#### **2.4.4 Single and ensemble molecule motility assays**

The single-molecule motility assay was performed as previously described (Markus et al., 2012) with minor modifications. Briefly, flow chambers constructed using slides and plasma cleaned and salinized coverslips attached with double-sided adhesive tape were coated with anti-tubulin antibody (8  $\mu\text{g/ml}$ , YL1/2; Accurate Chemical & Scientific Corporation) then blocked with a mixture of 1% Pluronic F-127 (Fisher Scientific) and 1 mg/ml  $\kappa$ -casein. Taxol-stabilized microtubules (either digested with subtilisin, as described below in *Microtubule recruitment assays*, or undigested) assembled from unlabeled and HiLyte647-labeled porcine tubulin (10:1 ratio; Cytoskeleton) were introduced into the chamber. Following a 5-10 minute incubation, the chamber was washed with dynein lysis buffer supplemented with 20  $\mu\text{M}$  taxol, at which point She1-488 was added to the chamber. After a 5-minute incubation, 6His-GST-dynein<sub>331</sub>-TMR diluted ( $\sim 10$  pM) in motility buffer (30 mM HEPES, pH 7.2, 50 mM potassium acetate, 2 mM magnesium acetate, 1 mM EGTA, 10% glycerol) supplemented with 1 mM DTT, 20  $\mu\text{M}$  taxol, 1 mM Mg-ATP, 0.05% Pluronic F-127, and an oxygen-scavenging system (1.5% glucose, 1 U/ $\mu\text{l}$  glucose oxidase, 125 U/ $\mu\text{l}$  catalase) was added. TIRFM images were collected using a 1.49 NA 100X TIRF objective on a Nikon Ti-E inverted microscope equipped with a Ti-S-E motorized stage, piezo Z-control (Physik Instrumente), and an iXon X3 DU897 cooled EM-CCD camera (Andor). 488 nm, 561 nm, and 640 nm lasers (Coherent) were used along with a multi-pass quad filter cube set (C-TIRF for 405/488/561/638 nm; Chroma) and emission filters mounted in

a filter wheel (525/50 nm, 600/50 nm and 700/75 nm; Chroma) to image She1-488, 6His-GST-dynein<sub>331</sub>-TMR, and HiLyte647-microtubules, respectively. We acquired images at 2 second intervals for 10 min. Velocity and run length values were determined from kymographs generated using the MultipleKymograph plugin for ImageJ ([http://www.embl.de/eamnet/html/body\\_kymograph.html](http://www.embl.de/eamnet/html/body_kymograph.html)). Run length and dwell time for individual runs were determined by fitting with cumulative distribution functions (see Fig. A1.2 and 5), as previously described (Reck-Peterson et al., 2006).

For super resolution stepping analysis, high temporal resolution (~10 fps) movies were acquired of Quantum dot-labeled dynein molecules as previously described (Reck-Peterson et al., 2006). Briefly, low concentrations (~10 pM) of chamber-immobilized microtubule-bound 6His-GST-dynein<sub>331</sub>-PEG-biotin molecules were incubated with 100 nM 525 Qdot streptavidin (Thermo Fisher) under conditions that yield monovalent Qdot attachment (Reck-Petersen et al., 2006; note that for experiments with She1, the chambers were pre-incubated with the indicated concentrations of She1 prior to motor addition). Subsequently, the chambers were washed sequentially with motility buffer (with, or without She1, as indicated), and then motility buffer supplemented with 0.05% Pluronic F-127, the oxygen-scavenging system (see above), and either 1 mM Mg-ATP, or 1  $\mu$ M Mg-ATP (see figures and/or figure legends), and the indicated concentration of She1. For low (1  $\mu$ M) ATP conditions, the motility buffer was further supplemented with an ATP regenerating system (1% pyruvate kinase and 10 mM phosphoenolpyruvate). TIRFM images were recorded every 100 ms, and fluorescent spots were fitted with a 2D Gaussian function to precisely localize their position as previously described (Morkisaki et al., 2016). We found that Qdot 525 provided us with the highest signal-to-noise images; however, this fluorophore exhibits overlapping excitation and emission profiles with the GFP near the N-terminus of GST-dynein<sub>331</sub> (*i.e.*, 6His-GFP-3HA-GST-dynein<sub>331</sub>-HALO; see Fig. A1.1a). With our imaging conditions, the GFP photobleached quite rapidly with respect to the photostable Qdot. Specifically, we found that there was a 99.5% probability that GFP

photobleached within 388 frames (38.8 seconds) of first appearing (Fig. A1.1b). This is in striking contrast to the Qdot<sup>525</sup>, which was extremely photostable. Thus, to ensure our particle detection algorithm was tracking Qdot-labeled dynein (*i.e.*, not GFP), the first 400 frames of each processive run were discarded. Steps were detected from the displacement records using a custom-written Mathematica (Wolfram Research) program (available upon request). Steps were assigned only if the dwells before and after contained at least three frames (Qui et al., 2012).

For microtubule gliding (*i.e.*, ensemble motor motility) assays (see Fig. 2.6e, top), flow chambers were coated with anti-His<sub>6</sub> (Roche) antibody for 5 minutes, and then blocked as above. 6His-GST-dynein<sub>331</sub> (wild-type or chimera; 5 µg/ml) was subsequently introduced into the chamber, incubated for 2 minutes, and then washed with one chamber volume of motility buffer. The chamber was then washed with motility buffer supplemented with the oxygen-scavenging system (see above), 1 mM Mg-ATP, and HiLyte647-microtubules (125 nM), after which TIRFM images were collected every 5 seconds. For experiments in which She1 was included, the motility mix with microtubules was pre-incubated with 10 nM She1-HALO for 10 minutes prior to its addition to the chamber. Velocity values were determined from kymographs generated as described above.

#### **2.4.5 Dynein ATPase assays**

Basal and microtubule-stimulated ATPase activities were determined using the EnzChek phosphate assay kit (Life Technologies). Assays were performed in motility buffer (see above) supplemented with 2 mM MgATP, with 0 – 2 µM taxol-stabilized microtubules, 5 nM 6His-GST-dynein<sub>331</sub>, and in the absence or presence of 200 nM She1. Reactions were initiated with the addition of dynein, and the absorbance at 360 nm was monitored by a spectrophotometer for 10–20 min. Background phosphate release levels (presumably from microtubules) for each reaction were measured for 5 min before addition of dynein to account for any variation as a consequence of differing microtubule concentrations, and were subtracted out from each data

point.  $K_{m(MT)}$ ,  $k_{basal}$ , and  $k_{cat}$  were determined from fitting the data to equation (1), as previously described (Kon et al., 2004), where  $k_{obs}$  and  $k_{basal}$  are the observed and basal ATPase rates, and  $x$  is the concentration of tubulin that used to generate microtubules for a given data point:

$$(1) \quad k_{obs} = \left( \frac{x(k_{cat} - k_{basal})}{(K_{m(MT)} + x) + k_{basal}} \right)^2$$

#### **2.4.6 Microtubule recruitment assays**

Taxol-stabilized microtubules were digested with a freshly dissolved preparation of 1-2 mg/ml subtilisin (Sigma; from a stock solution of 5 mg/ml) for 60-75 minutes at 37°C prior to each binding assay. Chambers were prepared as described above (see *Single and ensemble molecule motility assays*). After microtubules were adhered to the cover glass, mixtures of She1-TMR and dynein fragments (as described throughout the text and in figure legends) were flowed into the chambers for 5 minutes, after which the chambers were washed with motility buffer (see above), and immediately imaged. Buffer conditions for a given binding experiment were kept constant to ensure that buffer conditions (*e.g.*, salt concentration, *etc*) were not factors in the apparent degree of microtubule recruitment. For the SRS-MTBD/She1 recruitment assays, the pH of the reaction mixtures was kept constant between samples by mixing motility buffers (see above) that differed only in their pH: pH 6.7 and pH 8.0. The final reaction buffer consisted of 61% motility buffer pH 6.7, and 39% motility buffer pH 8.0 (resulting in a final pH of 7.4). For experiments in which relative She1 microtubule recruitment was quantitatively compared (*e.g.*, Fig. 2.4e and 2.5f), imaging conditions were kept constant (*i.e.*, laser power and camera exposures). Moreover, to control for differences in labeling efficiencies of She1-HALO (with the HALO-TMR ligand), protein from a given preparation was only compared to itself (*i.e.*, protein from different preps were never used for a given experimental replicate). Quantitation of the recruitment assays was performed using ImageJ software (National Institutes of Health). Fluorescence intensities in the red (She1-TMR) and green (dynein or kinesin fragments) channels were measured along microtubules (“signal”; determined from HiLyte-647-microtubule

fluorescence), and adjacent to microtubules (“background”). Mean corrected pixel intensity was determined by subtracting background from signal. To correct for differential microtubule binding affinity of the various protein fragments (*e.g.*, dynein<sub>MTBD</sub> vs SRS<sub>CC</sub>-dynein<sub>MTBD</sub>; see Fig. 2.5f), fluorescence intensity values in the green channel (GFP) were used in place of concentration. Binding curves and curve fitting for dissociation constants (where appropriate) were generated using GraphPad Prism.

#### **2.4.7 Live cell imaging experiments**

For the single time point spindle position assay, the percentage of cells with a misoriented anaphase spindle was determined after growth overnight (12-16 hours) at a low temperature (16°C), as previously described (Sheeman et al., 2003; Li et al., 2005; Markus et al., 2009). A single z-stack of wide-field fluorescence images was acquired for mRuby2-Tub1. For the spindle oscillation assay (Fig. 2.7g and h and Fig. A1.7c), cells were arrested with hydroxyurea (HU) for 2.5 hours, and then mounted on agarose pads containing HU for fluorescence microscopy. GFP-labeled microtubules (GFP-Tub1) were imaged every 10 seconds for 10 minutes. To image dynein localization in live *GAL1p:SHE1* cells (Fig. 2.7e and f, and Fig. A1.6), cells were grown as indicated in figure legends, and mounted on agarose pads. Images were collected on a Nikon Ti-E microscope equipped with a 1.49 NA 100X TIRF objective, a Ti-S-E motorized stage, piezo Z-control (Physik Instrumente), an iXon DU888 cooled EM-CCD camera (Andor), and a spinning disc confocal scanner unit (CSUX1; Yokogawa) with an emission filter wheel (ET480/40M for mTurquoise2, ET525/50M for GFP, ET520/40M for YFP, and ET632/60M for mRuby2; Chroma). 445 nm, 488 nm, 515 nm, and 561 nm lasers (housed in a LU-NV laser unit equipped with AOTF control; Nikon) were used to excite mTurquoise2, GFP, YFP and mRuby2, respectively. The microscope was controlled with NIS Elements software (Nikon). Image analysis was performed using ImageJ software (National Institutes of Health). Plus end and SPB foci were identified in two-color movies and scored accordingly. Specifically, plus end molecules were recognized as those foci that localized to the

distal tips of dynamic microtubules (identified via mTurquoise2- or mRuby2-Tub1 imaging), whereas spindle pole body (SPB)-associated molecules were recognized as those foci that localized to one of the spindle poles. Cortical molecules were identified as those foci not associated with an astral microtubule plus end that remained stationary at the cell cortex for at least three frames, whereas cytoplasmic foci were identified as those dynamic foci not meeting the criteria described for any of the above described categories (*i.e.*, not associating with astral microtubules, or SPBs).

#### **2.4.8 Yeast two-hybrid assay**

For each assay, an equivalent number of yeast cells containing plasmids expressing a GAL4-DNA binding domain (DBD) and transcriptional activation domain (“AD”) fusions were spotted onto histidine-containing plates (“+HIS”; as control), or selective media lacking histidine (“-HIS”), the latter of which contained 5 mM 3-amino-1,2,4-triazole (to reduce background growth due to autoactivation by GAL4-DBD-SRS<sub>CC</sub>-dynein<sub>MTBD</sub> bait; not shown). Both the +HIS and -HIS plates lacked tryptophan and leucine in order to select for cells containing both plasmids.

#### **2.4.9 Statistical analyses**

P-values were calculated using a two-tailed unpaired *t* test. For box-whisker plots, whiskers define the range, boxes encompass 25<sup>th</sup> to 75<sup>th</sup> quartiles, lines depict the medians, and circles depict outlier values (defined as values greater than [upper quartile + 1.5 x interquartile distance], or less than [lower quartile - 1.5 x interquartile distance]).

## **2.5 FIGURES**

Figure 2.1

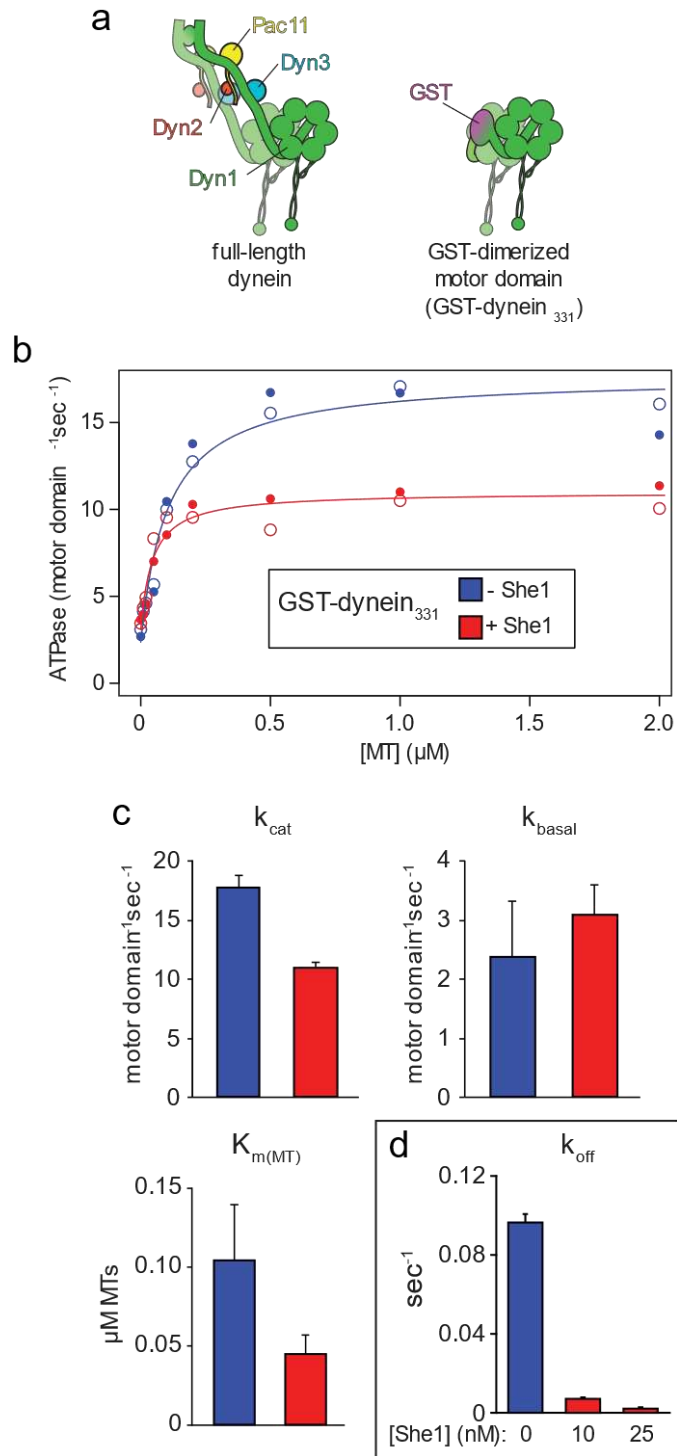


**Figure 2.1. She1 reduces dynein microtubule-stimulated ATPase activity, and enhances the affinity of dynein for microtubules.** (a) Cartoon representation of the full-length dynein complex (left, with associated accessory chains; Dyn2, dynein light chain; Dyn3, dynein light-intermediate chain; Pac11, dynein intermediate chain; Dyn1, dynein heavy chain), and the minimal GST-dimerized dynein motor domain (right). (b and c) Microtubule-stimulated ATPase activity in the absence (blue) and presence (red) of 200 nM She1. Data points from two replicate

experiments are shown (open and closed circles). Data were fit as described in Methods to obtain the basal ( $k_{\text{basal}}$ ; microtubule-unstimulated ATPase activity) and maximal ( $k_{\text{cat}}$ ; microtubule-stimulated) ATPase rates, and the microtubule concentration at which half-maximal ATPase activation is achieved ( $K_{m(\text{MT})}$ ), all of which are depicted in panel c (error bars, standard error of the fit). (d) Dissociation rates ( $k_{\text{off}}$ ) of GST-dynein<sub>331</sub> in the absence and presence of increasing She1 concentrations. Off rates represent the inverse of the time constant from exponential fits to dwell-time distributions as reported in Figure 2.6g (error bars, standard error).

Figure 2.2

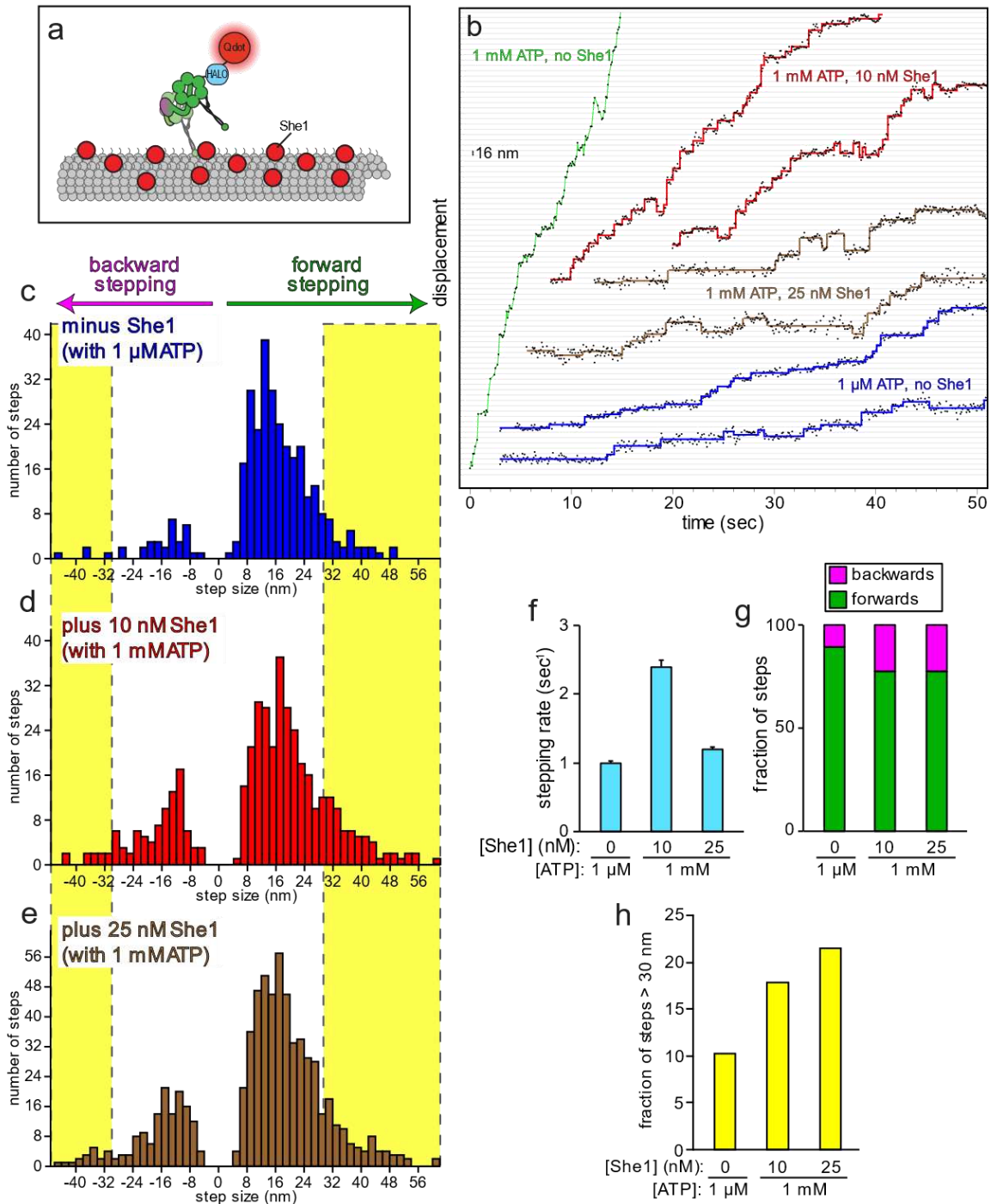


**Figure 2.2. She1 reduces stepping frequency of dynein, and increases fraction of backward and large steps.** (a) Schematic of experimental setup. (b) Representative traces of GST-dynein<sub>331</sub> movement tracked with high precision in the presence of 1 mM ATP (green), 1 μM ATP (blue), or 1 mM ATP and either 10 nM She1 (red) or 25 nM She1 (brown), as indicated. Steps were detected using custom written code (see Methods). (c – e) Histograms of step size distributions for GST-dynein<sub>331</sub> in the absence or presence of She1, and with either 1 μM or 1

mM ATP, as indicated (yellow boxes delineate steps > 30 nm in either direction; see panel h). (f) Histograms of dwell times between steps (see Fig. A1.1c) were fit to convolutions of two exponential functions with equal decay constants, which are plotted here as stepping rate (error bars, standard error of the fit). (g and h) The fraction of forward (*i.e.*, minus end-directed) and backward (*i.e.*, plus end-directed) steps (g), or large steps (h; in either the plus, or minus end direction; see yellow boxes in panels c – e) of GST-dynein<sub>331</sub> in the absence or presence of the indicated concentrations of She1 and ATP (n = 320 steps from 4 motors for no She1; 419 steps from 10 motors for 10 nM She1; 571 steps from 8 motors for 25 nM She1). See Figure A1.1.

Figure 2.3

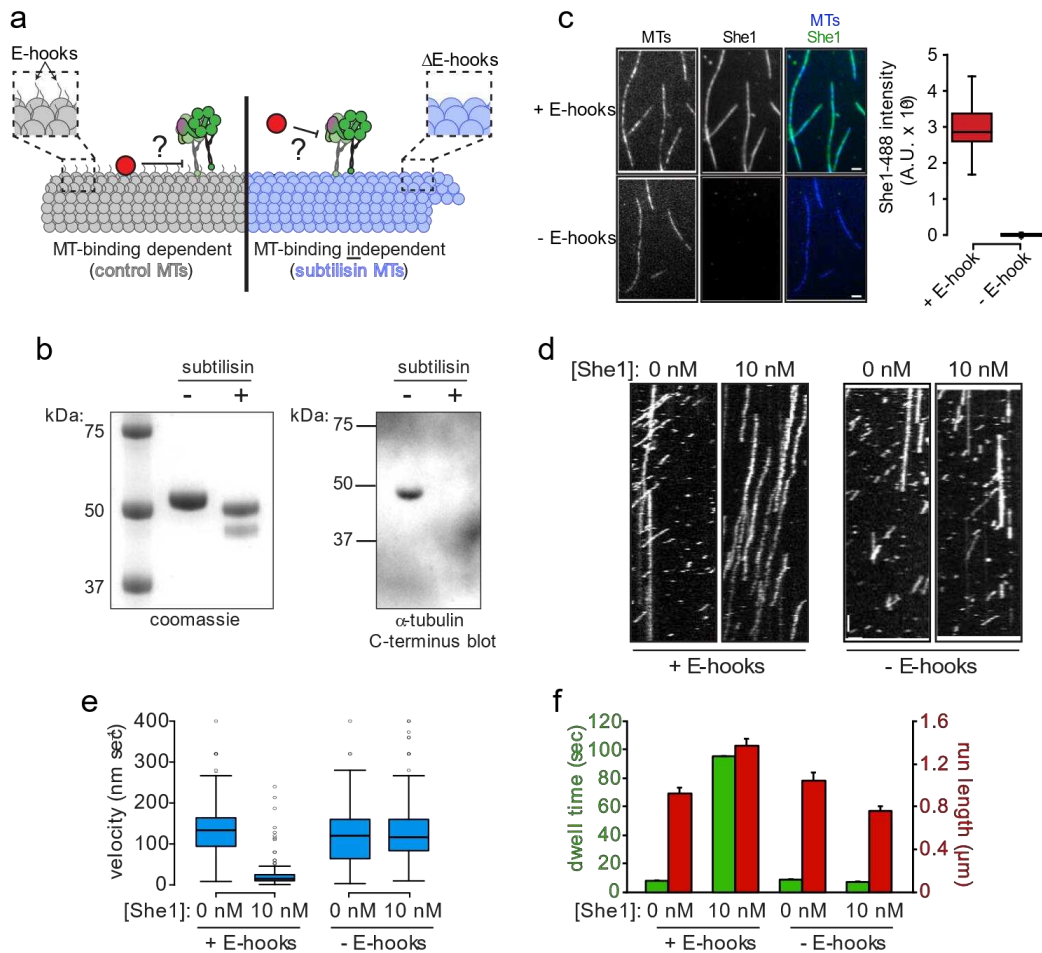


**Figure 2.3. Microtubule-binding by She1 is required for it to affect dynein motility.** (a) Schematic depicting two distinct mechanisms by which She1 may affect dynein motility. She1 either requires its microtubule-binding activity to affect dynein motility (left), or it affects dynein independently of its microtubule-binding activity (right). (b) Coomassie-stained SDS–polyacrylamide gel (left) and immunoblot (anti-alpha-tubulin-C-terminus; right) of taxol-stabilized HiLyte647-labeled microtubules incubated with or without subtilisin, as indicated (see Methods). (c) 10 nM She1-TMR was incubated with either control (“+ E-hooks”) or subtilisin-digested (“- E-hooks”) coverslip-immobilized HiLyte647-labeled microtubules for 5 minutes, then images were acquired by TIRF microscopy. Representative fluorescence images are shown (left) along with box plots of microtubule-bound She1-TMR fluorescence intensity values (scale bars, 2 μm). (d) Representative kymographs showing GST-dynein<sub>331</sub> motility in the absence or presence of 10 nM She1 on either control or subtilisin-digested microtubules. Note that for each experiment in which She1 is included, She1 was preincubated with the microtubules for 5 minutes before addition of GST-dynein<sub>331</sub>, which was diluted in motility mix that also included 10 nM She1 (horizontal scale bar, 2 μm; vertical scale bar, 1 min). (e) Box plot of GST-dynein<sub>331</sub> velocity values in indicated conditions. (f) Mean run lengths (red) and dwell times (green) for GST-dynein<sub>331</sub> molecules along either control or subtilisin digested microtubules in the absence or presence of She1 (error bars, standard error of the mean; n ≥ 199 individual motors for each

condition). For box-whisker plots in panels c and e, whiskers define the range, boxes encompass 25<sup>th</sup> to 75<sup>th</sup> quartiles, lines depict the medians, and circles depict outlier values (defined as values greater than [upper quartile + 1.5 x interquartile distance], or less than [lower quartile - 1.5 x interquartile distance]). See Figure A1.2.

Figure 2.4

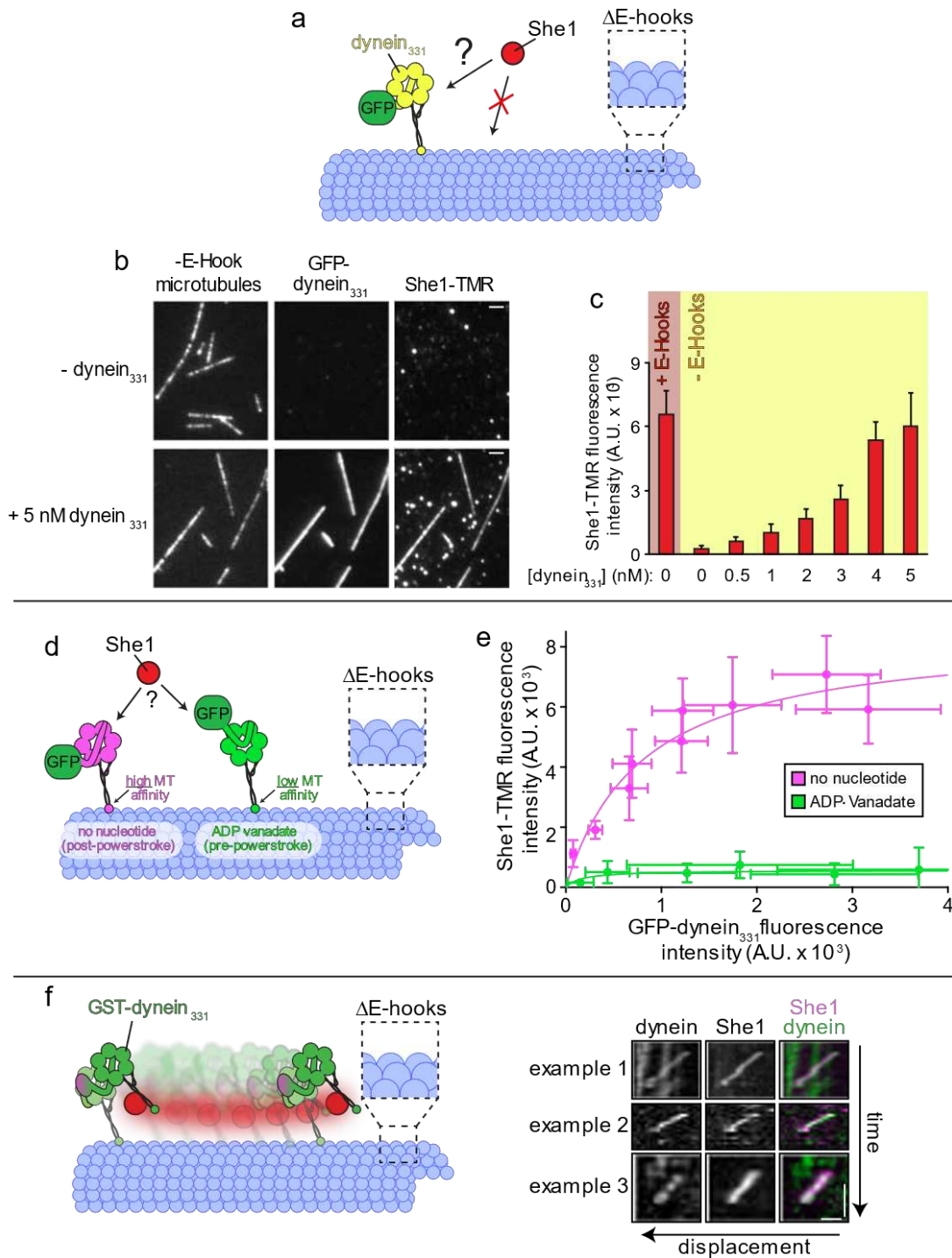


**Figure 2.4. She1 binds directly to dynein, and recognizes a specific nucleotide-bound state.** (a) Schematic of experimental setup. Note that for these experiments, a GFP-tagged monomeric dynein<sub>331</sub> (GFP-dynein<sub>331</sub>) fragment was used. (b – d) Representative fluorescence images (b) and quantitation (c) of She1-TMR recruitment (fixed at 40 nM) to control (“+ E-Hook”) or subtilisin-digested (“- E-hook”) microtubules by increasing concentrations of GFP-

dynein<sub>331</sub> (scale bars, 2  $\mu\text{m}$ ; error bars, standard deviation;  $n \geq 19$  microtubules, and  $\geq 75 \mu\text{m}$  of MT length for each condition). (d) Schematic of experimental setup. Note that the absence of nucleotide elicits a conformational state that is distinct from that of dynein in the presence of ATP and vanadate (see text). (e) Relative recruitment of She1-TMR by GFP-dynein<sub>331</sub> in the presence of either no nucleotide (apo) or 3 mM ATP and vanadate (ADP-vanadate). Different points reflect the mean fluorescence intensity values (along with standard deviations) of She1-TMR (fixed at 40 nM) versus increasing concentrations of GFP-dynein<sub>331</sub>. Given the different microtubule-binding affinity of GFP-dynein<sub>331</sub> in each nucleotide state (see Fig. A1.3a), the extent of She1-TMR microtubule recruitment was directly compared to the relative microtubule binding by GFP-dynein<sub>331</sub> ( $n \geq 10$  microtubules, and  $\geq 36 \mu\text{m}$  of MT length for each condition). (f) Cartoon (left) and three example kymographs (right) depicting that on subtilisin-digested microtubules, She1 remains bound to GST-dynein<sub>331</sub> as it walks, and thus transitions through many iterations of its mechanochemical cycle (horizontal scale bar, 1  $\mu\text{m}$ ; vertical scale bar, 30 sec). See Figure A1.3.

Figure 2.5

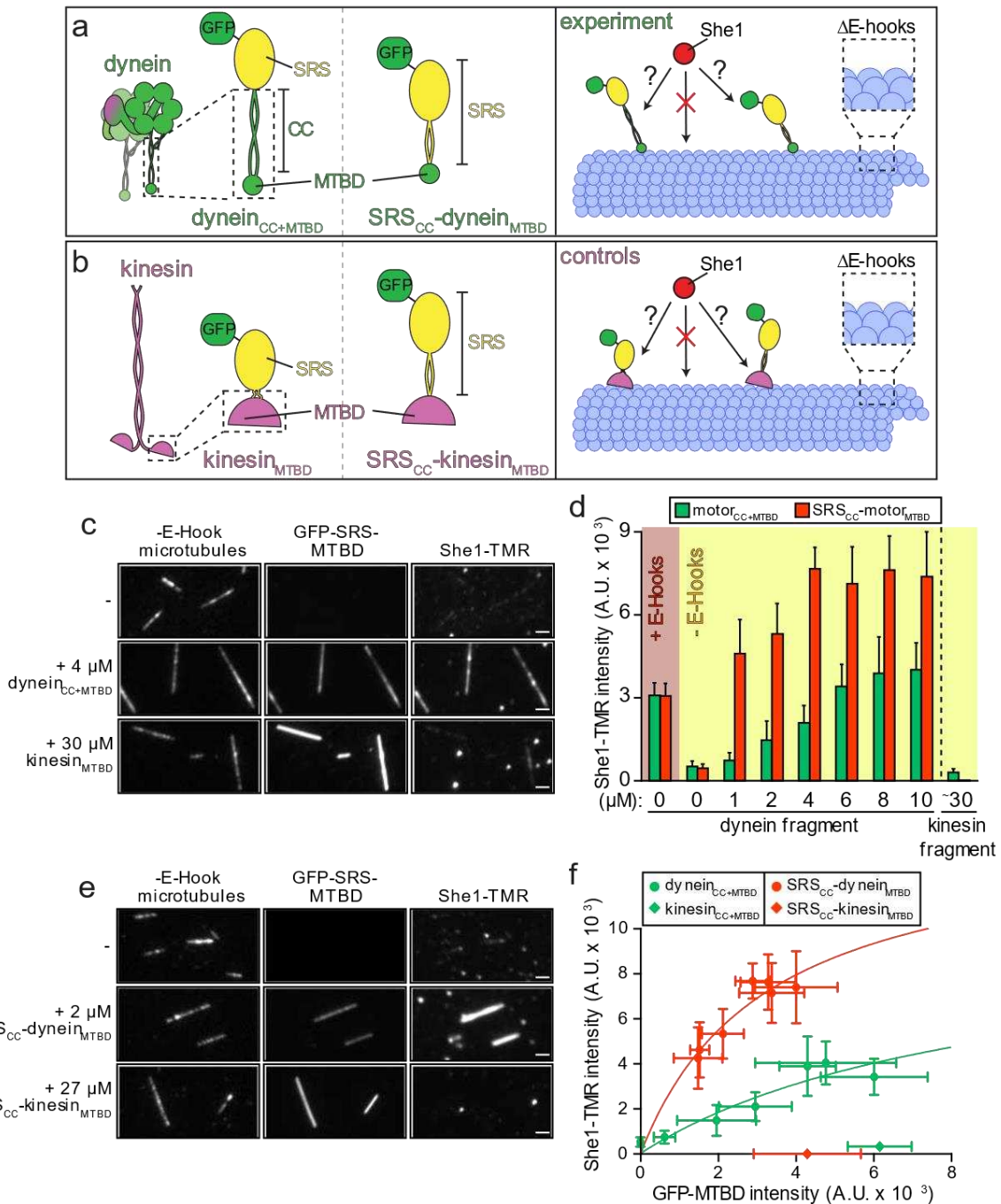


**Figure 2.5. She1 binds directly to the dynein microtubule-binding domain.** (a – b) Cartoon representations of the various GFP-seryl tRNA synthetase (SRS)-dynein (a) and kinesin (b) fusions used in the microtubule recruitment assays (left) along with a schematic of the experimental setup (right). The SRS globular domain fused to either the dynein coiled-coil (CC) and microtubule-binding domain (MTBD), or the kinesin MTBD, respectively are depicted in panels a and b, left, while panels a and b, middle, depict the SRS globular and coiled-coil domains fused to either the dynein or kinesin MTBD domains, respectively. (c and e)

Representative fluorescence images of She1-TMR recruitment to subtilisin-digested microtubules by GFP-SRS-dynein<sub>CC+MTBD</sub> (c) or GFP-SRS-SRS<sub>CC</sub>-dynein<sub>MTBD</sub> (e), but not the respective kinesin MTBD controls. Respective images acquired from each experiment are displayed with identical brightness and contrast levels. Note that in spite of the lesser degree of microtubule-binding by the SRS<sub>CC</sub>-dynein<sub>MTBD</sub> fusion (in panel e) compared to dynein<sub>CC+MTBD</sub> (in panel c), more She1-TMR is recruited to microtubules by the former (scale bars, 2  $\mu$ m). (d) Quantitation of the extent of She1-TMR recruitment to subtilisin-digested microtubules by increasing concentrations of the indicated GFP-SRS-MTBD fusion (error bars, standard deviation;  $n \geq 19$  microtubules, and  $\geq 82 \mu$ m of MT length for each condition). (f) Relative recruitment of She1-TMR by indicated GFP-SRS-MTBD fusion. Different points reflect the mean fluorescence intensity values (along with standard deviations) for She1-TMR (fixed at 20 nM) versus increasing concentrations of indicated GFP-SRS-MTBD fusions. Note that concentrations of the kinesin<sub>MTBD</sub> fusions were chosen such that the degree of their microtubule binding closely matched the maximal microtubule binding by the corresponding dynein fragment. As in Figure 4e, the extent of She1-TMR microtubule recruitment was directly compared to relative microtubule binding by each GFP-SRS-MTBD fragment. See Figure A1.3.

Figure 2.6

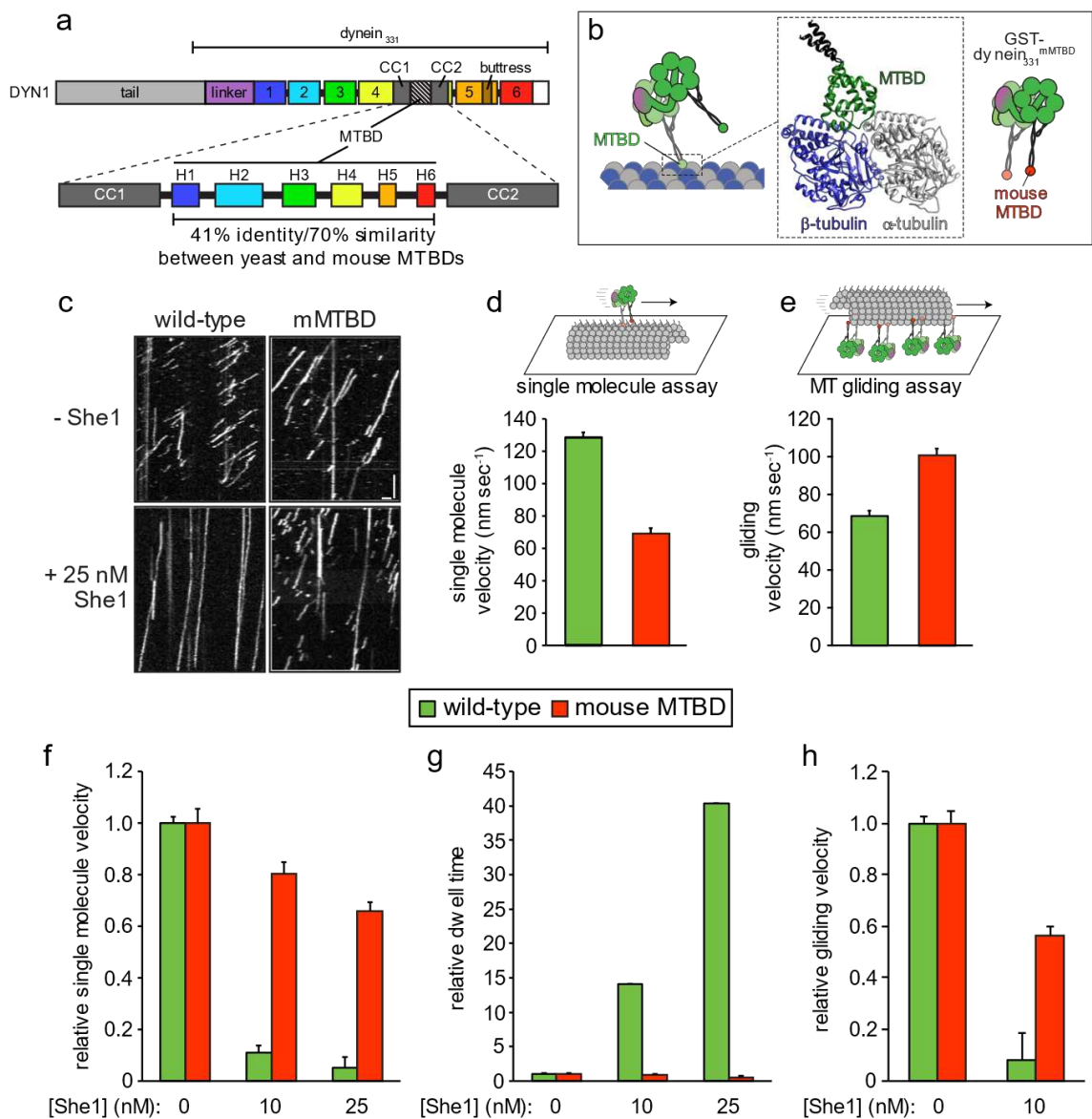


**Figure 2.6. A dynein motor with a mutated MTBD exhibits reduced She1 sensitivity.** (a) Schematic representation of the yeast dynein heavy chain (*DYN1*) with domain structure indicated (domains 1-6 represent the individual AAA domains; CC, coiled-coil; H1-H6, helices that comprise the MTBD). (b) Cartoon representation with homology model of the yeast dynein MTBD bound to alpha and beta-tubulin (green, MTBD; dark grey, CC1 and CC2; generated using one-to-one threading of yeast *DYN1* sequence into 3J1T (Redwine et al., 2012) on the Phyre2 server; Kelley et al., 2015). (c) Kymographs depicting single molecule motility of GST-dynein<sub>331</sub> and GST-dynein<sub>331</sub><sup>mMTBD</sup> in the absence (top) or presence (bottom) of 25 nM She1 (horizontal scale bar, 2 μm; vertical scale bar, 1 min). (d and e) Plots depicting mean velocity of GST-dynein<sub>331</sub> and GST-dynein<sub>331</sub><sup>mMTBD</sup> in single molecule (d) and ensemble microtubule gliding

assays (e; error bars, standard error). (f and g) Plots depicting effects of She1 on the relative velocity (f) and dwell time (g) of single molecules of GST-dynein<sub>331</sub> and GST-dynein<sub>331</sub><sup>mMTBD</sup>. (h) Plot depicting effects of She1 on the relative microtubule gliding velocity of coverslip immobilized GST-dynein<sub>331</sub> and GST-dynein<sub>331</sub><sup>mMTBD</sup> (error bars, standard error; n ≥ 147 individual motors for each condition for single molecule assay; n ≥ 21 microtubules for each condition for the ensemble motility assay). See Figures A1.4 and A1.5.

Figure 2.7

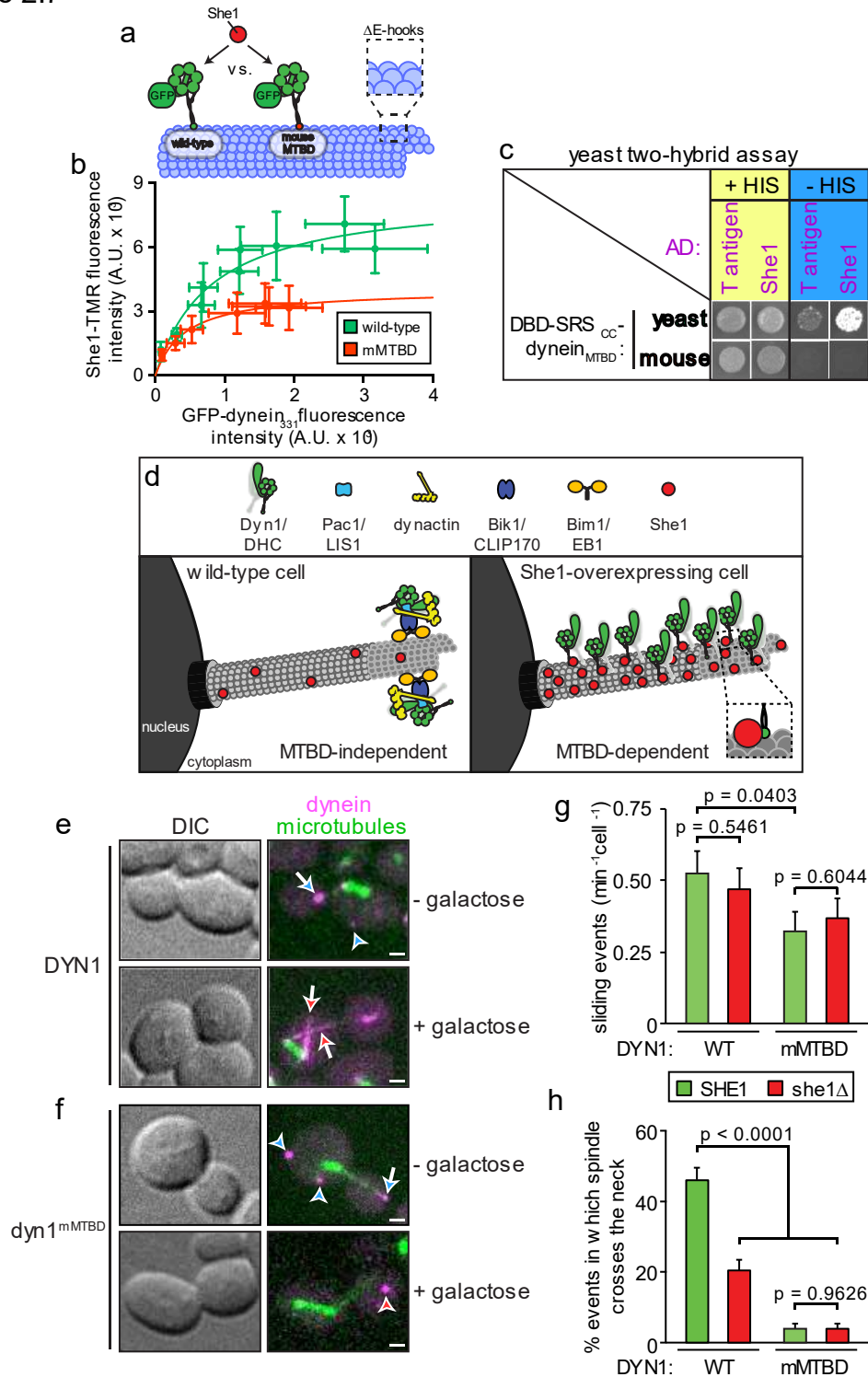


**Figure 2.7. Dynein<sup>mMTBD</sup> exhibits reduced affinity for She1 *in vitro* and is She1-insensitive *in vivo*.** (a) Schematic representation of the experimental setup used in panel b. (b) Relative recruitment of She1-TMR by monomeric GFP-dynein<sub>331</sub> or GFP-dynein<sub>331</sub><sup>mMTBD</sup>. Different points

reflect the mean fluorescence intensity values (along with standard deviations) for She1-TMR (fixed at 40 nM) versus increasing concentrations (0 – 30 nM for wild-type, and 0 – 100 nM for mMTBD) of indicated GFP-dynein<sub>331</sub>. (c) Two-hybrid assay demonstrating an interaction between the yeast derived dynein<sub>MTBD</sub> and She1 (see Methods). (d) Cartoon representation of the localization of full-length dynein heavy chain (Dyn1) in either wild-type (left) or She1-overexpressing cells (right). Note that the mechanism for plus end localization of dynein (which is MTBD-independent; Lammer et al., 2015) is distinct from that by which dynein binds along the length of astral microtubules upon She1-overexpression (MTBD-dependent; see Fig. A1.6). (e and f) Representative images of *GAL1p:SHE1* cells expressing mRuby2-Tub1 ( $\alpha$ -tubulin) and either Dyn1-3YFP (e) or Dyn1<sup>mMTBD</sup>-3YFP (f). Cells were grown to mid-log phase in SD media supplemented with raffinose (uninduced; - galactose) or galactose plus raffinose (induced for 3.5 hours; + galactose) and then mounted on agarose pads for confocal fluorescence microscopy (blue arrows, plus end foci; blue arrowheads, cortical foci; red arrows, astral microtubule decoration; red arrowhead, cytoplasmic focus). Foci were identified in two-color movies and scored accordingly (scale bars, 1  $\mu$ m). (g and h) Dynein-mediated spindle movements were quantitated in hydroxyurea (HU)-arrested *kar9* $\Delta$  cells with indicated *DYN1* and *SHE1* alleles. Cells were arrested with HU for 2.5 hours, and then mounted on agarose pads containing HU for confocal fluorescence microscopy. Full Z-stacks of GFP-labeled microtubules (GFP-Tub1) were acquired every 10 seconds for 10 minutes. Cells with buds of at least 2.5  $\mu$ m in diameter were chosen for analysis. Graphs depicting the number of dynein-mediated spindle movements (g) and the fraction of such events in which the spindle traversed the bud neck (h; in which the spindle midpoint crossed the bud neck) for the indicated yeast strains are shown (error bars, standard error of proportion; n  $\geq$  43 cells; n  $\geq$  155 events). P-values were calculated using a two-tailed unpaired *t* test.

## CHAPTER 3

### THE MAP SHE1 COORDINATES DYNEIN-MEDIATED SPINDLE POSITIONING BY SPATIALLY RESTRICTING DYNEIN ACTIVITY IN YEAST

#### 3.1 INTRODUCTION

Microtubule-based transport in eukaryotes by dynein and kinesin motors plays an important role in many biological processes including transport of vesicular cargoes and organelles and positioning the mitotic spindle during cell division. Novel insights into microtubule-based transport by the motor proteins kinesin and dynein has revealed the presence of a complex matrix of molecular mechanisms that have, until recently, remained unknown, but play a crucial role in regulating molecular motors. Microtubules and microtubule motors are regulated by many microtubule-associated proteins (MAPs), to achieve their distinct spatial and temporal functions in biological processes. The neuronal MAP tau, well known for its implication in Alzheimer's disease, inhibits kinesin-1-based transport of vesicles and organelles in neurons *in vivo* and is a potent inhibitor of kinesin-1, but not dynein motility *in vitro* (Trinczek et al., 1999; Seitz et al., 2002; Dixit et al., 2008). Many MAPs have even been shown to regulate one another, specifically, MAP7 competes tau off microtubules and enhances kinesin-1 recruitment, suggesting MAP7 may antagonize tau effects on kinesin transport *in vivo*. Like tau, MAP7 also does not have a dramatic effect on dynein motility *in vitro* (Monroy et al., 2018). Two known MAPs in higher eukaryotes inhibit dynein motility, specifically MAP9 and MAP4. MAP9 has a unique mechanism of action to inhibit dynein motility, specifically, it prevents the CAP-Gly domain of the p150 subunit of dynactin from binding microtubules, thereby preventing landing of the dynactin-dynein complex on microtubules (Monroy et al., 2020). In *Xenopus melanophores*, MAP4 inhibits dynein-based transport of melanosomes (Semenova et al., 2014). Additionally,

MAP4 inhibited excessive dynein-mediated activity *in vivo*, likely through binding the p150 subunit of dynactin (Samora et al., 2011).

In addition to transporting various cargoes on microtubules, both kinesin and dynein motors also transport the microtubule tracks themselves, a function that is critical for biological processes such as cell division and maintaining cell polarity (Straube et al., 2006; Tanenbaum et al., 2013). Cytoplasmic dynein, anchored to the cell cortex, along with kinesins, on the mitotic spindle, generate opposing forces to position and reorganize mitotic spindles during cell cycle progression, that can compromise the stability and shape of the mitotic spindle (reviewed in Dumont et al., 2009; Estrem et al., 2019). Resistance to these opposing forces, as well as coordinating them, requires specific regulation of MAPs to succeed (Manning et al., 2010; Manning et al., 2017). In budding yeast, spindle microtubules are stabilized by opposing forces of MAPs, and kinesins, that crosslink spindle microtubules, two MAPs of which are Ase1 and She1 (Lansky et al., 2015; Zhu et al., 2017). This stabilizing effect has even been shown to protect spindle and genomic integrity from external forces generated from spindle positioning (Estrem et al., 2019; Zhu et al., 2017). MAPs play an integral role in regulating microtubules and their associated molecular motors to achieve refined regulation during mitosis.

Cytoplasmic dynein functions at the cell cortex where minus end-directed motion drives movement of cytoplasmic microtubules to position the mitotic spindle. This function also requires regulation by MAPs, one of which is Bik1 and to a lesser extent, She1. Bik1 targets dynein and its cofactors to plus ends where it can be offloaded to the cortical anchor and adaptor protein Num1. The role of She1 in this process is not known, but prior work has established that She1 polarizes dynein-mediated spindle movements towards the daughter cell (Moore et al., 2009; Sheeman et al., 2003; Woodruff et al., 2009; Markus et al., 2012; Lee et al., 2003; Lee et al., 2005; Markus et al., 2009). The mechanism behind how She1 assists dynein-mediated spindle orientation through affecting the ability of dynein to move the spindle across the bud neck is unclear. Intriguingly, our recent *in vitro* data systematically dissected how She1

affects dynein motility through simultaneous interactions with the dynein microtubule binding domain and the microtubule. Specifically, She1 enhanced dynein-microtubule interactions through decreasing the dissociation rate and therefore stepping frequency and dwell time of dynein on microtubules. This binding was highly specific to dynein and not kinesin motors, and moreover, recognized the conformational states of the dynein microtubule binding domain (Chapter 2). Our data suggested a model where She1 assisted dynein force generation to move the large nucleus into the small bud neck. However, we demonstrate here that this model is not correct and instead we perform a careful analysis of dynein-mediated spindle movements in live cells, to assess She1 effects on dynein activity and motility *in vivo* to elucidate a mechanism that may reconcile our *in vivo* and *in vitro* data. Our *in vivo* assessment revealed that She1 does not assist dynein-mediated spindle translocation into the bud neck, but rather ensures that dynein maintains the spindle in proximity to the bud neck. Our findings suggest that this is a consequence of She1 attenuating dynein-mediated spindle movements predominantly in the mother cell. Thus, She1 promotes proper spindle positioning by ensuring dynein-mediated spindle movement events are polarized toward the daughter cell. Additionally, we find that this process likely depends on She1 binding to astral microtubules, and not spindle microtubules where She1 also localizes. Finally, She1 requires the microtubule binding domain of dynein for some aspects of this inhibition, partially reconciling our *in vivo* and *in vitro* data. We also determine that some aspects of this inhibition are independent of the dyneinMTBD. In summary, our findings describe the first evidence in budding yeast of a MAP spatially regulating a molecular motor by preferential localization on astral microtubules on in the mother cell during asymmetric cell division.

## **3.2 RESULTS**

### ***3.2.1 She1 assists dynein-mediated spindle positioning in budding yeast***

Previous work established that She1 plays a role in polarizing dynein-mediated spindle movements towards the bud (Markus et al., 2012), indeed, our prior work showed that *she1Δ* mutants displayed mild defects in positioning the spindle into the bud neck at anaphase onset when observed in a single time point spindle positioning assay. Given that She1 appears to assist dynein in moving the spindle into the bud neck, we expected to observe cell cycle delays, specifically, a mitotic exit (MEN) delay from an active spindle positioning checkpoint (SPOC) as a consequence of mispositioned spindles in *she1Δ* cells. Like the spindle assembly checkpoint (SAC), which prevents anaphase-promoting complex (APC) activation until chromosomes are properly attached to the spindle, an active SPOC delays cytokinesis and mitotic exit until the anaphase spindle is aligned parallel to the mother-bud axis, monitored by the entry of a spindle pole body into the bud neck (reviewed in Lew et al., 2003).

To this end, we used the CellAsic™ system to image the complete budding yeast cell cycle. In this system, cells are under constant flow to replenish nutrients, allowing imaging of live cells through several iterations of cell division. To monitor cell cycle progression, we imaged SHE1 and *she1Δ* cells expressing Spc110-Venus, NLS-3mCherry and mTurquoise2-Tub1 (to image SPBs, nucleus, and microtubules) in a microfluidics live cell imaging chamber (see Methods). Consistent with the single time point positioning assay, ~15% cells exhibit mispositioned spindles at anaphase onset (Fig 3.1a). There was a mild delay between anaphase onset to cytokinesis (*she1Δ* ~5 minute delay to cytokinesis; mean ~35 *she1Δ* versus ~30 minutes SHE1, not significant, Fig 2.1b, left). Separating of mispositioned spindles from positioned spindles, irrespective of being from SHE1 or *she1Δ* cells, did not reveal a more obvious SPOC delay (Fig 2.1b, right), indicating that a spindle positioning defect does not give a pronounced SPOC delay in our methods. However, we noted that mispositioned spindles in SHE1 cells exhibited an ~8 minute delay between anaphase onset to cytokinesis when compared to positioned spindles in SHE1 cells, whereas *she1Δ* cells showed no delay in timing from anaphase onset to cytokinesis when compared to positioned spindles *she1Δ* cells (see

Figure legend 3.2); the caveat being a sample size of only 5 mispositioned spindles in SHE1 cells for this calculation), suggesting *she1* may have a defective SPOC. Mitotic duration was also mildly increased (mean ~127 *she1*Δ versus ~111 minutes SHE1, not significant) along with timing to anaphase onset indicating possible delays in SAC/APC signaling (mean ~91 *she1*Δ versus ~80 minutes SHE1, not significant, Fig 3.1c), which may be correlated to other known She1 functional roles at the spindle.

### **3.2.2 *She1* does not assist dynein-mediated nuclear translocation success**

Budding yeast undergo cell division with their nuclear envelope kept intact. The diameter of the bud neck is about half the size of the diameter of the nucleus (~1 μm to ~2 μm, respectively). Therefore, it would not be surprising if the bud neck acts as a physical barrier that must be overcome to position the nucleus within. Our prior work showed that She1 enhances dynein-microtubule interactions through simultaneous binding with the dynein MTBD and the microtubule. Specifically, She1 reduces the dissociation rate of dynein from microtubules, leading to a reduced stepping frequency and prolonged contact with the microtubule. Given that SHE1 cells are more successful at positioning their spindles (Fig 3.1) and in light of this prior *in vitro* data, we hypothesized that She1 enhances dynein force generation on aMTs to assist entry of the large nucleus and spindle into the narrower bud neck connecting mother and bud cells. If this were true, we would expect to see scenarios where a dynein attempts to move the spindle into the bud neck but fails. To address this question, we imaged SHE1 and *she1*Δ live cells arrested in a metaphase-like state by treatment with the DNA-synthesis inhibitor hydroxyurea (HU). This arrest allows ample observation of dynein-mediated spindle movements in a short period of time, specifically, we can observe multiple events attempts to move the spindle into the bud neck (see Methods). This and all future experiments were done in the absence of KAR9, to ensure all active spindle movements are the result of a dynein-mediated event. Dynein-mediated spindle movements were scored based on their successful or unsuccessful spindle translocation into the bud neck (Fig 3.2a, cartoon, also see Methods). Consistent with

our hypothesis, *she1*Δ mutants were ~30% less successful in positioning their spindle in the bud neck during an attempt (Fig 3.1 a).

To determine if She1 increases dynein force generation, we used optical trapping with recombinant dynein and She1. 6His-GFP-GST-dynein<sub>331</sub> purified from yeast was coupled to the magnetic bead using an anti-HIS antibody and allowed to walk on cover-slip immobilized microtubules upon addition of ATP. Motility was observed in the presence or absence of She1-TMR purified from E.Coli (see Methods). Consistent with our prior single molecule data, bead velocity decreased from ~36 nm/sec to ~5 nm/sec in the presence of She1-TMR (Fig 3.2a, top). There was no appreciable change in the stall force upon addition of She1, but we observed a substantial increase in stall time of ~120 seconds (Fig 3.2a, middle and bottom). These results suggest that She1 does not increase dynein force generation but does enhance the ability of dynein to remain bound to microtubules under the high forces possibly generated by the large nucleus encountering the bud neck.

To test this hypothesis *in vivo*, we again imaged dynein-mediated spindle movements but this time with a nuclear label. We reasoned that if She1 assists dynein in successfully pulling the nucleus into the bud neck, then widening the bud neck should rescue She1 phenotypes. To that end we included *bni1*Δ mutants in our analysis, which widens the bud neck from ~1.1 μm to ~1.4 μm (Fig 3.2b). HU arrested SHE1 and *she1* cells were imaged and the frequency with which nuclei successfully crossed the neck was scored (see Methods). In contrast with the optical trapping data, loss of She1 had no depreciable effect on nuclear translocation success and though widening the bud neck did have a minor increase in nuclear translocation success there was no additive benefit in *she1*Δ cells (Fig 3.2c). This suggests that though the bud neck acts as a physical barrier, She1 does not assist dynein in overcoming it, and therefore a complete model that reconciles our *in vitro* and *in vivo* data is still lacking.

### **3.2.3 Cytoplasmic She1 inhibits dynein activity *in vivo***

Previous works support the idea that She1 inhibits dynein hyperactivity in cells. Specifically, cells lacking She1 exhibited dramatic and more frequent spindle movements where the astral microtubules glide along the cell cortex with increased velocity (Woodruff et al., 2009; Markus et al., 2012). Since She1 does not assist dynein during nuclear translocation into the bud neck, but we still observe a spindle neck cross defect (Fig 3.2), we revisited the behavior of dynein-mediated spindle movements in a more detailed analysis to discern with more clarity She1 effects on dynein function by characterizing dynein activity and various motility parameters in cells. HU arrested cells were imaged as described previously and dynein-mediated spindle movements manually curated from spindle tracking data (see Methods). It is currently unknown whether the spindle neck cross phenotype is attributed to cytoplasmic pools of She1, or nuclear pools of She1, which may affect spindle positioning through dynein-independent means (Woodruff et al., 2010; Bergman et al., 2012). She1 has been implicated in promoting spindle disassembly, playing a role in kinetochore function through affecting mitotic timing of Ipl1 activity, and through maintaining interpolar microtubule stability. All presumably through its localization to the nucleus and spindle microtubules (Wong et al., 2007; Woodruff et al., 2010; Zhu et al., 2017). To determine if regulation of dynein activity was due to cytoplasmic She1, we included a mutant of She1 that sequesters it in the nucleus through a C-terminal nuclear localization signal (see Methods) to maintain its nuclear but not cytoplasmic functions. We quantified the fraction dynein-mediated movements that move the spindle towards the bud neck and found similar defects in bud directed movements in both *she1Δ* and She1-NLS mutants as seen previously – which is illustrated clearly by the representative example tracks – suggesting cytoplasmic-localized She1 is responsible (Markus et al., 2012) (Fig 3.3a and b, SHE1, *she1Δ*, and She1-NLS). We also saw an enhancement in motility metrics, dynein-mediated spindle movement velocities and run lengths increased in *she1Δ* and She1-NLS mutants, indicating that She1 affects the motility properties of motors during a sliding event (Fig 3.3c and d, SHE1, *she1Δ*, and She1-NLS). General dynein activity is also increased in all metrics including the

number of sliding events per unit time, the fraction of time dynein is active, and dynein-dependent spindle displacement per unit time, indicating that cytoplasmic She1 inhibits dynein hyperactivity (Fig. 3.3e, SHE1, she1 $\Delta$ , and She1-NLS).

### **3.2.4 She1 requires astral microtubule binding to inhibit dynein activity**

As stated before, our previous work demonstrated that She1 must be bound to microtubules to affect dynein motility *in vitro*. Though She1 localizes to astral microtubules, this localization decreases prior to anaphase onset, when dynein is suspected to actively position the spindle. This suggests that She1 inhibits the premature activation of dynein prior to anaphase onset, however, She1 inhibition is also required in anaphase to prevent hyperactive dynein activity (Woodruff et al., 2010). The decrease in She1 fluorescent signal on astral microtubules in anaphase when She1 is also suspected to inhibit dynein activity leads to question whether She1 binds astral microtubules to inhibit dynein activity or if inhibition occurs through extrinsic factors in the cytoplasm or the bud neck, where She1 also localizes (Woodruff et al., 2009; Pigula et al., 2014). To address this, we used an  $\alpha$ -tubulin mutant containing a glycine to arginine amino acid substitution at position 437. This mutation leads to ~50% reduction in She1 binding to spindle microtubules (Fig A3.1a, top and b, also see Appendix 2). If She1 requires astral microtubule binding to inhibit dynein activity, then tub1-G437R mutants should partially phenocopy she1 $\Delta$ . Indeed, tub1-G437R mutants display defects in their ability to move the spindle across the bud neck, enhancements in dynein motility metrics, and increased dynein activity reminiscent of she1 $\Delta$  cells (Fig 3.3a-e, TUB1 G/R and TUB1 G/R she1 $\Delta$ ), suggesting She1 regulates dynein activity through its astral microtubule binding behavior.

Not surprisingly, She1 regulates the large dynein cofactor dynactin. Through an unknown mechanism dynactin recruitment to plus ends is limited by She1, which conserves the ratio of dynactin to dynein molecules at plus ends (1:3 dynactin:dynein versus 1:1 in she1 $\Delta$ ) (Markus et al., 2012). Presumably this regulation is not through She1 directly binding dynactin or through inhibiting dynactin component assembly but may be achieved through limiting dynein

and dynactin interaction (Woodruff et al., 2009; Bergman et al., 2012). To test if She1 regulates dynein activity through dynactin, it would be ideal to delete the complex, however dynactin is required for dynein function. The CAP-Gly domain is the microtubule binding domain of the dynactin subunit Nip100. This region has been shown to promote dynein activity and efficient dynein-dependent nuclear movement in budding yeast and neurons (Kardon et al., 2009; Moore et al., 2009; Nirschl et al., 2016). Additionally, a MAP9 in humans inhibits dynein-dynactin motility *in vitro* through blocking p150 (human CAP-Gly) binding to microtubules (Monroy et al., 2020). Given that the CAP-Gly domain promotes dynein activity (the inverse of She1 effects) and a previously described MAP in higher eukaryotes inhibits dynein motility through blocking dynactin-microtubule binding, we wondered if She1 may share this mechanism to inhibit dynein activity *in vivo*. If She1 regulates dynein activity through inhibiting CAP-Gly microtubule binding, then mutants lacking the CAP-Gly domain would be insensitive to She1 loss. Contrary to this idea, we saw a nearly equivalent decrease in the spindle neck cross phenotype, as well as equivalent increases in motility metrics and dynein activity, suggesting She1 does not regulate dynein through blocking dynactin-microtubule binding (Fig 3.3a-e,  $\Delta$ CAP-Gly and  $\Delta$ CAP-Gly she1 $\Delta$ ).

### ***3.2.5 She1 inhibits the initiation of dynein-mediated spindle movements in the mother compartment***

Astral microtubules make contacts with the cell cortex as they dynamically move and grow in the cytoplasm, but not all cortical contacts will convert to a dynein-mediated spindle movement, or productive slide (Fig 3.4a, cartoon). Initiation of a productive sliding event occurs upon activation of the dynein-dynactin complex through offloading from the plus end to the cortical anchor and adaptor protein Num1 (Lammers et al., 2015). We wondered if the increased frequency of sliding events in she1 $\Delta$  cells (Fig 3.3d, sliding events per unit time) is a consequence of more astral microtubule cortical contacts initiating into a productive slide or if it is simply the result of more astral microtubules encountering the cell cortex because of changes

in microtubule dynamics. To address this question, we manually counted cortical contacts and productive slides and corrected for differences in cortical contact number by dividing productive sliding events by the number of cortical contacts per cell. She1 inhibits ~20% of cortical contacts from converting to a productive slide, indicating that changes in cortical contact frequency is not the driver for the increased sliding events (Fig 3.4a, SHE1 and she1 $\Delta$ ). Note how this inhibition primarily occurs in the mother compartment and requires microtubule binding by She1, supporting a previously proposed hypothesis that She1 inhibits mother-localized dynein on astral microtubules (Fig 3.4a, She1-NLS, tub1-G437R, and tub1-G437R she1 $\Delta$ ) (Markus et al., 2012). And consistent with our previous *in vivo* data, does not occur through regulating the microtubule binding domain of dynactin (Fig 3.4a,  $\Delta$ CAP-Gly,  $\Delta$ CAP-Gly she1 $\Delta$ ).

### **3.2.6 *She1 maintains bud neck proximity through dynein-dependent and -independent mechanisms***

The consequences of dynein hyperactivity on spindle positioning may be inferred from our data that spindle displacement is increased and prior work that saw several instances where dramatic spindle movements lead to the spindle pole bodies encountering the mother-cell cortex (Markus et al., 2012). Indeed, our representative spindle tracks (Fig 3.3a) illustrate how dramatic spindle movements may be leading to the spindle residing far from the bud neck, abrogating spindle positioning attempts. We wondered how frequently dynein hyperactivity leads to these instances where the spindle is pulled far from the bud neck and within close proximity of the cell cortex (within 1  $\mu$ m, Fig 3.4b, cartoon). We scored the frequency of seeing the spindle reside within 1  $\mu$ m of the cell cortex, using spindle tracking data from before. Given that this analysis includes all spindle tracks, not just spindle tracks that are a consequence of dynein-mediated movement, we included dyn1 $\Delta$  mutants, to determine to what degree this phenotype depended on dynein hyperactivity. We found that all she1 $\Delta$ , tub1-G437R, and She1-NLS mutants displayed a 6-12 fold cortical proximity increase except in the case of dyn1 $\Delta$  and  $\Delta$ CAP-Gly mutants, suggesting this phenotype is a consequence of dynein hyperactivity in

she1 $\Delta$  cells, and consistent with previous figures that inhibition requires She1-microtubule binding (Fig 3.4b).

The mechanism behind how She1 promotes spindle positioning has not been elucidated. Our current and prior work show a defect in dynein-mediated spindle movements towards the bud neck coinciding with an increase in the initiation of dynein-mediated spindle movements in the mother compartment, supporting a previously proposed model where She1 inhibits dynein in the mother compartment, therefore allowing bud-localized dynein to polarize spindle movements towards the bud neck (Markus et al., 2012). However, though these explanations are logical, given our current and prior data, to attribute the spindle positioning defect in she1 $\Delta$  mutant to dynein hyperactivity, it has not been confirmed that this is the only mode by which She1 polarizes spindle movement towards the bud. Given that She1 also localizes prominently to the bud neck (Woodruff et al., 2009), a major epicenter for regulating polarity during cell division in budding yeast, it is reasonable to suggest She1 may play a role in polarizing spindle movement in a dynein-independent manner. To this end, we processed and binned spindle tracking data from our wild-type and mutant strains based on their relative distance from the bud neck (Fig. 3.4c and see Methods). The histograms of she1 $\Delta$  mutants display a broad distribution away from the bud neck as expected from dynein hyperactivity in all cases except in dyn1 $\Delta$  mutants (Fig 3.5). We then plotted the fraction of spindle tracks that reside within either the mother or bud compartments and observe an obvious bias towards the mother compartment in she1 $\Delta$  mutants consistent with the histograms (Fig 3.4c, bottom). Since dyn1 $\Delta$  mutants are devoid of any active spindle positioning pathway we also saw this bias, but it was not further exasperated in dyn1 $\Delta$  she1 $\Delta$  mutants (Fig 3.4c, bottom). Taken together our data support the idea that dynein hyperactivity in the mother compartment leads to the spindle being pulled away from the bud neck and sequestered in the mother compartment. Fascinatingly, the same cannot be said for a small region nearest the bud neck (a region within a relative distance of 20% proximal to the bud neck, Fig 3.4c, top, and gray rectangle). Though there is a sizable decrease in the

fraction of spindles within proximity of the bud neck, there is a further reduction in *dyn1Δ she1Δ* mutants (Fig 3.4c, top), and this defect does not require microtubule binding (Fig 3.4c, top, *tub1-G437R*) supporting the suspicion that She1 plays a role in dynein-independent polarization, through an unknown mechanism that promotes proximity of the spindle without actively moving it (Fig 3.4c, top She1-NLS and Fig 3.4d).

### **3.2.7 *She1* localizes to mother-associated astral microtubules**

The mechanism behind how She1 inhibits the initiation of dynein events in the mother compartment is unknown, however we do know that this inhibition requires she1 binding to astral microtubules, suggesting the possibility that She1 may preferentially localize to mother-associated astral microtubules (Fig 3.4a). We've chosen to circumvent the difficult visualization of She1 with a time-limited galactose over-expression of She1-GFP and mRuby2-tub1 in HU arrested cells (see Methods). Upon scoring of astral microtubules based on visible She1-GFP signal, we saw that ~80% of mother-associated astral microtubules had visible She1-GFP, compared to ~20% of bud-associated astral microtubules (Fig 3.6a and b). Given the binary nature of our initial analysis, we wondered if bud-localized astral microtubules were truly devoid of She1-GFP binding, or if binding was simply reduced below visual detection, so we measured the fluorescent intensity of She1-GFP and mRuby2-tub1 on mother and bud astral microtubules (Fig 3.6c, middle and right, also see Methods). We found that the intensity of She1-GFP on mother-associated astral microtubules was ~4x greater than on bud-associated astral microtubules and this difference is not due to astral microtubule density (Fig 3.6c), supporting the notion that She1 inhibits mother-localized dynein through biased binding to mother-associated astral microtubules.

The mechanism that drives biased localization of She1 to mother-associated astral microtubules is unknown, and the possibilities vast, but we hypothesize that it could be controlled through either a microtubule-independent or -dependent mechanism. For instance, if the bias depends on a microtubule-dependent mechanism, then the targeted depolymerization

of microtubules using nocodazole should lead to She1-GFP fluorescent signal in the cytoplasm equilibrating equally between mother and bud compartments. To that end, we treated our She1-GFP cells with 10 $\mu$ M nocodazole prior to imaging to fully depolymerize astral microtubules (see Methods). There was no statistical difference between She1-GFP in the cytoplasm of mother and bud compartments and the ratio dropped to a steady 1:1 mother:bud in nocodazole treated cells (Fig 3.6d), suggesting that biased localization of She1 on mother-associated astral microtubules is through a microtubule-dependent process, possibly through modulating the affinity of She1 for microtubules.

### **3.2.8 She1 requires the microtubule binding domain of dynein to inhibit dynein activity**

Our previous data demonstrated that She1 affects dynein motility through simultaneous interactions with the microtubule binding domain of dynein and the microtubule. We've demonstrated here that She1 must bind astral microtubules to regulate dynein activity, but to fully reconcile our *in vivo* and *in vitro* data, we must address if She1 also requires the microtubule binding domain of dynein to inhibit dynein activity. In our previous work we described a chimeric dynein MTBD mutant – where we swapped the yeast MTBD for the rat MTBD – which displayed reduced binding and sensitivity to She1 effects (see Figure 2.6 and 2.7). To test if She1 inhibition requires the dynein MTBD *in vivo*, we put this chimera through our detailed analysis as described previously (see Methods). Though we observed a defect in the spindle neck cross phenotype in the rat chimera, loss of She1 did not lead to further exacerbation of the positioning defect (Fig 3.7a and b, Dyn1-rat and Dyn1-rat she1 $\Delta$ ). Unexpectedly, we saw a partial rescue of the enhanced velocity seen in dynein motility metrics in our control strains, which incidentally have a 3YFP tag on dynein for the purpose of strain confirmation, (Fig 3.7c SHE1 and she1 $\Delta$ , also see Methods) but not in chimeric mutant, which also has Dyn-3YFP tags (Fig 3.7c Dyn1-rat and Dyn1-rat she1 $\Delta$ ). Additionally, we still saw the increase in sliding event run length in the chimeras (Fig 3.7c SHE1 and she1 $\Delta$  versus Dyn1-rat and Dyn1-rat she1 $\Delta$ ). Though we are not sure the implications of the unexpected result in our

velocity metric, both motility metrics suggest that the dynein motility phenotype seen in *she1Δ* mutants, is not regulated through the dynein MTBD. In contrast, we did not see a significant change in dynein activity upon loss of She1, even the spindle displacement which saw a statistically significant increase, was very subtle and likely a consequence of the increased run lengths seen in all *she1Δ* mutants (Fig 3.7d, Dyn1-rat and Dyn1-rat *she1Δ*), suggesting that some aspects of dynein hyperactivity in these cells is inhibited by She1 regulation through the dynein MTBD.

### ***3.2.9 Sensitivity to She1 is partially restored by enhancing the affinity state of the chimera MTBD***

We demonstrated in our prior *in vitro* work that She1 has a higher binding affinity for the nucleotide-free conformational state of the dynein motor domain, a state which has a high-affinity for microtubules (see Figure 2.4d and e). Though the purpose of this specificity is not understood, it may play a critical role in the mechanism by which She1 regulates dynein activity. Our chimeric dynein mutant – with the rat-MTBD – has a lower affinity for microtubules than the wild-type yeast motor (see Figure A1.4c). This led us to wonder if the chimeric dynein mutant displays partial insensitivity to She1 due to conformational differences between yeast and rat MTBD. To test this, we inserted two charge-reversal point mutations (E3289 -> K and E3378 -> K) in the coiled-coil and MTBD of the chimeric dynein mutant which have been previously reported to increase the microtubule binding affinity (Redwine et al., 2012) (see Methods). We should see a restoration of She1 sensitivity in this scenario. As before, even the high affinity chimera appears to have a defect in moving the spindle across the neck (Fig 3.7a, rE/K and rE/K *she1Δ*), however, the velocity still increased consistent with the idea that motility metrics of a sliding event are not governed by She1 binding the dynein MTBD (Fig 3.7c, rE/K and rE/K *she1Δ*). Consistent with our hypothesis, we did see a complete restoration in dynein activity, suggesting that She1 regulation of dynein activity is in part dependent to the conformational specificity of She1 for the dynein MTBD (Fig 3.7d, rE/K and rE/K *she1Δ*).

### **3.2.10 *She1 inhibits initiation of dynein-mediated spindle movements and maintains bud neck proximity through interaction with the microtubule binding domain of dynein***

If inhibition of the initiation of dynein sliding events and cortical proximity phenotypes require the MTBD of dynein, we would expect our chimeric dynein mutant to not display an increase in productive sliding events or cortical proximity, and in light of this reduced sensitivity correlating to a conformational difference in the motors, we should see a restoration of these phenotypes in the high affinity chimera, which we observed (Fig 3.8a and b). However, note that the chimera displays a partial increase in cortical proximity, albeit to a less significant degree than the *she1Δ* and rE/K *she1Δ* mutants (Fig 3.8b), suggesting some MTBD-independent mechanism may be contributing to this phenotype or – given that the chimera had reduced sensitivity, not complete insensitivity to She1 effects – this phenotype is more sensitive than our previous metrics in identifying subtle changes in dynein hyperactivity.

Recall our previous data which described a broad distribution away from the bud neck as a consequence of dynein hyperactivity (Fig 3.8). It is apparent from the histograms for our chimeric mutants (Fig 3.9, SHE1, *she1Δ*, Dyn1-rat, Dyn1-rat *she1Δ*, Dyn1-rE/K, and Dyn1-rE/K *she1Δ*), as well as from the spindle neck cross phenotype and dynein motility metrics (Fig 3.8b and c, SHE1, *she1Δ*, Dyn1-rE/K, and Dyn1-rE/K *she1Δ*) that the 3YFP have some inhibitory effect on dynein motility in general, partially masking some of our phenotypes which were significant before (see Figure 3.3 and fig 3.4, SHE1 versus *she1Δ*). When we plotted the fraction of spindle residencies within either the mother or bud compartment, we saw a similar increase the fraction within the mother compartment in *she1Δ* and Dyn1-rE/K *she1Δ* mutants, but not in the Dyn1-rat *she1Δ* mutant (Fig 3.8c), consistent with our hypothesis that She1 is sensitive to the conformational state of the motor. Finally, we again see the decreased fraction of spindles within close proximity of the bud neck in all *she1Δ* mutants (the small region surrounding the bud neck), which was previously attributed to a dynein-independent mechanism and further confirmed by this data demonstrating it is a MTBD-independent process, consistent

with findings that She1 also maintains the spindle close to the bud neck through a dynein-independent mechanism (Fig 3.8c).

### 3.3 DISCUSSION & FUTURE DIRECTIONS

In summary, we found that She1 regulates dynein-mediated spindle positioning through inhibiting dynein hyperactivity (Fig. 3.3, 3.4, 3.5). Specifically, She1 prevents astral microtubule cortical contacts in the mother cell from initiating into a dynein-mediated sliding event and this inhibition requires She1 binding to astral microtubules and the dynein MTBD to a moderate extent (Fig 3.6, 3.7, 3.8, 3.9). The compartmentally specific inhibition is achieved through She1 localizing to mother-associated aMTs via a microtubule-dependent mechanism and not through physically blocking She1 diffusion into the bud cell (Fig. 3.6). By inhibiting dynein hyperactivity in the mother cell She1 maintains the spindle within close proximity to the bud neck, consequently polarizing dynein-mediated spindle movements to promote proper positioning of the spindle into the bud neck (Fig 3.4, 3.5). However, the mechanism behind how dynein hyperactivity leads to the spindle positioning defect we observe in *she1Δ* cells is partially speculative. Our data support a model where She1 inhibition of dynein events in the mother cell allows bud-associated dynein to polarize spindle movements into the bud neck. In this case, the low frequency of spindle translocation success (Fig 3.2a) is likely a consequence of hyperactive dynein in the mother sabotaging spindle positioning attempts by dynein in the bud, which is further supported by the fact that fewer dynein-mediated spindle movements are directed towards the bud (Fig 3.3b). Despite this knowledge, we have still not completely reconciled our in vivo and in vitro data to suggest a complete mechanism.

We were surprised to see that the spindle positioning defect in *she1Δ* cells did not give a pronounced SPOC delay with our method, despite the significant observation of mispositioned spindles in our assay (Fig 3.1a). A likely explanation in these cells is the presence of a functionally redundant spindle positioning pathway, KAR9, which could compensate by rescuing

an otherwise doomed anaphase spindle, but could also be complicated by a lack of sensitivity either in our methods or our analyses. Congruent with the former, 29 of the 33 mispositioned anaphase spindles we observed were eventually forced into the bud neck before cytokinesis (data not shown), suggesting their survival. However, in spite of the low frequency of seeing cells undergoing cytokinesis with the spindle still in the mother cell (occurring in only 4 out of 33 mispositioned spindles), many of these mispositioned spindles that went on to correct their positioning may still have resulted in aneuploid or partially aneuploid cells, but with chromosome abnormalities not severe enough to lose cell viability. We noted that all mispositioned spindles that underwent anaphase with their spindles in the mother cell (4 cells) were from *she1Δ* cells. This, along with our observation that mispositioned spindles in *she1Δ* cells had no delay in timing from anaphase to cytokinesis when compared to positioned cells in *she1Δ* cells (whereas WT cells displayed a 5 minute delay), suggests these cells may be deficient of SPOC signaling and gives us reason to suspect that She1 may play a role in regulation of the SPOC network. It might be no coincidence that She1 localizes prominently to the bud neck throughout mitosis and localizes to mother-associated aMTs (Woodruff et al., 2009; Pigula et al., 2014; and Fig 3.6). Incidentally, SPOC regulation is highly correlated with polarity-associated factors in the cytoplasm, spindle pole bodies, and bud neck. Specifically, for example, Kin4 kinase counterbalances the FEAR-dependent activation of the mitotic exit network (MEN) in the mother compartment by maintaining SPOC activation on both spindle pole bodies, until the event when one SPB passes the bud neck. Another kinase Elm1, associated with the bud neck, activates Kin4 to promote SPOC activation in the mother cell. Upon proper alignment (when one SPB passes into the bud neck), Kin4, among other factors, dissociate from the bud-localized SPB and relocalize to the bud neck as a consequence of Lte1 regulation (a bud-localized factor), in which Lte1 binds to and promotes hyperphosphorylation of Kin4, releasing it from SPBs and thereby inactivating the SPOC (Bertazzi et al., 2011). Interestingly, cells with non-functional

Kin4 or Elm1 kinases are deficient in SPOC signaling (Caydasi et al., 2009; Caydasi et al., 2010; Falk et al., 2011; Pereira et al., 2005).

Our close analysis of how She1 regulates dynein activity in budding yeast has revealed new insights into how a MAP could spatially regulate molecular motors. Specifically, we found that She1 inhibits dynein in the mother compartment, through specific localization on mother-associated astral microtubules during metaphase (Fig 3.6). Though the mechanism driving this preferential binding is unknown, there are many future possibilities to explore and test. With our overexpressed She1-GFP mutant cells we determined that the localization depends on a microtubule-dependent mechanism, and that there is not a physical barrier that prevents She1 diffusion (aka affects She1's microtubule binding capacity, not compartment localization in the cytoplasm). Many MAP functions are regulated by phosphorylation, specifically, MAPs exhibit reduced binding to microtubules when phosphorylated, a mechanism which is not entirely surprising given most recognize the negatively charged CTTs of microtubules to bind. Specifically, the potential She1 homolog MAP4, along with MAP2 and tau, exhibit reduced binding to microtubules and actin (MAP2) upon phosphorylation by p110 microtubule-affinity regulating kinase (MARK) at KxGS motifs. This proposes a means by which to regulate microtubule dynamics and protein function (reviewed in Tassan et al., 2004; Illenberger et al., 1996; Drewes et al., 1995; Drewes 1997; Selden et al., 1983; Vallee et al 1980; Burns et al., 1984). Consistent with this notion, a phosphomimetic mutant of She1 (She1<sub>5D</sub>; Markus et al., 2012) has reduced binding affinity to microtubules. Par1 is essential in establishing the anterior-posterior polarity in *C. elegans* embryo (Kemphues et al., 1988) and MARK2, a mouse family MARK, is critical for neuronal polarity of neurites (Biernat et al., 2002). Interestingly, Kin1 and Kin2 are budding yeast orthologs of MARK/Par1. Kin2 localizes within the bud cell and incidentally the bud neck in *S. cerevisiae* (where She1 also localizes throughout mitosis; Pigula et al., 2014) where it is suspected to regulate septin organization. Kin1 also displays asymmetric localization to sites of polarized growth and the bud neck of *S. pombe* (Cadou et al., 2010; Levin

et al., 1990; Elbert et al., 2005; Yuan et al., 2016; Tassan et al., 2004). Additionally, She1 contains KxGS motif at Serine amino acid position 85, which could potentially be phosphorylated by Kin1 or Kin2 (Fig A3.1a). There are also many mitogen-activated kinases (MAPKs) belonging to signaling cascades that may be activated in compartmentally controlled mechanisms. Specifically, Hog1 is a MAPK activated by rapid phosphorylation through a signaling cascade that starts with activation of the Sho1 signaling cascade in response to osmotic cell stress (Proft et al., 2004; Babazadeh et al., 2014). Sho1 is incidentally asymmetrically localized to the bud cell as well (Reiser et al., 2000). Given that She1 has been implicated in HOG1 pathway function, this presents an interesting mode by which to spatially inhibit She1 binding to microtubules in the bud cell. She1, which has been shown to be maximally phosphorylated during mitosis (data not published), is suspected to be phosphorylated by mitotically regulated kinases Ipl1 and Hog1 *in vitro*, and this phosphorylation is critical for She1's role in spindle disassembly and spindle positioning (see Appendix 4; Woodruff et al., 2010; Pigula et al., 2014; Markus et al., 2012). Additionally, recall that She1 may be involved in SPOC signaling, meaning it may be prevented from localizing to aMTs in the bud compartment in a similar manner to Kin4 through Lte1 pathway regulation. This would inevitably prevent She1 from inhibiting dynein in the bud compartment, supporting our data. She1 may not localize to aMTs in the bud due to regulation by Lte1, or upstream factors, inducing hyperphosphorylation of She1 in the bud to dissociate it from aMTs, possibly relocalizing She1 to the bud neck (akin to Kin4). We could test this hypothesis using a temperature sensitive mutant of *cdc12* that leads to loss of the bud-specific localization of Lte1 (Seshan et al., 2002). If She1 relies on Lte1 or upstream factors for asymmetric localization, then temperature inactivation of a *cdc12* temperature sensitive allele should also lead to a loss in She1 asymmetry. This, among evidence that kinases drive polarity of budding yeast asymmetry by localization (such as Kin1, Kin2, and Kin4), suggests She1 binding to microtubules may be modulated by phosphorylation *in vivo* in a compartmentally dependent

manner. A specific assessment of phospho-mimic and phospho-null mutants of She1 (see Appendix 4), to determine if phosphorylation, or lack of a phosphorylation, leads to reduced binding of She1 on mother-localized aMTs or leads to increased She1 binding on bud-localized aMTs (respectively) *in vivo* may be enlightening.

Alternatively, the preferential localization could be driven by the differences in cytosolic environments of the mother and bud cell. Specifically, pH of the cytosol and organelles is tightly regulated to control the cell health. Subtle changes in pH can lead to potential charge changes on amino acid residues on weakly acidic and basic protein side chains (reviewed in Moreno-Garcia et al., 2009; reviewed in Demarex et al., 2002). In budding yeast, the acidity of the vacuole of mother cells declines over time, owing to the accumulation of Pma1 (plasma membrane associated ATPase proton pump) in the mother cell, which regulates cytosolic pH by pumping protons out of the cell. (Ferreira et al., 2001; Egilmez et al., 1989; Hughes et al., 2012; Henderson et al., 2014). This pH asymmetry is also mildly conserved between mother and bud compartment cytosols (which have a mean pH of ~7.1), in which case the bud cell is ~0.2-0.1 pH units below the mother cell, and increases ~0.5 pH units nearest to the cell cortex (Henderson et al., 2014). In the case of higher acidity in the bud, we propose that She1 may not bind (or have reduced binding) to microtubules due to charge shifts on She1 critical to microtubule binding, likely in the C-terminal half of She1 (Appendix 3). Unfortunately, given that Pma1 is an essential gene, testing this hypothesis is not trivial. An approach to test this hypothesis might include temperature dependent depletion of Pma1 and overexpression of Pma1, both of which been demonstrated to be a viable approach (Henderson et al., 2014). In the case of overexpression of Pma1, we should hit a theoretical threshold to which the bud pH equates the mother pH in a wild-type scenario (when Pma1 is not overexpressed). With a pH that mimics the original mother pH, She1 binding to microtubules should theoretically be rescued in the bud cell and we should therefore see loss of asymmetric localization of She1.

The inhibitory effect of She1 on dynein-dynactin motility metrics, which best represents inherent dynein motor properties during prolonged movement (*i.e.* the sliding event that follows initiation of the event) *in vivo*, did not require the dynein MTBD, and potentially may be independent of She1-MT binding, which presents some interesting questions (Fig 3.3c and d). Our prior *in vitro* data showed that She1 binds the dynein MTBD to inhibit motility (Chapter 2), this had suggested to us that She1 inhibition was most likely to occur during prolonged movement, when dynein walks away from the plus end and along the microtubule lattice where it would encounter She1, but this is clearly not the case from our data, which suggests She1 inhibition of prolonged events is MTBD-independent. Our data then suggests there may be two modes of inhibition by She1 and they both may occur under distinct mechanisms, namely, one requires She1 binding to the dynein MTBD (inhibition of initiation) and one does not (inhibiting motility of prolonged movement), and importantly, one mechanism does not preclude the other (*i.e.* the rat chimera still exhibited enhanced motility metrics *in vivo* despite the MTBD-dependent mechanism being non-functional; Fig. 3.7b and c versus d and Fig 3.8a). In light of this, it becomes necessary to investigate alternative explanations for how She1 could regulate dynein-dynactin motility. It has been shown previously that microtubule stability plays a role in the duration and frequency of dynein-mediated sliding events, specifically, microtubule stabilizing factors result in greater frequency of sliding events and duration of sliding events (Estrem et al., 2017; Hayashi et al., 2005), similar to what is seen in *she1Δ* dynein-dynactin motility metrics (Fig 3.3b and c). Additionally, dynein and dynactin have been shown to alter microtubule dynamics directly, and in antagonistic ways, specifically, dynein promotes depolymerization events while dynactin stabilizes microtubules during a productive slide (Estrem et al., 2017; Hayashi et al., 2005). Though we do not yet know if She1 affects microtubule dynamics. Our *tub1* mutant (*tub1-G437R*) has enhanced dynamicity, which may be a direct consequence of reduced She1 binding (reviewed in Appendix 2). Alternatively, the enhanced dynamics could be a consequence of other reasons such as reduced binding of other

proteins or inherent heterodimer structure. Either way She1 may affect microtubule dynamics, thus indirectly altering the trajectory of a sliding event by changing the stability of the microtubule track. Additionally, it remains within the realm of possibilities that She1 directly affects the dynein-dynactin complex's ability to regulate microtubule dynamics during a sliding event. This is especially interesting given that She1 wild-type cells maintain a 3:1 ratio of dynein:dynactin at plus ends, and *she1Δ* cells drop this ratio to 1:1 dynein:dynactin. Therefore, She1 maintains fewer stabilizing factors at the plus ends (dynactin) and more destabilizing factors (dynein; Markus et al., 2011). Therefore, She1 would indirectly reduce sliding event frequency and duration (when compared to *she1Δ*), through maintaining a stoichiometry that favors a higher dynein (MT destabilizer) stoichiometry at plus ends, consistent with our observations. Future studies to investigate if She1 affects microtubule dynamics, either directly or indirectly, will be highly enlightening in this regard, and given that we have established yeast tubulin purification in our lab, *in vitro* assays that accurately assess dynein pathway component effects on microtubule dynamics, is possible (see Appendix 5).

As mentioned previously, the mechanism behind She1 regulating the ratio of dynein and dynactin at plus ends is largely unresolved, and currently it is unknown whether it requires the dynein MTBD, leaving room for investigation of several different avenues to reveal potential mechanisms. Bim1 plays a role at the spindle midzone in microtubule stability, like She1, during mitosis, and incidentally, cells lacking *she1* exhibit a reduction in Bim1 localization at the spindle midzone (Zhu et al., 2017). She1 has been shown to interact with Bim1 in yeast-2-hybrid assays (Wong et al., 2007), and She1 does appear to contain a C-terminal SxIP binding motif that may bind Bim1 starting at residue 229 (Fig. A3.1c). Additionally, She1 interacts with the C-terminal tails of microtubules with its C-terminal region, demonstrating that She1 could theoretically interact with both Bim1 and microtubules simultaneously as seen with the dynein MTBD and the microtubule, and also suggests She1 could not interact with the dynein MTBD at the same time as it would interact with Bim1 (see Chapter 2 and Appendix 3). Previous work in

mammalian cells show that the Cap-Gly domain of p150 (mammalian Nip100) interacts with both the C-terminal residues (EET) and the SxIP binding region of EB1 to track plus ends, which can engage in competition with SxIP and LxxPTPh binding motifs on other EB1 binding proteins (Badin-Larçon et al., 2004; Stangier et al., 2018; reviewed in Kumar et al., 2012; Duellberg et al., 2014; Roberts et al., 2014). In contrast, in yeast, the Bik1 Cap-Gly domain has been shown to interact specifically with the EEF on Bim1 C-terminal tails, leaving the Bim1 SxIP and LxxPTPh binding regions available for ternary complex assembly, as has been shown with Kar9 and Stu2 (Stangier et al., 2018). Bim1 has been shown to have a diverse set of binding partners to achieve multiple different functions during spindle alignment and yeast mating, including interaction with microtubules and actin that could be competed (or exist harmoniously) with other binding partners to achieve these functions (Honnappa et al., 2006; Manatschal et al., 2016). Perhaps the potential She1 interaction with Bim1 could be involved in She1 effects on dynein activity in cells. Yet, budding yeast dynactin has been shown to need dynein, and not Bim1 to a large extent, to perform its function in spindle positioning. In turn, dynein needs Bik1 and Pac1, but Bik1 does not necessarily need Bim1 to localize to plus ends, to achieve its spindle positioning function. Though, loss of Bim1 still leads to mild loss of dynein and Bik1 concentration at plus ends, suggesting it does have a role in plus end targeting (Markus et al., 2011; Carvalho et al., 2004; Sheeman et al., 2003; Stangier et al., 2018). Still, the binding interaction of all of these plus end complexes is largely unknown, nor do we understand if they occur in large ternary assemblies or in competition with one another. Our data do not currently support She1 regulating dynactin through its microtubule binding domain (CAP-Gly), either in the inhibition of initiation of dynein-mediated sliding events or in the prolonged movement, suggesting it is not directly competing with the dynactin Cap-Gly domain for interaction with microtubule C-terminal tails or Bim1 (Fig 3.3, 3.4). But since She1 plays a role in dynactin localization to plus ends, and dynactin does not require its Cap-Gly domain for this behavior, perhaps there is another explanation. We would propose determining if *bim1*Δ cells display

changes dynactin plus end targeting and dynein activity metrics that is not further aggravated by she1 $\Delta$ . Alternatively, Bik1, which is required for dynein localization to plus ends, also has a Cap-Gly domain which interacts with the C-terminal EEF of  $\alpha$ -tubulin and Bim1. Bim1 presumably can bind a protein with a Cap-Gly domain and another protein with a SxIP motif simultaneously, suggesting She1 may bind to Bim1 at the same time as Bim1 is interacting with Bik1. Perhaps She1 may play a role in restricting interaction of dynactin and dynein through an interaction with Bim1. A more detailed mechanism for how this might influence dynein activity, is rather difficult to envision. We could begin to address this question by determining if She1 binds Bim1, or if She1 affects Bim1 and Bik1 binding with each other or microtubules *in vitro*, or whether addition of dynein or dynactin would exhibit differential targeting to plus ends in the presence of She1 and +TIP targeting components. Though we do not visually see comet-like decoration by She1 when She1 is overexpressed, perhaps a She1 interaction with Bim1 could be a means by which She1 could localize and therefore directly modulate dynein and dynactin interaction.

Our currently proposed model is in direct contrast with our previous model, where She1 enhances dynein force generation to move the large nucleus into the narrow bud neck. Though we found that the bud neck does behave as a barrier that must be overcome, She1 does not assist in this regard (Fig 3.2c), leaving questions as to the mechanism behind how She1 enhancing dynein association with microtubules would achieve an inhibitory effect on dynein activity *in vivo*. It is notable that, as far as we know, only inhibition of the initiation of a dynein-mediated sliding events require the dynein MTBD, and moreover, it appears to be specific to the conformational state of the dynein MTBD (as shown by the high-affinity rat chimera, Fig 3.7, 3.8 also see Chapter 2). The MTBD-dependent mechanism may occur directly at the plus ends, before or when a sliding event begins, possibly implicating She1 in dynein-dynactin plus-end targeting or offloading as previously alluded to. She1 directly affects plus-end localized dynein and dynactin ratios (Markus et al., 2011). It is important to note that She1 also affects the offloading of the dynein-dynactin complexes as well, specifically, She1 perhaps drives offloading

of dynein: (1) dynein plus end targeting was reduced in *she1Δ*, yet cortical targeting of dynein remained unchanged (plus end localized dynein went from 16 to 9 molecules, but cortical targets still maintained 6 molecules of dynein, indicating *she1Δ* enhanced dynein offloading) but (2) the offloading ratio of dynactin did not change very much (plus end localized dynactin increased from 14 to 21 molecules yet cortical foci increased to a similar degree, 8 and 12 molecules, respectively; Markus et al., 2011). Though this enhanced offloading could be a consequence of increased dynactin at plus ends, we propose an alternative interpretation of these data which may be supported by some preliminary evidence. Interestingly, wild-type yeast dynein, which can undergo stochastic switching between autoinhibited and uninhibited conformations, exhibited no enhancement in microtubule binding when compared to an uninhibited mutant *in vitro*, suggesting autoinhibition does not restrict wild-type yeast dynein from associating with microtubules in budding yeast (Marzo et al., 2020). This suggests that yeast dynein may require alternative modes of inhibition *in vivo*, to prevent excess dynein-mediated initiation (aka offloading) of dynein complexes in the mother compartment, without restricting bud-localized dynein. Interestingly, dynactin interaction and dynein offloading can also be regulated by the open (uninhibited) and closed (autoinhibited; phi) state of the motor, specifically, a phi mutant (Dyn1-D2868K), that remains in the open state, was offloaded to the cortex more frequently, and incidentally recruited more dynactin to plus ends (Marzo et al., 2020). Perhaps She1 might regulate the autoinhibited state to prevent interaction with dynactin. This would not be an entirely novel concept given that it was previously shown MAP7 plays a role in relieving kinesin-1 autoinhibition in neurons through a microtubule-independent mechanism (Barlan et al., 2013). Consistent with this notion, preliminary evidence suggests dynactin cannot interact with dynein in the presence of She1 on microtubules *in vitro*. Though we saw landing of dynein molecules on microtubules, we saw now colocalization with dynactin (Fig 3.10a, left). This mildly supports the notion that She1 may interact with the open conformation of dynein, and induce the closed conformation. She1 may induce an autoinhibited

conformation by binding the dynein MTBD, and subsequently block dynein offloading to the cell cortex through abrogating interactions with dynactin, and likely Pac1. It would be beneficial to determine if the phenotype described in chapter 1 where dynein relocates along aMTs upon overexpression of She1 also brings Pac1 or dynactin with it, to determine if they can remain bound when dynein is bound to She1 *in vivo*. Inconsistent with this thought is that She1 also inhibits dynactin interaction of the phi mutant *in vitro* (Fig 3.10a), however, we are not certain if She1 does not regulate the autoinhibited conformation or if the phi mutant is not impervious to forming the autoinhibited conformation when bound to She1. Interestingly, the phi mutant shares a high cortical proximity fraction with *she1Δ* preliminarily, but doesn't exhibit other phenotypes (Fig 3.10 b-d). However, we do not have a control where *she1* is deleted in this strain, which will be pertinent to add to these data. Historically, in our data, increased cortical proximity often coincides with prolonged motility metrics seen in *she1Δ*, indicating She1 may be regulating the autoinhibited state during a productive slide. Alternatively, She1 inhibition may occur prior to dynein targeting at plus ends as a means to control the ratio of dynein:dynactin there. These hypotheses make more sense than models where She1 might inhibit dynein at plus ends, given that She1 is not largely seen at plus ends, and even overexpressed signal appears homogenous along the length of the microtubule, and not comet-like (see Fig 3.6). The enhanced offloading of dynein in *she1Δ* may be a consequence of dynein exhibiting the open conformation more frequently and readily interacting with Pac1, where it will be more readily targeted to plus ends to interact with dynactin. Contrarily, *she1Δ*, exhibits a slight decrease in dynein plus end targeting (Markus et al., 2011) or no change (Woodruff et al., 2009). It would be interesting to test if dynein accumulates at the SPBs due to hyperactive dynein, leading to some plus end depletion seen in *she1Δ* cells. It would be informative to investigate if She1 abrogates Pac1 binding and to confirm our preliminary data that She1 interrupts dynactin binding to dynein *in vitro* (Fig 3.10a, left). Additional experiments should also determine if She1 can inhibit the dynactin-dynein-Num1 complex *in vivo* and *in vitro*, such as if the Num1 adaptor would make a

difference in our preliminary *in vitro* data where dynactin cannot interact with dynein on a She1-decorated microtubule. Perhaps She1 cannot inhibit the full complex, and only plays a role in regulating dynein before it is offloaded to the cell cortex.

Though our rat chimeras have given us valuable insight into how She1 may regulate dynein activity through binding the dynein MTBD *in vivo*, the data also brings up several questions that will be informative to answer in future experiments. Our prior work demonstrated that She1 had reduced affinity for the motor with the rat MTBD when compared to a wild-type yeast MTBD. These two MTBDs only share ~41% sequence identity and 70% similarity with each other (Fig 2.6), making it likely that residue differences are the cause of this reduced affinity. Yet, we noticed that this motor also has reduced affinity for microtubules (Fig A1.4), and we showed that a motor mimicking the ADP+Pi state (which is a low-MT affinity conformation) also had lower affinity for She1 (Fig 2.4d), implying that She1 may recognize a region on the motor that undergoes large conformational changes during dynein's mechanochemical cycle. It could imply that She1 forms a more stable complex when interacting with a dynein that is bound to the microtubule in a high-MT affinity state. It is unclear at this point if She1 requires dynein to be bound to microtubules to interact with the MTBD. Our prior data showing that She1 moved with dynein through iterations of its mechanochemical cycle may have been an artefact of HALO-TMR ligand dyes from the She1 purification binding to dynein (Fig 2.4f). We have not observed them binding in solution in the absence of microtubules except by yeast-2-hybrid assays, which could mean that She1 requires microtubules to adopt the appropriate conformation to bind the MTBD (Fig A3.1, A3.2). In any case, She1 binding could be compromised due to structural differences between the two motors as a consequence of differences in the affinity state of the motor. It was also unclear that the impaired binding of She1 to the rat chimera was due to both conformational incompatibility and residue differences, which may not be mutually exclusive. We non-the less hoped to learn something from using a high affinity rat mutant in cells. This mutant has two mutations, E3289K and E3378K, the former

is located in coiled-coil 1, which makes the greatest conformation change, along with helix 1, during the transition from low to high affinity. E3378K is on helix 6, located on the microtubule binding domain of dynein, which makes several contacts with the  $\alpha$ -tubulin within the interprotofilament valley. These mutations were shown to increase dynein microtubule affinity and dwelling time on the microtubule (Redwine et al., 2012). In our assay, we saw that the low affinity chimera was not sensitive to She1 loss. But vice versa, we saw a rescue in She1 phenotypes with the high affinity chimera. This might indicate that She1 requires the MTBD to inhibit dynein activity and that improving the microtubule affinity of dynein can rescue, at least to some degree, a mutant with compromised She1 binding. And yet, we saw a complete rescue of She1 phenotypes (except in the neck cross frequency, which may be due to impaired force generation of the rat MTBDs), not a partial rescue. Though it is hard to conceptualize what this might mean, it would be pertinent, before making judgments, to follow-up this *in vivo* data with some critical *in vitro* characterization. Namely, future experiments should determine the degree of binding of She1 to the high affinity rat chimera using *in vitro* recruitment assays and see if it compares to the wild-type yeast motor. Additionally, as a second control for our *in vivo* data, testing a low affinity yeast MTBD mutant, in both recruitment assays and *in vivo*, would be informative. It would be curious if a low affinity yeast MTBD displayed the same insensitivity to She1 effects *in vivo*. Indeed, if this were true, it would support that She1 must interact with a specific conformational state to maximally or to properly inhibit dynein in an *in vivo* context. On a final note, the low affinity rat MTBD didn't phenocopy she1 $\Delta$  in the dynein activity and productive sliding events metrics, it phenocopied wild-type, suggesting it may not even require She1 to inhibit these metrics. Perhaps a low-MT affinity yeast MTBD mutant would also negate the need for She1 in cells and therefore rescue She1 null phenotypes *in vivo*. If not, it would support that the residues within helix 6 and coiled-coil 1 may be critical residues involved in She1 binding and inhibition of the dynein MTBD.

We would like to mention one other thought that might be pertinent to the project moving forward. As previously mentioned, She1 can regulate the fate of a sliding event independent of the MTBD. This may be reminiscent of how Pac1 affects dynein and dynactin motility, incidentally, it was shown that Pac1 promotes motility of dynein and dynactin complexes *in vitro* even after it has already dissociated from the motor. This is presumably through improving dynein interaction with dynactin during complex formation, and through increasing the number of dyneins that bind to each dynactin (Elshenawy et al., 2020; Htet et al., 2020). Perhaps She1 plays a role in negatively regulating the efficiency of dynein and dynactin complex assembly or may regulate the binding or assembly of more than one dynein per dynactin (though there is currently no evidence of this phenomena happening in yeast). Previously, a tail mutation within the heavy chain Dyn1, K540C, previously reported to have slightly increased dynein activity (Marzo et al., 2019), also exhibits an increased productive sliding ratio reminiscent of she1 $\Delta$  (Fig 3.10 b-d). The tail domain likely makes many interactions with dynactin and between the tails of neighboring dyneins on the same dynactin (Schlager et al., 2014; Urnavicius et al., 2015; Urnavicius et al., 2018), and this residue, K540, is located within the N-terminal region of Dyn1 closest to suspected interaction points with the neighboring dynein tail intermediate chain, suggesting mutation of this residue may lead disruption of the interaction or alignment of the dynein motor heads on dynactin (Urnavicius et al., 2018; Marzo et al., 2019). It was shown *in vitro* that dynactin complexed with more dynein dimers exhibits increased motility, which would be consistent with our She1 data (Urnavicius et al., 2018). The mechanism behind how She1 inhibits dynein is not clear, it may be possible that She1 regulates interaction through disrupting the interactions within the tail directly. Prior work found that the dynein intermediate chain makes contacts with the dynactin p150 (NIP100 in yeast) (Siglin et al., 2013). This is one interesting mode by which She1 may disrupt dynein and dynactin interaction within the tail domain (or perhaps loading of multiple dynein's on dynactin). Interestingly, prior work showed that a phosphomimetic mutant of She1 (She1<sub>5D</sub>) had reduced affinity for microtubules yet

increased ability to inhibit dynein motility and activity *in vitro* and *in vivo* (Markus et al, 2012). We showed that She1 likely interacts with the dynein MTBD through the N-terminus of She1 and microtubules through the C-terminus (Appendix 3). Perhaps upon phosphorylation, She1 can release microtubules and project toward the tail domain of dynein, to inhibit dynactin interaction. She1 has a long contour length, ~121 nm, indicating it may have long disordered projections away from the microtubule reminiscent of other MAPs. In order to reach the height of the tail domain, She1 must only reach about 50 nm away from the microtubule, which seems reasonable given that even if the C-terminal half of She1 must interact with the dynein MTBD, following phosphorylation and release of microtubules there is still 60 nm of length that can reach the tail domain and compete for interactions between dynein and dynactin, or dynein and dynein. Future experiments should determine if the tail mutant K450C displays She1 phenotypes our *in vivo* motility metrics and dynein activity (like previously published), and at the same time, must include a control with she1 $\Delta$  with this mutation, to determine if it is insensitive to She1 loss. That will inform our data if She1 phenotypes may be due to disrupted interaction within the dynein tail. Spindle oscillation assays with a dynactin NIP100 that has been truncated at the region that interacts with the dynein light chain (not just a CAP-Gly deletion, that we have shown) will also inform if She1 is regulating this interaction *in vivo*.

Though there are currently no known functional homologs of She1 in higher eukaryotes, our analysis will be beneficial to identify possible homologs in the future. Our data do not currently support MAP9 or MAP4 as being functional homologs of She1, which are two MAPs in higher eukaryotes that exhibit inhibitory effects on dynein. Specifically, both MAP9 and MAP4 presumably regulate dynein through the dynactin Cap-Gly domain. All phenotypic metrics presented here demonstrated that the Cap-Gly mutants were still sensitive to loss of She1, indicating that these phenotypes are not through Cap-Gly domain regulation. This is consistent with prior *in vitro* data demonstrating that She1 does not interact with any dynactin subunits or

prevent dynactin subunit assembly (Bergman et al., 2012). Moreover, residue sequence alignments did not reveal any similarities between MAP4 and She1 (using BLASTP algorithms). MAP4 has a well characterized N-terminal tau-like microtubule binding domain, whereas She1 has no proline-rich regions, assembly-promoting (AP) sequence, or extended basic regions near the N-terminus which is suspected to bind microtubules (Katsuki et al., 1999; also see Fig A4.1). There are still however very striking, uncanny similarities worth highlighting between She1 and MAP4. Namely, MAP4 indiscriminately binds along the length of the microtubule lattice *in vitro* and associates with both spindle and astral microtubules during mitosis in HeLa cells, and MAP4 potently reduces dynein-dynactin velocity in *in vitro* gliding assays (Samora et al., 2011). Additionally, MAP4 siRNA knockdowns result in abnormal spindle morphologies, specifically, spindles are longer and appear bent, a phenotype previously reported for *she1Δ* spindles (Woodruff et al., 2009; Samora et al., 2011; Zhu et al., 2017). Fascinatingly, MAP4 depletion also resulted in excessive and frequent sliding on the cell cortex due to dynein hyperactivity, suggesting MAP4 also inhibits dynein-dynactin activity at the cell cortex like She1 (Samora et al., 2011). It is also worth noting that MAP4 also interacts with septins, whose filamentous network is involved in many cellular functions in mammalian cells (Kremer et al., 2005; Ghossoub et al., 2013). This is potentially relevant because She1 also localizes to the bud neck, where many septins localize in budding yeast, to drive cell polarity and cell cycle progression (Woodruff et al., 2009; reviewed in Glomb et al., 2016). Discussed above, we proposed that there may be two modes of regulation of dynein by She1. Specifically, She1 binding the dynein MTBD was required to inhibit the initiation of dynein-mediated events, but the effect on dynein-dynactin motility parameters (*i.e.* sliding velocity and run length of sliding events) during prolonged movement did not. It's possible that the regulatory mechanisms may be shared or be similar to MAP4 regulation of dynein in higher eukaryotes, and possibly reveal MAP4 as a functional homolog.

## **3.4 METHODS**

### ***3.4.1 Media and strain construction***

Strains are derived from YEF473A (Bi and Pringle, 1996). We transformed yeast strains using the lithium acetate method (Knop et al., 1999). Strains carrying mutations were constructed by PCR product-mediated transformation (Longtine et al., 1998) or by mating followed by tetrad dissection. Proper tagging and mutagenesis were confirmed by PCR (all chimeras were confirmed by sequencing). Fluorescent tubulin-expressing yeast strains were generated using plasmids and strategies described previously (Markus et al., 2015; Song and Lee, 2001). Yeast synthetic defined (SD) media was obtained from Sunrise Science Products (San Diego, CA).

### ***3.4.2 Live cell imaging experiments***

Spindle positioning was done with the CellAsic™ ONIX2 microfluidic system using microfluidic cassettes designed for yeast (MilliporeSigma). Cells were grown overnight in SD-complete media supplemented with 2% glucose at 30°C. Cells were diluted 1:50 upon addition into microfluidic cassette which was primed with SD prior to addition of cells (see manufacturer's instructions). Pressure was maintained at a constant 0.7 psi to refresh media over course of imaging which took place at 30°C. Multiple XY planes (10 XY planes for replicate 1, 5 XY planes for replicate 2) were imaged for 10 hours at 90 second intervals with 7-Z-stacks (0.5µm spacing) of mTurquoise2-tub1 labeled microtubules, Spc110-Venus labeled spindle pole bodies, and NLS-3mCherry labeled nuclei. Bud emergence was identified by differential interference contrast. Spindle pole body duplication was determined by the first frame where two spindle pole bodies were visible. Anaphase onset was defined as the first frame where the spindle begins to elongate. Cytokinesis was defined as obvious independent movement of the spindle pole bodies (with respect to each other, indicating complete spindle disassembly) and congruent visible separation by differential interference contrast of the mother and bud.

For spindle oscillation and nuclear translocation assays, cells were arrested with hydroxyurea (HU) for 2.5 hours in SD-complete supplemented with 2% glucose and mounted on agarose pads containing HU for confocal fluorescence microscopy. Full z-stacks (19 planes with 0.2  $\mu\text{m}$  spacing) of GFP-labeled microtubules (GFP-Tub1) and NLS-3mCherry labeled nuclei (for nuclear translocation assays only) were acquired every 10 seconds for 15 minutes on a stage pre-warmed to 28°C. Images were collected on a Nikon Ti-E microscope equipped with a 1.49 NA 100X TIRF objective, a Ti-S-E motorized stage, piezo Z-control (Physik Instrumente), an iXon DU888 cooled EM-CCD camera (Andor), a stage-top incubation system (Okolab), and a spinning disc confocal scanner unit (CSUX1; Yokogawa) with an emission filter wheel (ET525/50M for GFP, ET632/60M for 3mCherry; Chroma). Lasers (488 nm, 515 nm, 594 nm) housed in a LU-NV laser unit equipped with AOTF control (Nikon) were used to excite GFP and 3mCherry, respectively. The microscope was controlled with NIS Elements software (Nikon).

### ***3.4.3 Data processing & statistical analysis***

We tracked spindles over the course of the movie using a MATLAB algorithm which tracks a threshold of fluorescence intensity designated by the user. Code was edited to track only in the XY direction, therefore all movies were processed into maximum intensity projections prior to running the MATLAB scripts using Grouped Z Project in ImageJ. Dynein-mediated spindle movements were manually curated from spindle track output data to obtain various metrics. To measure cortical proximity, a MATLAB code was generated where the user manually defines the cell cortex of the mother and bud cell. Bud neck proximity data was also obtained from a MATLAB script that uses spindle tracking data, which defines the outer-left and right edge of the cell and normalizes spindle residencies based on the position of the bud neck (user defined).

Statistical tests were performed as described in the figure legends. Unpaired Welch's t tests and Mann-Whitney tests were performed using Graphpad Prism. Z scores, which are a

quantitative measure of difference between two proportions, were calculated using the following formula:

$$Z = \frac{(\hat{p}_1 - \hat{p}_2)}{\hat{p}(1 - \hat{p}) \left( \frac{1}{n_1} + \frac{1}{n_2} \right)}$$

where:

$$\hat{p} = \frac{y_1 + y_2}{n_1 + n_2}$$

Z scores were converted to two-tailed P values using an online calculator.

### **3.5 FIGURES**

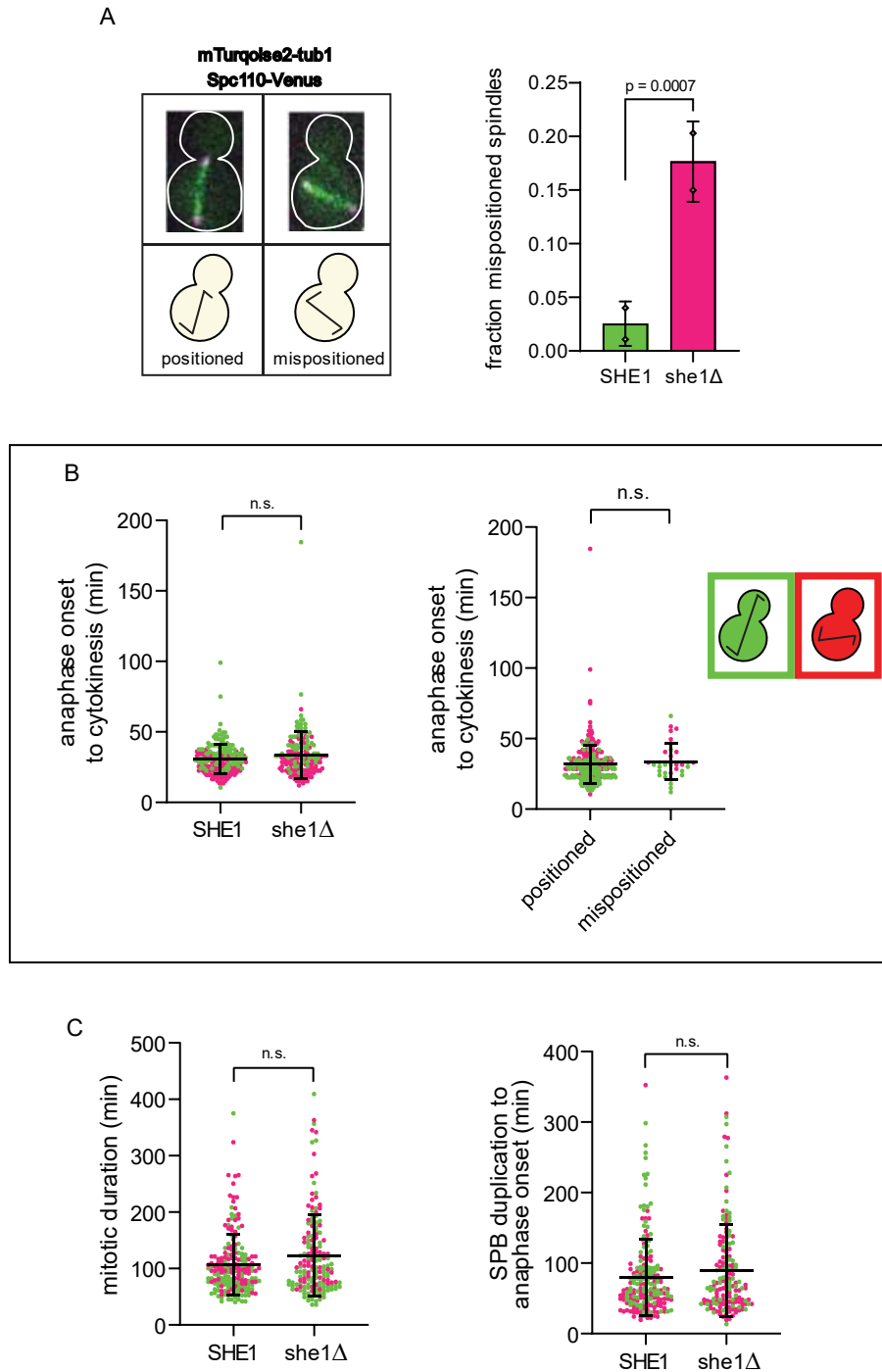
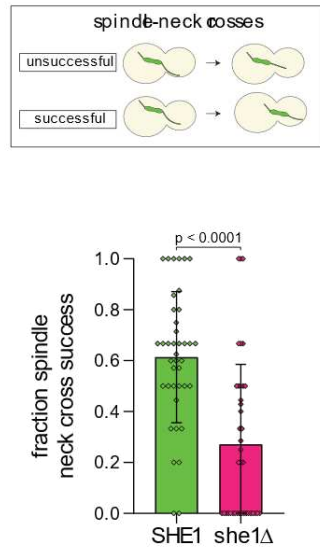


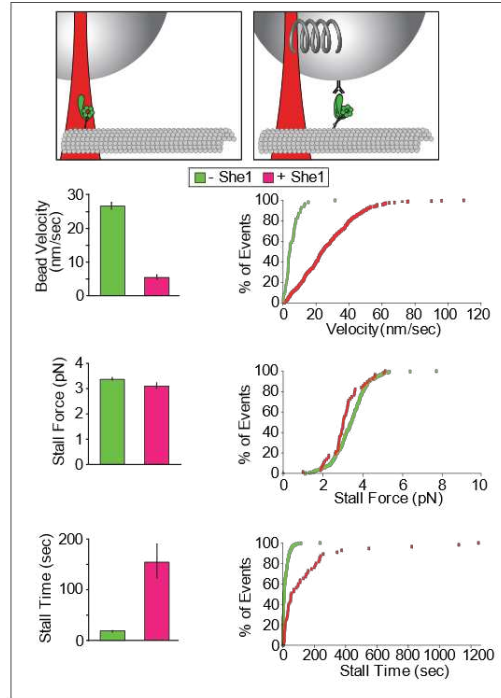
**Figure 3.1. She1 regulates spindle positioning and cell cycle progression in *saccharomyces cerevisiae*.** (a) Spindle positioning was done using live cell confocal imaging with the CellAsic™ system (see Methods). Example confocal images and cartoons (left; top and bottom) representing positioned and mispositioned spindles at anaphase onset (top; mTurquoise2-tub1 in green and Spc110-Venus in magenta, DIC outline of cell in white). Note the alignment perpendicular to the mother-bud axis in mispositioned spindles. The bar graph (right) shows the mean fraction of mispositioned spindles in SHE1 wild-type (green) and she1Δ

(magenta) strains. Each diamond represents the mean fraction of mispositioned spindles ( $n = 2$  replicates,  $n_1 = 100$  cells,  $n_2 \geq 62$  cells). Error bars represent standard deviation. P-value was calculated from Z-scores, see methods). (b) Timing of anaphase onset to cytokinesis for SHE1 and *she1* $\Delta$  (min; left) and anaphase onset to cytokinesis of mispositioned and positioned spindles (min; right) is defined as the frame when the spindle first began to elongate to the instant the bud neck closed (by DIC; see Methods). Note that mispositioned spindles have a delay between anaphase onset to cytokinesis by ~4 minutes, consistent with spindle mispositioning resulting in mitotic exit delay. (c) Mitotic duration defined here as spindle-pole body duplication to cytokinesis, for SHE1 and *she1* $\Delta$ . (a-c) Imaging was done by live cell confocal microscope using the CellAsic™ system. Cells were imaged over 10 hours at 30 degrees Celsius under constant flow with SD-complete media containing 2% glucose (see Methods). (b, c) Each diamond represents a single cell and each replicate is colored separately,  $n_1 =$  magenta,  $n_2 =$  green ( $n = 2$  replicates each containing  $\geq 62$  cells). Bold lines represent the mean and error bars are the standard deviation. P-values from Mann-Whitney test (b, c) since data distributions that did not pass the D'Agostino and Pearson normality test (see Methods).

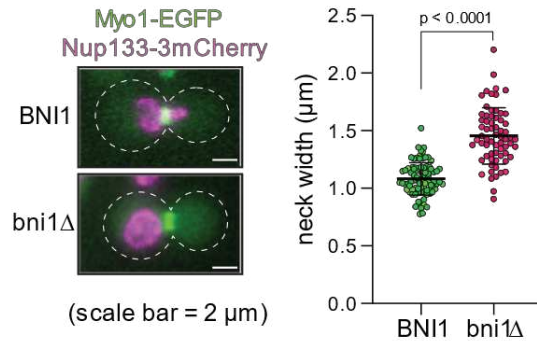
A



B



C



D

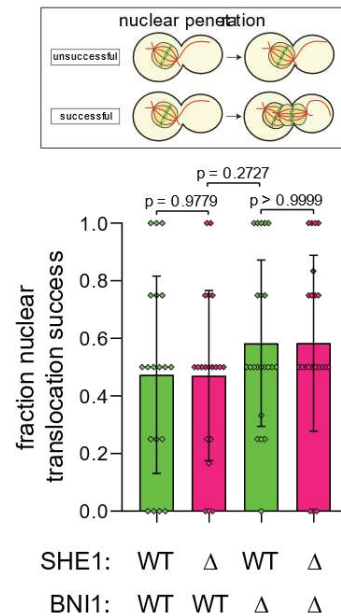


**Figure 3.2. She1 increases dynein stalling time *in vitro* but does not increase nuclear translocation success *in vivo*.** (a) Bar graph showing the fraction of dynein-mediated spindle movements that successfully move the spindle halfway or more into the bud neck as a function of the dynein-mediated movements that unsuccessfully move the spindle into the bud neck; by moving less than halfway into the bud neck (see cartoon). To score spindle neck cross success, cells were arrested with HU to observe multiple dynein-mediated spindle movements per cell

and imaged for 15 minutes using confocal microscopy (see Methods). Each diamond represents the fraction of successful spindle neck crosses per cell ( $n = 2$  replicates,  $n_1, n_2 = 20$  cells each.  $n_1, n_2 \geq 73$  observed spindle neck cross attempts each. P-values were calculated from Welch's t test). (b) Schematic of optical trapping experimental setup. GST-dynein<sub>331</sub> is attached using GST-antibody and walks along coverslip-immobilized microtubules with (magenta) or without (green) 20nM She1 (see Methods). Column (left) and frequency distribution plots (right) show the effect of She1 on dynein velocity (top), stall force (middle), and stall time (bottom), when anchored to a cargo with resistive force – reminiscent of dynein anchored to the cell cortex during spindle positioning in budding yeast. Note that stall force is defined as the maximal force before letting go of the microtubule and stall time is time dynein remained bound under stall force. She1 increases stalling time but not stalling force. (c) Representative wide-field images of HU-arrested cells with a Nup133-3mCherry labeled nucleus (magenta) and Myo1-EFGP labeled bud neck (green). Myo1-EGFP signal was used to measure the width of the bud neck in a BNI1 and *bni1Δ* strains. The scatter plot shows that the bud neck is  $\sim 0.4 \mu\text{m}$  wider in *bni1Δ*. If She1 assists dynein in moving the nucleus into the bud neck, widening the bud neck should relieve *she1Δ* phenotypes ( $n = 2$  replicates,  $n_1 \geq 13$  cells  $n_2 = 54$  cells. P-value from Welch's t test). (d) The bar graph shows the fraction of nuclear translocation success into the bud neck as a function of unsuccessful nuclear translocation. Successful translocation is defined as the nucleus moving halfway or more into the bud neck, while unsuccessful translocation is when the nucleus moves less than halfway into the bud neck (see cartoon, top). Note that widening the bud neck has a slight increase in nuclear penetration success, though not statistically significant ( $p = 0.2727$ ). Columns represent the mean and each diamond represents the nuclear translocation success of one cell ( $n = 2$  replicates,  $n_1 \geq 14$  cells,  $n_2 = 20$ ,  $n_1, n_2$  containing  $\geq 22$  nuclear translocation attempts. Error bars indicate standard deviation. P-values were calculated from z-scores.

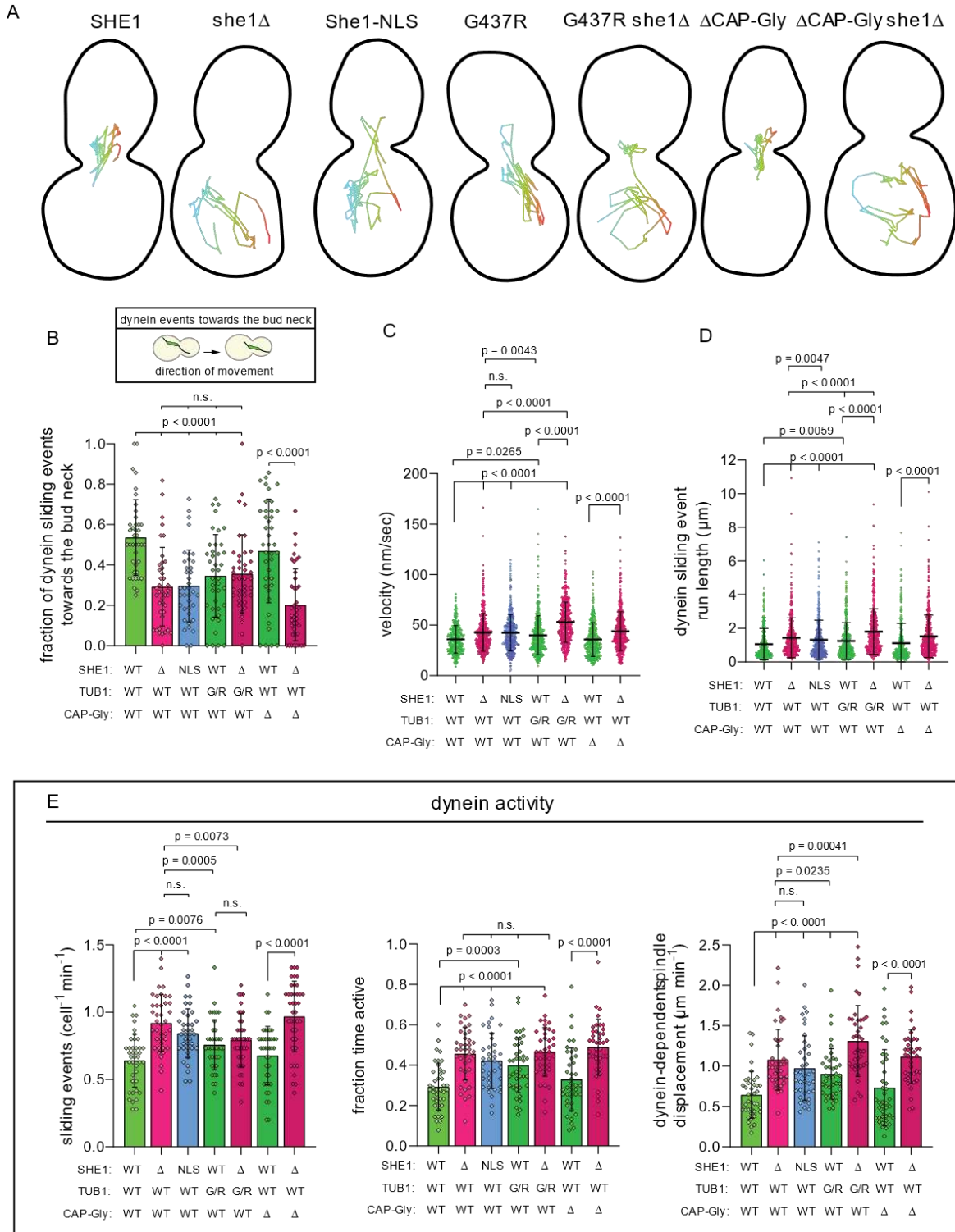


**Figure 3.3. She1 inhibits dynein activity through She1-microtubule binding but not through inhibiting the dynactin MT-binding domain *in vivo*.** (a) Example spindle tracks for wild-type She1 (data in following graphs b-e shown in green) and mutant strain as indicated (She1-NLS; cyan, she1Δ; magenta). Cells are arrested with HU for 2.5 hours. Cells were imaged using confocal fluorescence microscopy on HU containing agarose pads using GFP-

Tub1 to observe spindle movements. Image processing was done using ImageJ and MATLAB scripts (see Methods). (b) Schematic showing an example of a dynein sliding event towards the bud neck. Note that the aMT is captured by dynein in the compartment opposite the spindle (top). Bar graph shows the mean fraction of dynein sliding events that move the spindle towards the bud neck in control and mutant strains. Each diamond represents the fraction for one cell. (c, d) Scatter plots of velocity (c) and run length (d) for dynein sliding events. Each dot represents the mean velocity or the total run length of one dynein sliding event. (e) Three parameters defining dynein activity; dynein sliding events, fraction of time active, and dynein-dependent spindle displacement per minute indicate a greater amount of dynein activity in *she1Δ* strains. Bar graphs represent the mean and each diamond represents one cell (b, c, d, e)  $n = 2$  replicates,  $n_1, n_2 = 20$  cells per replicate. There were  $\geq 160$  dynein sliding events per replicate. Error bars show standard deviations. P-values from Welch's t test for data with normal distributions (b, e; sliding events and fraction time active) or Mann-Whitney test (c, d, e; dynein-dependent spindle displacement) for data distributions that did not pass the D'Agostino and Pearson normality test (see Methods).

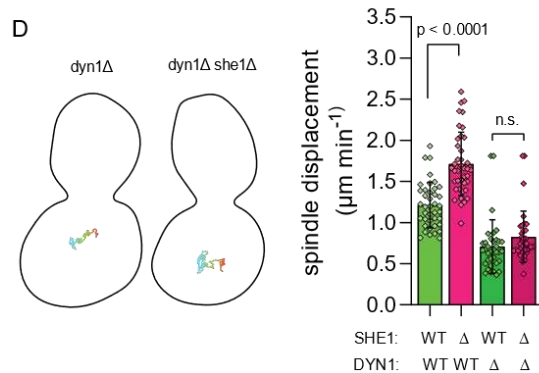
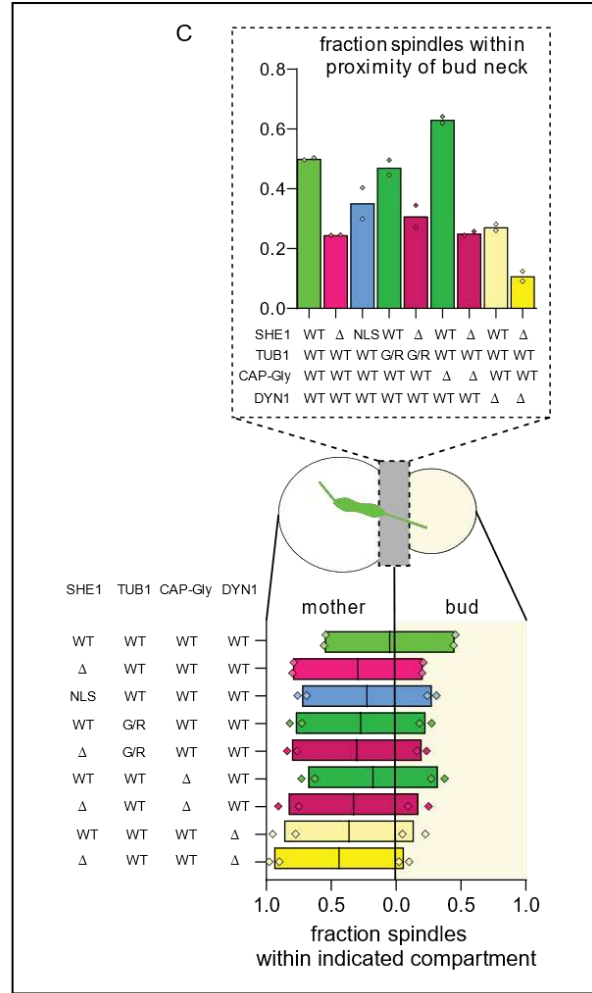
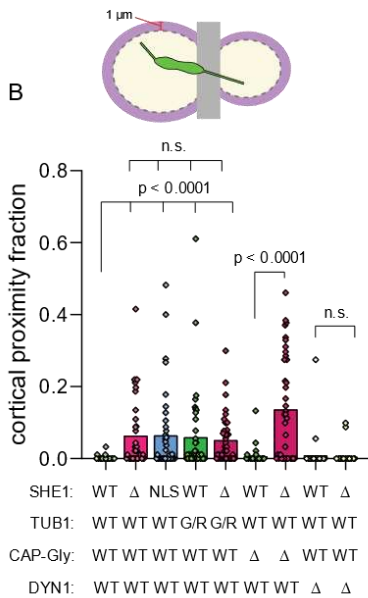
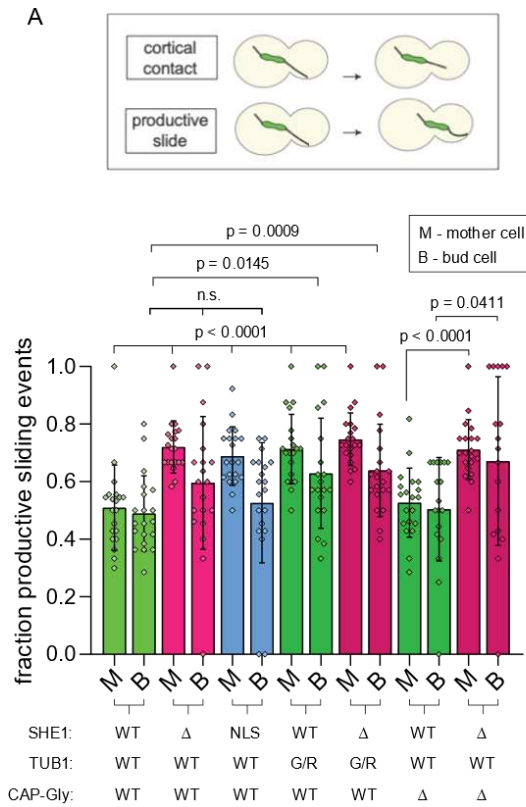


**Figure 3.4. She1 maintains bud neck proximity and prevents dynein hyperactivity through inhibiting initiation of dynein sliding events in the mother cell.** Wild-type and mutant strains used in figure 3.3 were used in addition to *dyn1* $\Delta$  strains to assess if the following phenotypes were associated with dynein hyperactivity. Confocal fluorescence images and

spindle tracking data from figure 3.3 was also used for this analysis (see Methods). (a) Example cartoon of cortical contacts that do (bottom) and do not (top) convert into a productive sliding event with quantitation below. The bar graph is divided into productive sliding events in the mother compartment (M) and bud compartment (B) as indicated (see Methods). This quantitation was done manually using both XY and XZ maximum projections for accurate observation of cortical contacts ( $n = 2$  replicates, 10 cells per replicate, see Methods). Note that the productive sliding events increase significantly in the mother compartment and to a much smaller degree in the bud compartment. P-values were calculated from Z-scores. (b) Bar graph shows the fraction of spindle tracks found within close proximity of the cortex (defined as being within  $1 \mu\text{m}$  of the cell cortex, excluding the bud neck; see cartoon above graph). (c) Spindle tracking data was used in determining the compartment location of spindle tracks and the distance of spindle tracks from the bud neck (see Methods). The bar graph (bottom) plots the fraction of spindle tracks either in the mother or bud compartment. The line at the origin (0.0) designates the bud neck and the line within the bars indicate the mean distance from the bud neck of all spindle tracks. The mother cell is on the left (white) and bud cell is on the right (tan; see cartoon, middle). Diamonds represent each replicate. Spindle tracking data was then binned based to their distance from the bud neck (see Methods, and Figure 3.5). The bar graph (top) shows the fraction of spindle tracks found within close proximity of the bud neck (defined as tracks within the 20<sup>th</sup> percentile of the bud neck in either the mother or bud compartment, also see gray box in cartoon, middle). Note how she1 maintaining the spindle within close proximity of the bud neck is partially dynein and microtubule binding independent, but maintaining low cortical proximity is dependent on dynein activity and microtubule binding of She1. Additionally, the biased increase in spindle tracks in the mother compartment is dependent on dynein activity and microtubule binding of She1. (d) The bar graph shows spindle displacement (in  $\mu\text{m}$  per minute) - note how this displacement metric includes both dynein-dependent and dynein-independent spindle movements, separate from figure 3.3e. (b, c, d)  $n = 2$  replicates,  $n_1, n_2 = 20$  cells per replicate and each replicate contains  $\geq 1362$  total spindle tracks. P-values were obtained from Mann-Whitney test (b-d) for data distributions that did not pass the D'Agostino and Pearson normality test (see Methods).

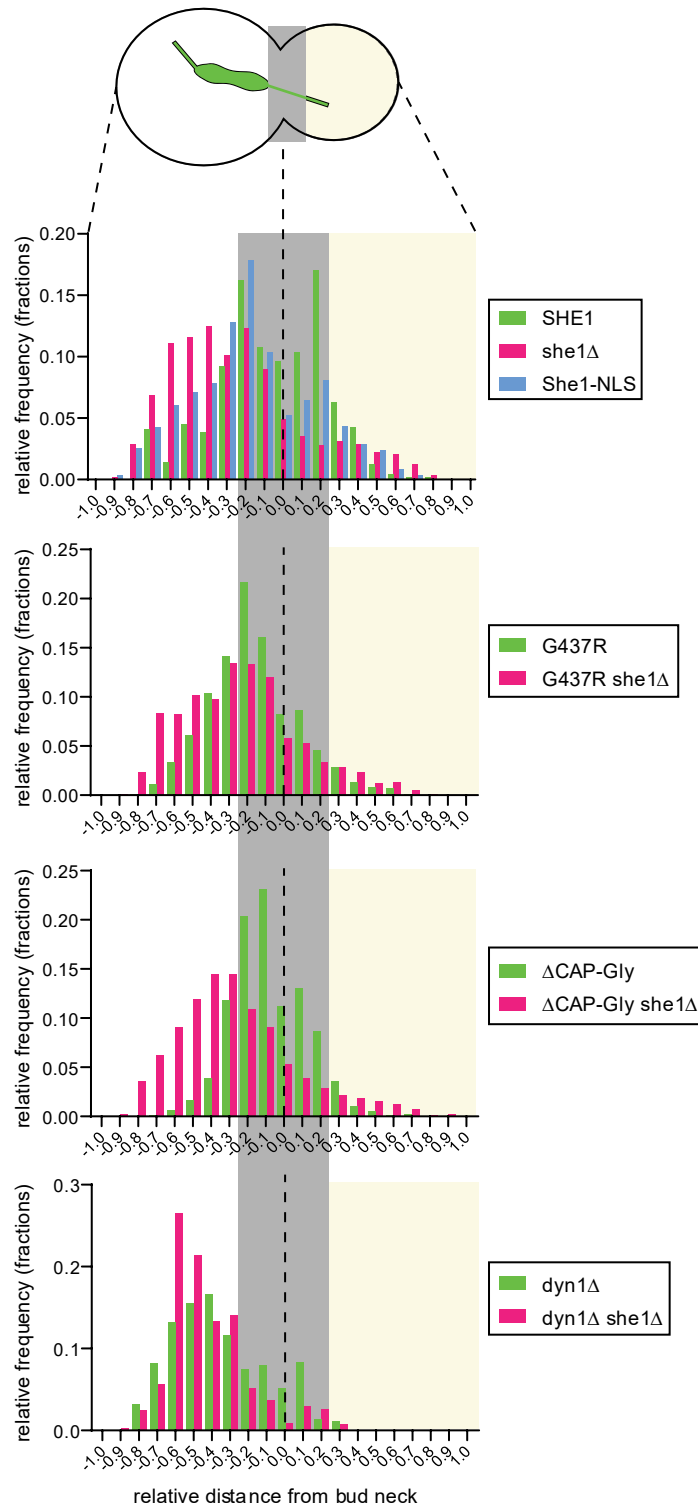


**Figure 3.5. She1 maintains bud neck proximity.** Histograms were created using tracking data for wild-type and mutant strains obtained during analysis in figure 3.3. *dyn1Δ* strains were included to assess if the following phenotypes were associated with dynein hyperactivity. Spindle tracking data was processed based on relative distance to the bud neck, binned in 10<sup>th</sup>s of a whole, and plotted by relative frequency in fractions of a whole (see Methods). The line at

the origin (0.0) designates the bud neck and gray region indicates the region within close proximity to the bud neck: -0.2 - 0.0 mother side and 0.0 - 0.2 bud side (see Figure 3.4). The mother cell is on the left (white) and bud cell is on the right (tan; see cartoon, middle). Note the relative distance from the bud neck is most prominent in the mother compartment in *she1Δ* and this phenotype is partially dependent on dynein (*dyn1Δ* vs. *dyn1Δ she1Δ*). n = 2 replicates, 20 cells per replicate and each replicate contains  $\geq 1362$  total spindle tracks.

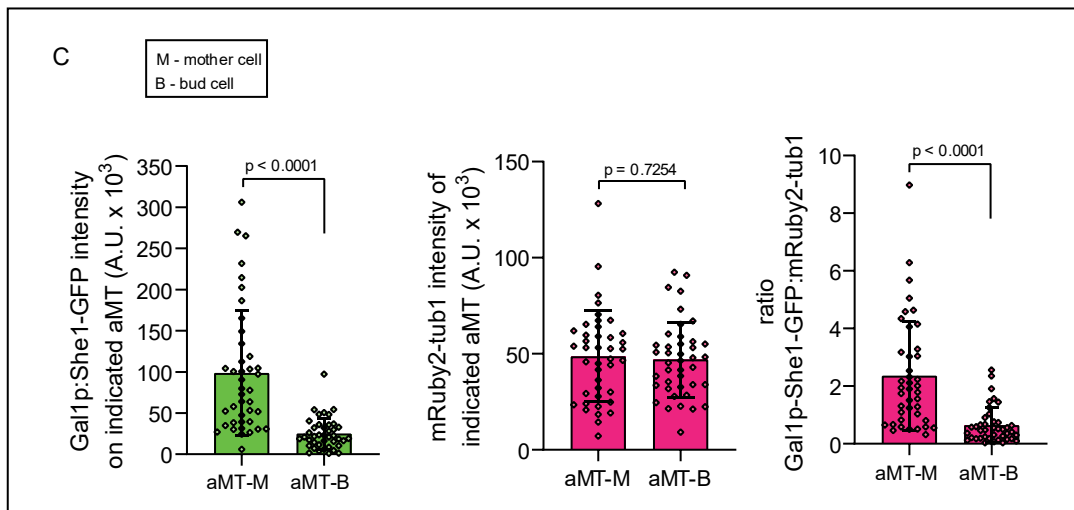
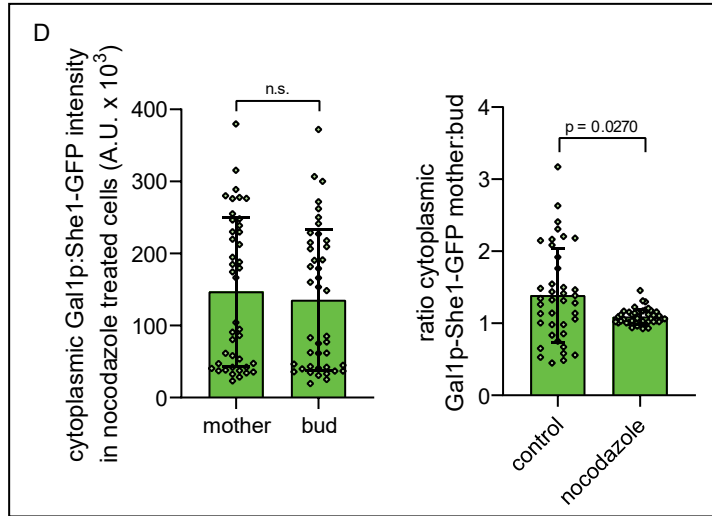
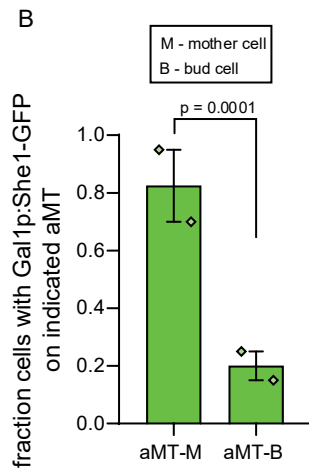
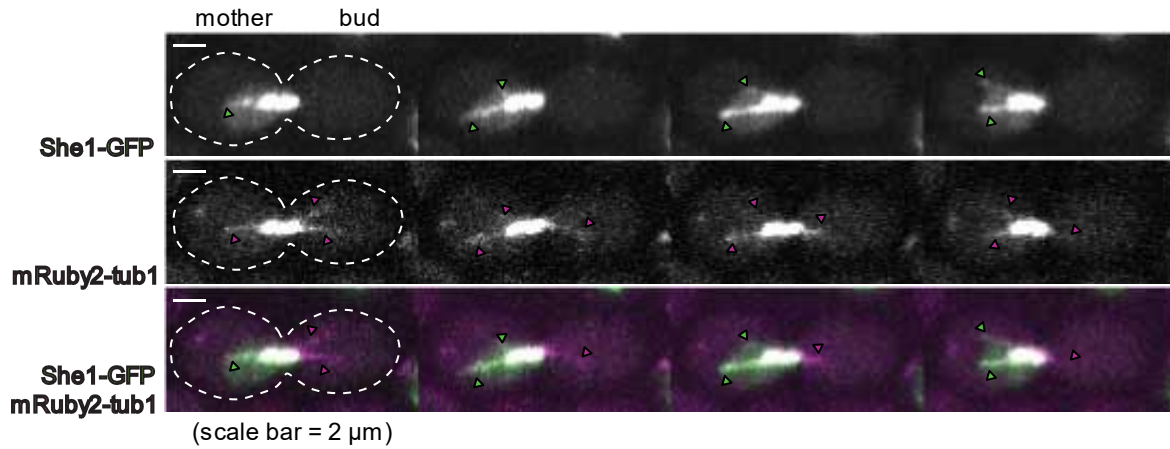


**Figure 3.6. She1 preferentially localizes to aMTs in the mother compartment.** (a) Representative fluorescent images of a HU-arrested cell with Gal1p:She1-GFP (top) and mRuby2-tub1 (middle). The merge (bottom) shows Gal1p:She1-GFP in green and mRuby2-tub1 in magenta. Note She1 binds along the length of the aMTs in the mother compartment, but not

bud-associated aMTs. She1-GFP was overexpressed for 3 hours before to imaging under a galactose inducible promoter for a bright signal on aMTs. Cells were arrested with HU for 2.5 hours before imaging on a confocal fluorescence microscope. (b) Qualitative bar graph showing the fraction of cells with visible Gal1p:She1-GFP on either mother (M) or bud (B) aMTs. Only cells with aMTs in both mother and bud compartments were analyzed. Diamonds represent replicates and error bars are the standard deviation. (n = 2 replicates, 20 cells per replicate). (c) Quantitation of Gal1p:She1-GFP intensity on aMTs in mother and bud compartments (left). The mRuby2-tub1 signal was used to draw a line along the length of aMTs and transfer to the Gal1p:She1-GFP channel since She1 signal is not visible on bud aMTs (see Methods). mRuby2-tub1 intensity was also measured (middle) to normalize Gal1p:She1-GFP to microtubule intensity (right). (d) Cells were treated with nocodazole for 30 minutes to destroy aMTs and background intensity of Gal1p:She1-GFP quantified to measure cytoplasmic differences between mother and bud compartments (left, see Methods). The bar graph (right) shows the mean ratio of Gal1p:She1-GFP in the mother and bud compartments for control and nocodazole treated cells (see Methods). Note that the mean ratio in control cells is greater than nocodazole treated cells, indicating that Galp:She1-GFP intensity is greater in the mother compartment when aMTs are present. (c, d) Diamonds represent one cell and error bars are standard deviation. n = 2 replicates,  $\geq 19$  cells per replicate. P values from Welch's t test for data with normal distributions (b, c mRuby2-tub1 intensity), or Mann-Whitney test (c) Gal1p:She1-GFP intensity and ratio Gal1p:She1-GFP:mRuby2-tub1, (d) for data distributions that did not pass the D'Agostino and Pearson normality test (see Methods).

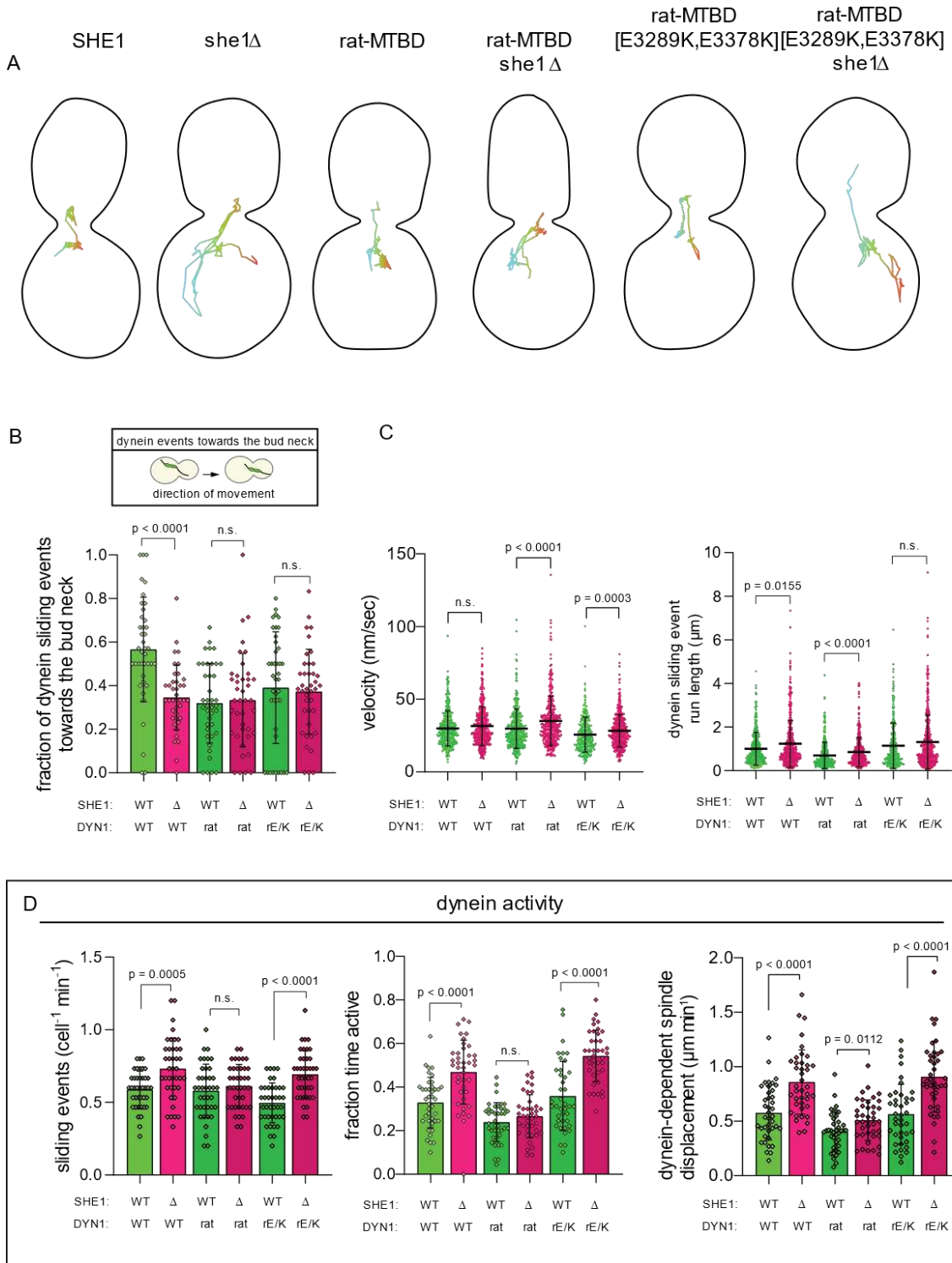


**Figure 3.7. She1 requires the microtubule binding domain of dynein to inhibit dynein activity but not prolonged motility.** (a) Example spindle tracks for wild-type She1 (data in following graphs b-e shown in green) and chimeric ratMTBD dynein strains as indicated (*she1*Δ; magenta). All strains contain a YFP fused to wild-type dynein and chimeric dynein used to

confirm functionality. Cells are arrested with HU for 2.5 hours. Cells were imaged using Confocal microscopy on HU containing agarose pads using GFP-Tub1 to observe spindle movements. Image processing was done using ImageJ and MATLAB scripts, and YFP signal was manually omitted from tracking data (see Methods). (b) Schematic showing an example of a dynein sliding event towards the bud neck. Note that the aMT is captured by dynein in the compartment opposite the spindle (top). Bar graph shows the mean fraction of dynein sliding events that move the spindle towards the bud neck in control and mutant strains. Each diamond represents the fraction for one cell. (c, d) Scatter plots of velocity (c) and run length (d) for dynein sliding events. Each dot represents the mean velocity or the total run length of one dynein sliding event. (e) Three parameters defining dynein activity; dynein sliding events, fraction of time active, and dynein-dependent spindle displacement per minute indicate a greater amount of dynein activity in *she1Δ* strains, however the *ratMTBD* chimera is insensitive to *She1* loss, which is restored by changing the conformational state to a high MT binding state (rE/K). Bar graphs represent the mean and each diamond represents one cell (b, c, d, e)  $n = 2$  replicates,  $n_1, n_2 = 20$  cells per replicate. There were  $\geq 141$  dynein sliding events per replicate. Error bars show standard deviations. P-values from Welch's t test for data with normal distributions (b, e; sliding events and fraction time active) or Mann-Whitney test (c, d, e; dynein-dependent spindle displacement) for data distributions that did not pass the D'Agostino and Pearson normality test (see Methods).

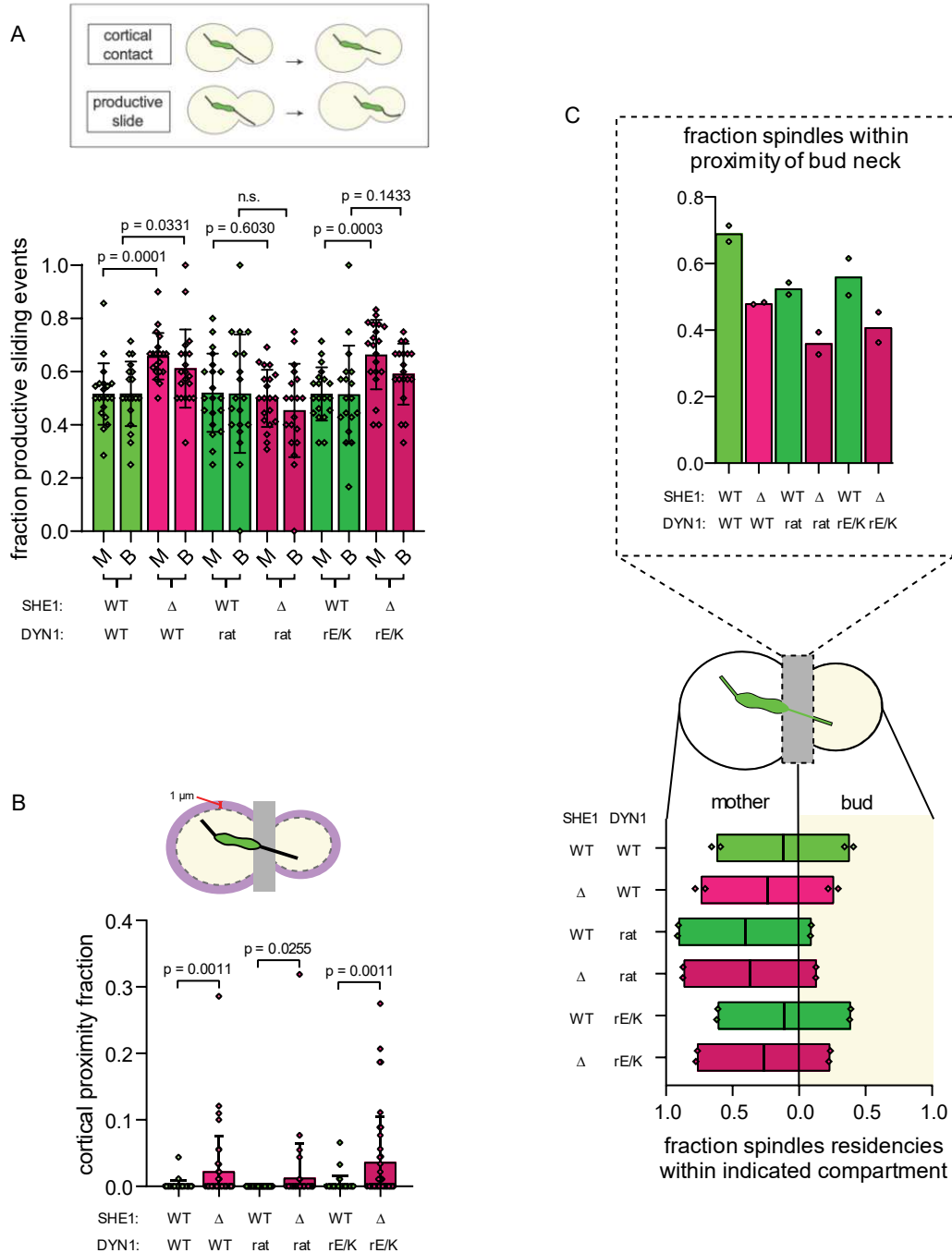


**Figure 3.8. She1 requires the microtubule binding domain to inhibit the initiation of dynein events and maintain bud neck proximity.** Wild-type and mutant strains used in figure 6 were used to assess if She1 requires the microtubule binding domain of dynein in the following phenotypes. Confocal fluorescence images and spindle tracking data from figure 6 was also used (see Methods). (a) Spindle tracking data was used in determining the compartment location of spindle tracks and the distance of spindle tracks from the bud neck (see Methods). The bar graph (bottom) plots the fraction of spindle tracks either in the mother or bud compartment. The line at the origin (0.0) designates the bud neck and the line within the

bars indicate the mean distance from the bud neck of all spindle tracks. The mother cell is on the left (white) and bud cell is on the right (tan; see cartoon, middle). Diamonds represent each replicate. Spindle tracking data was then binned based to their distance from the bud neck (see Methods, also Fig 3.8). The bar graph (top) shows the fraction of spindle tracks found within close proximity of the bud neck (defined as tracks within the 20<sup>th</sup> percentile of the bud neck in either the mother or bud compartment, also see gray box in cartoon, middle). (b) Bar graph shows the fraction of spindle tracks found within close proximity of the cortex (defined as being within 1  $\mu\text{m}$  of the cell cortex, excluding the bud neck; see cartoon above graph). Note how she1 maintaining the spindle within close proximity of the bud neck is partially dynein and microtubule binding independent, but maintaining low cortical proximity is dependent on dynein activity and microtubule binding of She1. Additionally, the biased increase in spindle tracks in the mother compartment is dependent on dynein activity and microtubule binding of She1. Diamonds represent the cortical proximity fraction of one cell and error bars are the standard deviations ( $n = 2$  replicates,  $n_1, n_2 = 20$  cells per replicate and each replicate contains  $\geq 1793$  total spindle tracks). (d) Example cartoon of cortical contacts that do (bottom) and do not (top) convert into a productive sliding event with quantitation below. The bar graph is divided into productive sliding events in the mother compartment (M) and bud compartment (B) as indicated. This quantitation was done manually using both XY and XZ maximum projections for accurate observation of cortical contacts ( $n = 2$  replicates, 10 cells per replicate, see Methods). P-values were calculated from Z-scores (a) or Mann-Whitney test (b, c) for data distributions that did not pass the D'Agostino and Pearson normality test (see Methods).

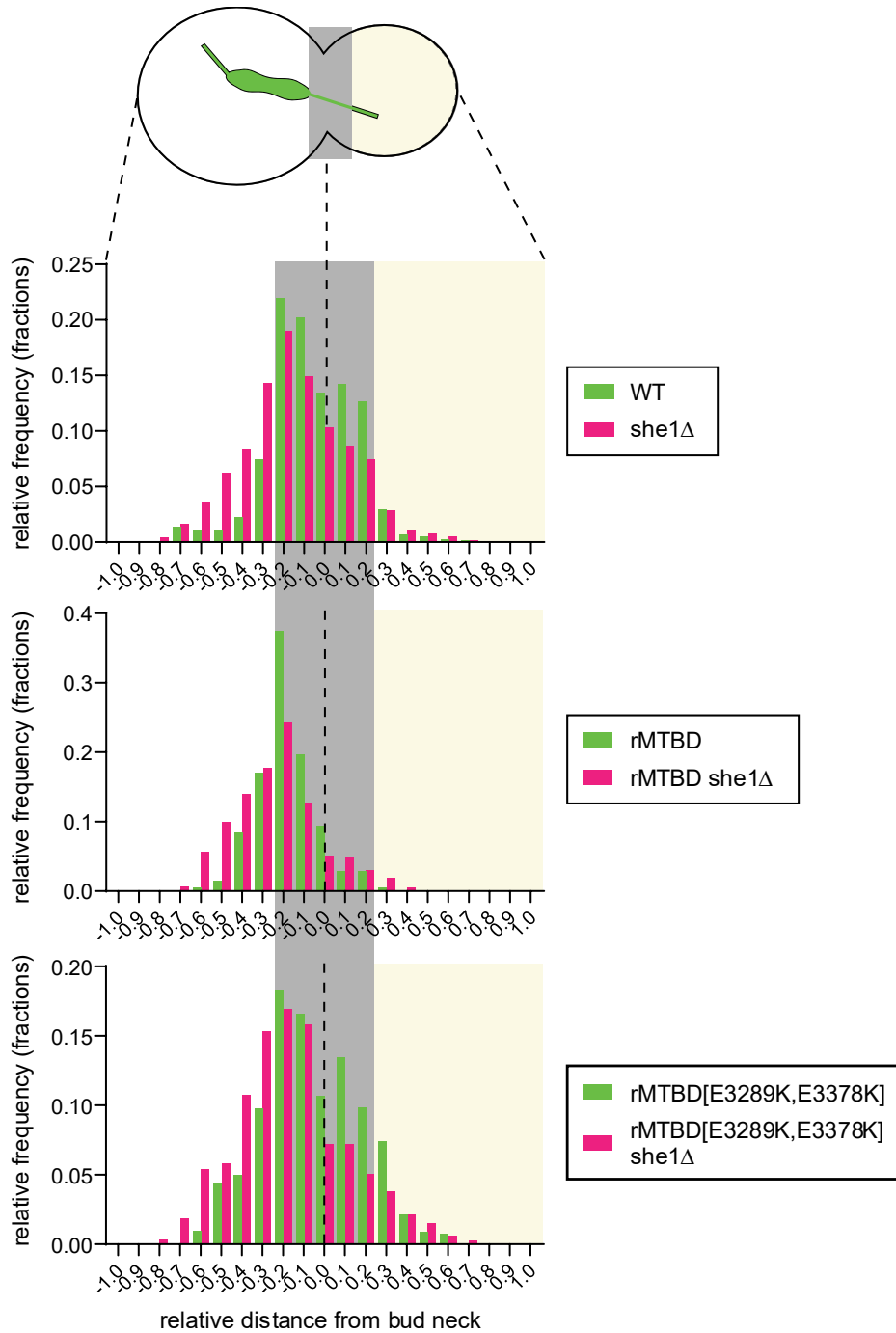


**Figure 3.9. She1 maintains bud neck proximity.** Histograms for wild-type and rat chimerias were created using data obtained from analysis for figure 3.7. Spindle tracking data was processed based on relative distance to the bud neck, binned in  $10^{\text{ths}}$  of a whole, and plotted by relative frequency in fractions of a whole (see Methods). The line at the origin (0.0) designates the bud neck and gray region indicates the region within close proximity to the bud neck: -0.2 - 0.0 mother side and 0.0 - 0.2 bud side (see Figure 3.8). The mother cell is on the left (white) and bud cell is on the right (tan; see cartoon, middle). Note the relative distance from the bud neck is most prominent in the mother compartment in she1Δ and high-affinity ratMTBD she1Δ.

However, the phenotypes in these cells was less dramatic (see Figure 3.7 and 3.8).  $n = 2$  replicates, 20 cells per replicate and each replicate contains  $\geq 1793$  total spindle tracks.

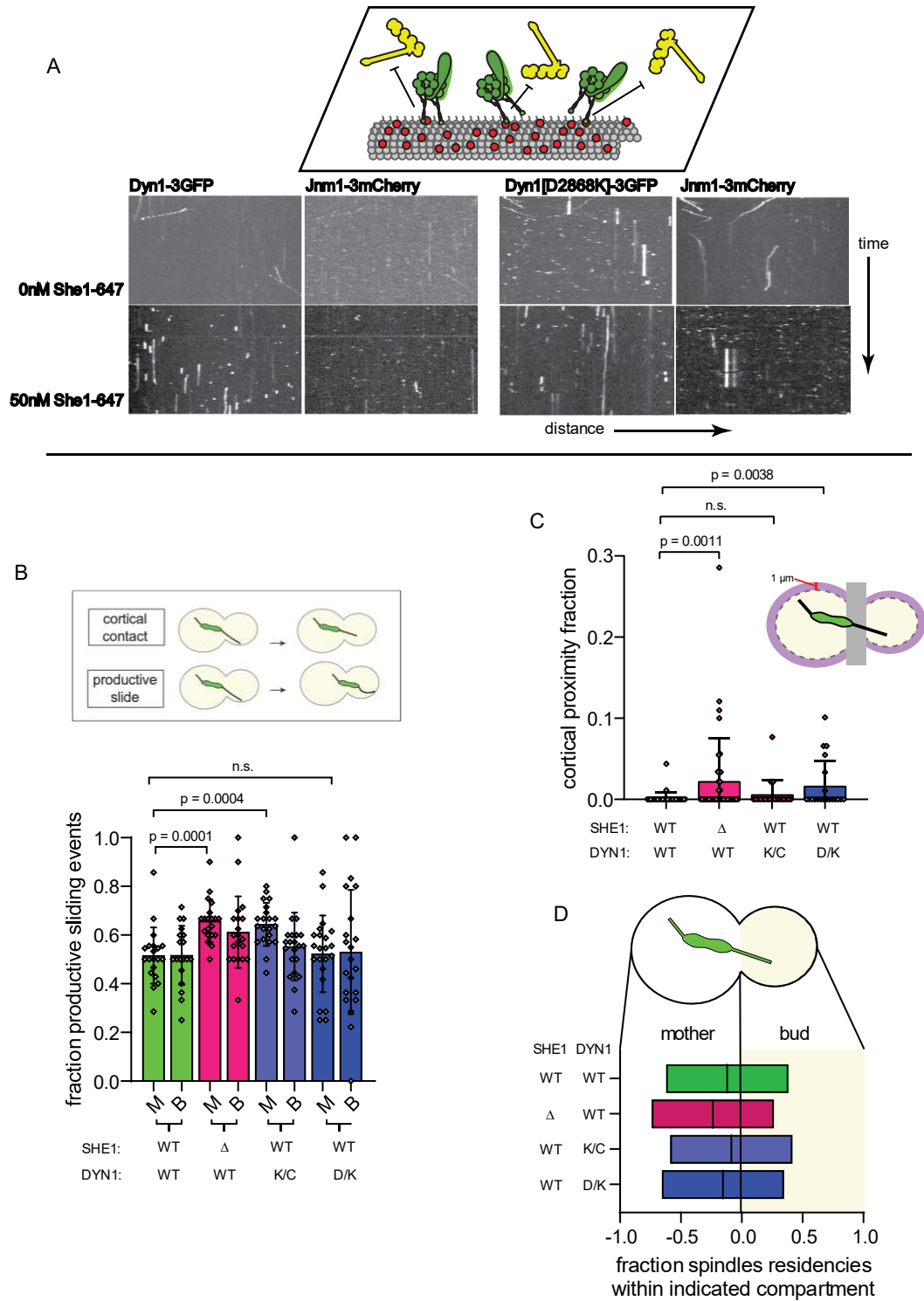


**Figure 3.10. She1 disrupts interaction of dynein and dynactin complex *in vitro* and dynein mutants display some She1 phenotypes *in vivo*.** (a) Single molecule assays with yeast cell lysates. (b) fraction of productive sliding events

## REFERENCES

- Ahmad FJ, Yu W, McNally FJ, Baas PW. An essential role for katanin in severing microtubules in the neuron. *J Cell Biol.* 1999;145(2):305-315. doi:10.1083/jcb.145.2.305
- Aiken J, Sept D, Costanzo M, Boone C, Cooper JA, Moore JK. Genome-wide analysis reveals novel and discrete functions for tubulin carboxy-terminal tails. *Curr Biol.* 2014;24(12):1295-1303. doi:10.1016/j.cub.2014.03.078
- Akhmanova A, Steinmetz MO. Control of microtubule organization and dynamics: two ends in the limelight. *Nat Rev Mol Cell Biol.* 2015;16(12):711-726. doi:10.1038/nrm4084
- Akhmanova, A., Hoogenraad, C. C., Drabek, K., Stepanova, T., Dortland, B., Verkerk, T., Vermeulen, W., Burgering, B. M., De Zeeuw, C. I., Grosveld, F. & Galjart, N. Clasps are CLIP-115 and -170 associating proteins involved in the regional regulation of microtubule dynamics in motile fibroblasts. *Cell.* 2001;104(6):923-935.
- Alushin GM, Lander GC, Kellogg EH, Zhang R, Baker D, Nogales E. High-resolution microtubule structures reveal the structural transitions in  $\alpha\beta$ -tubulin upon GTP hydrolysis. *Cell.* 2014;157(5):1117-1129. doi:10.1016/j.cell.2014.03.053
- Ayaz P, Munyoki S, Geyer EA, et al. A tethered delivery mechanism explains the catalytic action of a microtubule polymerase. *Elife.* 2014;3:e03069. Published 2014 Aug 5. doi:10.7554/eLife.03069
- Babazadeh R, Furukawa T, Hohmann S, Furukawa K. Rewiring yeast osmostress signalling through the MAPK network reveals essential and non-essential roles of Hog1 in osmoadaptation. *Sci Rep.* 2014;4:4697. Published 2014 Apr 15. doi:10.1038/srep04697
- Badin-Larçon AC, Boscheron C, Soleilhac JM, et al. Suppression of nuclear oscillations in *Saccharomyces cerevisiae* expressing Glu tubulin. *Proc Natl Acad Sci U S A.* 2004;101(15):5577-5582. doi:10.1073/pnas.0307917101
- Bahi-Buisson N, Poirier K, Boddaert N, et al. Refinement of cortical dysgeneses spectrum associated with TUBA1A mutations. *J Med Genet.* 2008;45(10):647-653. doi:10.1136/jmg.2008.058073
- Balchand, S. K., Mann, B. J., Titus, J., Ross, J. L. & Wadsworth, P. TPX2 Inhibits Eg5 by Interactions with Both Motor and Microtubule. *J Biol Chem.* 2015;290(28):17367-17379.
- Barlan K, Lu W, Gelfand VI. The microtubule-binding protein ensconsin is an essential cofactor of kinesin-1. *Curr Biol.* 2013;23(4):317-322. doi:10.1016/j.cub.2013.01.008
- Bechstedt S, Lu K, Brouhard GJ. Doublecortin recognizes the longitudinal curvature of the microtubule end and lattice. *Curr Biol.* 2014;24(20):2366-2375. doi:10.1016/j.cub.2014.08.039
- Bergman ZJ, Wong J, Drubin DG, Barnes G. Microtubule dynamics regulation reconstituted in budding yeast lysates. *J Cell Sci.* 2018;132(4):jcs219386. Published 2018 Sep 24. doi:10.1242/jcs.219386

Bergman ZJ, Xia X, Amaro IA, Huffaker TC. Constitutive dynein activity in She1 mutants reveals differences in microtubule attachment at the yeast spindle pole body. *Mol Biol Cell*. 2012;23(12):2319-2326. doi:10.1091/mbc.E12-03-0223

Berlin V, Styles CA, Fink GR. BIK1, a protein required for microtubule function during mating and mitosis in *Saccharomyces cerevisiae*, colocalizes with tubulin. *J Cell Biol*. 1990;111(6 Pt 1):2573-2586. doi:10.1083/jcb.111.6.2573

Bertazzi DT, Kurtulmus B, Pereira G. The cortical protein Lte1 promotes mitotic exit by inhibiting the spindle position checkpoint kinase Kin4. *J Cell Biol*. 2011;193(6):1033-1048. doi:10.1083/jcb.201101056

Bhabha, G., Cheng, H. C., Zhang, N., Moeller, A., Liao, M., Speir, J. A., Cheng, Y. & Vale, R. D. Allosteric communication in the Dynein motor domain. *Cell*. 2014;159(4):857-868.

Bi, E. & Pringle, J. R. ZDS1 and ZDS2, genes whose products may regulate Cdc42p in *Saccharomyces cerevisiae*. *Mol Cell Biol*. 1996;16(10):5264-5275.

Biernat J, Wu YZ, Timm T, et al. Protein kinase MARK/PAR-1 is required for neurite outgrowth and establishment of neuronal polarity. *Mol Biol Cell*. 2002;13(11):4013-4028. doi:10.1091/mbc.02-03-0046

Bieling P, Telley IA, Surrey T. A minimal midzone protein module controls formation and length of antiparallel microtubule overlaps. *Cell*. 2010;142(3):420-432. doi:10.1016/j.cell.2010.06.033

Bieling P, Kandels-Lewis S, Telley IA, van Dijk J, Janke C, Surrey T. CLIP-170 tracks growing microtubule ends by dynamically recognizing composite EB1/tubulin-binding sites. *J Cell Biol*. 2008;183(7):1223-1233. doi:10.1083/jcb.200809190

Blake-Hodek, K. A., Cassimeris, L. & Huffaker, T. C. Regulation of microtubule dynamics by Bim1 and Bik1, the budding yeast members of the EB1 and CLIP-170 families of plus-end tracking proteins. *Mol Biol Cell*. 2010;21(12):2013-2023.

Bodakuntla S, Jijumon AS, Villablanca C, Gonzalez-Billault C, Janke C. Microtubule-Associated Proteins: Structuring the Cytoskeleton. *Trends Cell Biol*. 2019;29(10):804-819. doi:10.1016/j.tcb.2019.07.004

Bode CJ, Gupta ML, Suprenant KA, Himes RH. The two alpha-tubulin isotypes in budding yeast have opposing effects on microtubule dynamics in vitro. *EMBO Rep*. 2003;4(1):94-99. doi:10.1038/sj.embor.embor716

Boleti H, Karsenti E, Vernos I. Xklp2, a novel *Xenopus* centrosomal kinesin-like protein required for centrosome separation during mitosis. *Cell*. 1996;84(1):49-59. doi:10.1016/s0092-8674(00)80992-7

Botstein D, Fink GR. Yeast: an experimental organism for 21st Century biology. *Genetics*. 2011;189(3):695-704. doi:10.1534/genetics.111.130765

Botstein D, Fink GR. Yeast: an experimental organism for modern biology. *Science*. 1988;240(4858):1439-1443. doi:10.1126/science.3287619

Bouxsein NF, Bachand GD. Single filament behavior of microtubules in the presence of added divalent counterions. *Biomacromolecules*. 2014;15(10):3696-3705. doi:10.1021/bm500988r

Brewster JL, de Valoir T, Dwyer ND, Winter E, Gustin MC. An osmosensing signal transduction pathway in yeast. *Science*. 1993;259(5102):1760-1763. doi:10.1126/science.7681220

Brouhard GJ, Stear JH, Noetzel TL, et al. XMAP215 is a processive microtubule polymerase. *Cell*. 2008;132(1):79-88. doi:10.1016/j.cell.2007.11.043

Brunet, S., Sardon, T., Zimmerman, T., Wittmann, T., Pepperkok, R., Karsenti, E. & Vernos, I. Characterization of the TPX2 domains involved in microtubule nucleation and spindle assembly in *Xenopus* egg extracts. *Mol Biol Cell*. 2004;15(12):5318-5328.

Buey RM, Mohan R, Leslie K, et al. Insights into EB1 structure and the role of its C-terminal domain for discriminating microtubule tips from the lattice. *Mol Biol Cell*. 2011;22(16):2912-2923. doi:10.1091/mbc.E11-01-0017

Burgess, S. A., Walker, M. L., Sakakibara, H., Knight, P. J. & Oiwa, K. Dynein structure and power stroke. *Nature*. 2003;421(6924):715-718.

Burns RG, Islam K, Chapman R. The multiple phosphorylation of the microtubule-associated protein MAP2 controls the MAP2:tubulin interaction. *Eur J Biochem*. 1984;141(3):609-615. doi:10.1111/j.1432-1033.1984.tb08236.x

Byers B, Goetsch L. Behavior of spindles and spindle plaques in the cell cycle and conjugation of *Saccharomyces cerevisiae*. *J Bacteriol*. 1975;124(1):511-523. doi:10.1128/JB.124.1.511-523.1975

Cadou A, Couturier A, Le Goff C, et al. Kin1 is a plasma membrane-associated kinase that regulates the cell surface in fission yeast. *Mol Microbiol*. 2010;77(5):1186-1202. doi:10.1111/j.1365-2958.2010.07281.x

Carter, A. P., Garbarino, J. E., Wilson-Kubalek, E. M., Shipley, W. E., Cho, C., Milligan, R. A., Vale, R. D. & Gibbons, I. R. Structure and functional role of dynein's microtubule-binding domain. *Science*. 2008;322(5908):1691-1695.

Carvalho P, Gupta ML Jr, Hoyt MA, Pellman D. Cell cycle control of kinesin-mediated transport of Bik1 (CLIP-170) regulates microtubule stability and dynein activation. *Dev Cell*. 2004;6(6):815-829. doi:10.1016/j.devcel.2004.05.001

Caydasi AK, Kurtulmus B, Orrico MI, Hofmann A, Ibrahim B, Pereira G. Elm1 kinase activates the spindle position checkpoint kinase Kin4. *J Cell Biol*. 2010;190(6):975-989. doi:10.1083/jcb.201006151

Caydasi AK, Pereira G. Spindle alignment regulates the dynamic association of checkpoint proteins with yeast spindle pole bodies. *Dev Cell*. 2009;16(1):146-156. doi:10.1016/j.devcel.2008.10.013

- Chapin SJ, Bulinski JC. Non-neuronal 210 x 10<sup>3</sup> Mr microtubule-associated protein (MAP4) contains a domain homologous to the microtubule-binding domains of neuronal MAP2 and tau. *J Cell Sci.* 1991;98 ( Pt 1):27-36.
- Cleary, F. B., Dewitt, M. A., Bilyard, T., Htet, Z. M., Belyy, V., Chan, D. D., Chang, A. Y. & Yildiz, A. Tension on the linker gates the ATP-dependent release of dynein from microtubules. *Nature communications.* 2014;5:4587.
- Collins ES, Balchand SK, Faraci JL, Wadsworth P, Lee WL. Cell cycle-regulated cortical dynein/dynactin promotes symmetric cell division by differential pole motion in anaphase. *Mol Biol Cell.* 2012;23(17):3380-3390. doi:10.1091/mbc.E12-02-0109
- Conway, L., Wood, D., Tuzel, E. & Ross, J. L. Motor transport of self-assembled cargos in crowded environments. *Proc Natl Acad Sci U S A.* 2012;109(51):20814-20819.
- Cook KE, O'Shea EK. Hog1 controls global reallocation of RNA Pol II upon osmotic shock in *Saccharomyces cerevisiae*. *G3 (Bethesda).* 2012;2(9):1129-1136. doi:10.1534/g3.112.003251
- Dehmelt L, Halpain S. The MAP2/Tau family of microtubule-associated proteins. *Genome Biol.* 2005;6(1):204. doi:10.1186/gb-2004-6-1-204
- Demaurex N. pH Homeostasis of cellular organelles. *News Physiol Sci.* 2002;17:1-5. doi:10.1152/physiologyonline.2002.17.1.1
- Díaz-Valencia JD, Morelli MM, Bailey M, Zhang D, Sharp DJ, Ross JL. Drosophila katanin-60 depolymerizes and severs at microtubule defects. *Biophys J.* 2011;100(10):2440-2449. doi:10.1016/j.bpj.2011.03.062
- Dimitrov A, Quesnoit M, Moutel S, Cantaloube I, Poüs C, Perez F. Detection of GTP-tubulin conformation in vivo reveals a role for GTP remnants in microtubule rescues. *Science.* 2008;322(5906):1353-1356. doi:10.1126/science.1165401
- Dixit, R., Ross, J. L., Goldman, Y. E. & Holzbaaur, E. L. Differential regulation of dynein and kinesin motor proteins by tau. *Science.* 2008;319(5866):1086-1089.
- Drewes G, Ebneth A, Preuss U, Mandelkow EM, Mandelkow E. MARK, a novel family of protein kinases that phosphorylate microtubule-associated proteins and trigger microtubule disruption. *Cell.* 1997;89(2):297-308. doi:10.1016/s0092-8674(00)80208-1
- Drewes G, Trinczek B, Illenberger S, et al. Microtubule-associated protein/microtubule affinity-regulating kinase (p110mark). A novel protein kinase that regulates tau-microtubule interactions and dynamic instability by phosphorylation at the Alzheimer-specific site serine 262. *J Biol Chem.* 1995;270(13):7679-7688. doi:10.1074/jbc.270.13.7679
- Driskell OJ, Mironov A, Allan VJ, Woodman PG. Dynein is required for receptor sorting and the morphogenesis of early endosomes. *Nat Cell Biol.* 2007;9(1):113-120. doi:10.1038/ncb1525
- Duellberg C, Trokter M, Jha R, Sen I, Steinmetz MO, Surrey T. Reconstitution of a hierarchical +TIP interaction network controlling microtubule end tracking of dynein. *Nat Cell Biol.* 2014;16(8):804-811. doi:10.1038/ncb2999

Dumont S, Mitchison TJ. Force and length in the mitotic spindle. *Curr Biol*. 2009;19(17):R749-R761. doi:10.1016/j.cub.2009.07.028

Ebneth A, Godemann R, Stamer K, Illenberger S, Trinczek B, Mandelkow E. Overexpression of tau protein inhibits kinesin-dependent trafficking of vesicles, mitochondria, and endoplasmic reticulum: implications for Alzheimer's disease. *J Cell Biol*. 1998;143(3):777-794. doi:10.1083/jcb.143.3.777

Eckerdt, F., Eyers, P. A., Lewellyn, A. L., Prigent, C. & Maller, J. L. Spindle pole regulation by a discrete Eg5-interacting domain in TPX2. *Curr Biol*. 2008;18(7):519-525.

Egan MJ, McClintock MA, Reck-Peterson SL. Microtubule-based transport in filamentous fungi. *Curr Opin Microbiol*. 2012;15(6):637-645. doi:10.1016/j.mib.2012.10.003

Egilmez NK, Jazwinski SM. Evidence for the involvement of a cytoplasmic factor in the aging of the yeast *Saccharomyces cerevisiae*. *J Bacteriol*. 1989;171(1):37-42. doi:10.1128/jb.171.1.37-42.1989

Elbert M, Rossi G, Brennwald P. The yeast par-1 homologs kin1 and kin2 show genetic and physical interactions with components of the exocytic machinery. *Mol Biol Cell*. 2005;16(2):532-549. doi:10.1091/mbc.e04-07-0549

Elshenawy MM, Kusakci E, Volz S, Baumbach J, Bullock SL, Yildiz A. Lis1 activates dynein motility by modulating its pairing with dynactin. *Nat Cell Biol*. 2020;22(5):570-578. doi:10.1038/s41556-020-0501-4

Espinet C, de la Torre MA, Aldea M, Herrero E. An efficient method to isolate yeast genes causing overexpression-mediated growth arrest. *Yeast*. 1995;11(1):25-32. doi:10.1002/yea.320110104

Estrem C, Moore JK. Astral microtubule forces alter nuclear organization and inhibit DNA repair in budding yeast. *Mol Biol Cell*. 2019;30(16):2000-2013. doi:10.1091/mbc.E18-12-0808

Estrem C, Fees CP, Moore JK. Dynein is regulated by the stability of its microtubule track. *J Cell Biol*. 2017;216(7):2047-2058. doi:10.1083/jcb.201611105

Ettinger A, van Haren J, Ribeiro SA, Wittmann T. Doublecortin Is Excluded from Growing Microtubule Ends and Recognizes the GDP-Microtubule Lattice. *Curr Biol*. 2016;26(12):1549-1555. doi:10.1016/j.cub.2016.04.020

Falk JE, Chan LY, Amon A. Lte1 promotes mitotic exit by controlling the localization of the spindle position checkpoint kinase Kin4. *Proc Natl Acad Sci U S A*. 2011;108(31):12584-12590. doi:10.1073/pnas.1107784108

Fees CP, Moore JK. Regulation of microtubule dynamic instability by the carboxy-terminal tail of  $\beta$ -tubulin. *Life Sci Alliance*. 2018;1(2):e201800054. doi:10.26508/lsa.201800054

Ferreira T, Mason AB, Slayman CW. The yeast Pma1 proton pump: a model for understanding the biogenesis of plasma membrane proteins. *J Biol Chem*. 2001;276(32):29613-29616. doi:10.1074/jbc.R100022200

Fourniol FJ, Sindelar CV, Amigues B, et al. Template-free 13-protofilament microtubule-MAP assembly visualized at 8 Å resolution. *J Cell Biol.* 2010;191(3):463-470. doi:10.1083/jcb.201007081

Francis F, Koulakoff A, Boucher D, et al. Doublecortin is a developmentally regulated, microtubule-associated protein expressed in migrating and differentiating neurons. *Neuron.* 1999;23(2):247-256. doi:10.1016/s0896-6273(00)80777-1

Frixione E. Recurring views on the structure and function of the cytoskeleton: a 300-year epic. *Cell Motil Cytoskeleton.* 2000;46(2):73-94. doi:10.1002/1097-0169(200006)46:2<73::AID-CM1>3.0.CO;2-0

Fourniol FJ, Sindelar CV, Amigues B, et al. Template-free 13-protofilament microtubule-MAP assembly visualized at 8 Å resolution. *J Cell Biol.* 2010;191(3):463-470. doi:10.1083/jcb.201007081

Fu J, Bian M, Xin G, et al. TPX2 phosphorylation maintains metaphase spindle length by regulating microtubule flux. *J Cell Biol.* 2015;210(3):373-383. doi:10.1083/jcb.201412109

Fu, C., Ward, J. J., Liodice, I., Velve-Casquillas, G., Nedelec, F. J. & Tran, P. T. Phospho-regulated interaction between kinesin-6 Klp9p and microtubule bundler Ase1p promotes spindle elongation. *Dev Cell.* 2009;17(2):257-267.

Garcia-Moreno B. Adaptations of proteins to cellular and subcellular pH. *J Biol.* 2009;8(11):98. doi:10.1186/jbiol199

Gardner MK, Charlebois BD, Jánosi IM, Howard J, Hunt AJ, Odde DJ. Rapid microtubule self-assembly kinetics [published correction appears in *Cell.* 2014 Sep 25;159(1):215]. *Cell.* 2011;146(4):582-592. doi:10.1016/j.cell.2011.06.053

Gartz Hanson M, Aiken J, Sietsema DV, et al. Novel  $\alpha$ -tubulin mutation disrupts neural development and tubulin proteostasis. *Dev Biol.* 2016;409(2):406-419. doi:10.1016/j.ydbio.2015.11.022

Geyer EA, Burns A, Lalonde BA, et al. A mutation uncouples the tubulin conformational and GTPase cycles, revealing allosteric control of microtubule dynamics. *Elife.* 2015;4:e10113. Published 2015 Oct 6. doi:10.7554/eLife.10113

Ghossoub R, Hu Q, Failler M, et al. Septins 2, 7 and 9 and MAP4 colocalize along the axoneme in the primary cilium and control ciliary length. *J Cell Sci.* 2013;126(Pt 12):2583-2594. doi:10.1242/jcs.111377

Gibbons, I. R., Garbarino, J. E., Tan, C. E., Reck-Peterson, S. L., Vale, R. D. & Carter, A. P. The affinity of the dynein microtubule-binding domain is modulated by the conformation of its coiled-coil stalk. *J Biol Chem.* 2005;280(25):23960-23965.

Gibson, D. G., Young, L., Chuang, R. Y., Venter, J. C., Hutchison, C. A., 3rd & Smith, H. O. Enzymatic assembly of DNA molecules up to several hundred kilobases. *Nat Methods.* 2009;6(5):343-345.

- Gireesh KK, Shine A, Lakshmi RB, Vijayan V, Manna TK. GTP-binding facilitates EB1 recruitment onto microtubules by relieving its auto-inhibition. *Sci Rep.* 2018;8(1):9792. Published 2018 Jun 28. doi:10.1038/s41598-018-28056-y
- Glomb O, Gronemeyer T. Septin Organization and Functions in Budding Yeast. *Front Cell Dev Biol.* 2016;4:123. Published 2016 Nov 3. doi:10.3389/fcell.2016.00123
- Goodwin, S. S. & Vale, R. D. Patronin regulates the microtubule network by protecting microtubule minus ends. *Cell.* 2010;143(2):263-274.
- Gross SP, Tuma MC, Deacon SW, Serpinskaya AS, Reilein AR, Gelfand VI. Interactions and regulation of molecular motors in *Xenopus melanophores*. *J Cell Biol.* 2002;156(5):855-865. doi:10.1083/jcb.200105055
- Gsponer J, Futschik ME, Teichmann SA, Babu MM. Tight regulation of unstructured proteins: from transcript synthesis to protein degradation. *Science.* 2008;322(5906):1365-1368. doi:10.1126/science.1163581
- Guharoy M, Szabo B, Contreras Martos S, Kosol S, Tompa P. Intrinsic structural disorder in cytoskeletal proteins. *Cytoskeleton (Hoboken).* 2013;70(10):550-571. doi:10.1002/cm.21118
- Guedes-Dias P, Holzbaur ELF. Axonal transport: Driving synaptic function. *Science.* 2019;366(6462):eaaw9997. doi:10.1126/science.aaw9997
- Halpain, S. & Dehmelt, L. The MAP1 family of microtubule-associated proteins. *Genome biology.* 2006;7(6):224.
- Hayashi I, Wilde A, Mal TK, Ikura M. Structural basis for the activation of microtubule assembly by the EB1 and p150Glued complex. *Mol Cell.* 2005;19(4):449-460. doi:10.1016/j.molcel.2005.06.034
- Hayashi I, Ikura M. Crystal structure of the amino-terminal microtubule-binding domain of end-binding protein 1 (EB1). *J Biol Chem.* 2003;278(38):36430-36434. doi:10.1074/jbc.M305773200
- Henderson KA, Hughes AL, Gottschling DE. Mother-daughter asymmetry of pH underlies aging and rejuvenation in yeast. *Elife.* 2014;3:e03504. Published 2014 Sep 4. doi:10.7554/eLife.03504
- Honnappa S, Okhrimenko O, Jaussi R, et al. Key interaction modes of dynamic +TIP networks. *Mol Cell.* 2006;23(5):663-671. doi:10.1016/j.molcel.2006.07.013
- Honnappa S, Gouveia SM, Weisbrich A, et al. An EB1-binding motif acts as a microtubule tip localization signal. *Cell.* 2009;138(2):366-376. doi:10.1016/j.cell.2009.04.065
- Howes SC, Geyer EA, LaFrance B, et al. Structural and functional differences between porcine brain and budding yeast microtubules. *Cell Cycle.* 2018;17(3):278-287. doi:10.1080/15384101.2017.1415680
- Howes SC, Geyer EA, LaFrance B, et al. Structural differences between yeast and mammalian microtubules revealed by cryo-EM. *J Cell Biol.* 2017;216(9):2669-2677. doi:10.1083/jcb.201612195

- Htet ZM, Gillies JP, Baker RW, Leschziner AE, DeSantis ME, Reck-Peterson SL. LIS1 promotes the formation of activated cytoplasmic dynein-1 complexes. *Nat Cell Biol.* 2020;22(5):518-525. doi:10.1038/s41556-020-0506-z
- Huang, J., Roberts, A. J., Leschziner, A. E. & Reck-Peterson, S. L. Lis1 acts as a "clutch" between the ATPase and microtubule-binding domains of the dynein motor. *Cell.* 2012;150(5):975-986.
- Hughes AL, Gottschling DE. An early age increase in vacuolar pH limits mitochondrial function and lifespan in yeast. *Nature.* 2012;492(7428):261-265. doi:10.1038/nature11654
- Hwang E, Kusch J, Barral Y, Huffaker TC. Spindle orientation in *Saccharomyces cerevisiae* depends on the transport of microtubule ends along polarized actin cables. *J Cell Biol.* 2003;161(3):483-488. doi:10.1083/jcb.200302030
- Iakoucheva LM, Radivojac P, Brown CJ, et al. The importance of intrinsic disorder for protein phosphorylation. *Nucleic Acids Res.* 2004;32(3):1037-1049. Published 2004 Feb 11. doi:10.1093/nar/gkh253
- Igaev M, Grubmüller H. Microtubule assembly governed by tubulin allosteric gain in flexibility and lattice induced fit. *Elife.* 2018;7:e34353. Published 2018 Apr 13. doi:10.7554/eLife.34353
- Illenberger S, Drewes G, Trinczek B, et al. Phosphorylation of microtubule-associated proteins MAP2 and MAP4 by the protein kinase p110mark. Phosphorylation sites and regulation of microtubule dynamics. *J Biol Chem.* 1996;271(18):10834-10843. doi:10.1074/jbc.271.18.10834
- Imamura, K., Kon, T., Ohkura, R. & Sutoh, K. The coordination of cyclic microtubule association/dissociation and tail swing of cytoplasmic dynein. *Proc Natl Acad Sci U S A.* 2007;104(41):16134-16139.
- Janke C, Bulinski JC. Post-translational regulation of the microtubule cytoskeleton: mechanisms and functions. *Nat Rev Mol Cell Biol.* 2011;12(12):773-786. Published 2011 Nov 16. doi:10.1038/nrm3227
- Janke C, Magiera MM. The tubulin code and its role in controlling microtubule properties and functions. *Nat Rev Mol Cell Biol.* 2020;21(6):307-326. doi:10.1038/s41580-020-0214-3
- Kanaba T, Maesaki R, Mori T, Ito Y, Hakoshima T, Mishima M. Microtubule-binding sites of the CH domain of EB1 and its autoinhibition revealed by NMR. *Biochim Biophys Acta.* 2013;1834(2):499-507. doi:10.1016/j.bbapap.2012.10.013
- Kardon JR, Reck-Peterson SL, Vale RD. Regulation of the processivity and intracellular localization of *Saccharomyces cerevisiae* dynein by dynactin. *Proc Natl Acad Sci U S A.* 2009;106(14):5669-5674. doi:10.1073/pnas.0900976106
- Katsuki M, Tokuraku K, Murofushi H, Kotani S. Functional analysis of microtubule-binding domain of bovine MAP4. *Cell Struct Funct.* 1999;24(5):337-344. doi:10.1247/csf.24.337
- Kelley, L. A., Mezulis, S., Yates, C. M., Wass, M. N. & Sternberg, M. J. The Phyre2 web portal for protein modeling, prediction and analysis. *Nat Protoc.* 2015;10(6):845-858.

Kellogg EH, Hejab NMA, Poepsel S, Downing KH, DiMaio F, Nogales E. Near-atomic model of microtubule-tau interactions. *Science*. 2018;360(6394):1242-1246. doi:10.1126/science.aat1780

Kemphues KJ, Priess JR, Morton DG, Cheng NS. Identification of genes required for cytoplasmic localization in early *C. elegans* embryos. *Cell*. 1988;52(3):311-320. doi:10.1016/s0092-8674(88)80024-2

Keyes BE, Burke DJ. Irc15 Is a microtubule-associated protein that regulates microtubule dynamics in *Saccharomyces cerevisiae*. *Curr Biol*. 2009;19(6):472-478. doi:10.1016/j.cub.2009.01.068

Khmelniskii, A., Roostalu, J., Roque, H., Antony, C. & Schiebel, E. Phosphorylation-dependent protein interactions at the spindle midzone mediate cell cycle regulation of spindle elongation. *Dev Cell*. 2009;17(2):244-256.

Knop, M., Siegers, K., Pereira, G., Zachariae, W., Winsor, B., Nasmyth, K. & Schiebel, E. Epitope tagging of yeast genes using a PCR-based strategy: more tags and improved practical routines. *Yeast*. 1999;15(10B):963-972.

Kollman JM, Greenberg CH, Li S, et al. Ring closure activates yeast  $\gamma$ TuRC for species-specific microtubule nucleation. *Nat Struct Mol Biol*. 2015;22(2):132-137. doi:10.1038/nsmb.2953

Kon, T., Nishiura, M., Ohkura, R., Toyoshima, Y. Y. & Sutoh, K. Distinct functions of nucleotide-binding/hydrolysis sites in the four AAA modules of cytoplasmic dynein. *Biochemistry*. 2004;43(35):11266-11274.

Kon, T., Mogami, T., Ohkura, R., Nishiura, M. & Sutoh, K. ATP hydrolysis cycle-dependent tail motions in cytoplasmic dynein. *Nat Struct Mol Biol*. 2005;12(6):513-519.

Kon, T., Imamula, K., Roberts, A. J., Ohkura, R., Knight, P. J., Gibbons, I. R., Burgess, S. A. & Sutoh, K. Helix sliding in the stalk coiled coil of dynein couples ATPase and microtubule binding. *Nat Struct Mol Biol*. 2009;16(3):325-333.

Kon, T., Oyama, T., Shimo-Kon, R., Imamula, K., Shima, T., Sutoh, K. & Kurisu, G. The 2.8 Å crystal structure of the dynein motor domain. *Nature*. 2012;484(7394):345-350.  
Koonce MP. Dictyostelium, a model organism for microtubule-based transport. *Protist*. 2000;151(1):17-25. doi:10.1078/1434-4610-00004

Kotani S, Murofushi H, Maekawa S, Aizawa H, Sakai H. Isolation of rat liver microtubule-associated proteins. Evidence for a family of microtubule-associated proteins with molecular mass of around 200,000 which distribute widely among mammalian cells. *J Biol Chem*. 1988;263(11):5385-5389.

Kremer BE, Haystead T, Macara IG. Mammalian septins regulate microtubule stability through interaction with the microtubule-binding protein MAP4. *Mol Biol Cell*. 2005;16(10):4648-4659. doi:10.1091/mbc.e05-03-0267

Kumar P, Wittmann T. +TIPs: SxIPping along microtubule ends. *Trends Cell Biol*. 2012;22(8):418-428. doi:10.1016/j.tcb.2012.05.005

- Kusch J, Meyer A, Snyder MP, Barral Y. Microtubule capture by the cleavage apparatus is required for proper spindle positioning in yeast. *Genes Dev.* 2002;16(13):1627-1639. doi:10.1101/gad.222602
- Lacroix B, van Dijk J, Gold ND, et al. Tubulin polyglutamylation stimulates spastin-mediated microtubule severing. *J Cell Biol.* 2010;189(6):945-954. doi:10.1083/jcb.201001024
- Lammers LG, Markus SM. The dynein cortical anchor Num1 activates dynein motility by relieving Pac1/LIS1-mediated inhibition. *J Cell Biol.* 2015;211(2):309-322. doi:10.1083/jcb.201506119
- Lancaster AK, Nutter-Upham A, Lindquist S, King OD. PLAAC: a web and command-line application to identify proteins with prion-like amino acid composition. *Bioinformatics.* 2014;30(17):2501-2502. doi:10.1093/bioinformatics/btu310
- Lansbergen G, Grigoriev I, Mimori-Kiyosue Y, et al. CLASPs attach microtubule plus ends to the cell cortex through a complex with LL5beta. *Dev Cell.* 2006;11(1):21-32. doi:10.1016/j.devcel.2006.05.012
- Lansky Z, Braun M, Lüdecke A, et al. Diffusible crosslinkers generate directed forces in microtubule networks. *Cell.* 2015;160(6):1159-1168. doi:10.1016/j.cell.2015.01.051
- Lee WL, Kaiser MA, Cooper JA. The offloading model for dynein function: differential function of motor subunits. *J Cell Biol.* 2005;168(2):201-207. doi:10.1083/jcb.200407036
- Lee WL, Oberle JR, Cooper JA. The role of the lissencephaly protein Pac1 during nuclear migration in budding yeast. *J Cell Biol.* 2003;160(3):355-364. doi:10.1083/jcb.200209022
- Levin DE, Bishop JM. A putative protein kinase gene (*kin1+*) is important for growth polarity in *Schizosaccharomyces pombe*. *Proc Natl Acad Sci U S A.* 1990;87(21):8272-8276. doi:10.1073/pnas.87.21.8272
- Lew DJ, Burke DJ. The spindle assembly and spindle position checkpoints. *Annu Rev Genet.* 2003;37:251-282. doi:10.1146/annurev.genet.37.042203.120656
- Li, J., Lee, W. L. & Cooper, J. A. NudEL targets dynein to microtubule ends through LIS1. *Nat Cell Biol.* 2005;7(7):686-690.
- Li L, Zhang Q, Lei X, Huang Y, Hu J. MAP4 as a New Candidate in Cardiovascular Disease. *Front Physiol.* 2020;11:1044. Published 2020 Aug 26. doi:10.3389/fphys.2020.01044
- Liakopoulos D, Kusch J, Grava S, Vogel J, Barral Y. Asymmetric loading of Kar9 onto spindle poles and microtubules ensures proper spindle alignment. *Cell.* 2003;112(4):561-574. doi:10.1016/s0092-8674(03)00119-3
- Loïdice I, Staub J, Setty TG, Nguyen NP, Paoletti A, Tran PT. Ase1p organizes antiparallel microtubule arrays during interphase and mitosis in fission yeast. *Mol Biol Cell.* 2005;16(4):1756-1768. doi:10.1091/mbc.e04-10-0899
- Lombino FL, Muhia M, Lopez-Rojas J, et al. The Microtubule Severing Protein Katanin Regulates Proliferation of Neuronal Progenitors in Embryonic and Adult Neurogenesis. *Sci Rep.* 2019;9(1):15940. Published 2019 Nov 4. doi:10.1038/s41598-019-52367-3

Longtine, M. S., McKenzie, A., 3rd, Demarini, D. J., Shah, N. G., Wach, A., Brachat, A., Philippsen, P. & Pringle, J. R. Additional modules for versatile and economical PCR-based gene deletion and modification in *Saccharomyces cerevisiae*. *Yeast*. 1998;14(10):953-961.

Loughlin R, Wilbur JD, McNally FJ, Nédélec FJ, Heald R. Katanin contributes to interspecies spindle length scaling in *Xenopus*. *Cell*. 2011;147(6):1397-1407. doi:10.1016/j.cell.2011.11.014

Ma, N., Titus, J., Gable, A., Ross, J. L. & Wadsworth, P. TPX2 regulates the localization and activity of Eg5 in the mammalian mitotic spindle. *J Cell Biol*. 2011;195(1):87-98

Maayan I, Beenstock J, Marbach I, Tabachnick S, Livnah O, Engelberg D. Osmostress induces autophosphorylation of Hog1 via a C-terminal regulatory region that is conserved in p38 $\alpha$ . *PLoS One*. 2012;7(9):e44749. doi:10.1371/journal.pone.0044749

Maekawa H, Usui T, Knop M, Schiebel E. Yeast Cdk1 translocates to the plus end of cytoplasmic microtubules to regulate bud cortex interactions. *EMBO J*. 2003;22(3):438-449. doi:10.1093/emboj/cdg063

Manatschal C, Farcas AM, Degen MS, et al. Molecular basis of Kar9-Bim1 complex function during mating and spindle positioning [published online ahead of print, 2016 Sep 28]. *Mol Biol Cell*. 2016;27(23):3729-3745. doi:10.1091/mbc.E16-07-0552

Mandelkow EM, Stamer K, Vogel R, Thies E, Mandelkow E. Clogging of axons by tau, inhibition of axonal traffic and starvation of synapses. *Neurobiol Aging*. 2003;24(8):1079-1085. doi:10.1016/j.neurobiolaging.2003.04.007

Manka SW, Moores CA. The role of tubulin-tubulin lattice contacts in the mechanism of microtubule dynamic instability. *Nat Struct Mol Biol*. 2018;25(7):607-615. doi:10.1038/s41594-018-0087-8

Manning AL, Compton DA. SnapShot: Nonmotor proteins in spindle assembly. *Cell*. 2008;134(4):694. doi:10.1016/j.cell.2008.08.001

Manning AL, Compton DA. Structural and regulatory roles of nonmotor spindle proteins. *Curr Opin Cell Biol*. 2008;20(1):101-106. doi:10.1016/j.ceb.2007.11.004

Markus SM, Kalutkiewicz KA, Lee WL. She1-mediated inhibition of dynein motility along astral microtubules promotes polarized spindle movements. *Curr Biol*. 2012;22(23):2221-2230. doi:10.1016/j.cub.2012.10.017

Markus SM, Plevock KM, St Germain BJ, Punch JJ, Meaden CW, Lee WL. Quantitative analysis of Pac1/LIS1-mediated dynein targeting: Implications for regulation of dynein activity in budding yeast. *Cytoskeleton (Hoboken)*. 2011;68(3):157-174. doi:10.1002/cm.20502

Markus, S. M., Kalutkiewicz, K. A. & Lee, W. L. Astral microtubule asymmetry provides directional cues for spindle positioning in budding yeast. *Experimental cell research*. 2012;318(12):1400-1406.

Markus, S. M. & Lee, W. L. Regulated offloading of cytoplasmic dynein from microtubule plus ends to the cortex. *Dev Cell*. 2011;20(5):639-651.

Markus, S. M., Omer, S., Baranowski, K. & Lee, W. L. Improved Plasmids for Fluorescent Protein Tagging of Microtubules in *Saccharomyces cerevisiae*. *Traffic*. 2015;16(7):773-786.

Markus SM, Punch JJ, Lee WL. Motor- and tail-dependent targeting of dynein to microtubule plus ends and the cell cortex. *Curr Biol*. 2009;19(3):196-205. doi:10.1016/j.cub.2008.12.047

Marzo MG, Griswold JM, Markus SM. Pac1/LIS1 stabilizes an uninhibited conformation of dynein to coordinate its localization and activity. *Nat Cell Biol*. 2020;22(5):559-569. doi:10.1038/s41556-020-0492-1

Matsushima K, Tokuraku K, Hasan MR, Kotani S. Microtubule-associated protein 4 binds to actin filaments and modulates their properties. *J Biochem*. 2012;151(1):99-108. doi:10.1093/jb/mvr119

Maurer SP, Fourniol FJ, Bohner G, Moores CA, Surrey T. EBs recognize a nucleotide-dependent structural cap at growing microtubule ends. *Cell*. 2012;149(2):371-382. doi:10.1016/j.cell.2012.02.049

Maurer SP, Cade NI, Bohner G, Gustafsson N, Boutant E, Surrey T. EB1 accelerates two conformational transitions important for microtubule maturation and dynamics. *Curr Biol*. 2014;24(4):372-384. doi:10.1016/j.cub.2013.12.042

McKenney, R. J., Vershinin, M., Kunwar, A., Vallee, R. B. & Gross, S. P. LIS1 and NudE induce a persistent dynein force-producing state. *Cell*. 2010;141(2):304-314.

McKenney, R. J., Huynh, W., Tanenbaum, M. E., Bhabha, G. & Vale, R. D. Activation of cytoplasmic dynein motility by dynactin-cargo adapter complexes. *Science*. 2014;345(6194):337-341.

McNally FJ, Roll-Mecak A. Microtubule-severing enzymes: From cellular functions to molecular mechanism. *J Cell Biol*. 2018;217(12):4057-4069. doi:10.1083/jcb.201612104

McNally K, Audhya A, Oegema K, McNally FJ. Katanin controls mitotic and meiotic spindle length. *J Cell Biol*. 2006;175(6):881-891. doi:10.1083/jcb.200608117

McNally FJ, Vale RD. Identification of katanin, an ATPase that severs and disassembles stable microtubules. *Cell*. 1993;75(3):419-429. doi:10.1016/0092-8674(93)90377-3

McKenney, R. J., Huynh, W., Vale, R. D. & Sirajuddin, M. Tyrosination of alpha-tubulin controls the initiation of processive dynein-dynactin motility. *EMBO J*. 2016;35(11):1175-1185.

Miki, H., Setou, M., Kaneshiro, K. & Hirokawa, N. All kinesin superfamily protein, KIF, genes in mouse and human. *Proc Natl Acad Sci U S A*. 2001;98(13):7004-7011.

Miller RK, Cheng SC, Rose MD. Bim1p/Yeb1p mediates the Kar9p-dependent cortical attachment of cytoplasmic microtubules. *Mol Biol Cell*. 2000;11(9):2949-2959. doi:10.1091/mbc.11.9.2949

Mimori-Kiyosue, Y., Shiina, N. & Tsukita, S. Adenomatous polyposis coli (APC) protein moves along microtubules and concentrates at their growing ends in epithelial cells. *J Cell Biol.* 2000;148(3):505-518.

Mishima M, Maesaki R, Kasa M, et al. Structural basis for tubulin recognition by cytoplasmic linker protein 170 and its autoinhibition. *Proc Natl Acad Sci U S A.* 2007;104(25):10346-10351. doi:10.1073/pnas.0703876104

Mitchison T, Kirschner M. Microtubule assembly nucleated by isolated centrosomes. *Nature.* 1984;312(5991):232-237. doi:10.1038/312232a0

Moens PB, Rapport E. Spindles, spindle plaques, and meiosis in the yeast *Saccharomyces cerevisiae* (Hansen). *J Cell Biol.* 1971;50(2):344-361. doi:10.1083/jcb.50.2.344

Mollinari, C., Kleman, J. P., Jiang, W., Schoehn, G., Hunter, T. & Margolis, R. L. PRC1 is a microtubule binding and bundling protein essential to maintain the mitotic spindle midzone. *J Cell Biol.* 2002;157(7):1175-1186.

Molodtsov MI, Mieck C, Dobbelaere J, Dammermann A, Westermann S, Vaziri A. A Force-Induced Directional Switch of a Molecular Motor Enables Parallel Microtubule Bundle Formation. *Cell.* 2016;167(2):539-552.e14. doi:10.1016/j.cell.2016.09.029

Monroy BY, Sawyer DL, Ackermann BE, Borden MM, Tan TC, Ori-McKenney KM. Competition between microtubule-associated proteins directs motor transport. *Nat Commun.* 2018;9(1):1487. Published 2018 Apr 16. doi:10.1038/s41467-018-03909-2

Monroy BY, Tan TC, Oclaman JM, et al. A Combinatorial MAP Code Dictates Polarized Microtubule Transport. *Dev Cell.* 2020;53(1):60-72.e4. doi:10.1016/j.devcel.2020.01.029

Moore, J. K., Sept, D. & Cooper, J. A. Neurodegeneration mutations in dynactin impair dynein-dependent nuclear migration. *Proc Natl Acad Sci U S A.* 2009;106(13):5147-5152.

Moore JK, Stuchell-Brereton MD, Cooper JA. Function of dynein in budding yeast: mitotic spindle positioning in a polarized cell. *Cell Motil Cytoskeleton.* 2009;66(8):546-555. doi:10.1002/cm.20364

Morisaki, T., Lyon, K., DeLuca, K. F., DeLuca, J. G., English, B. P., Zhang, Z., Lavis, L. D., Grimm, J. B., Viswanathan, S., Looger, L. L., Lionnet, T. & Stasevich, T. J. Real-time quantification of single RNA translation dynamics in living cells. *Science.* 2016;352(6292):1425-1429.

Nirschl JJ, Magiera MM, Lazarus JE, Janke C, Holzbaur EL.  $\alpha$ -Tubulin Tyrosination and CLIP-170 Phosphorylation Regulate the Initiation of Dynein-Driven Transport in Neurons. *Cell Rep.* 2016;14(11):2637-2652. doi:10.1016/j.celrep.2016.02.046

Parker AL, Teo WS, Pandzic E, et al.  $\beta$ -tubulin carboxy-terminal tails exhibit isotype-specific effects on microtubule dynamics in human gene-edited cells. *Life Sci Alliance.* 2018;1(2):e201800059. doi:10.26508/lsa.201800059

Parysek LM, del Cerro M, Olmsted JB. Microtubule-associated protein 4 antibody: a new marker for astroglia and oligodendroglia. *Neuroscience*. 1985;15(3):869-875. doi:10.1016/0306-4522(85)90084-3

Pasqualone D, Huffaker TC. STU1, a suppressor of a beta-tubulin mutation, encodes a novel and essential component of the yeast mitotic spindle. *J Cell Biol*. 1994;127(6 Pt 2):1973-1984. doi:10.1083/jcb.127.6.1973

Pereira G, Schiebel E. Kin4 kinase delays mitotic exit in response to spindle alignment defects. *Mol Cell*. 2005;19(2):209-221. doi:10.1016/j.molcel.2005.05.030

Peris L, Thery M, Fauré J, et al. Tubulin tyrosination is a major factor affecting the recruitment of CAP-Gly proteins at microtubule plus ends. *J Cell Biol*. 2006;174(6):839-849. doi:10.1083/jcb.200512058

Presley JF, Cole NB, Schroer TA, Hirschberg K, Zaal KJ, Lippincott-Schwartz J. ER-to-Golgi transport visualized in living cells. *Nature*. 1997;389(6646):81-85. doi:10.1038/38001

Pigula A, Drubin DG, Barnes G. Regulation of mitotic spindle disassembly by an environmental stress-sensing pathway in budding yeast. *Genetics*. 2014;198(3):1043-1057. doi:10.1534/genetics.114.163238

Podolski M, Mahamdeh M, Howard J. Stu2, the budding yeast XMAP215/Dis1 homolog, promotes assembly of yeast microtubules by increasing growth rate and decreasing catastrophe frequency. *J Biol Chem*. 2014;289(41):28087-28093. doi:10.1074/jbc.M114.584300

Porter KR. Cytoplasmic Microtubules and Their Functions. CIBA Foundation Symp. In: Wolstenholme GEW, O'Connor MJ, editors. Principles of Biomolecular Organizations. A. Churchill Ltd.; London: 1966. pp. 308–345.

Proft M, Struhl K. MAP kinase-mediated stress relief that precedes and regulates the timing of transcriptional induction. *Cell*. 2004;118(3):351-361. doi:10.1016/j.cell.2004.07.016

Qiu, W., Derr, N. D., Goodman, B. S., Villa, E., Wu, D., Shih, W. & Reck-Peterson, S. L. Dynein achieves processive motion using both stochastic and coordinated stepping. *Nat Struct Mol Biol*. 2012;19(2):193-200.

Reck-Peterson, S. L., Yildiz, A., Carter, A. P., Gennerich, A., Zhang, N. & Vale, R. D. Single-molecule analysis of dynein processivity and stepping behavior. *Cell*. 2006;126(2):335-348.

Redwine, W. B., Hernandez-Lopez, R., Zou, S., Huang, J., Reck-Peterson, S. L. & Leschziner, A. E. Structural basis for microtubule binding and release by dynein. *Science*. 2012;337(6101):1532-1536.

Reiser V, Raitt DC, Saito H. Yeast osmosensor Sln1 and plant cytokinin receptor Cre1 respond to changes in turgor pressure. *J Cell Biol*. 2003;161(6):1035-1040. doi:10.1083/jcb.200301099

Rickard, J. E. & Kreis, T. E. Identification of a novel nucleotide-sensitive microtubule-binding protein in HeLa cells. *J Cell Biol*. 1990;110(5):1623-1633.

Roberts, A. J., Malkova, B., Walker, M. L., Sakakibara, H., Numata, N., Kon, T., Ohkura, R., Edwards, T. A., Knight, P. J., Sutoh, K., Oiwa, K. & Burgess, S. A. ATP-driven remodeling of the linker domain in the dynein motor. *Structure*. 2012;20(10):1670-1680.

Roberts AJ, Goodman BS, Reck-Peterson SL. Reconstitution of dynein transport to the microtubule plus end by kinesin. *Elife*. 2014;3:e02641. Published 2014 Jun 10. doi:10.7554/eLife.02641

Robison P, Prosser BL. Microtubule mechanics in the working myocyte. *J Physiol*. 2017;595(12):3931-3937. doi:10.1113/JP273046

Roll-Mecak A, McNally FJ. Microtubule-severing enzymes. *Curr Opin Cell Biol*. 2010;22(1):96-103. doi:10.1016/j.ceb.2009.11.001

Roll-Mecak A, Vale RD. Making more microtubules by severing: a common theme of noncentrosomal microtubule arrays?. *J Cell Biol*. 2006;175(6):849-851. doi:10.1083/jcb.200611149

Saillour Y, Broix L, Bruel-Jungerman E, et al. Beta tubulin isoforms are not interchangeable for rescuing impaired radial migration due to Tubb3 knockdown. *Hum Mol Genet*. 2014;23(6):1516-1526. doi:10.1093/hmg/ddt538

Samora, C. P., Mogessie, B., Conway, L., Ross, J. L., Straube, A. & McAinsh, A. D. MAP4 and CLASP1 operate as a safety mechanism to maintain a stable spindle position in mitosis. *Nat Cell Biol*. 2011;13(9):1040-1050.

Sanchez AD, Feldman JL. Microtubule-organizing centers: from the centrosome to non-centrosomal sites. *Curr Opin Cell Biol*. 2017;44:93-101. doi:10.1016/j.ceb.2016.09.003

Schatz PJ, Pillus L, Grisafi P, Solomon F, Botstein D. Two functional alpha-tubulin genes of the yeast *Saccharomyces cerevisiae* encode divergent proteins. *Mol Cell Biol*. 1986a;6(11):3711-3721. doi:10.1128/mcb.6.11.3711

Schatz PJ, Solomon F, Botstein D. Genetically essential and nonessential alpha-tubulin genes specify functionally interchangeable proteins. *Mol Cell Biol*. 1986b;6(11):3722-3733. doi:10.1128/mcb.6.11.3722

Schmidt, H., Zalyte, R., Urnavicius, L. & Carter, A. P. Structure of human cytoplasmic dynein-2 primed for its power stroke. *Nature*. 2015;518(7539):435-438.

Schlager, M. A., Hoang, H. T., Urnavicius, L., Bullock, S. L. & Carter, A. P. In vitro reconstitution of a highly processive recombinant human dynein complex. *EMBO J*. 2014;33(17):1855-1868.

Schwartz K, Richards K, Botstein D. BIM1 encodes a microtubule-binding protein in yeast. *Mol Biol Cell*. 1997;8(12):2677-2691. doi:10.1091/mbc.8.12.2677

Seitz A, Kojima H, Oiwa K, Mandelkow EM, Song YH, Mandelkow E. Single-molecule investigation of the interference between kinesin, tau and MAP2c. *EMBO J*. 2002;21(18):4896-4905. doi:10.1093/emboj/cdf503

Selden SC, Pollard TD. Phosphorylation of microtubule-associated proteins regulates their interaction with actin filaments. *J Biol Chem*. 1983;258(11):7064-7071.

Semenova, I., Ikeda, K., Resaul, K., Kraikivski, P., Aguiar, M., Gygi, S., Zaliapin, I., Cowan, A. & Rodionov, V. Regulation of microtubule-based transport by MAP4. *Mol Biol Cell*. 2014;25(20):3119-3132.

Seshan A, Bardin AJ, Amon A. Control of Lte1 localization by cell polarity determinants and Cdc14. *Curr Biol*. 2002;12(24):2098-2110. doi:10.1016/s0960-9822(02)01388-x

Sheeman B, Carvalho P, Sagot I, et al. Determinants of *S. cerevisiae* dynein localization and activation: implications for the mechanism of spindle positioning. *Curr Biol*. 2003;13(5):364-372. doi:10.1016/s0960-9822(03)00013-7

Sherwood NT, Sun Q, Xue M, Zhang B, Zinn K. *Drosophila* spastin regulates synaptic microtubule networks and is required for normal motor function. *PLoS Biol*. 2004;2(12):e429. doi:10.1371/journal.pbio.0020429

Shigematsu H, Imasaki T, Doki C, et al. Structural insight into microtubule stabilization and kinesin inhibition by Tau family MAPs. *J Cell Biol*. 2018;217(12):4155-4163. doi:10.1083/jcb.201711182

Siglin AE, Sun S, Moore JK, et al. Dynein and dynactin leverage their bivalent character to form a high-affinity interaction. *PLoS One*. 2013;8(4):e59453. doi:10.1371/journal.pone.0059453

Sikorski, R. S. & Hieter, P. A system of shuttle vectors and yeast host strains designed for efficient manipulation of DNA in *Saccharomyces cerevisiae*. *Genetics*. 1989;122(1):19-27.

Sirajuddin M, Rice LM, Vale RD. Regulation of microtubule motors by tubulin isotypes and post-translational modifications. *Nat Cell Biol*. 2014;16(4):335-344. doi:10.1038/ncb2920

Slep KC, Vale RD. Structural basis of microtubule plus end tracking by XMAP215, CLIP-170, and EB1. *Mol Cell*. 2007;27(6):976-991. doi:10.1016/j.molcel.2007.07.023

Soundararajan, H. C. & Bullock, S. L. The influence of dynein processivity control, MAPs, and microtubule ends on directional movement of a localising mRNA. *eLife*. 2014;3:e01596.

Splinter, D., Razafsky, D. S., Schlager, M. A., Serra-Marques, A., Grigoriev, I., Demmers, J., Keijzer, N., Jiang, K., Poser, I., Hyman, A. A., Hoogenraad, C. C., King, S. J. & Akhmanova, A. BICD2, dynactin, and LIS1 cooperate in regulating dynein recruitment to cellular structures. *Mol Biol Cell*. 2012;23(21):4226-4241.

Srayko M, O'toole ET, Hyman AA, Müller-Reichert T. Katanin disrupts the microtubule lattice and increases polymer number in *C. elegans* meiosis. *Curr Biol*. 2006;16(19):1944-1949. doi:10.1016/j.cub.2006.08.029

Stangier MM, Kumar A, Chen X, Farcas AM, Barral Y, Steinmetz MO. Structure-Function Relationship of the Bik1-Bim1 Complex. *Structure*. 2018;26(4):607-618.e4. doi:10.1016/j.str.2018.03.003

Straube A, Hause G, Fink G, Steinberg G. Conventional kinesin mediates microtubule-microtubule interactions in vivo. *Mol Biol Cell*. 2006;17(2):907-916. doi:10.1091/mbc.e05-06-0542

Subramanian R, Wilson-Kubalek EM, Arthur CP, et al. Insights into antiparallel microtubule crosslinking by PRC1, a conserved nonmotor microtubule binding protein. *Cell*. 2010;142(3):433-443. doi:10.1016/j.cell.2010.07.012

Sulimenko V, Dráberová E, Sulimenko T, et al. Regulation of microtubule formation in activated mast cells by complexes of gamma-tubulin with Fyn and Syk kinases. *J Immunol*. 2006;176(12):7243-7253. doi:10.4049/jimmunol.176.12.7243

Tanenbaum ME, Vale RD, McKenney RJ. Cytoplasmic dynein crosslinks and slides anti-parallel microtubules using its two motor domains. *Elife*. 2013;2:e00943. Published 2013 Sep 3. doi:10.7554/eLife.00943

Tanenbaum ME, Macurek L, van der Vaart B, Galli M, Akhmanova A, Medema RH. A complex of Kif18b and MCAK promotes microtubule depolymerization and is negatively regulated by Aurora kinases. *Curr Biol*. 2011;21(16):1356-1365. doi:10.1016/j.cub.2011.07.017

Tassan JP, Le Goff X. An overview of the KIN1/PAR-1/MARK kinase family. *Biol Cell*. 2004;96(3):193-199. doi:10.1016/j.biolcel.2003.10.009

Telley, I. A., Bieling, P. & Surrey, T. Obstacles on the microtubule reduce the processivity of Kinesin-1 in a minimal in vitro system and in cell extract. *Biophys J*. 2009;96(8):3341-3353.

Tkach JM, Yimit A, Lee AY, et al. Dissecting DNA damage response pathways by analysing protein localization and abundance changes during DNA replication stress. *Nat Cell Biol*. 2012;14(9):966-976. doi:10.1038/ncb2549

Tompa P. Unstructural biology coming of age. *Curr Opin Struct Biol*. 2011;21(3):419-425. doi:10.1016/j.sbi.2011.03.012

Toropova, K., Zou, S., Roberts, A. J., Redwine, W. B., Goodman, B. S., Reck-Peterson, S. L. & Leschziner, A. E. Lis1 regulates dynein by sterically blocking its mechanochemical cycle. *eLife*. 2014;3.

Trinczek B, Ebner A, Mandelkow EM, Mandelkow E. Tau regulates the attachment/detachment but not the speed of motors in microtubule-dependent transport of single vesicles and organelles. *J Cell Sci*. 1999;112 ( Pt 14):2355-2367.

Trotta N, Orso G, Rossetto MG, Daga A, Brodie K. The hereditary spastic paraplegia gene, spastin, regulates microtubule stability to modulate synaptic structure and function. *Curr Biol*. 2004;14(13):1135-1147. doi:10.1016/j.cub.2004.06.058

Trudeau T, Nassar R, Cumberworth A, Wong ET, Woollard G, Gsponer J. Structure and intrinsic disorder in protein autoinhibition. *Structure*. 2013;21(3):332-341. doi:10.1016/j.str.2012.12.013

Tsai JW, Bremner KH, Vallee RB. Dual subcellular roles for LIS1 and dynein in radial neuronal migration in live brain tissue. *Nat Neurosci*. 2007;10(8):970-979. doi:10.1038/nn1934

Uchimura, S., Fujii, T., Takazaki, H., Ayukawa, R., Nishikawa, Y., Minoura, I., Hachikubo, Y., Kurisu, G., Sutoh, K., Kon, T., Namba, K. & Muto, E. A flipped ion pair at the dynein-microtubule interface is critical for dynein motility and ATPase activation. *J Cell Biol*. 2015;208(2):211-222

- Urnavicius, L., Zhang, K., Diamant, A. G., Motz, C., Schlager, M. A., Yu, M., Patel, N. A., Robinson, C. V. & Carter, A. P. The structure of the dynactin complex and its interaction with dynein. *Science*. 2015;347(6229):1441-1446.
- Urnavicius L, Lau CK, Elshenawy MM, et al. Cryo-EM shows how dynactin recruits two dyneins for faster movement. *Nature*. 2018;554(7691):202-206. doi:10.1038/nature25462
- Vale, R. D. The molecular motor toolbox for intracellular transport. *Cell*. 2003;112(4):467-480.
- Vale RD. Severing of stable microtubules by a mitotically activated protein in *Xenopus* egg extracts. *Cell*. 1991;64(4):827-839. doi:10.1016/0092-8674(91)90511-v
- Vallee R. Structure and phosphorylation of microtubule-associated protein 2 (MAP 2). *Proc Natl Acad Sci U S A*. 1980;77(6):3206-3210. doi:10.1073/pnas.77.6.3206
- van Beuningen SF, Hoogenraad CC. Neuronal polarity: remodeling microtubule organization. *Curr Opin Neurobiol*. 2016;39:1-7. doi:10.1016/j.conb.2016.02.003
- Vemu A, Szczesna E, Zehr EA, et al. Severing enzymes amplify microtubule arrays through lattice GTP-tubulin incorporation. *Science*. 2018;361(6404):eaau1504. doi:10.1126/science.aau1504
- Vizeacoumar, F. J., van Dyk, N., F, S. V., Cheung, V., Li, J., Sydorsky, Y., Case, N., Li, Z., Datti, A., Nislow, C., Raught, B., Zhang, Z., Frey, B., Bloom, K., Boone, C. & Andrews, B. J. Integrating high-throughput genetic interaction mapping and high-content screening to explore yeast spindle morphogenesis. *J Cell Biol*. 2010;188(1):69-81.
- Voter WA, Erickson HP. The kinetics of microtubule assembly. Evidence for a two-stage nucleation mechanism. *J Biol Chem*. 1984;259(16):10430-10438.
- Wall KP, Pagratis M, Armstrong G, et al. Molecular Determinants of Tubulin's C-Terminal Tail Conformational Ensemble. *ACS Chem Biol*. 2016;11(11):2981-2990. doi:10.1021/acschembio.6b00507
- Wang PJ, Huffaker TC. Stu2p: A microtubule-binding protein that is an essential component of the yeast spindle pole body. *J Cell Biol*. 1997;139(5):1271-1280. doi:10.1083/jcb.139.5.1271
- Westfall PJ, Patterson JC, Chen RE, Thorner J. Stress resistance and signal fidelity independent of nuclear MAPK function. *Proc Natl Acad Sci U S A*. 2008;105(34):12212-12217. doi:10.1073/pnas.0805797105
- Widlund PO, Stear JH, Pozniakovskiy A, et al. XMAP215 polymerase activity is built by combining multiple tubulin-binding TOG domains and a basic lattice-binding region. *Proc Natl Acad Sci U S A*. 2011;108(7):2741-2746. doi:10.1073/pnas.1016498108
- Wittmann T, Wilm M, Karsenti E, Vernos I. TPX2, A novel *xenopus* MAP involved in spindle pole organization. *J Cell Biol*. 2000;149(7):1405-1418. doi:10.1083/jcb.149.7.1405
- Wong J, Nakajima Y, Westermann S, et al. A protein interaction map of the mitotic spindle. *Mol Biol Cell*. 2007;18(10):3800-3809. doi:10.1091/mbc.e07-06-0536

- Woodruff JB, Drubin DG, Barnes G. Mitotic spindle disassembly occurs via distinct subprocesses driven by the anaphase-promoting complex, Aurora B kinase, and kinesin-8. *J Cell Biol.* 2010;191(4):795-808. doi:10.1083/jcb.201006028
- Woodruff JB, Drubin DG, Barnes G. Dynein-driven mitotic spindle positioning restricted to anaphase by She1p inhibition of dynactin recruitment. *Mol Biol Cell.* 2009;20(13):3003-3011. doi:10.1091/mbc.e09-03-0186
- Xia P, Liu X, Wu B, et al. Superresolution imaging reveals structural features of EB1 in microtubule plus-end tracking. *Mol Biol Cell.* 2014;25(25):4166-4173. doi:10.1091/mbc.E14-06-1133
- Yajima H, Ogura T, Nitta R, Okada Y, Sato C, Hirokawa N. Conformational changes in tubulin in GMPCPP and GDP-taxol microtubules observed by cryoelectron microscopy. *J Cell Biol.* 2012;198(3):315-322. doi:10.1083/jcb.201201161
- Yeh, E., Yang, C., Chin, E., Maddox, P., Salmon, E. D., Lew, D. J. & Bloom, K. Dynamic positioning of mitotic spindles in yeast: role of microtubule motors and cortical determinants. *Mol Biol Cell.* 2000;11(11):3949-3961.
- Yin H, Pruyne D, Huffaker TC, Bretscher A. Myosin V orientates the mitotic spindle in yeast. *Nature.* 2000;406(6799):1013-1015. doi:10.1038/35023024
- Yu I, Garnham CP, Roll-Mecak A. Writing and Reading the Tubulin Code. *J Biol Chem.* 2015;290(28):17163-17172. doi:10.1074/jbc.R115.637447
- Yuan SM, Nie WC, He F, Jia ZW, Gao XD. Kin2, the Budding Yeast Ortholog of Animal MARK/PAR-1 Kinases, Localizes to the Sites of Polarized Growth and May Regulate Septin Organization and the Cell Wall. *PLoS One.* 2016;11(4):e0153992. Published 2016 Apr 20. doi:10.1371/journal.pone.0153992
- Zanic M, Widlund PO, Hyman AA, Howard J. Synergy between XMAP215 and EB1 increases microtubule growth rates to physiological levels. *Nat Cell Biol.* 2013 Jun;15(6):688-93. doi: 10.1038/ncb2744. Epub 2013 May 12. PMID: 23666085.
- Zhang D, Grode KD, Stewman SF, et al. Drosophila katanin is a microtubule depolymerase that regulates cortical-microtubule plus-end interactions and cell migration. *Nat Cell Biol.* 2011;13(4):361-370. doi:10.1038/ncb2206
- Zhang J, Ahmad S, Mao Y. BubR1 and APC/EB1 cooperate to maintain metaphase chromosome alignment [published correction appears in *J Cell Biol.* 2007 Oct 22;179(2):357]. *J Cell Biol.* 2007;178(5):773-784. doi:10.1083/jcb.200702138
- Zhang, K., Foster, H. E., Rondelet, A., Lacey, S. E., Bahi-Buisson, N., Bird, A. W. & Carter, A. P. Cryo-EM Reveals How Human Cytoplasmic Dynein Is Auto-inhibited and Activated. *Cell.* 2017;169(7):1303-1314 e1318.
- Zhang K, Foster HE, Rondelet A, et al. Cryo-EM Reveals How Human Cytoplasmic Dynein Is Auto-inhibited and Activated. *Cell.* 2017;169(7):1303-1314.e18. doi:10.1016/j.cell.2017.05.025

Zhu Y, An X, Tomaszewski A, Hepler PK, Lee WL. Microtubule cross-linking activity of She1 ensures spindle stability for spindle positioning. *J Cell Biol.* 2017;216(9):2759-2775. doi:10.1083/jcb.201701094

## APPENDIX 1

### SUPPLEMENTARY FIGURES FOR CHAPTER 2

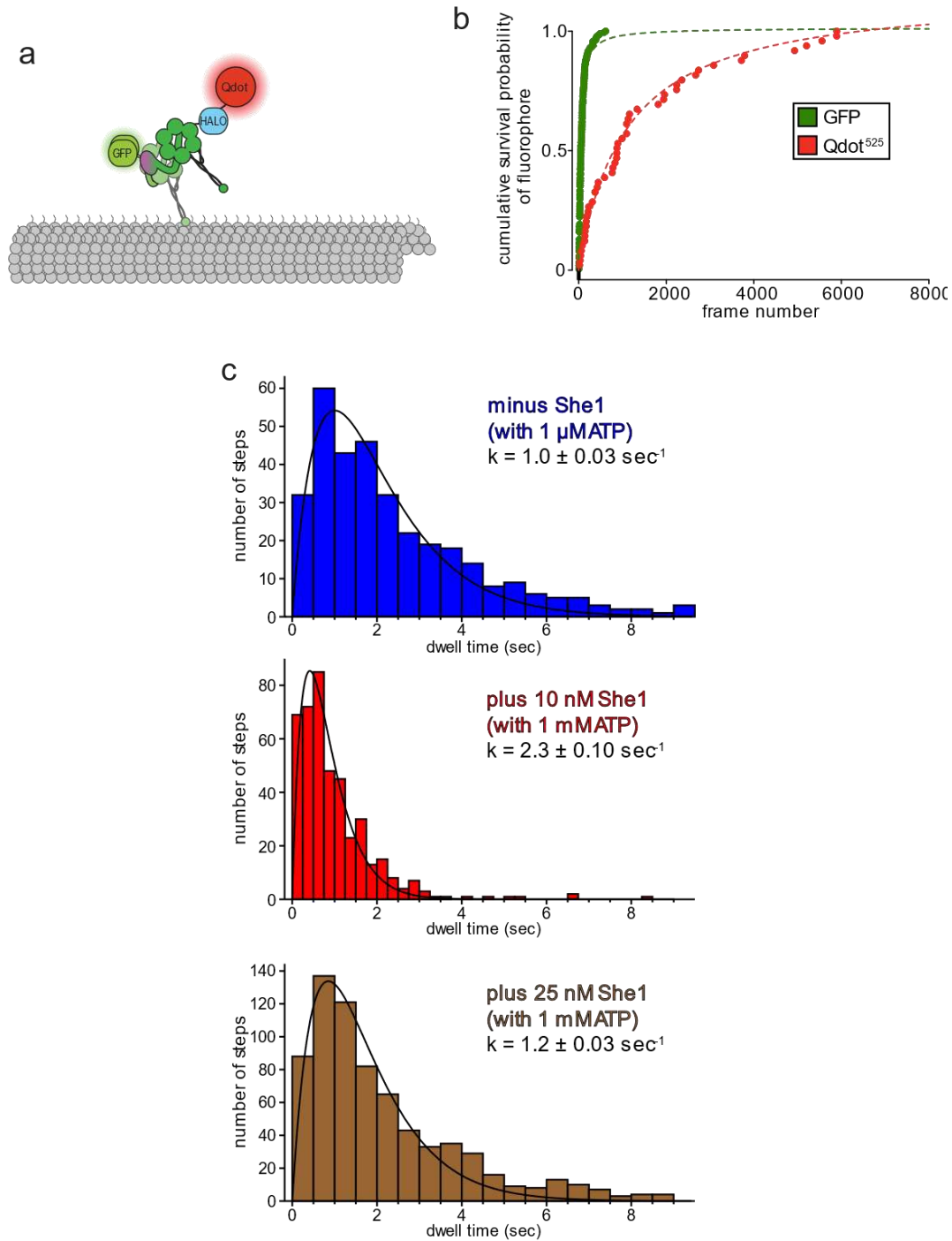


**Figure A1.1. She1 increases dwell time between individual steps of dynein.** (a) Cartoon representation of the GFP-GST-dynein<sub>331</sub>-HALO-Qdot<sup>525</sup> used in the stepping assays. (b) Plots and fits of the cumulative survival probabilities of the N-terminal GFP and the C-terminal (motor) HALO tag-coupled Qdot<sup>525</sup>. Note the large difference in photostability between the two

fluorophores (see Methods;  $n \geq 190$  motors for each). (c) Histograms of dwell times (duration between individual steps) for motor domain labeled (via Qdot<sup>525</sup>) GST-dynein<sub>331</sub> in the absence or presence of She1, and with either 1  $\mu$ M or 1 mM ATP, as indicated. The histograms were fit to a convolution of two exponential functions [ $t^2 \exp(-kt)$ ] with equal decay constants,  $k$ , which reflects the number of steps taken per second (Yildiz et al., 2003; Reck-Peterson et al., 2006;  $k \pm$  standard error of the fit is shown).

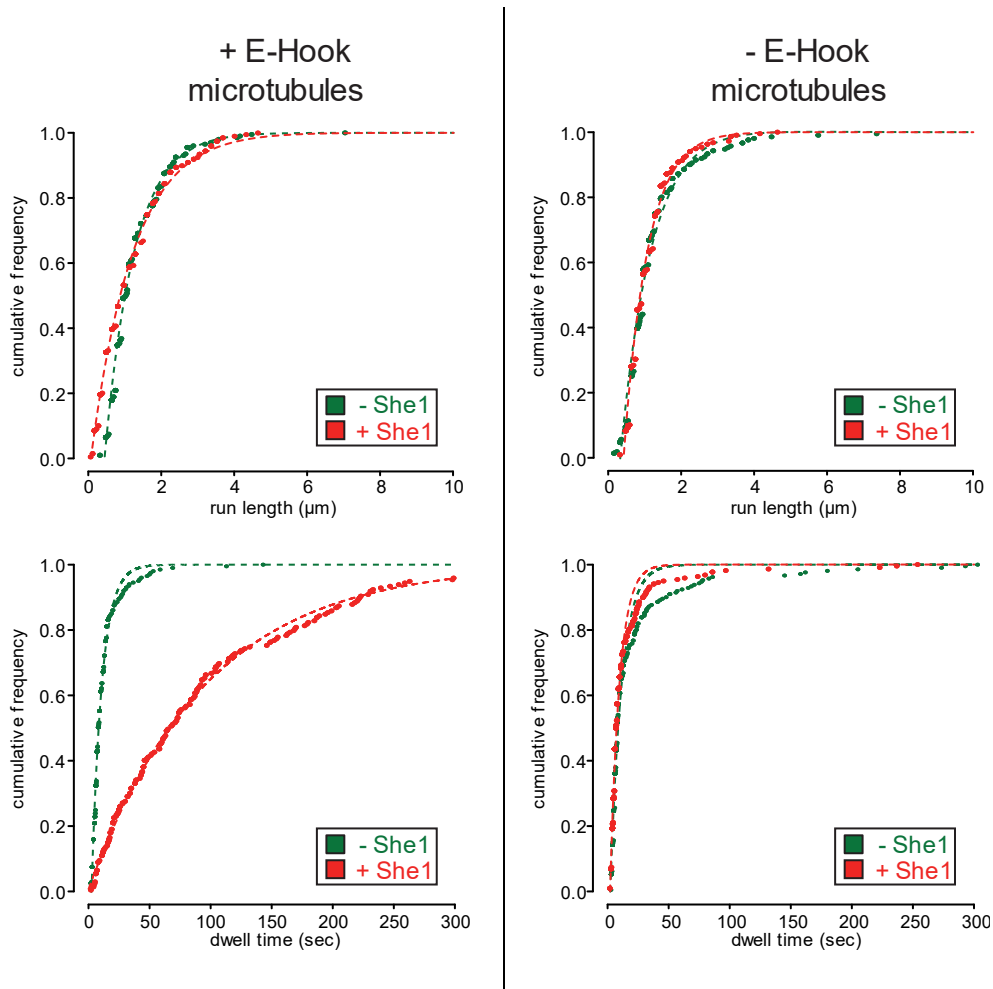


**Figure A1.2. Cumulative probability functions used for determination of mean run length and dwell time values of dynein with and without She1 on control and subtilisin-treated microtubules.** Raw data (circles) and fits (dashed lines) are shown for run length (top) and dwell time (bottom) in the absence (green) and presence of She1 (red) on control (left) or subtilisin-treated microtubules (right;  $n \geq 199$  individual motors for each condition). Data were fit as previously described (Reck-Peterson et al., 2006).

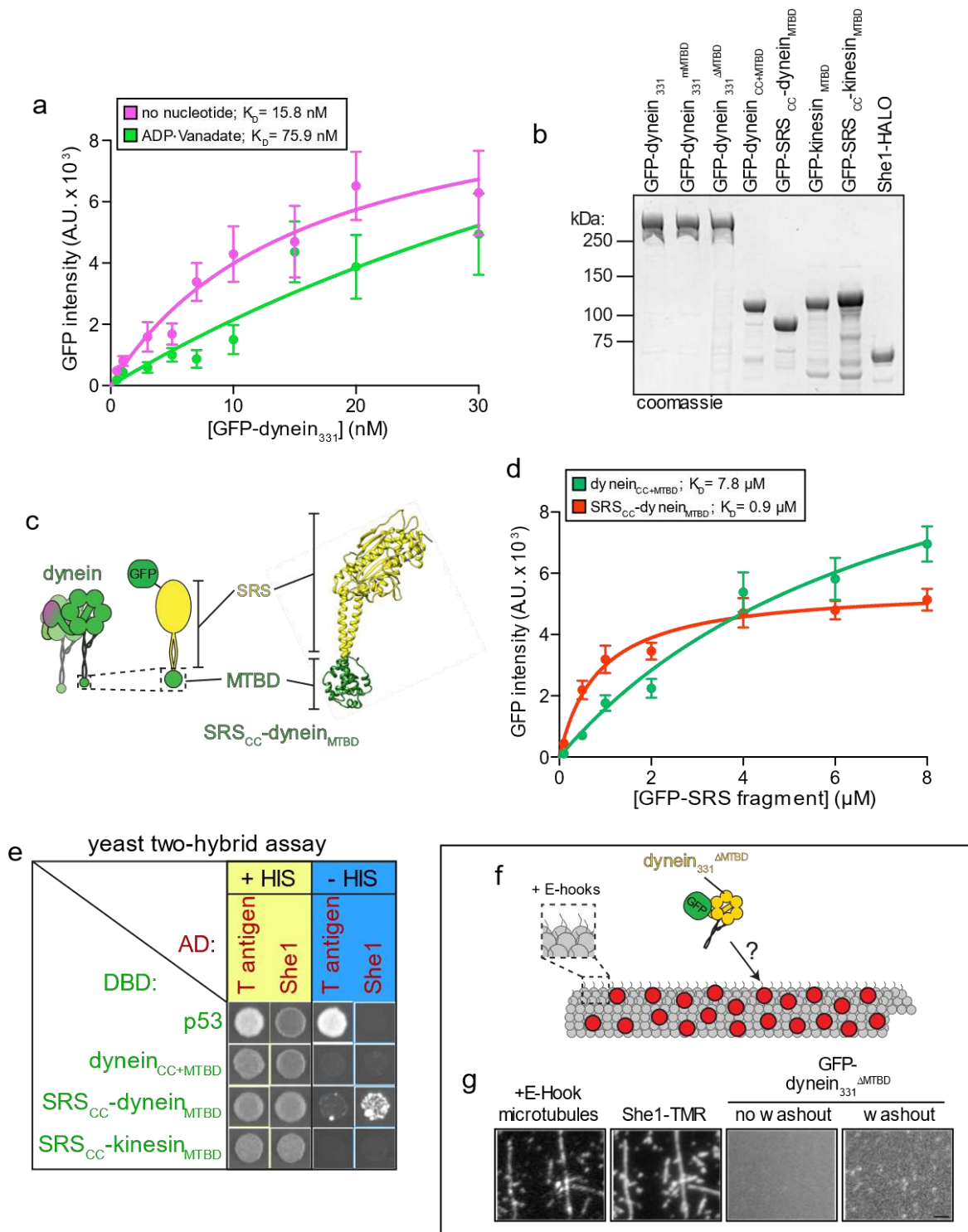


**Figure A1.3. Characterization of recombinant fragments used in the recruitment assays, and two-hybrid data.** (a) Mean fluorescence intensity values (along with standard deviations) of microtubule-bound monomeric GFP-dynein<sub>331</sub> in the absence (magenta) or presence of ATP and vanadate (green). (b) Recombinant protein fragments used in the recruitment assays. With

the exception of the dynein motor domain fragments, which were purified from yeast, all proteins were purified from *E. coli* (see Methods). (c) Cartoon representation and reconstructed structural model of the SRS<sub>CC</sub>-dynein<sub>MTBD</sub> fusion. Image was generated from a yeast model of the *DYN1* MTBD (threaded into 3ERR; Carter et al., 2008) and 1SRY (Fujinaga et al., 1993). (d) Mean fluorescence intensity values (along with standard deviations) of microtubule-bound GFP-SRS<sub>CC</sub>-dynein<sub>MTBD</sub> (red) and GFP-dynein<sub>CC+MTBD</sub> (green;  $n \geq 19$  microtubules, and  $\geq 151 \mu\text{m}$  of MT length for each condition) along with fits and resulting dissociation constants ( $K_D$ ). (e) Two-hybrid assay demonstrating an interaction between dynein<sub>MTBD</sub> and She1 (see Methods). (f) Schematic representation of the experimental setup used for panel g. (g) Representative images depicting the inability of microtubule-bound She1 to recruit GFP-dynein<sub>331 $\Delta$ MTBD</sub> to microtubules. Images were acquired prior and subsequent to washing the chamber with motility buffer (see Methods; scale bar, 1  $\mu\text{m}$ ).

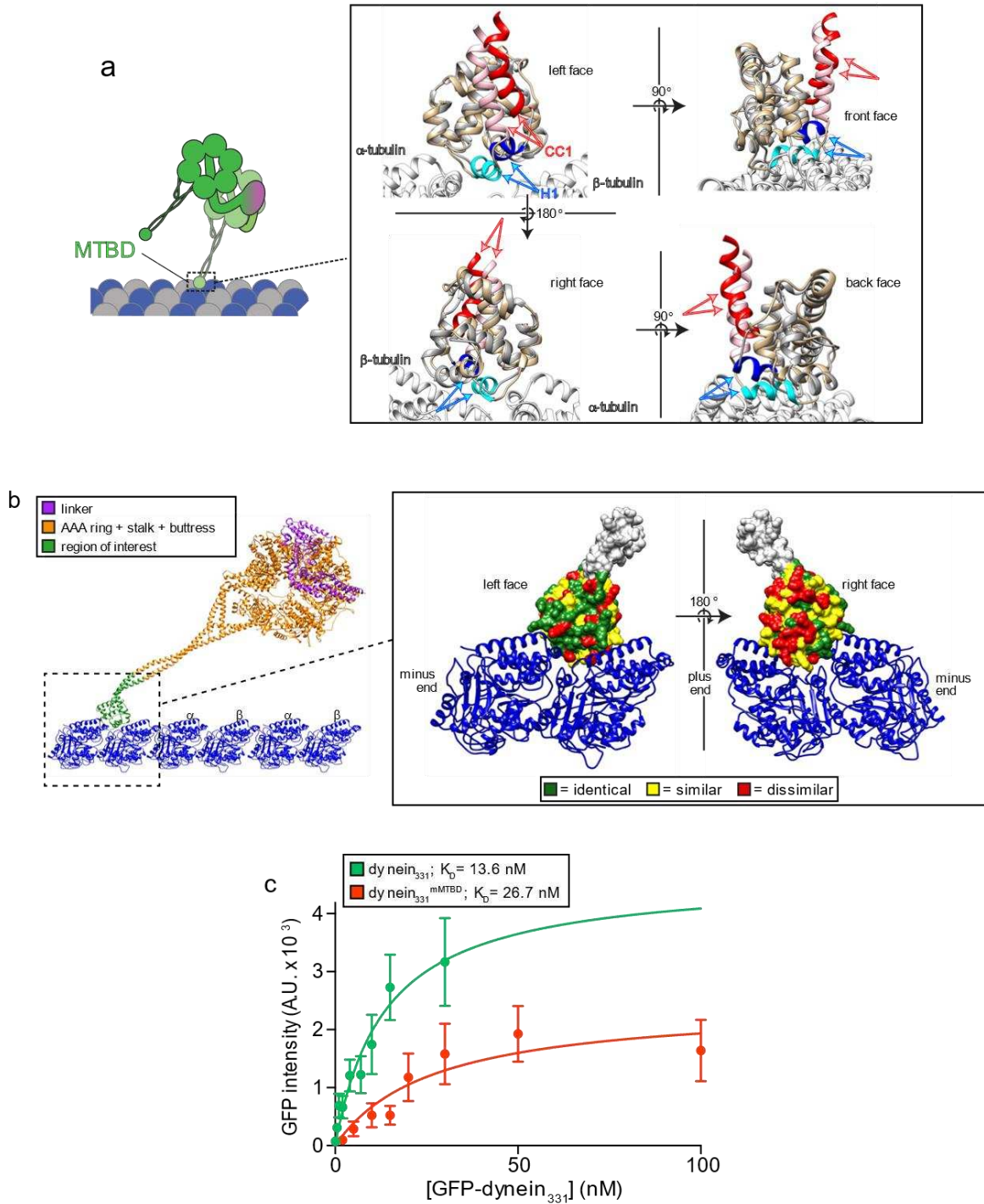


**Figure A1.4. Comparison of various dynein MTBDs.** (a) Cartoon and homology models of the yeast dynein MTBD bound to  $\alpha$  and  $\beta$ -tubulin in the high (grey) and low (tan) microtubule affinity states. The models were generated using one-to-one threading of the yeast *DYN1* sequence into 3J1T (Redwine et al., 2012; high affinity) and 3J1U (low affinity). CC1 and H1, which exhibit the largest differences between the two structures, are depicted as follows: CC1, red and pink, for high and low affinity states; H1, blue and cyan, for high and low affinity states,

respectively. (b, left) Crystal structure of human dynein-2 (4RH7) docked onto microtubules (from 3J1T). (right) Homology model of the yeast MTBD (colored) – along with a short region of the CC (grey) – bound to  $\alpha$  and  $\beta$ -tubulin in the high microtubule affinity state. The residues are colored to reflect the degree of conservation between yeast and mouse primary sequence (see legend). (c) Mean fluorescence intensity values (along with standard deviations) of microtubule-bound GFP-dynein<sub>331</sub> (green) and GFP-dynein<sub>331</sub><sup>mMTBD</sup> (red;  $n \geq 15$  microtubules, and  $\geq 68 \mu\text{m}$  of MT length for each condition) along with fits and resulting dissociation constants ( $K_D$ ). Note the differences in apparent  $B_{\text{max}}$  values ( $4645 \pm 763$  A.U. for wild-type, and  $2452 \pm 517$  A.U. for mMTBD;  $\pm$  SE of fit) are likely a consequence of microtubule unbinding during the chamber washes (see Methods), and likely differences in microtubule dissociation rates between the two motor domains.



motors for each condition). Data were fit as previously described (Reck-Peterson et al., 2006). (c and d) Mean run length (c) and dwell time (d) for GST-dynein<sub>331</sub><sup>mMTBD</sup> in the presence of the indicated concentration of She1 (error bars, standard error). Dashed line indicates the mean run length or dwell time for wild-type (WT) GST-dynein<sub>331</sub> in the absence of She1.

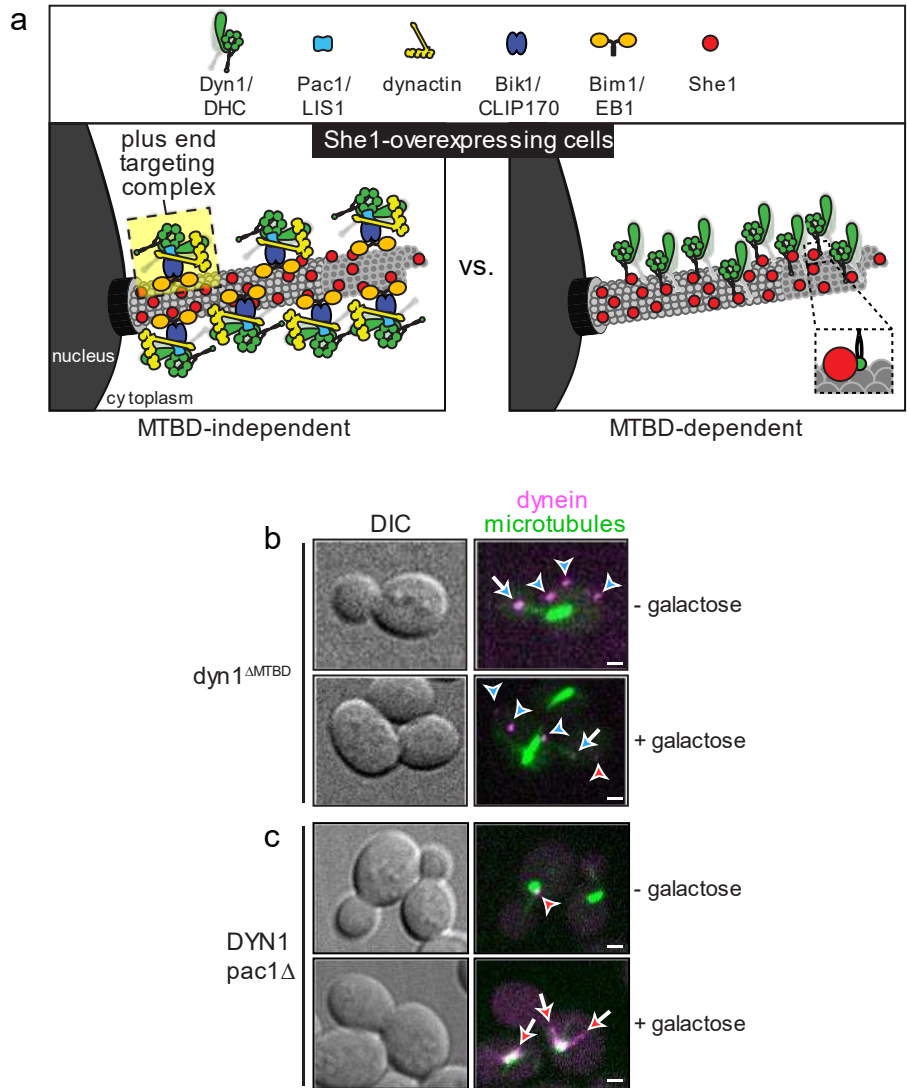


**Figure A1.6. Dynein relocalization to astral microtubules upon She1 overexpression requires the dynein MTBD, but not Pac1.** (a) Cartoon representation of the two possible models to account for dynein relocalization upon She1 overexpression. The model on the left depicts a mechanism whereby the entire plus end targeting complex (composed of Dyn1, Pac1, Bik1 and Bim1; note that dynactin is not an obligate component of this complex; Lee et al., 2003) is required for the relocalization. Given the dispensable nature for the MTBD in plus end targeting (Lammers et al., 2015), this would indicate an MTBD-independent mechanism. The model on the right depicts a mechanism whereby dynein microtubule binding activity via the MTBD is required. (b and c) Representative images of *GAL1p:SHE1* cells expressing mTurquoise2-Tub1 (b), or mRuby2-Tub1 (c), and either Dyn1<sup>ΔMTBD</sup>-3YFP (b) or Dyn1-3GFP (c), the latter of which is deleted for *PAC1*. Cells were grown to mid-log phase in SD media supplemented with raffinose (uninduced; “- galactose”) or galactose plus raffinose (induced for 3.5 hours; “+ galactose”) and then mounted on agarose pads for confocal fluorescence

microscopy. Foci were identified in two-color movies and scored accordingly (see Methods; blue arrows, plus end foci; blue arrowheads, cortical foci; red arrowhead, dynamic cytoplasmic foci not associated with microtubules or spindle poles). Note the accumulation of Dyn1 near the spindle poles in *pac1Δ GAL1p:SHE1* cells grown in galactose-containing media (the same was observed in *GAL1p:SHE1 PAC1* cells; not shown). Movies reveal these spots exhibit dynamic movements in a manner that is consistent with them localizing to short astral microtubules, and not the spindle poles themselves. Note that our data support the MTBD-dependent model, depicted in panel a, right.

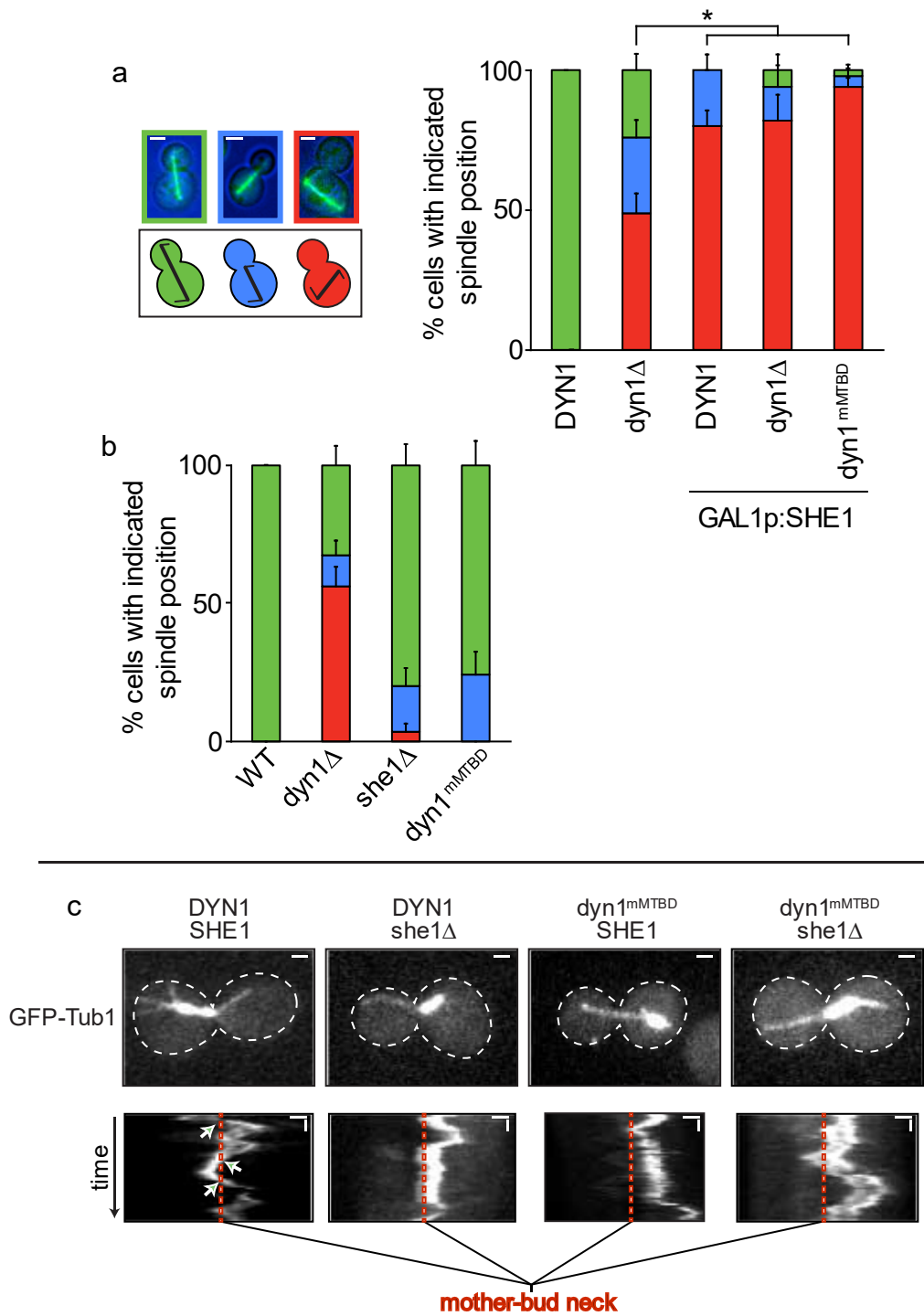


**Figure A1.7. *In vivo* assessment of dynein<sup>mMTBD</sup> mutant function.** (a and b) The percentage of cells with the indicated spindle orientation phenotype (green, normal; blue, aligned along mother-bud axis, but not through the neck; red, improperly aligned) is plotted for the indicated yeast strains (WT, wild-type). Anaphase spindles were visualized using mRuby2-Tub1 ( $\alpha$ -tubulin). Strains were imaged after growth to mid-log phase in SD media supplemented with

either (a) 2% galactose, or (b) 2% glucose, the former of which induces overexpression of She1 in *GAL1p:SHE1* cells (scale bars, 2  $\mu\text{m}$ ; error bars, standard error of proportion;  $n \geq 17$  and  $n \geq 21$  anaphase spindles for each strain in panels a and b, respectively). Note the higher prevalence of misoriented spindles in She1-overexpressing cells (*GAL1p:SHE1*) than in cells lacking dynein (*dyn1 $\Delta$* ; \*,  $p \leq 0.015$ ). This suggests that She1-overexpression disrupts other non-dynein-mediated spindle orientation processes (e.g., Kar9 pathway; Markus et al., 2012). (c) Representative fluorescence images of *kar9 $\Delta$* , hydroxyurea (HU)-arrested GFP-Tub1 ( $\alpha$ -tubulin) expressing cells with the indicated *SHE1* and *DYN1* alleles (scale bars, 1  $\mu\text{m}$ ), along with kymographs depicting spindle movements over time (horizontal scale bars, 1  $\mu\text{m}$ ; vertical scale bars, 1 min). Dashed lines indicate the position of the bud neck in each example. Note the frequency with which the spindle traverses the bud neck in wild-type, but not mutant cells (green arrows; see Fig. 2.7g for quantitation). P-values were calculated using a two-tailed unpaired *t* test.

## APPENDIX 2

### A GLYCINE TO ARGININE MUTATION IN TUB1 POSITION 437 COMROMISES SHE1 BINDING<sup>2</sup> AND REVEALS NEW INSIGHT INTO $\alpha$ -TUBULIN ISOFORMS

#### A2.1 INTRODUCTION

##### A2.1.1 A glycine to arginine substitution in $\alpha$ -tubulin with reduced *She1* binding

*S. cerevisiae*, or budding yeast, has been a popular model system for understanding eukaryotic cell biology due to the ease of which you can apply classical genetic manipulation, and the similar, yet simple, biological processes they share. Nearly 31% of protein-encoding genes of yeast share sequence homology with mammalian genomes, and this number does not represent the greater degree of functional homology between mammalian and yeast proteins (Botstein et al., 2011; Botstein et al., 1988). In mammalian cells, understanding the molecular basis of how tubulin mutations lead to disease in humans is complicated by existence of nine isotypes of  $\alpha$ -tubulin. Additionally, mutagenesis in human cell culture is no simple task. Contrarily, budding yeast presents as an excellent model system to begin investigating the molecular mechanism behind tubulin mutations, specifically because there exists only two  $\alpha$ -tubulin (TUB1 and TUB3) and one  $\beta$ -tubulin (TUB2), and as mentioned previously, yeast is easy to manipulate genetically.

A single *de novo* heterozygous glycine to arginine substitution in the  $\alpha$ -tubulin gene TUBA1A at positioned 436 was previously reported in a patient with severe microcephaly (Bahi-Buisson et al., 2008). The predominant  $\alpha$ -tubulin isoform in humans, TUBA1A, shares ~75%

<sup>2</sup>This appendix references data from an incomplete manuscript that has not been published and has not yet passed peer review. The data presented in this appendix include my contribution to the unpublished work, but has been changed to fit this dissertation.

Suggested reference:

Denarier E., Ecklund K.H., Berthier G., Poitevin, M., Favier, A., Gory, S., De Macedo L., Delphin, C., Andrieux A., Markus, S.M. and Boscheron C. Modeling disease-correlated TUBA1A mutation in budding yeast reveals a molecular basis for tubulin dysfunction.

protein sequence identity with yeast TUB1, including a terminal glycine that is only one amino acid position different in yeast (at position 436, instead of 437), making it an excellent candidate with which to study the overall phenotypic effects of this mutation in yeast. We sought to understand the consequences of the G436R (437 in yeast) mutation in a budding yeast system by replacing the endogenous TUB1 locus with a tub1-G437R mutant allele. In summary, the tub1-G437R mutation leads to increased dynein-mediated sliding events and defects in spindle positioning that are reminiscent of what is seen in *she1* $\Delta$  cells (Denarier et al., see footnote<sup>2</sup> and Chapter 3). From this new insight, it was confirmed that She1 binding to tub1-G437R was disrupted by yeast-2-hybrid *in vivo* and in a peptide competition assay *in vitro* (Denarier et al., see footnote<sup>2</sup>). The question remained if She1 binding was disrupted in the context of polymerized microtubules *in vivo*. We sought to answer this question using fluorescence microscopy techniques to visualize She1 on spindle microtubules, where She1 localization is most prominent *in vivo*.

### **A2.1.2 $\alpha$ -tubulin isoforms**

In budding yeast, there are only 2 isotypes of  $\alpha$ -tubulin. (1) TUB1, which is likely the most abundant and important  $\alpha$ -tubulin, is located on chromosome 13 along with its paralog (2) TUB3, which likely arose from a whole genome duplication event (Schatz et al., 1986b; Bode et al., 2003). Though their protein sequences share ~91% identity, microtubules composed of only Tub1 heterodimers exhibited greater dynamicity compared to microtubules containing only Tub3 heterodimers *in vitro*. Interestingly, their residue differences are located on the outer surface, 12 of which are charge reversals (Bode et al., 2003). Yeast cells are inviable without the predominant  $\alpha$ -tubulin TUB1 but can survive without the lesser isoform TUB3 (Schatz et al., 1986a). This supports evidence that the ratio of TUB1 and TUB3 in budding yeast is ~70-90% TUB1 and ~30%-10% TUB3 (Schatz et al., 1986b; Bode et al., 2003; Gartz-Hanson et al., 2016). We present here preliminary evidence that this ratio may be closer to ~50% TUB1 and ~50% TUB3, based on western blotting and spindle-microtubule incorporation.

## A2.2 RESULTS

### A2.2.1 *She1 binding the G437R containing microtubules is reduced*

The G437R mutation is located at the base of the last C-terminal alpha-helix of  $\alpha$ -tubulin, just proximal to the disordered C-terminal tail (CTT; Fig A2.1a). The CTTs of tubulin are required for She1 binding, presenting many interesting possibilities to how this mutation could disrupt binding (Fig. 2.3c; Markus et al., 2012). To understand tub1-G437R disrupts She1 binding to assembled microtubules *in vivo*, we measured the fluorescence intensity of She1 localization to spindle microtubules, where She1 fluorescence is brightest, in TUB1 and tub1-G437R cells. She1 was fused to seven self-assembling GFPs and microtubules were visualized with mRuby2 (see Methods). We saw ~1.2-fold reduction in She1 fluorescence on spindle microtubules containing tub1-G437R, consistent with the yeast-2-hybrid *in vivo* and *in vitro* peptide binding results (Fig A2.1 b, GFP<sub>11x7</sub>-She1, and c). However, we also saw ~0.8-fold decreased spindle incorporation of mRuby2-tub1-G437R conjunctly with ~0.9-fold increased incorporation of mRuby2-Tub3 in tub1-G437R mutant cells (Fig A2.1 a, mRuby2-tub1 and mRuby2-tub3, d and e), indicating that Tub3 can compensate for the reduced capacity of tub1-G437R to incorporate into spindle microtubules. In light of this, we reasoned that the reduced She1 recruitment to spindle microtubules in the tub1-G437R mutant could alternatively be explained by She1 having a reduced binding affinity to Tub3. She1 has been shown to require the disordered C-terminal tails (CTTs) of microtubules to bind and Tub3 has two residues, glutamic acids, missing in its CTTs that is present on Tub1. Perhaps these two residues compromise She1's ability to bind Tub3. Test if She1 has reduced binding to Tub3 *in vivo*, we needed to measure She1 fluorescence on spindle microtubules whose  $\alpha$ -tubulin content is composed of only Tub3. To do this, we overexpressed Tub3 using a constitutively active promoter in a tub1 $\Delta$  mutant background (tub1 $\Delta$  cells are inviable, yet can be rescued by overexpressing Tub3, see Methods; Schatz et al., 1986b). Incidentally, we did not see reduced She1 fluorescence on Tub3-only containing spindle microtubules, in contrast, we saw increased

She1 binding, indicating that the reduced She1 binding on tub1-G437R containing spindle microtubules is likely due to the tub1-G437R mutant and not Tub3 (Fig A2.1f). Note however that we could not correct for microtubule density in these cells (mRuby2-Tub3 was not incorporated into the spindle of Tub3 overexpressing cells), so the increased She1 binding may be a consequence of increased microtubule density, not a higher affinity of She1 for Tub3. To assess spindle morphology, we will use electron-microscopy techniques in the near future.

The ~0.8-fold decrease in incorporation of tub1-G437R into spindle microtubules (Fig A2.1d) led us to wonder if the tub1-G437R mutant expression was compromised. An arginine substitution places a large, positively charged side chain in place of a small, nonpolar glycine. Though it seemed unlikely that a single point mutation located at the surface of  $\alpha$ -tubulin would be severe enough to compromise the integrity of the tubulin structure, this hypothesis was supported by our inability to purify recombinant tub1-G437R mutant over-expressed from a selectable plasmid in conjunction with wild-type Tub2 – a purification process that was successful in purifying functional, wild-type Tub1 and Tub2 heterodimers (see Appendix 5). Additionally, in genetic studies we saw a reliance of the tub1-G437R mutation on Tub3, which is dispensable in a wild-type TUB1 cells, also suggesting a problem with the mutant tubulin (Denarier et al, see footnote<sup>2</sup>). To determine if the decreased incorporation was due to compromised expression levels, we performed a western blot to detect  $\alpha$ -tubulin content in TUB1 and tub1-G437R cells, including a tub3 $\Delta$  strain to approximate the levels of Tub1 (see Methods). We saw a decrease in total  $\alpha$ -tubulin in tub1-G437R cells, supporting the notion that tub1-G437R expression is slightly compromised (Fig A2.2a, total  $\alpha$ -tubulin in tub1-G437R/TUB3 decreased ~30% when compared to wild-type TUB1/TUB3). This result may explain the reduction of tub1-G437R mutant incorporation into spindle microtubules. We noted that since the total  $\alpha$ -tubulin content in these cells was reduced (despite Tub3 compensation in spindle microtubules), some of the phenotypes we saw previously, including changes in microtubule dynamics, (Denarier et al., see footnote<sup>2</sup>), may be due to a loss of overall  $\alpha$ -tubulin in the cell.

Testing these hypotheses through different avenues may be necessary. Specifically, EM-tomography of the yeast spindles to assess morphological changes in TUB1 and tub1-G437R cells may elucidate any possibility that spindle density is compromised due to this mutation.

### ***A2.2.2 $\alpha$ -tubulin isoforms exhibit equal incorporation into mitotic spindle microtubules***

It has been widely accepted that Tub1 makes up ~90-70% whereas Tub3 makes up ~10-30% of total  $\alpha$ -tubulin content in budding yeast (Schatz et al., 1986b; Bode et al., 2003; Gartz-Hanson et al., 2016). Our results showing that the ~0.8-fold drop tub1-G437R spindle incorporation coinciding with a nearly identical increase in Tub3 incorporation led us down the path that eventually led us to question the validity of this widely accepted claim. Specifically, the ratio of Tub1 to Tub3 in our western blot was ~1:2, respectively, which directly contrasts previously published work (Fig A2.2 TUB1/TUB3 versus TUB1/tub3 $\Delta$ ). However, it is important to highlight that our contrasting results may simply be due to differences between extraction methods, or antibodies, but it may also be due to strain differences, which still contrasts the idea that Tub1 is the most prominent  $\alpha$ -tubulin isotype. In line with this reasoning, we wondered if our mRuby2 tagged  $\alpha$ -tubulin genes, which are incorporated into the LEU or TRP locus through homologous recombination of a transformed plasmid (see Methods), displayed varying brightness, meaning we could not directly compare mRuby2-Tub1 and mRuby2-Tub3 signals. To this end, we measured the fluorescence intensity of mRuby2-Tub1 and mRuby2-Tub3 spindles using the same imaging exposures and using three different isolates from the same plasmid transformation (see Methods). In this experiment, cells retain the endogenously expressed Tub1, Tub3, and/or tub1-G437R in addition to one copy of an mRuby2-tagged  $\alpha$ -tubulin under a HIS promoter (see Methods). We saw no significant difference in the fluorescent intensity of mRuby2-Tub1 and -Tub3 isolates at spindles, suggesting that mRuby2 signals are directly comparable. Consistent with previous results, incorporation of the two isotypes into spindle microtubules is ~50/50 (Fig A2.2b, mRuby2-tub1 versus mRuby2-tub3), further suggesting there is equal incorporation of Tub1 and Tub3 heterodimers. Finally, consistent with

prior results, mRuby2-Tub3 compensated for loss of mRuby2-tub1-G437R incorporation into spindle microtubules (Tub1 signal dropped by ~ 3.5 A.U. while Tub3 signal increased ~2.7 A.U.). Taken together, our findings indicate the possibility that the two  $\alpha$ -tubulin isotypes may be represented equally within yeast cells.

### **A2.3 DISCUSSION & FUTURE DIRECTIONS**

One interesting note to consider is that tub1-G437R microtubules exhibited greater dynamicity than wild-type Tub1 in G2/M phase *in vivo* (Denarier et al., see footnote<sup>2</sup>) and also incorporated more mRuby2-Tub3 heterodimers into spindle microtubules (Fig A2.1e). Isotype composition has been shown to play a role in the dynamics of microtubules, specifically, yeast cells with Tub1 as their only  $\alpha$ -tubulin are more sensitive to microtubule destabilizing drugs, and *in vitro* microtubules composed of only Tub1 heterodimers exhibit more dynamicity than microtubules composed of only Tub3 heterodimers (Bode et al., 2003), suggesting Tub3 heterodimer may inhibit microtubule dynamics *in vivo*. Given that tub1-G437R exhibited greater dynamicity in G2/M yet also incorporated more Tub3 into HU arrested microtubules – which should theoretically offset some of the dynamicity induced by tub1-G437R incorporation – we suspect that tub1-G437R may have a more substantial impact on microtubule dynamics than our studies suggest, indicating that tub1-G437R heterodimers may be incapable of forming microtubules alone (hence the Tub3 reliance; Denarier et al., see footnote<sup>2</sup>). It is unknown if effect on microtubule dynamics in this mutant is due to intrinsic changes to the properties of the polymer or if it is due to loss of She1 binding (two scenarios which are not necessarily mutually exclusive). To determine if the change in microtubule dynamics is due to one, or even both, of these explanations, it would be beneficial to do *in vitro* molecular dynamics assays with recombinant mutant. Unfortunately, attempts to purify tub1-G437R have been unsuccessful. An alternative approach would be to use yeast cell lysates with which to measure microtubules dynamics *in vitro*, a method that has been recently described (Bergman et al., 2018). Clearly,

tub1-G437R mutants rely on Tub3 to survive, implying that this mutation leads to severe defects that are not entirely due to loss of She1. If tub1-G437R is lethal as a consequence of tub1-G437R heterodimers being incapable of forming microtubules (therefore relying on the increased stability of Tub3 heterodimers), then the lethality of tub3 $\Delta$  may be rescued by the overexpression of microtubule stabilizing factors, such as Stu2, or the removal of catastrophe inducing factors (Podolski et al., 2014; Estrem et al., 2017). It is also worth determining if the introduction of EpoB might partially rescue some of the phenotypes seen in tub1-G437R cells. This would also elucidate if any of the effects are due to loss of She1 binding or are due to the inherent properties of the heterodimer.

Though the mechanism behind how this mutation leads to decreased She1 binding is unknown, its close proximity to the disordered C-terminal tails may give logical insight. It is reasonable to suggest that putting a large positively charged molecule at the base of a negatively charged, disordered region may have dramatic consequences on the dynamic nature of the CTTs. The diverse conformational ensemble of disordered proteins (such as CTTs) has been proposed to be critical for cellular function, especially to accommodate binding to multiple different partners, such as She1 (reviewed in Guhharoy et al., 2013; Tompa., 2011; Parker et al., 2018; Fees et al., 2011). Also, it has been hypothesized that the CTTs interact with the tubulin body of adjacent dimers which may provide a stabilizing force on growing microtubule protofilaments (Wall et al., 2016; Bouxsein et al., 2014). This interaction could be modulated by MAPs interacting with CTTs or vice versa – regulate MAP binding to the microtubule lattice, which may be compromised in the case of tub1-G437R. It is possible that this mutation leads to not only abrogated She1 binding, but also impaired binding of other MAPs and associated factors which interact with microtubule C-terminal tails (Aiken et al., 2014; Sirajuddin et al., 2014; Lacroix et al., 2010).

Microtubule dynamicity in tub1-G437R cells changed significantly only in the G2/M phase of the cell cycle, and not G1 (Denarier et al., see Footnote<sup>2</sup>). This could arguably be a

case of differential MAP binding in a cell-cycle dependent manner, which in this scenario, suggests that She1 is critical for stabilizing microtubule dynamics during mitosis, but does not play a role in microtubule stability during G1, and that the tub1-G437R mutation does not inherently lead to any microtubule defects. Alternatively, there could be a microtubule stabilizing factor responsible for maintenance and stability of G1 microtubules that is not disrupted by the tub1-G437R mutation. The fact that  $\alpha$ -tubulin isotypes possess differing properties in growing protofilaments, suggests a mode by which cells can regulate microtubule dynamics through tubulin isotypes. The lack of change in G1 microtubule dynamics in tub1-G437R mutants may reveal differential incorporation of tubulin isoforms in a cell cycle dependent manner. In this scenario, the reason we saw no significant change in dynamicity in G1 was due to tubulin isotype composition of microtubules, indicating Tub3 is the predominant G1  $\alpha$ -tubulin. Microtubule dynamics in yeast cell extracts have been shown to vary between stages of the cell cycle, suggesting these properties are cell cycle regulated (Bergman et al., 2018). Though this is likely due to activity of different MAPs and microtubule factors, it is still an interesting possibility. Either way, a cell cycle investigation of mRuby2-Tub1 and mRuby2-Tub3 incorporation into microtubules may prove to be interesting.

## **A2.4 METHODS**

### ***A2.4.1 Plasmid and strain construction***

Strains used in this study were YEF473 (Bi et al., 1996; *ura3-52 lys2-801 leu2- $\Delta$ 1 his3- $\Delta$ 200 trp1- $\Delta$ 63*). The TUB1 integrating plasmid, pCR2-TUB1 consists of the region of the TUB1 locus from the intron (situated close the 5' end of the gene) to 385 bp after the stop codon cloned into the pCR2 vector (Invitrogen). The HIS3 gene expression cassette was ligated into the BsrGI site within the 3' untranslated region of the TUB1 sequence within pCR2 (pCR2-TUB1). The G437R mutation was subsequently introduced into pCR2-TUB1 by PCR, generating pCR2-tub1<sup>G437R</sup>. For integration into the native TUB1 locus, pCR2-TUB1 (either wild-type or

mutant) was digested with SphI, transformed into yeast using the lithium acetate method, and transformants were selected on media lacking histidine. Transformants were confirmed by PCR and sequencing.

We generated pHIS3p:*mRuby2-tub1<sup>G437R</sup>+3'UTR::LEU2* to visualize microtubules in mutant cells. To this end, we engineered the G437R point mutation into pHIS3p:*mRuby2-TUB1+3'UTR::LEU2* (Markus et al., 2015) using traditional molecular biological methods. For comparison of relative  $\alpha$ -tubulin incorporation into mitotic spindles, we used yeast strains with similarly integrated mRuby2- $\alpha$ -tubulins (pHIS3p:*mRuby2-TUB1+3'UTR::LEU2*, or pHIS3p:*mRuby2-tub1<sup>G437R</sup>+3'UTR::LEU2*). To assess incorporation of Tub3 into the mitotic spindle, we replaced the *TUB1+3'UTR* cassette in pHIS3p:*mRuby2-TUB1+3'UTR::TRP1* (Markus et al., 2015) with the *TUB3* genomic sequence, including 150 bp of the 3'UTR. This plasmid, pHIS3p:*mRuby2-TUB3+3'UTR::TRP1*, was digested with BbvCI, transformed into yeast using the lithium acetate method, and transformants were selected on media lacking tryptophan. To visualize She1 on microtubules we used a method involving self-assembling fragments of GFP. A PCR product containing seven GFP strand-11s in tandem and ending in a short GSGS linker and specificity to the upstream region of the SHE1 locus was amplified. The PCR product was transformed to replace a URA upstream of the SHE1 locus and selected by the 5-FOA method. A PCR product corresponding to TEF1p:GFP strands 1-10::TRP were amplified from pACUH:GFP11x7:mCherry-beta-Tubulin (Cabantoud et al., 2005). The PCR product was transformed with selection on -TRP plates. For assessment of She1 on Tub3 only containing spindles, we constructed pTEF1p:TUB3+3'UTR::URA. PCR products corresponding to TEF1p and TUB3+3'UTR were amplified and assembled by isothermal assembly (Gibson et al., 2009) into plasmid pBJ090 digested with LpnI/NotI (Longtine et al., 1998). pTEF1p:TUB3+3'UTR was digested with Apal and transformed in diploid TUB1/tub1 $\Delta$ ::HPH strains for integration into URA locus. Diploids were subsequently sporulated to obtain TEF1p:TUB3+3'UTR::URA in a haploid tub1 $\Delta$ ::HPH background. The haploid strain was mated

and subsequently sporulated to obtain TEF1p:TUB3+3'UTR::URA with GFP<sub>11x7</sub>-She1 TEF1p:GFP1-10::TRP1 to visualize She1.

#### **A2.4.2 Live cell imaging experiments**

For spindle intensity measurements, cells were arrested with hydroxyurea (HU) for 2.5 hours to enrich for metaphase spindles, and then mounted on agarose pads containing HU for fluorescence microscopy. 11 Z-planes with 0.3  $\mu\text{m}$  spacing were captured using 2x2 binning (the exposure time varied between constructions). We measured background-corrected She1, Tub1, or Tub3 spindle-localized fluorescence from maximum intensity projections using ImageJ (NIH). Images were collected on a Nikon Ti-E microscope equipped with a 1.49 NA 100X TIRF objective, a Ti-S-E motorized stage, piezo Z-control (Physik Instrumente), an iXon DU888 cooled EM-CCD camera (Andor), and a spinning disc confocal scanner unit (CSUX1; Yokogawa) with an emission filter wheel (ET525/50M for GFP and ET632/60M for mRuby2; Chroma). 488 nm and 561 nm lasers (housed in a LU-NV laser unit equipped with AOTF control; Nikon) were used to excite GFP and mRuby2, respectively. The microscope was controlled with NIS Elements software (Nikon).

#### **A2.4.3 Yeast cell lysis and western blotting**

Untagged versions of TUB1, tub1-G437R, and tub3 $\Delta$  were used in western blotting (see Plasmid and strain construction). For western blotting, yeast cells were grown overnight at 30 degrees Celsius and diluted the next morning in 3 mL fresh SD-complete media containing 2% glucose. Cells were left to grow for several hours before harvested prior to the stationary phase densities (OD600 < 1.0). Cell pellets were resuspended in 0.2 mL of 0.1 M NaOH and incubated for 10 minutes at room temperature as described in (Kushnirov et al., 2000). Following centrifugation, the resulting cell pellet was resuspended in 200  $\mu\text{L}$  sample buffer. Equal amounts of total cell lysate (as determined by UV A600) were loaded into each lane, transferred to PVDF and blocked with BSA before probing with monoclonal 4A1 antibody (at 1:100; DSHB) followed by goat anti-mouse IRDye<sup>R</sup>700 antibody (at 1:10,000; licor). Electroblothing to PVDF

was performed in 25 mM Tris, 193 mM glycine supplemented with 0.05% SDS and 20% methanol. Near-infrared 700 signal was acquired on an Odyssey CLx with solid-state laser diode (685 nm laser; licor). ImageJ software was used to quantify blots from raw integrated density of bands and background corrected.

#### ***A2.4.4 Statistical analysis***

P-values were calculated using a two-tailed unpaired t test using Graphpad Prism software. Columns depict the means and error bars represent the standard deviations. Diamonds are described in the figure legends.

### **A2.5 FIGURES**

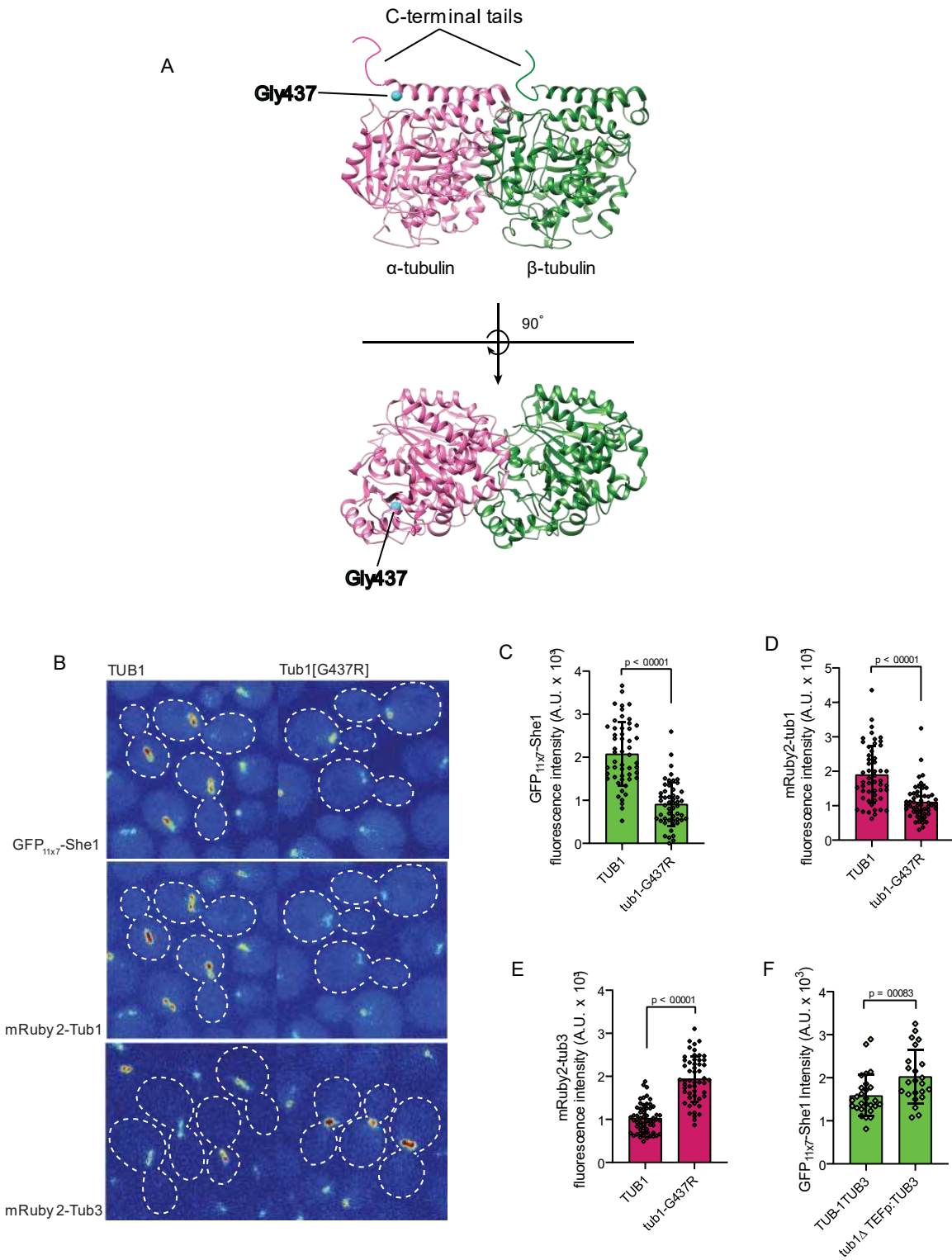


**Figure A2.1 Tub1-G437R mutant has reduced She1 binding *in vivo*.** (a) 3.7Å EM of yeast tubulin polymerized with GTP *in vitro* (PDB: 5W3F, Howes et al., 2017). Side eye view (top) shows  $\alpha$ -tubulin (left, pink) and  $\beta$ -tubulin (right, green) with a 90° rotated to a bird's eye view

(bottom). The Glycine 437 residue has been highlighted by a sphere (cyan). Note the closeness of the G437 to the C-terminal tail of  $\alpha$ -tubulin. (b) Fluorescence microscopy images showing in heat map form signal of GFP<sub>11x7</sub>-She1, mRuby2-tub1, mRuby2-tub1-G437R or mRuby2-Tub3 in Tub1 or tub1-G437R backgrounds. Red indicates higher fluorescence intensities. (c) Quantification of GFP<sub>11x7</sub>-She1 fluorescence intensity on the spindle in either Tub1 or tub1-G437R cells. (d) Quantification of mRuby2-tub1 or mRuby2-tub1-G437R fluorescence intensity on the spindle in either Tub1 or tub1-G437R (respectively). (e) Quantification of mRuby2-tub3 fluorescence intensity on the spindle in either Tub1 or tub1-G437R. (f) Quantification of GFP<sub>11x7</sub>-She1 fluorescence intensity on the spindle in TEFp-Tub3 background. Note that these cells are tub1 $\Delta$ , therefore the spindle contains only Tub1 heterodimers (see Methods). (c-f) Diamonds represent one spindle measurement. Errors bars are equal to the standard deviations and columns are equal to the mean of the dataset. n = 2 replicates  $\geq$  20 cells each or  $\geq$  10 cells for TEFp-Tub3. P-values calculated from Welch's t test.

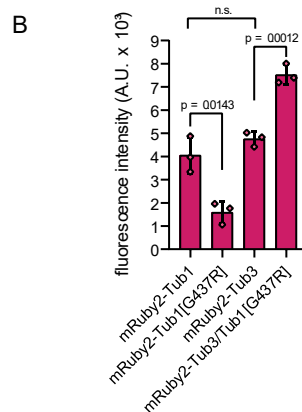
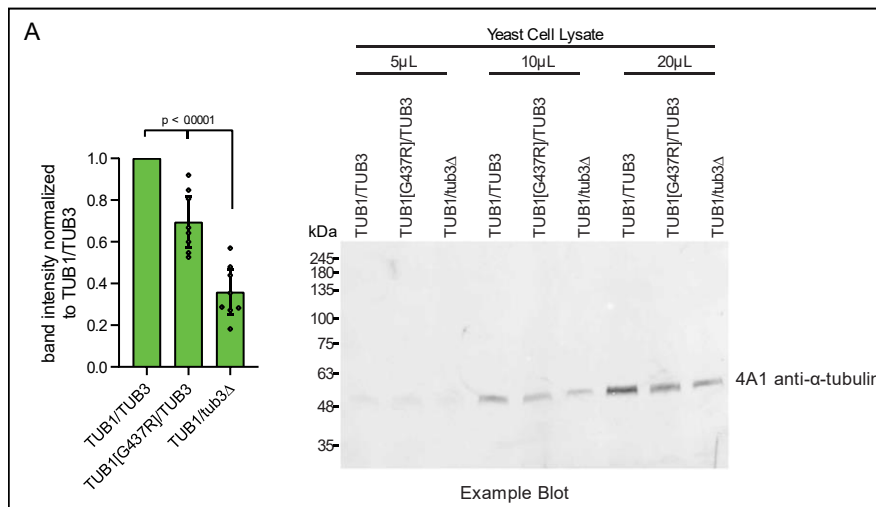


**Figure A2.2 Tubulin isoforms Tub1 and Tub3 exhibit comparable expression and spindle microtubule incorporation *in vivo*.** (a) Western blot of yeast cell extracts using 4A1 mouse anti- $\alpha$ -tubulin primary antibody and IR700 rabbit-anti-mouse secondary antibody with

quantification on the left. Three loading amounts were used to assess ideal conditions for blotting. Quantitation is normalized to wild-type Tub1+Tub3 (n = 3 blots replicates, each loading amount was included to assess variance between blots; see Methods). Note the 30% drop in  $\alpha$ -tubulin in tub1-G437R and 40% subsequent drop in tub3 $\Delta$ , suggesting Tub3 makes up a significant portion of  $\alpha$ -tubulin. (b) Measurement of fluorescence intensity of various mRuby2-tubulin mutants in HU-arrested spindles (see Methods). Note the intensities of both mRuby2-Tub1 and mRuby2-Tub3 are statistically similar in wild-type cells.

## APPENDIX 3

### SYSTEMATIC INVESTIGATION INTO SHE1 BINDING DOMAINS

#### **A3.1 INTRODUCTION**

Our previous work demonstrated that She1 binds the microtubule binding domain of dynein, narrowing the binding region down to just 123 amino acids out of the large 500 kD motor domain. Similarly, the region of She1 binding on microtubules has been narrowed down to the C-terminal tails, possibly the CTT of  $\alpha$ -tubulin, and possibly including a C-terminal region proximal to the tail (Fig A2.1a; Markus et al., 2012). She1 is a 38 kDa protein, predicted to have a high degree of disorder (via FoldIndex). Most MAPs historically are considered to be highly disordered, since most do not form defined structures in solution. She1 is no exception to this rule, yet with many advances in cryo-EM, MAPs previously expected to be disordered form extended secondary structures that can bind microtubule surfaces and interact with other binding partners, for example tau and DCX (Kellogg et al., 2018; Shigematsu et al., 2018; Fourniol et al., 2010). The formation of secondary structure upon microtubule binding has allowed structural analysis of the microtubule binding regions of some MAPs. Additionally, many of these proteins' domain regions have been characterized through basic biochemical techniques. Though we are not in a position to throw She1 into any CryoEM experiments, we attempted to understand if it had functional domains that could be mapped, using a systematic, biochemical approach.

#### **A3.2 RESULTS**

##### ***A3.2.1 The N-terminus of She1 binds dynein***

Previous attempts to discern if She1 can interact with dynein in the absence of microtubules has been unsuccessful (Fig A3.1a and b). However, this may be explained by our

data showing that She1 cannot inhibit dynein activity *in vitro*, without binding microtubules. It may also be a consequence of the conditions we used. Either way, we wondered if we could narrow down regions on She1 that are binding domains for dynein and microtubules. To do this we made seven fragments of She1, that cover the complete sequence (Fig A3.2a). To test if any of these fragments interacted with the dynein microtubule binding domain, She1 fragments were fused with a transcriptional activation domain (GAL4-AD-She1). Our previously described SRS<sub>cc</sub>-dynein<sub>MTBD</sub> construct (see Chapter 2) was fused to a DNA-binding domain (GAL4-DBD-SRS<sub>cc</sub>-dynein<sub>MTBD</sub>). Yeast-2-hybrid was performed in cells with GAL4 reporter genes and under three separate conditions with varying degrees of stringency (1mM, 5mM 3AT, or adenine deficient plates) to evaluate all corresponding fragments, including a negative control (activation domain fused to T7 antigen, GAL4-AD-T7; see Methods). We observed positive interaction between our constructs by growth of yeast on plates lacking histidine. Unlike our co-pelleting assays, which displayed no interaction between dynein and She1 in solution, we observed positive interaction by yeast-2-hybrid. Interestingly, She1 fragment [1-112] had the strongest interaction with SRS<sub>cc</sub>-dynein<sub>MTBD</sub> and we also observed interaction with She1-[1-168], She1-[1-224], She1-[113-224], making a strong argument for She1 to bind dynein in an N-terminal region (Fig A3.2a). We did however see some degree of binding with all fragments, above the negative control. In contrast to this argument, She1-[1-168] was the poorest interactor, despite it encompassing a longer region than She1-[1-112]. And oddly, She1 full-length was one of the poorest interactors as well (Fig A3.2a), which could be interpreted in many ways, indicating that more information is needed to understand the binding between the dynein MTBD and She1.

### **A3.2.2 The C-terminus of She1 binds microtubules**

To determine regions necessary for microtubule binding and to determine the minimal region necessary to inhibit dynein motility *in vitro*, we purified recombinant She1-TMR fragments and tested their ability to bind microtubules and inhibit motility in single molecule assays *in vitro* (Fig A3.2b, see Methods). We were able to purify all fragments except for She1-[224-338] (Fig.

A3.2b). Consistent with another paper published around the same time, She1 binds microtubules with the C-terminal region (Fig. A3.2b ; Zhu et al., 2017), however, qualitatively, the longest C-terminal fragment (She1[169-338]) had the highest binding affinity (Fig. A3.2b), suggesting many residues, or several regions of the C-terminus, are required for microtubule binding. Interestingly, none of our fragments inhibited dynein velocity as potently as full-length She1. This is consistent with the idea that the N-terminus is important for She1 binding to the dynein MTBD, moreover, the only fragments that induced subtle inhibition contain a partial region of the N-terminus that were shown to bind  $SRS_{cc}$ -dynein<sub>MTBD</sub> by yeast-2-hybrid (Fig 3.2a and b; She1-[1-224] and She1-[169-338] to a lesser extent). This also demonstrates that She1 binding of microtubules is not sufficient to inhibit dynein motility, and that binding by other elements in the N-terminus are required. This is however, contrasted by She1-[113-338], which should theoretically inhibit dynein motility most closely to full-length She1, because it bound stronger to  $SRS_{cc}$ -dynein<sub>MTBD</sub> than She1-[169-338], and encompasses more of the microtubule binding region (Fig A3.2a and b). Clearly, more investigation is necessary to understand the binding activity of She1 to both microtubules and the dynein MTBD.

### **A3.3 DISCUSSION & FUTURE DIRECTION**

We demonstrated that full-length She1 has the strongest inhibitory effect on dynein motility and yet has one of the worst binding interactions to  $SRS_{cc}$ -dynein<sub>MTBD</sub> by yeast-2-hybrid (Fig A3.2a). In light of this data, perhaps She1 has a self-regulatory mechanism, for example, She1 is autoinhibited by the C-terminus when unbound from microtubules, and upon unbinding the C-terminal region is released to bind dynein through the N-terminus. Autoinhibition has been shown to play a significant role in regulating activity of many proteins, including kinesins and dynein motors (Marzo et al., 2020; Siddiqui et al., 2019), and often times, autoinhibited proteins are enriched with regions of intrinsic disorder whose structural dynamicity can facilitate activation of functional domains. Even some MAPs have displayed autoinhibitory regulation of

binding domains, such as EB1 (Trudeau et al., 2013; Kanaba et al., 2012; Gireesh et al., 2018). This notion is further supported by our data demonstrating that She1 cannot interact with dynein in the absence of microtubules (see Chapter 2) and that She1 is predicted to be highly disordered. A more likely explanation is that many disordered proteins can adopt secondary and tertiary structures upon binding with a diverse set of partners (Gsponder et al., 2009). In this scenario, microtubule binding by She1 may induce a conformational change, and possibly adoption of a structure, that is capable of interaction with the dynein MTBD. Though this scenario is enticing, more investigation is necessary to understand the mechanism behind She1 binding to microtubules, one of which might be an EM study. If She1 adopts secondary structure, or even if it becomes stabilized by interaction with microtubules, akin to Tau or DCX MAPs, it may be structured enough to be revealed by EM, as was the case for many other MAPs prior.

## **A3.4 METHODS**

### ***A3.4.1 Protein Purification***

We purified She1-HALO fragments as previously described (Markus et al., 2012), but with minor modifications. Briefly, *E. coli* BL21 (Rosetta DE3 pLysS) cells transformed with pProEX-HTb-TEV:*SHE1-HALO* fragments were grown at 37°C in LB supplemented with 1% glucose, 100 µg/ml carbenicillin and 34 µg/ml chloramphenicol to OD<sub>600</sub> 0.4-0.6, shifted to 16°C for 2 hours, then induced with 0.1 mM IPTG for 14-16 hours at 16°C. The cells were harvested, washed with cold water, resuspended in 0.5 volume of cold 2X lysis buffer [1X buffer: 30 mM HEPES pH 7.2, 50 mM potassium acetate, 2 mM magnesium acetate, 0.2 mM EGTA, 10% glycerol, 1 mM DTT, and protease inhibitor tablets (Pierce)] and then lysed by sonication (5 x 30 second pulses) with 1 minute on ice between each pulse. The lysate was clarified at 22,000 x g for 20 minutes, adjusted to 0.01% triton X-100, then incubated with glutathione agarose for 1 hour at 4°C. The resin was then washed three times in wash buffer (30 mM HEPES pH 7.2, 50

mM potassium acetate, 2 mM magnesium acetate, 0.2 mM EGTA, 300 mM KCl, 0.01% Triton X-100, 10% glycerol, 1 mM DTT, protease inhibitor tablets) and twice in TEV digest buffer (10 mM Tris pH 8.0, 150 mM KCl, 0.01% Triton X-100, 10% glycerol, 1 mM DTT). To fluorescently label She1-HALO, the bead-bound protein was incubated with 6.7  $\mu$ M HaloTag-TMR ligand (Promega) for 15 minutes at room temperature. The resin was then washed three more times in TEV digest buffer, then incubated in TEV buffer supplemented with TEV protease for 1 hour at 16°C. The resulting eluate was collected using a centrifugal filter unit (0.1  $\mu$ m, Millipore), aliquoted, drop frozen in liquid nitrogen and stored at -80°C. For the ATPase assays, purified She1-HALO fragments was dialyzed against dynein motility buffer (see below) lacking EGTA, but supplemented with 1 mM DTT.

Purification of ZZ-TEV-6His-GFP-3HA-GST-dynein<sub>331</sub>-HALO (under the control of the galactose-inducible promoter, *GAL1p*) was performed as previously described<sup>33</sup>, with minor modifications. Briefly, yeast cultures were grown in YPA supplemented with 2% galactose, harvested, washed with cold water, and then resuspended in a small volume of water. The resuspended cell pellet was drop frozen into liquid nitrogen and then lysed in a coffee grinder (Hamilton Beach). After lysis, 0.25 volume of 4X lysis buffer (1X buffer: 30 mM HEPES, pH 7.2, 50 mM potassium acetate, 2 mM magnesium acetate, 0.2 mM EGTA, 1 mM DTT, 0.1 mM Mg-ATP, 0.5 mM Pefabloc SC, 0.7  $\mu$ g/ml Pepstatin) was added, and the lysate was clarified at 22,000 x g for 20 min. The supernatant was then bound to IgG sepharose 6 fast flow resin (GE) for 1 hour at 4°C, which was subsequently washed three times in wash buffer (30 mM HEPES, pH 7.2, 50 mM potassium acetate, 2 mM magnesium acetate, 0.2 mM EGTA, 300 mM KCl, 0.005% Triton X-100, 10% glycerol, 1 mM DTT, 0.1 mM Mg-ATP, 0.5 mM Pefabloc SC, 0.7  $\mu$ g/ml Pepstatin), and twice in TEV buffer (50 mM Tris, pH 8.0, 150 mM potassium acetate, 2 mM magnesium acetate, 1 mM EGTA, 0.005% Triton X-100, 10% glycerol, 1 mM DTT, 0.1 mM Mg-ATP, 0.5 mM Pefabloc SC). Note that for binding experiments involving vanadate (e.g., Fig. 2.4e), EGTA was excluded from the TEV buffer. To fluorescently label 6His-GFP-GST-3HA-

dynein<sub>331</sub>-HALO (for single molecule analyses), the bead-bound protein was incubated with either 6.7  $\mu$ M HaloTag-TMR or HaloTag-PEG-biotin ligand (Promega) for 15 minutes at room temperature. The resin was then washed four more times in TEV digest buffer, then incubated in TEV buffer supplemented with TEV protease for 1 hour. Following TEV digest, the bead solution was transferred to a spin column (Millipore) and centrifuged at 20,000 x g for 10 seconds. The resulting protein solution was aliquoted, flash frozen in liquid nitrogen, and then stored at -80°C. Protein concentrations were determined by running a dilution series of dynein along with a dilution series of tubulin on a 4-12% SDS-PAGE gel, and then staining the gel with Sypro Red gel stain (Thermo Fisher). Band intensities were quantitatively determined following imaging on a Typhoon gel imaging system (FLA 9500).

#### ***A3.4.2 Single and ensemble molecule motility assays***

The single-molecule motility assay was performed as previously described (Markus et al., 2012) with minor modifications. Briefly, flow chambers constructed using slides and plasma cleaned and salinized coverslips attached with double-sided adhesive tape were coated with anti-tubulin antibody (8  $\mu$ g/ml, YL1/2; Accurate Chemical & Scientific Corporation) then blocked with a mixture of 1% Pluronic F-127 (Fisher Scientific) and 1 mg/ml  $\kappa$ -casein. Taxol-stabilized microtubules assembled from unlabeled and HiLyte647-labeled porcine tubulin (10:1 ratio; Cytoskeleton) were introduced into the chamber. Following a 5-10 minute incubation, the chamber was washed with dynein lysis buffer supplemented with 20  $\mu$ M taxol, at which point She1-TMR was added to the chamber. After a 5-minute incubation, 6His-GST-dynein<sub>331</sub>-488 diluted (~10 pM) in motility buffer (30 mM HEPES, pH 7.2, 50 mM potassium acetate, 2 mM magnesium acetate, 1 mM EGTA, 10% glycerol) supplemented with 1 mM DTT, 20  $\mu$ M taxol, 1 mM Mg-ATP, 0.05% Pluronic F-127, and an oxygen-scavenging system (1.5% glucose, 1 U/ $\mu$ l glucose oxidase, 125 U/ $\mu$ l catalase) was added. TIRFM images were collected using a 1.49 NA 100X TIRF objective on a Nikon Ti-E inverted microscope equipped with a Ti-S-E motorized stage, piezo Z-control (Physik Instrumente), and an iXon X3 DU897 cooled EM-CCD camera

(Andor). 488 nm, 561 nm, and 640 nm lasers (Coherent) were used along with a multi-pass quad filter cube set (C-TIRF for 405/488/561/638 nm; Chroma) and emission filters mounted in a filter wheel (525/50 nm, 600/50 nm and 700/75 nm; Chroma) to image She1-TMR, 6His-GST-dynein<sub>331</sub>-488, and HiLyte647-microtubules, respectively. We acquired images at 2 second intervals for 10 min. Velocity and run length values were determined from kymographs generated using the MultipleKymograph plugin for ImageJ.

### **A3.5 FIGURES**

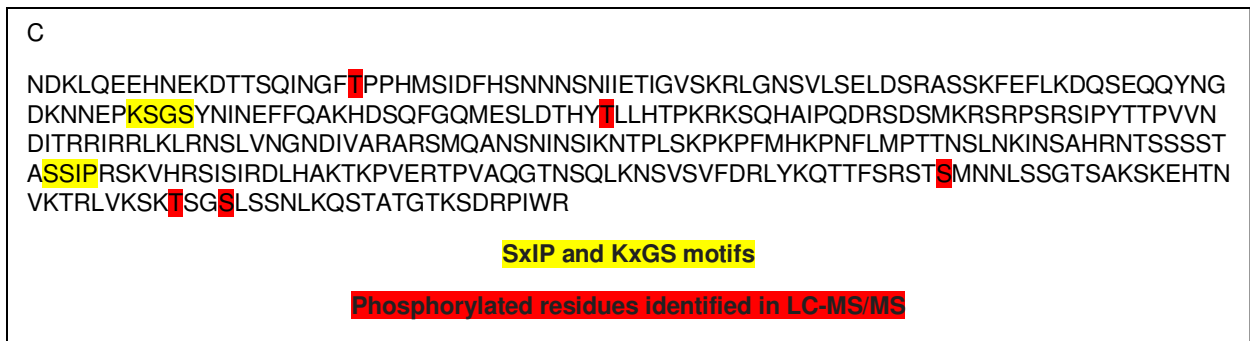
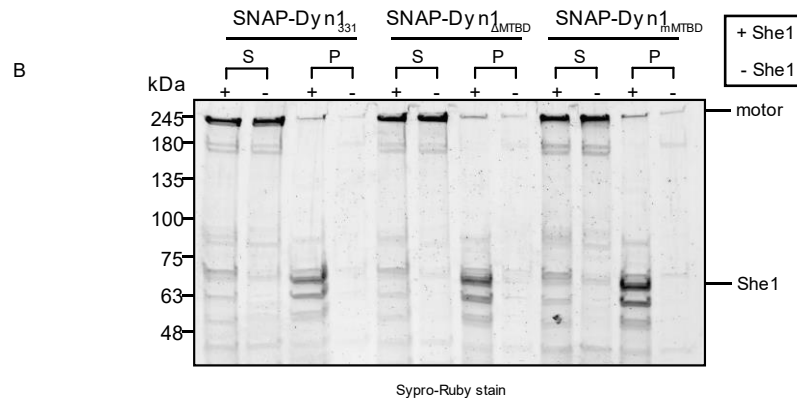
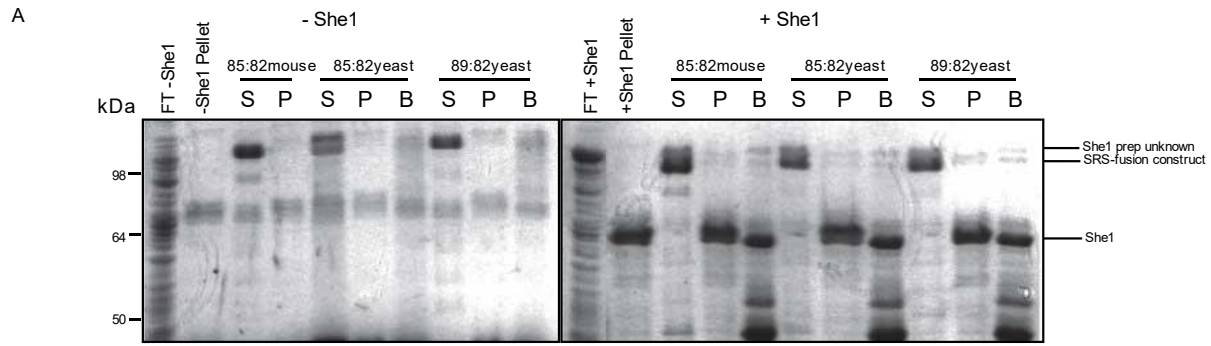


**Figure A3.1 Co-pelleting assays and She1 amino acid sequence.** (a, b) Co-pelleting assays with and without GST-She1-HALO purified from *E. Coli*. She1 on GST beads or free GST beads (control) were incubated with indicated dynein. (a) Minimal SRS-constructs with indicated coiled-coil registry 85:82, 89:82 (see Methods) and a yeast MTBD. The MTBD of the 85:82 was replaced with mouse MTBD which exhibits reduced sensitivity to She1. (b) Monomeric motors (SNAP-Dyn1) with yeast MTBD, mouse MTBD, or  $\Delta$ MTBD. Note that the constructs and monomeric motors are not visible more than background in the pellet but is visible in the supernatant with and without She1. This indicates the conditions may not be sufficient to observe She1 binding. (c) She1 amino acid sequence with phosphorylation sites identified from Mass-spectrometry: T22, T113 T314, S287, S317 (highlighted in Red). Sequence also includes motifs for potential Bim1 binding (SxIP) and Kin1/Kin2 phosphorylation motifs (KxGS) (highlighted in Yellow).

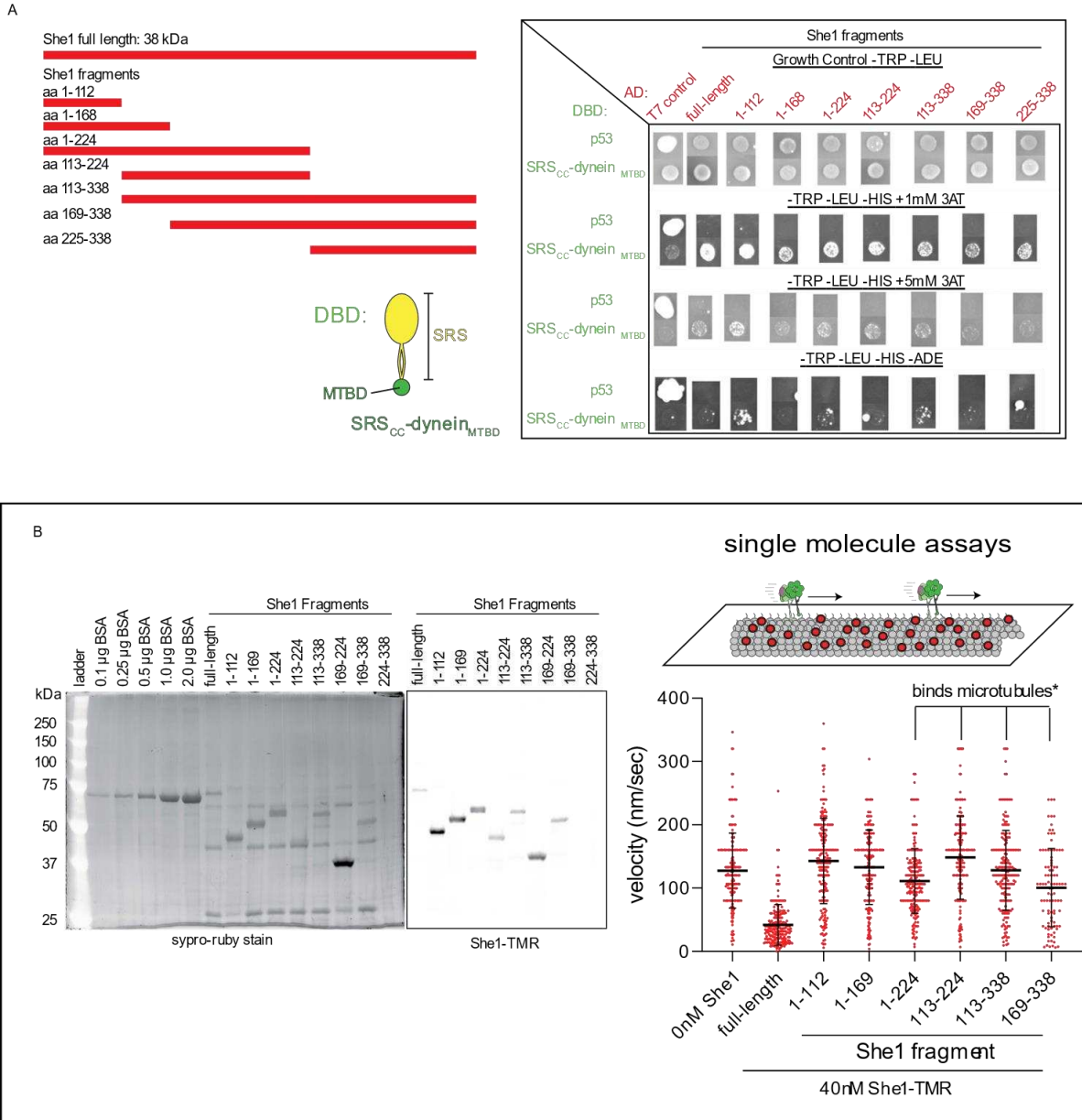


**Figure A3.2 Assessment of She1 fragments identifies binding regions on the dynein MTBD and the microtubule.** (a) Cartoon representation of She1 fragments used in (a) and (b) and the SRS<sub>cc</sub>-dynein<sub>MTBD</sub> construct used in (a) the yeast-2-hybrid assay. The activation domain was fused to She1 fragments and the DNA binding domain was fused to the SRS<sub>cc</sub>-dynein<sub>MTBD</sub> construct. Four conditions were used with varying degrees of stringency, with the most stringent condition shown on the bottom (also see Methods). (b) Sypro Ruby stain (left) and accompanying fluorescent scan of She1-TMR fragments (right). BSA was used to calculate the concentration of each fragments (see Methods). Quantitation of single molecule assays are shown on the right for each fragment, including She1 full-length and a 0nM She1 control. Fragments that bound microtubules are indicated on the plot (data not shown). Note only fragments that bound microtubules had a noticeable effect on dynein velocity, consistent with previous observations from Chapter 2.

## APPENDIX 4

### SHE1 MASS-SPECTROMETRY REVEALS PHOSPHORYLATION SITES & PROTEIN INTERACTIONS

#### A4.1 Introduction

Phosphorylation is one way by which cells can regulate protein function. Fascinatingly, one group noted disordered regions of a group of proteins analyzed were more highly enriched in phosphorylation than their structured counterparts (Iakoucheva et al., 2004; Gsponer et al., 2008). She1 has been shown to be regulated by phosphorylation in a cell-cycle dependent manner and in response to environmental stress factors (Pigula et al., 2014; Markus et al., 2012; Wong et al., 2007). Hog1 is a protein MAP kinase involved in a long signaling cascade involved in osmotic stress response, specifically, Hog1 prevents S-phase checkpoint satisfaction and replication and transcription in response to unfavorable environmental factors and DNA replication stress by phosphorylating target substrates, one of which is She1 (Brewster et al., 1993; Cook et al., 2012; Tkach et al., 2012; Maayan et al., 2012; Westfall et al., 2004). Additionally, She1 is suspected to be substrate of Ipl1 (Aurora B), in its role at the mitotic spindle (Woodruff et al., 2010; Markus et al., 2012). Interestingly, She1 binding to microtubules was notably reduced in a phosphomimetic mutant of She1, designed using Ipl1 consensus sequences (She1<sub>5D</sub> Markus et al., 2012). However, previously reported phosphorylation sites were determined from Ipl1 and Hog1 consensus sequences and may not represent true phosphorylation sites *in vivo*. We wished to identify endogenous phosphorylation sites using mass-spectrometry.

#### A4.2 RESULTS & DISCUSSION

A She1 mutant containing phosphomimetics at Ipl1 consensus sites, She1<sub>5D</sub>, was shown to have a decreased affinity for microtubules but had an enhanced effect on dynein motility, but whether these suspected phosphorylation sites are relevant *in vivo* is yet to be determined. In our first attempt to identify phosphorylation sites by mass-spectrometry, we reported four possible residues from the LC-MS/MS 3-hour gradient, Threonine 113 and 314, and Serine 287 and 317 (Fig A3.1), none of which were the five previously suspected consensus sites for Ipl1 or the two suspected for Hog1. S287 and T314 look like possible Ipl1 consensus sites, but neither T113 or S317 match Hog1 of Ipl1 consensus sites (Markus et al., 2012; Pigula et al., 2014). Interestingly, T113 is on the N-terminus, which we suspect interacts with the dynein MTBD and S287, S317, T314 are within the region expected to bind microtubules (see Appendix 3). However, this purification was done with She1 overexpressed. The Hog1 pathway is activated in response to environmental and cellular stress (*e.g.* overexpression of a protein) and has been shown to lead to excessive phosphorylation of She1 (Pigula et al., 2014). Moreover, overexpression of She1 arrests cells in G1 phase (Espinete et al., 1995). This suggests that these four residues likely represent phosphorylated sites during G1, or during high cellular stress, but not during active spindle positioning.

To identify phosphorylation sites that are relevant to dynein-pathway function, we purified endogenously expressed She1 arrested in metaphase by depleting cells of CDC20 (see Methods). Protein samples were again sent for LC-MS/MS in the CU-Boulder MS-facility (see Methods), which identified one novel phosphorylation site at Threonine 22 (Fig A3.1), which matches the phosphorylation consensus sequence of Hog1 (Pigula et al., 2014). Unfortunately, the endogenous expression has proven to be a challenge, in this mass-spec, only 14% of She1 sequence was covered by peptides, indicating that any phosphorylation sites outside of this sequence coverage could not be identified. Despite this, investigation into our one phosphorylation site may be interesting. It is located within the region identified by yeast-2-hybrid to interact strongly with the dynein MTBD, suggesting this site could be relevant to She1

regulation of dynein *in vivo*. A plasmid with which to integrate phosphorylation mimics or null mutants into the She1 locus has already been developed. Future studies should test if this site is relevant for the regulation of dynein activity *in vivo* and dynein motility *in vitro*, as well as determine if it regulates She1 binding to microtubules. To attempt to identify more sites using endogenous expression, it is likely that this protein purification must be upscaled dramatically. A good starting point might be to triple the cell mass by growing cell in a fermenter (see Methods).

In addition to phosphorylation data, we also received a list of proteins that were identified in the purification. Note that this protein purification was not done to minimize loss of interacting proteins, meaning many of these peptide hits are likely non-specific interactions with elements used in the purification process (such as agarose beads, She1, Halo, etc). However, we did note that Actin was highly represented in peptides (20), sequence coverage (73%), and MS/MS count (67), and was accompanied by many actin-related proteins. Many MAPs have the capacity to bind actin and microtubules, enlisting in a dual role of regulating the cytoskeleton. One of which is the potential She1 homolog MAP4, which inhibits dynein activity in cells (Samora et al., 2011; Matsushima et al., 2012). MAP4 was shown to bind actin with the same C-terminal region that is also responsible for microtubule binding *in vivo* indicating that it cannot bind both microtubules and actin at the same time. MAP4-actin interaction plays a role in the distal region of developing neurites, but very little is known about this function (Matsushima et al., 2012). Unfortunately, no factors related to dynein were identified.

## **A4.3 METHODS**

### ***A4.3.1 Plasmid and strain construction***

Strains are derived from YEF473A (Bi and Pringle, 1996). We transformed yeast strains using the lithium acetate method (Knop et al., 1999). Strains carrying mutations were constructed by PCR product-mediated transformation to obtain ARSH/CEN sequence (from addgene pRS315) or by mating followed by tetrad dissection. Proper tagging and mutagenesis

were confirmed by PCR (also confirmed by sequencing). Yeast synthetic defined (SD) media was obtained from Sunrise Science Products (San Diego, CA).

#### ***A4.3.2 Protein Purification***

The first attempt to identify phosphorylation sites by mass-spec was done using ARSH/CEN-Gal1p:8xHis-ZZ-2xTEV-She1-HALO in protease deficient yeast. Yeast cells were transformed with ARSH/CEN-Gal1p:8xHis-ZZ-2xTEV-She1-HALO and grown in 3 mL YPD + 100 µg/ml G418 in 16 hours, then upscaled to 200 mL YPD + 100 µg/ml G418 for 16 hours, and then 1L 16 hours (x16 for 16 L). Cell were pelleted in sterile bottles and resuspended in 1L YPG for 6 hours before harvesting. The second attempt to identify phosphorylation sites by mass-spec was done using ARSH/CEN-She1p:8xHis-ZZ-2xTEV-She1-HALO in a Gal1p:CDC20 background for metaphase arrest. Yeast cells transformed with ARSH/CEN-She1p:8xHis-ZZ-2xTEV-She1-HALO and were grown at 30°C in 3 mL YPG/R + 100 µg/ml G418 for 16 hours, then upscaled to 200 mL YPG/R + 100 µg/ml G418 for 16 hours, and 1 L YPG/R + 100 µg/ml G418 for 16 hours (x16 for 16 L). Then 20 g glucose was added to each liter and left to shake for 5 hours to arrest in metaphase before harvesting.

After growth cells were harvested, washed with cold water, and resuspended in small volume of water. The resuspended pellet was drop frozen into liquid nitrogen and the lysed in a coffee grinder (Hamilton Beach). After lysis, cells were resuspended in 0.5 volume of cold 2X lysis buffer [1X buffer: 30 mM HEPES pH 7.2, 50 mM potassium acetate, 2 mM magnesium acetate, 0.2 mM EGTA, 10% glycerol, 1 mM DTT, Phostop and protease inhibitor tablets (Pierce)]. The lysate was clarified at 22,000 x g for 20 minutes, adjusted to 0.01% triton X-100, then incubated with IgG sepharose six fast flow resin (GE) for 1 hour at 4°C. The resin was then washed three times in wash buffer (30 mM HEPES pH 7.2, 50 mM potassium acetate, 2 mM magnesium acetate, 0.2 mM EGTA, 300 mM KCl, 0.01% Triton X-100, 10% glycerol, 1 mM DTT, phostop, protease inhibitor tablets) and twice in TEV digest buffer (10 mM Tris pH 8.0, 150 mM KCl, 0.01% Triton X-100, 10% glycerol, 1 mM DTT, phostop), then incubated in TEV buffer

supplemented with TEV protease for 1 hour at 16°C. The resulting eluate was collected using a centrifugal filter unit (0.1 µm, Millipore), concentrated, aliquoted, drop frozen in liquid nitrogen and stored at -80°C until shipment on dry ice to mass-spectrometry facility in Boulder. We would like to thank Thomas Lee at the Central Analytical Mass Spectrometry Lab at UC Boulder for answering all our questions, performing the mass-spectrometry and identifying the phosphorylation sites.

## APPENDIX 5

### PURIFICATION OF YEAST TUBULIN AND ASSESSMENT OF SHE1 BINDING AND DYNEIN MOTILITY

#### A5.1 INTRODUCTION

*In vitro* microtubule assays with recombinant proteins has revolutionized our understanding of many microtubule-based processes. Efficient, simple characterization of microtubule motors and other microtubule-associated proteins and processes are made possible by using recombinant tubulin. These assays forgo the complicated answers we often get from cell biology, where all the players are on the field at once, and most of these players we haven't even met yet. In these assays we can instead introduce our players one-by-one in a systematic and methodical approach and assess their properties, which can then be applied to the system (or in this case, the cell). But while *in vitro* assessment of cell biological questions is highly advantageous, it also has one obvious flaw: the players are no longer in their native system. As dutiful researchers we must always try to replicate the native system, to obtain as accurate a picture of what our players are doing in the cell as possible, and often this means doing difficult and sometimes painstaking assays.

Many studies today still rely on commercially available tubulin for *in vitro* assays (e.g. cytoskeleton.com). However, these products are almost exclusively purified from porcine or bovine brain tissue extracts which represent a broad mixture of tubulin isotypes and post-translational modifications representative of these mammalian brain tissues (reviewed in Janke et al., 2011 and Janke et al., 2020). Though tubulin is conserved between species and between isotypes, recent structural and *in vitro* studies have shown they can exhibit different protofilament properties (Bode et al., 2003) and affect MAP binding (Howes et al., 2018; Howes et al., 2017; Kollman et al., 2015; Podolski et al., 2014). This is true of plus-end tracking protein

Bim1, the yeast CLIP170, which tip tracks on yeast tubulin but not mammalian tubulin *in vitro* (Molodtsov et al., 2016; Geyer et al., 2015). Additionally, it is not currently possible to commercially purchase mutants of tubulin or single isoforms, limiting investigation into the properties of mutant and isotypes of tubulin *in vitro* without in-house methods to purify tubulin.

We wanted to establish yeast tubulin purification in our lab to allow for the use of yeast tubulin in our future *in vitro* studies. Additionally, we wanted to purify a specific mutant tubulin (tub1-G437R) and the yeast  $\alpha$ -tubulin isotype Tub3, to assess She1 binding *in vitro*. This would allow us to determine if She1 or tub1-G437R were causative of the changes in microtubule dynamics seen in cells (Denarier et al., see footnote<sup>2</sup>), and, confirm our prior *in vivo* data that reduced She1 binding on spindle microtubules was a consequence of tub1-G437R and not the  $\alpha$ -tubulin isotype Tub3 (see Appendix 2). Additionally, all our studies up to now have been on mammalian tubulin purchased through Cytoskeleton™, we were curious if we might observe discrepancies in She1 binding and inhibition of dynein motility on yeast versus mammalian microtubules. Testing this hypothesis requires the purification of yeast tubulin, which has proved to be a challenge outside of a few research groups. Here, we describe the critical aspects of yeast tubulin purification and polymerization steps adapted for using with our systems and reagents to ensure this method will be successfully utilized by others in our lab and in the future, and provide the first *in vitro* assessment of She1 and dynein on yeast microtubules.

## **A5.2 RESULTS & DISCUSSION**

While the purification and polymerization of yeast tubulin proved to be a challenge, we successfully established the method in our lab (see Figure A5.1 and Methods). To assess binding affinity of She1 on wild-type tubulin, She1-TMR was purified from yeast (see Methods). We found that She1 had an apparent  $K_d$  of 12nM by fluorescence microscopy (Fig A5.2a), nearly identical to previous work on mammalian microtubules ( $K_d$  9.7nM; Markus et al., 2012). We know from prior work that She1 requires the C-terminal tails to bind microtubules (Markus et

al., 2012). This suggests that, despite the C-terminal tails from these species being of different lengths, and mammalian CTTs being post-translationally modified, whereas yeast tubulin is not, the highly acidic properties of the tails of both species are sufficient to exhibit similar binding affinities to She1, supporting the use of mammalian tubulin to assess She1 functions. We cannot, however, assess from these data that the structural elements involved in this binding are identical on the molecular level. We assessed She1 effects on dynein motility by single molecule assay using recombinant dynein from yeast (see Methods). When we assessed She1 effects on dynein motility, we saw a reduction in dynein velocity (Fig A5.2b), albeit to a lesser extent than what we observed on mammalian microtubules with equivalent concentrations of She1-TMR and in equivalent buffers (however dynein constructs were different, the prior motility assay used a tailless GST-dimerized dynein, see Fig A3.1; see Methods). Additionally, it is important to note that She1-TMR represented here was purified from yeast, whereas previously used She1-TMR was purified from *E. Coli* (Fig. A3.1, see Methods). Meaning, we cannot accurately compare these conditions to each other.

Finally, we have successfully implemented the use of yeast tubulin in our lab, which we've shown here will be useful for assessment of dynein motility. Our lab will benefit, financially and scientifically, from using recombinant yeast tubulin in our *in vitro* assays. With this system, we will be able to use recombinant yeast tubulin in microtubule dynamics assays with reconstituted dynein, dynactin, Pac1, She1, and even +TIP tracking components Bik1 and Bim1, in a system that more closely resembles tip tracking in budding yeast *in vivo*, to further elucidate the roles of these proteins in dynein pathway function. Future experiments will also include purification of the tubulin isotype Tub3, to assess if different tubulin isotypes affect She1 binding and microtubule dynamics. Unfortunately, attempts to purify tub1-G437R with this system has thus far proved unsuccessful, for currently unknown reasons (data not shown).

### **A5.3 METHODS**

### **A5.3.1 Media**

- *CSM -URA -TRP: We buy premade powder minus the amino acids from Sunrise Products®; follow manufacturer instructions to make and add appropriate amino acid deficient powders.*
- *YPG/L: add per 1 Liter:*
  - *10 g yeast extract (fisher BP1422 <-ALWAYS!)*
  - *20 g peptone*
  - *30 mL glycerol<sup>β</sup>*
  - *33 mL lactate<sup>3</sup>*

### **A5.3.2 Growth Protocol**

- *Day 1-3/4: Grow transformed yeast colonies in 5 mL CSM -URA -TRP with 2% glucose for minimum 3 days, maximum 4 (ex. Friday afternoon – Monday morning) at 30 degrees Celsius in shaker. (Note: one 5 mL tube per 1 L final; I usually grow 16 L)*
- *Day 4/5: In the morning on day 3 or 4, inoculate 50 mL CSM -URA -TRP with 2% glucose with 5 mL tube. Grow overnight at 30 degrees Celsius in shaker; JEL1 tends to pellet, shake as high as you are comfortable shaking for maximum growth. (Note: one 5 mL tube per 50 mL flask)*
- *Day 4/5: In the morning inoculate 1 L flask with 50 mL flask. Take the starting OD of the 50 mL cultures, which should be between 0.5 and 0.8. Let grow 20-24 hours before induction at 30 degrees Celsius at the fastest speed you are comfortable with (there is a ~10 g final difference with 16 L preps between shaking at 180 rpm throughout growth and shaking at 230+ rpm throughout growth) (Note: one 50 mL flask per 1 L flask)*

- *Day 5/6: When cultures are between OD 5.0-9.0, 20 g/L galactose powder can be added straight to the media. Let induce for 5 hours at 30 degrees Celsius in shaker.*

<sup>3</sup>*very viscous, be sure it doesn't get left behind in the graduated cylinder; measure the amount into the graduated cylinder and pour into your mixing beaker containing minimal ddH<sub>2</sub>O. Then you can rinse the graduated cylinder with ddH<sub>2</sub>O to get excess stuck on sides and pour it into the mixing beaker without going over your final volume.*

### **A5.3.3 Harvesting**

1. *To harvest cells after 5 hour induction spin at 4000 rpm for 20 minutes. Resuspend pellet in ddH<sub>2</sub>O to clear pellet of leftover media and repeat the spin.*
2. *Weigh a thick plastic bag you will use to store the pellet and make note of the weight. To store cell pellet, scoop cells out of the centrifuge bottles using a spatula and into a plastic bag (thickest bag so it doesn't tear easily in -80 C. I usually use the same single plastic bag for multiple preps, only washing with different tubulin mutants). Weigh the plastic bag with the cell pellet and minus the weight of the bag to get the final cell pellet volume and write the weight on the bag and your notebook in our nicest markers (they keep well in the -80 C). Pelleted cells can be stored indefinitely according to Luke Rice's lab, but I have always used them within a week.*

### **A5.3.4 Purification buffers<sup>4</sup>**

- *Lysis Buffer*
  - *50 mM HEPES pH 7.4*
  - *500 mM NaCl*
  - *10 mM MgSO<sub>4</sub>*
  - *30 mM Imidazole*
- *Nickel Wash Buffer*
  - *25 mM K-PIPES pH 6.9*
  - *1 mM MgSO<sub>4</sub>*
  - *30 mM Imidazole*

- 200 mM NaCl (NO SALT FOR WILD-TYPE TUBS!)
- *Nickel Elution Buffer*
  - 25 mM K-PIPES pH 6.9
  - 1 mM MgSO<sub>4</sub>
  - 300 mM Imidazole
  - 200 mM NaCl (NO SALT FOR WILD-TYPE TUBS!)
- *Mono Q Buffer A*
  - 25 mM K-PIPES pH 6.9
  - 2 mM MgSO<sub>4</sub>
  - 1 mM EGTA
- *Mono Q Buffer B*
  - 25 mM K-PIPES pH 6.9
  - 2 mM MgSO<sub>4</sub>
  - 1 mM EGTA
  - 1 M NaCl
- *Tubulin Storage Buffer*
  - 10mM K-PIPES 6.9
  - 1mM EGTA
  - 1mM MgSO<sub>4</sub>
- *Tubulin Polymerization Buffer*
  - 500 mM K-PIPES 6.9
  - 25% Glycerol
  - 5 mM MgSO<sub>4</sub>

<sup>4</sup>Filter all buffers through 0.22µm filter and store in 4 degrees Celsius refrigerator. Pre-make all solutions to ensure buffers are cold before use.  
 Add GTP to final concentration of 50.0 µM to all buffers just before use.  
 Add protease inhibitor tablets (Roche) to lysis buffer so they will dissolve before you add the buffer to the yeast pellet.

- 5 mM EGTA

### **A5.3.5 Lysis of cell pellet**

- 1) *Keep everything cold – prechill all buffers, beakers and tubes on ice to inhibit MT polymerization and aggregation.*
- 2) *Thaw GTP stock and add to final 50 $\mu$ M in all buffers.*
- 3) *Get yeast pellet from -80°C, thaw on bench: break into chunks, transfer to cold 250ml beakers. Do this before adding lysis buffer to avoid freezing the buffer.*
- 4) *For every 75 g cell pellet, add ~70 mL lysis buffer (+ GTP) to beaker for a final resuspension volume of ~150 mL. Thaw on ice and bench (if buffer starts to freeze) with occasional stirring.*
- 5) *During thaw, prepare microfluidizer for lysis at 23 kpsi (see manufacturer instructions). It is critical to keep the microfluidizer cold during operation; fill to the brim with ice and put ice in a plastic bag to cover the spout for the whole lysis process.*
- 6) *Pass 5-6 times through microfluidizer, you can check degree of lysis on microscope. During the first pass, be sure to be ready to start collecting immediately after hitting “start” to minimize lysate loss (it goes quickly! It’s ok to get mostly clear liquid for the first few “pumps” out of the spout).*
- 7) *After each pass, you must wait at least 5 minutes before the next pass. Be sure to keep the beaker of lysate on ice always. Before each pass, touch your finger to the spout, coils, beaker, and cell lysate to ensure everything remains cold. If not, wait longer; it took 5 days to grow this yeast pellet, what’s 10 more minutes! This step is the hardest step to keep the lysates cold; I usually expect to spend an hour on this step. Luke’s lab was also very adamant about keeping lysates very cold here!*
- 8) *To collect final lysate left in coils, run ~50 mL lysis buffer through the system, collecting all. You should end up with ~200-250 mL resuspension volume after lysis.*
- 9) *Take SDS-PAGE sample of lysed cells (20 $\mu$ L), divide the lysate into centrifuge tubes.*

- 10) Clarify cell lysate at 16000 rpm, 30min, 4°C. Note: the faster the better.
- 11) Decant supernatant into cold beaker, take PAGE sample of clarified lysate (20 µL).

Clarified lysate is ready for nickel-column loading.

#### **A5.3.6 Nickel-affinity purification of yeast $\alpha\beta$ -tubulin**

- 1) Use the AKTA FPLC for both Nickel affinity and Mono Q purifications. To navigate software and set up sample pump, follow manufacturers' instructions or ask somebody in the lab that has already used it.
- 2) Equilibrate 5 mL Ni-column by running 10 column volumes (CVs) of cold lysis buffer with 50 µM GTP. No need to use protease inhibitors in the lysis buffer in this step. For each 75 g, use one 5 mL Nickel column. Load and wash multiple columns in parallel but when eluting, connect two columns in series to reduce volume of elution pool.
- 3) Load the clarified lysate onto the Ni-column using the sample pump at 4 mL/min (or adjusted to be below the pressure limit of the column).
- 4) Wash the Ni-column with 10 CVs of lysis buffer with 50 µM GTP.
- 5) Wash the Ni-column with 10 CVs of nickel wash buffer with 50 µM GTP.
- 6) Elute  $\alpha\beta$ -tubulin from the Ni-column with 6 CV of elution buffer with 50 µM GTP. Collect elution in 1.5ml fractions. Use the spectra to determine how many fractions to pool (Fig A5.1a). Alternatively, you may want to perform a Bradford to determine which fractions have protein if this is your first time trying this prep (see below).
- 7) Proceed to the anion-exchange. If you don't have enough time, add cold glycerol to a final concentration of ~20% and flash-freeze the Ni-pool in liquid nitrogen and store at -80°C.
- 8) Take SDS-PAGE samples of flow-through, wash, and Ni-pool. Run only 0.5-1µL of lysed cells, clarified lysate, and flow-through to clearly see protein bands (Fig A5.1a and c).

### **A5.3.7 Determining which fractions have protein by Bradford assay**

- 1) Add 995 $\mu$ l Bradford dye to as many cuvettes as you have fractions. Blank the spectrophotometer at 595 nm with Bradford dye.
- 2) Add 5  $\mu$ l of each fraction to each cuvette. Make sure that the solution in any given cuvette is well mixed before measuring Abs. Measure and record the A595 for each fraction.
- 3) Collect fractions giving an A595  $\geq$  0.2.

### **A5.3.8 Purification of yeast $\alpha\beta$ -tubulin by anion-exchange chromatography**

- 1) Thaw Ni-pool on wet ice if purifying from frozen Ni-pool stored at  $-80^{\circ}\text{C}$ . Add nuclease treatment (Pierce Universal Nuclease product #88702, see manufacturer,  $\sim$ 10 $\mu$ L per 20mL pooled lysate) to lysate and incubate at room temperature for 15 minutes. Return to ice.
- 2) Dilute Ni-pool as little as possible so that Imidazole concentration is below 200mM using Mono Q A buffer (including the glycerol as a diluent if you froze your Ni-pool). Don't forget to add 50  $\mu$ M GTP to buffers!
- 3) Equilibrate Mono Q column with 5 CVs of 90% buffer A, 10% buffer B.
- 4) Load the Ni-pool onto the Mono Q.
- 5) Elute with a 40-60CV gradient of 10 to 70% buffer B. Wild-Type yeast  $\alpha\beta$ -tubulin usually elutes around 38 to 40% Mono Q buffer B. If tubulin is still coming through flow-through, dilute Ni-pool Imidazole to below 100mM. Collect fractions (Fig A5.1b).
- 6) Pick fractions to pool according to chromatogram and/or SDS-PAGE (Fig A5.1b,d and e). Measure  $\alpha\beta$ -tubulin concentration in pool by measuring UV absorbance spectra.
- 7) Concentrate and dialyze (see sections below) into tubulin storage buffer (+ GTP; Fig A5.1.f). Flash freeze 50  $\mu$ L sized aliquots in liquid nitrogen and store at  $-80^{\circ}\text{C}$ . One aliquot will be used at a time to polymerize yeast microtubules for TIRF assays.

### **A5.3.9 Concentrating $\alpha\beta$ -tubulin**

- 1) Concentrate using a centrifugal filter (30 kDa MWCO filter). First spin ddH<sub>2</sub>O, then Mono Q buffer through the filter to remove any glycerol that might interfere with concentration by promoting MT polymerization and/or aggregation.
- 2) Spin at 1000 x g, 4°C for 5 minutes at a time to concentrate  $\alpha\beta$ -tubulin. Resuspend vigorously in between spins to minimize loss of protein to aggregation. Avoid making bubbles. Collect flow-through in a separate container. Measure UV-Vis spectrum to monitor concentration (A<sub>280</sub> Protein) and check for aggregation (A<sub>260</sub>/A<sub>280</sub> ratio). The goal concentration for storage is ~2-3  $\mu$ M (Fig A5.1f).

### **A5.3.10 Dialyzing large volume of $\alpha\beta$ -tubulin**

- 1) We use Thermo Slide-A-Lyzer dialysis cassettes for concentrated  $\alpha\beta$ -tubulin volumes > 500  $\mu$ L. Use the cassette made for your volume (see manufacturer).
- 2) Submerge cassette in cold tubulin storage buffer (+ GTP) for 10 minutes in the cold room.
- 3) Add concentrated  $\alpha\beta$ -tubulin using a syringe and needle (see manufacturer).
- 4) Let dialyze in 500 mL tubulin storage buffer in cold room for 1 hour. Be sure there is constant movement by placing beaker on a stir plate and using a stir bar.
- 5) Discard buffer and swap for fresh 500 mL tubulin storage buffer (+ GTP). Let dialyze overnight in cold room with constant stirring.
- 6) The next morning remove the  $\alpha\beta$ -tubulin from cassette the same way you added it (take care to create no bubbles) and measure the concentration again (using the dialyses buffer to blank the UV-vis; see Figure A5.1f for before and after concentration).

### **A5.3.11 Dialyzing small volumes of $\alpha\beta$ -tubulin**

- 1) We use the 7K MWCO 0.5mL bed volume Thermo Zeba spin desalting columns to buffer exchange a small volumes (< 500  $\mu$ L) concentrated  $\alpha\beta$ -tubulin. (see manufacturer)

- 2) Loosen (not remove!) cap on spin column and remove bottom closure and place in 1.5 mL eppendorf. Spin column at 1500 x g for 1 minute to remove column storage solution and form size exclusion bed. Mark the side of the column where the compacted resin is slanted upward. This is to remember which direction you placed the column in the centrifuge to maintain the bed shape in future spins for maximal protein recovery and desalting. Always have that mark facing up when spinning!
- 3) Blot bottom to remove excess storage solution.
- 4) Add 300 uL tubulin storage buffer (+ GTP) to resin bed. Centrifuge 1500 x g 1 minute.
- 5) Repeat step 4 2-3 times.
- 6) Place column in new eppendorf and remove the cap. Apply 30-130 uL of concentrated  $\alpha\beta$ -tubulin to the center of the compacted resin bed (you will have to use more than one if you have more sample). If sample is less than 70  $\mu$ L, add 15 uL appropriate buffer to act as a stacker after the sample has absorbed into the bed.
- 7) Centrifuge 1500 x g for 2 minutes. Sample is now buffer exchanged into tubulin storage buffer.

#### **A5.3.12 Polymerization of yeast microtubules for TIRF assays**

- 1) Thaw one aliquot of  $\alpha\beta$ -tubulin in tubulin storage buffer (50 uL).
- 2) To the aliquot: add 15 uL tubulin polymerization buffer, EpoB (final concentration 50  $\mu$ M), and GTP (final concentration 2 mM).
- 3) Place in foam boat in a beaker filled with water and place in 30 °C incubator.
- 4) Let polymerize overnight or check for polymerization after 30 minutes (better at 1-2 hours or best overnight).
- 5) To stick microtubules to salinized coverslip, use anti-his antibody (~ 200  $\mu$ g/mL; can probably do less, never refined this concentration). Block the coverslip with 1% Pluronic per usual. Ensure all buffers that contact the microtubules contain 50 uM EpoB. We

*noted that these microtubules do not stick to rigor kinesin (K560), or to YL1/2 anti-alpha tubulin antibody.*

#### **A5.3.13 Protein purification of She1 from yeast**

We purified She1 from protease deficient (from Reck-Peterson) yeast using ARSH/CEN-GAL1p:8xHis-ZZ-2xTEV-She1-HALO. Yeast cells transformed with ARSH/CEN-GAL1p:8xHis-ZZ-2xTEV-She1-HALO and were grown at 30°C in 3 mL YPG/R + 100 µg/ml G418 for 16 hours, then upscaled to 200 mL YPG/R + 100 µg/ml G418 for 16 hours, and 1 L YPG/R + 100 µg/ml G418 for 16 hours (x16 for 16 L). Then 20 g glucose was added to each liter and left to shake for 5 hours to arrest in metaphase before harvesting. After growth cells were harvested, washed with cold water, and resuspended in small volume of water. The resuspended pellet was drop frozen into liquid nitrogen and the lysed in a coffee grinder (Hamilton Beach). After lysis, cells were resuspended in 0.5 volume of cold 2X lysis buffer [1X buffer: 30 mM HEPES pH 7.2, 50 mM potassium acetate, 2 mM magnesium acetate, 0.2 mM EGTA, 10% glycerol, 1 mM DTT, and protease inhibitor tablets (Pierce)]. The lysate was clarified at 22,000 x g for 20 minutes, adjusted to 0.01% triton X-100, then incubated with IgG sepharose six fast flow resin (GE) for 1 hour at 4°C. The resin was then washed three times in wash buffer (30 mM HEPES pH 7.2, 50 mM potassium acetate, 2 mM magnesium acetate, 0.2 mM EGTA, 300 mM KCl, 0.01% Triton X-100, 10% glycerol, 1 mM DTT, protease inhibitor tablets) and twice in TEV digest buffer (10 mM Tris pH 8.0, 150 mM KCl, 0.01% Triton X-100, 10% glycerol, 1 mM DTT), then incubated in TEV buffer supplemented with TEV protease for 1 hour at 16°C. The resulting eluate was collected using a centrifugal filter unit (0.1 µm, Millipore), concentrated, aliquoted, drop frozen in liquid nitrogen and stored at -80°C.

#### **A5.3.13 Single and ensemble molecule motility assays**

The single-molecule motility assay was performed as previously described (Markus et al., 2012) with minor modifications. Briefly, flow chambers constructed using slides and plasma cleaned and salinized coverslips attached with double-sided adhesive tape were coated with

anti-His antibody (200 µg/ml) then blocked with a mixture of 1% Pluronic F-127 (Fisher Scientific). EpoB-stabilized microtubules assembled from unlabeled yeast tubulin (see purification above for assembly conditions) were introduced into the chamber. Following a 5-10 minute incubation, the chamber was washed with dynein lysis buffer supplemented with 50 µM EpoB and 2 mM GTP, at which point She1-HALO-TMR was added to the chamber. After a 5-minute incubation 3XHA-DYN1-GS-HALO-647 diluted (~1:1000) in motility buffer (30 mM HEPES, pH 7.2, 50 mM potassium acetate, 2 mM magnesium acetate, 1 mM EGTA, 10% glycerol) supplemented with 1 mM DTT, 50 µM EpoB, 2 mM GTP, 1 mM Mg-ATP, 0.05% Pluronic F-127, and an oxygen-scavenging system (1.5% glucose, 1 U/µl glucose oxidase, 125 U/µl catalase) was added. TIRFM images were collected using a 1.49 NA 100X TIRF objective on a Nikon Ti-E inverted microscope equipped with a Ti-S-E motorized stage, piezo Z-control (Physik Instrumente), and an iXon X3 DU897 cooled EM-CCD camera (Andor). 561 nm, and 640 nm lasers (Coherent) were used along with a multi-pass quad filter cube set (C-TIRF for 405/488/561/638 nm; Chroma) and emission filters mounted in a filter wheel (525/50 nm, 600/50 nm and 700/75 nm; Chroma) to image She1-HALO-TMR and DYN1-HALO-647, respectively. We acquired images at 2 second intervals for 10 min. Velocity and run length values were determined from kymographs generated using the MultipleKymograph plugin for ImageJ ([http://www.embl.de/eamnet/html/body\\_kymograph.html](http://www.embl.de/eamnet/html/body_kymograph.html)).

#### **A5.4 FIGURES**

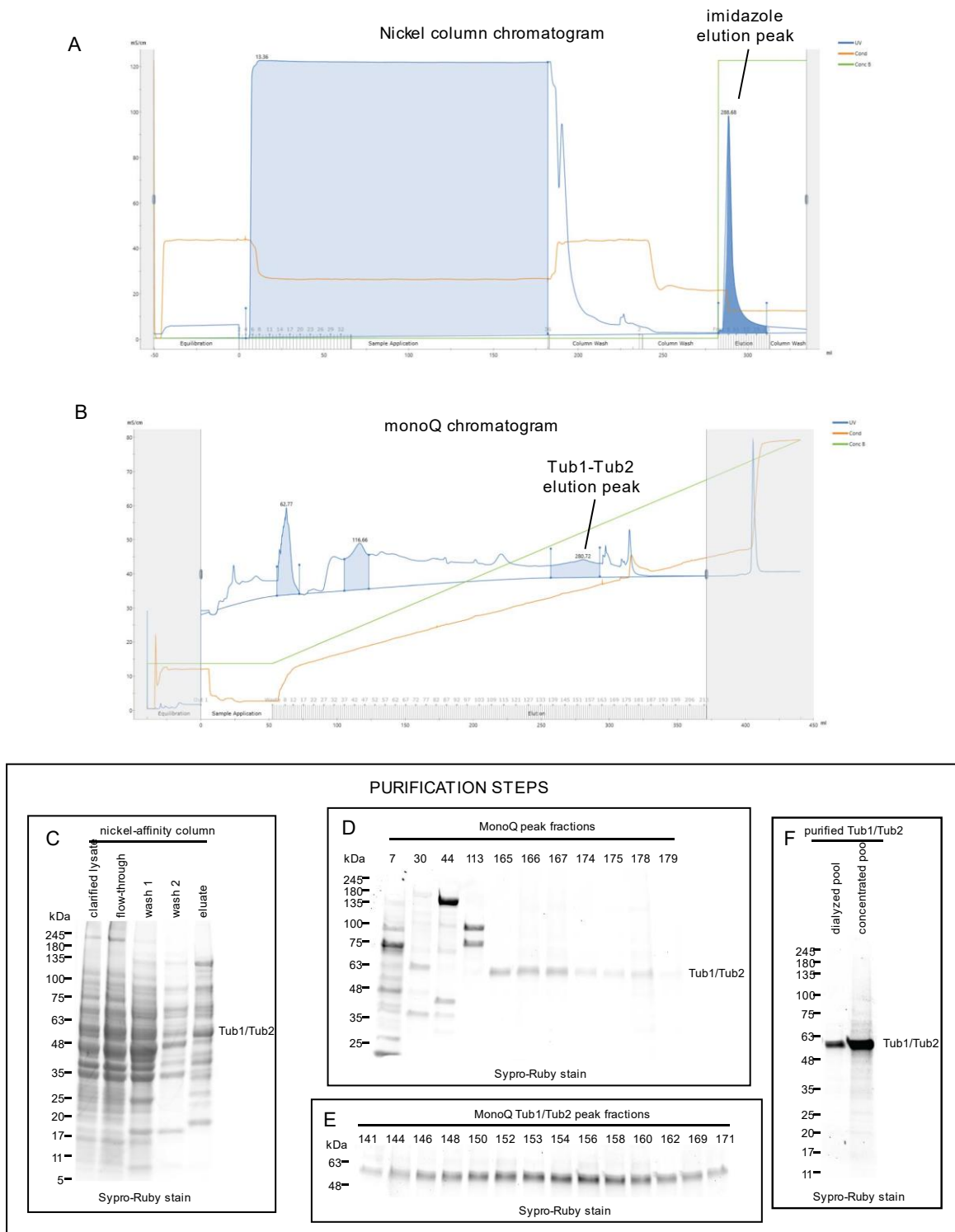


**Figure A5.1 Purification of yeast Tub1xTub2.** (a, b) Chromatogram for nickel affinity column and MonoQ column purification of wild-type yeast tubulin. (c) SDS-Page gel for nickel affinity fractions as indicated. (d-f) SDS-Page gel for MonoQ peak fractions as indicated, (e) shows tubulin fractions that were pooled for (f) dialysis and concentration (see Methods).

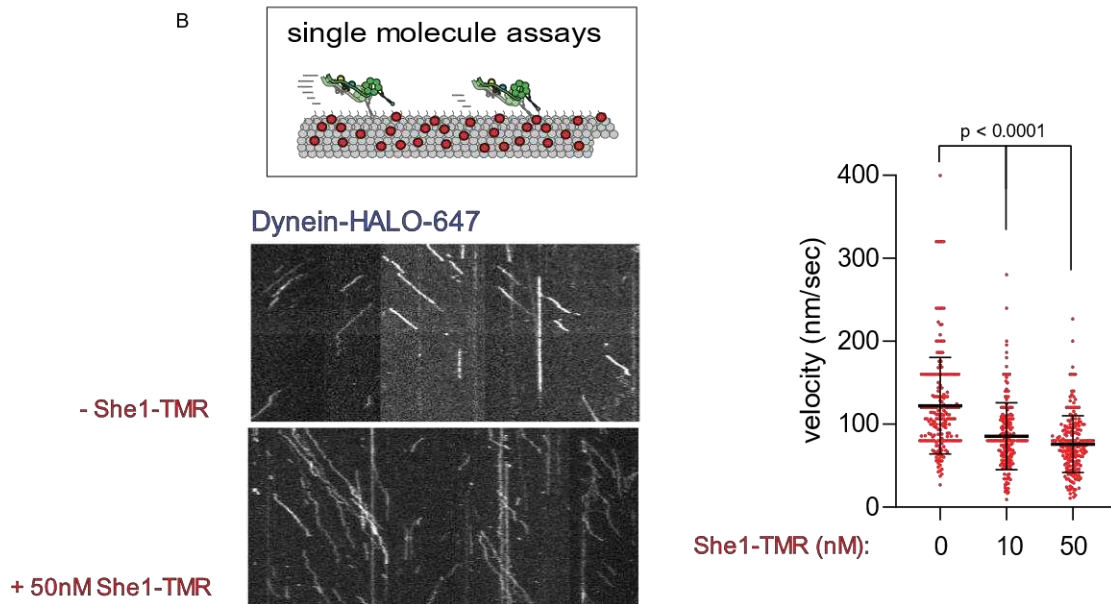
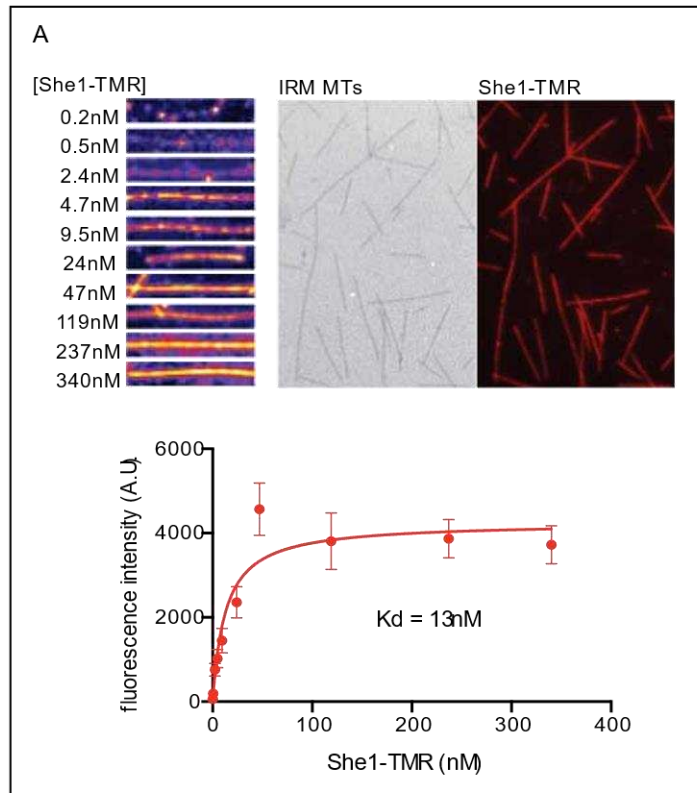


**Figure A5.2 Assessment of recombinant yeast tubulin.** (a) TIRF microtubule binding assay of She1-TMR purified from yeast on polymerized yeast microtubules stabilized with EpoB (see Methods). Heat maps representative on each She1-TMR concentration (left) and 24nM representative IRM and TMR channel (right). (b) Single molecule assay (cartoon, top) with full-length dynein motor tagged with 647 and She1-TMR purified from yeast. Representative

kymographs (where Y = time and X = distance) of Dyn1-HALO-647 have been combined without She1-TMR (top) and with She1-TMR (bottom). Quantitation on the right plots velocity in nm/sec for control and two concentrations of She1-TMR. P-values calculated from Welch's t-test using Graphad Prism software.